

การพัฒนาเทคนิค โกลบอลเรน โบล์แบบใหม่ สำหรับกำหนดลักษณะสมบัติของสเปร์ย์ที่เกิดจาก
หัวฉีดคลื่นเหนือเสียง



นางสาว สาวิตรี แสงแก้ว

สถาบันวิทยบริการ จุฬาลงกรณ์มหาวิทยาลัย

วิทยานิพนธ์นี้เป็นส่วนหนึ่งของการศึกษาตามหลักสูตรปริญญาวิศวกรรมศาสตรดุษฎีบัณฑิต

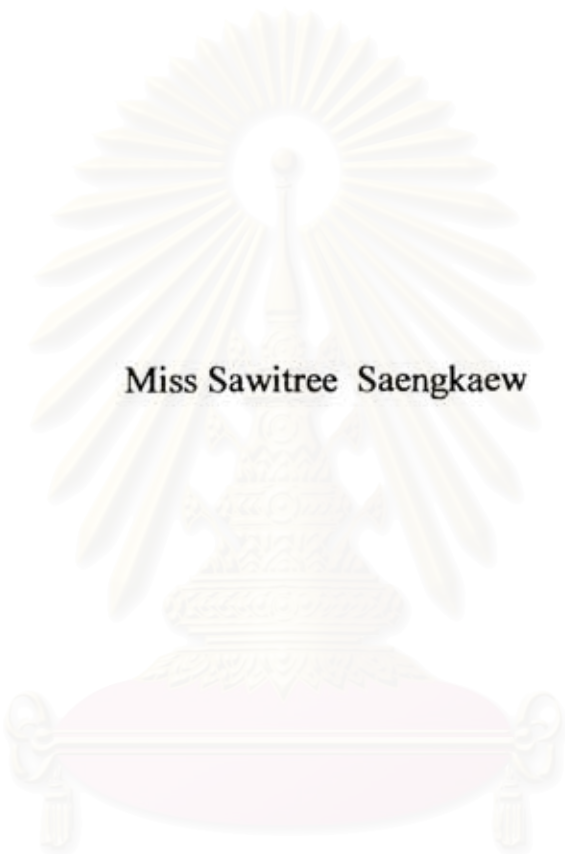
สาขาวิชาวิศวกรรมเคมี ภาควิชาวิศวกรรมเคมี
คณะวิศวกรรมศาสตร์ จุฬาลงกรณ์มหาวิทยาลัย

ปีการศึกษา 2548

ISBN 974-53-2416-7

ลิขสิทธิ์ของจุฬาลงกรณ์มหาวิทยาลัย

DEVELOPMENT OF NOVEL GLOBAL RAINBOW TECHNIQUE FOR
CHARACTERIZING SPRAY GENERATED BY ULTRASONIC NOZZLE



Miss Sawitree Saengkaew

สถาบันวิทยบริการ
จุฬาลงกรณ์มหาวิทยาลัย

A Dissertation Submitted in Partial Fulfillment of the Requirements
for the Degree of Doctor of Engineering Program in Chemical Engineering
Department of Chemical Engineering
Faculty of Engineering
Chulalongkorn University
Academic Year 2005
ISBN 974-53-2416-7

Thesis Title DEVELOPMENT OF NOVEL GLOBAL RAINBOW
TECHNIQUE FOR CHARACTERIZING SPRAY
GENERATED BY ULTRASONIC NOZZLE

By Miss Sawitree Saengkaew


Filed of study Chemical Engineering

Thesis Advisor Associate Professor Tawatchai Charinpanitkul

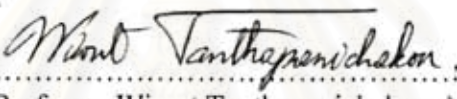
Thesis Co-advisor Assistant Professor Hathaichanok Vanisri

Thesis Co-advisor Gerard Grehan, Ph.D.

Accepted by the Faculty of Engineering, Chulalongkorn University in Partial
Fulfillment of the Requirements for the Doctor's Degree

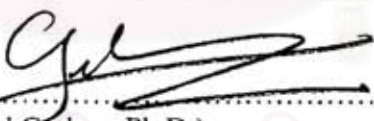

..... Dean of Faculty of Engineering
(Professor Direk Lavansiri, Ph.D.)

THESIS COMMITTEE



..... Chairman
(Professor Wiwut Tanthapanichakoon)


..... Thesis Advisor
(Associate Professor Tawatchai Charinpanitkul)


..... Thesis Co-advisor
(Assistant Professor Hathaichanok Vanisri)


..... Thesis Co-advisor
(Gerard Grehan, Ph.D.)


..... Member
(Associate Professor Suttichai Assabumrungrat)


..... Member
(Assistant Professor Pumyos Vallikul)

สาวิตรี แสงแก้ว : การพัฒนาเทคนิคโกลบอลเรนโบล์แบบใหม่ สำหรับกำหนดลักษณะสมบัติของสเปรย์ที่เกิดจากหัวฉีดคลื่นเหนือเสียง (DEVELOPMENT OF NOVEL GLOBAL RAINBOW TECHNIQUE FOR CHARACTERIZING SPRAY GENERATED BY ULTRASONIC NOZZLE) อ.ที่ปรึกษา : รศ.ดร. ธวัชชัย ชรินพานิชกุล, อ.ที่ปรึกษาร่วม : ผศ.ดร. หทัยชนก วานิชศรี, Dr. Gerard Grehan, 238 หน้า. ISBN 974-53-2416-7.

วิกฤตการณ์น้ำมันนำมาซึ่งความต้องการน้ำมันเชื้อเพลิงทดแทนน้ำมันจากปิโตรเลียม ไบโอดีเซลนับเป็นทางเลือกหนึ่งที่กำลังได้รับความสนใจเป็นอย่างมาก เนื่องจากไบโอดีเซลสามารถสังเคราะห์ได้จากพืชชนิดต่างๆ สำหรับประเทศไทยให้ความสำคัญในการสังเคราะห์ไบโอดีเซลจากปาล์มน้ำมันและสนุ่นดำ สิ่งที่สำคัญในการเพิ่มประสิทธิภาพในการเผาไหม้และลดมลพิษที่เกิดจากการเผาไหม้น้ำมันเชื้อเพลิง ก็คือ การควบคุมการถ่ายเทความร้อนและอัตราการระเหยของหยดละอองเชื้อเพลิง อย่างไรก็ตามยังไม่มีผู้ศึกษาวิจัยในประเด็นดังกล่าวอย่างจริงจัง

ประเด็นสำคัญในการออกแบบห้องเผาไหม้ได้อย่างมีประสิทธิภาพ ก็คือ ความเข้าใจอย่างลึกซึ้งซึ่งเกี่ยวกับพฤติกรรมของหยดละอองเชื้อเพลิง ซึ่งเป็นปัจจัยที่มีอิทธิพลและควบคุมกระบวนการเผาไหม้ ทั้งนี้การวัดคุณสมบัติของหยดละอองเชื้อเพลิงเป็นประโยชน์อย่างยิ่งต่อการศึกษาดังกล่าว ดังนั้นจุดประสงค์ของงานวิจัยนี้ จึงเป็นการมุ่งพัฒนาเทคนิคโกลบอลเรนโบล์ เพื่อใช้ในการวัดคุณสมบัติและการกระจายขนาดของหยดละอองจากการสเปรย์น้ำมันเชื้อเพลิงก่อนและระหว่างการเผาไหม้ สเปรย์ที่ใช้ในการศึกษามาผลิตจากหัวฉีดคลื่นเหนือเสียง ซึ่งสามารถผลิตหยดละอองที่มีขนาดเล็ก สม่ำเสมอกัน และมีความเร็วต่ำ เทคนิคเรนโบล์ และโกลบอลเรนโบล์ เป็นเทคนิคที่วัดค่าดัชนีหักเหจากตำแหน่งของการเกิดรุ้ง ซึ่งค่าดัชนีการหักเหดังกล่าวมีความสัมพันธ์โดยตรงกับคุณสมบัติและองค์ประกอบของหยดละออง ในการนี้ได้นำกระบวนการวิเคราะห์สัญญาณการกระเจิงของแสงแบบใหม่ โดยอาศัยทฤษฎีของ Nussenzweig มาใช้ ซึ่งทฤษฎีดังกล่าวนี้มีความแม่นยำสูง ในการคำนวณการกระเจิงของแสงเท่ากับทฤษฎีของ Lorenz-Mie และรวดเร็วเทียบเท่ากับทฤษฎีของ Airy

ด้วยเทคนิคใหม่ที่พัฒนาขึ้น สามารถปรับปรุงเทคนิคเรนโบล์ และโกลบอลเรนโบล์ให้มีประสิทธิภาพในการวัดมากขึ้น สำหรับการวัดอนุภาคเดี่ยวโดยการใช้เทคนิคเรนโบล์มีความแม่นยำในการวัดเท่ากับ 0.01 ไมครอนสำหรับการวัดขนาดของหยดละออง และ เท่ากับ 0.0001 สำหรับการวัดค่าดัชนีหักเห (เท่ากับ 1 องศาเซลเซียส) ในขณะที่เทคนิคโกลบอลเรนโบล์ได้พัฒนาขึ้นเพื่อวัดคุณสมบัติของหยดละอองสเปรย์ ด้วยเครื่องมือที่พัฒนาขึ้นเองนี้ สามารถบันทึกสัญญาณการกระเจิงของแสงได้ประมาณ 30 องศา ทำให้สามารถวัดการเปลี่ยนแปลงของอนุภาคเท่ากับ 300 องศา สำหรับน้ำมันก๊าด

โดยสรุป กล่าวได้ว่า ในงานวิทยานิพนธ์นี้ เทคนิคโกลบอลเรนโบล์สามารถนำมาประยุกต์เพื่อใช้วัดคุณสมบัติของละอองน้ำมันไบโอดีเซลจากน้ำมันปาล์มที่ถูกลสเปรย์ภายใต้สภาวะการเผาไหม้ ณ ความดันบรรยากาศ ได้สำเร็จเป็นครั้งแรก

ภาควิชา วิศวกรรมเคมี
สาขาวิชา วิศวกรรมเคมี
ปีการศึกษา 2548

ลายมือชื่อนิสิต *S. Sampkarn*
ลายมือชื่ออาจารย์ที่ปรึกษา *V. Charinpanichkul*
ลายมือชื่ออาจารย์ที่ปรึกษาร่วม *H. Vanisri*
ลายมือชื่ออาจารย์ที่ปรึกษาร่วม *Grehan*

4571824021 : MAJOR CHEMICAL ENGINEERING

KEY WORD: ULTRASONIC SPRAYS/ NUSSENZVEIG'S THEORY/ RAINBOW REFRACTOMETRY/ GLOBAL RAINBOW REFRACTOMETRY/ DROPLET EVAPORATION AND COMBUSTION/ TEMPERATURE MEASUREMENT/ LIGHT SCATTERING

SAWITREE SAENGKAEW : (DEVELOPMENT OF NOVEL GLOBAL RAINBOW TECHNIQUE FOR CHARACTERIZING SPRAY GENERATED BY ULTRASONIC NOZZLE) THESIS ADVISOR : [ASSOC. PROF. TAWATCHAI CHARINPANITKUL], THESIS COADVISOR : ASST. PROF. HATHAICHANOK VANISRI, GERARD GREHAN, Ph.D., 238 pp. ISBN: 974-53-2416-7.

The energy crisis leads to the increasing demand of other alternative fuel instead of petrol. Among others, many attentions are dedicated to biodiesel which can be synthesized from many different plants. For Thailand, the interest is focused on palm oil and Jatropha. As a key issue to optimize the energy extraction and to reduce the pollutant formation from liquid fuel combustion, it is essential to control heat up and evaporation of fuel droplets. However, it has not been yet systematically studied.

In order to obtain good engineering design of stable spray combustors, it is essential to develop a complete understanding of the fundamental phenomena of droplets that influence and control the overall combustion process. Also it would be advantageous to measure the fuel droplet temperature. Therefore, the objective of this work is to develop a novel global rainbow technique to determine the droplet temperature and size distribution in a free spray before and during combustion. The spray taken into account is generated by ultrasonic nozzles which could provide a relatively small mono-disperse droplets with low velocities. Rainbow and global rainbow techniques are developed based on measurement of absolute angular position of the rainbow angle depending on the refractive index of droplets, which is in turn affected by droplets temperature and composition. A new processing concept based on a development of Nussenzveig's theory is introduced to gain information of the scattered light intensity. This approach could provide accurate results comparable with Lorenz-Mie's theory and be also as fast as Airy's theory.

With this new tool, improvements of rainbow and global rainbow techniques are obtained and reported in this work. For the measurement of individual droplet, using the classical rainbow technique, it has been proved that measurement accuracy of $0.01 \mu\text{m}$ can be obtained for droplet diameter and of 0.0001 for the refractive index (corresponding to 1°C). Meanwhile, the global rainbow technique has been developed to measure the temperature of droplet sprays. The developed global rainbow setup could be employed to record the scattered light in a solid angle of about 30° , permitting to measure the variation of the refractive index on a large range, corresponding to about an evolution of 300°C for kerosene.

Finally, the developed global rainbow technique is applied to measure the temperature of biodiesel spray created by an ultrasonic nozzle under ambient and combustion conditions. To our knowledge, measurements of droplets temperature in a pure biodiesel spray flame are successfully achieved for the first time.

Department of	<u>Chemical Engineering</u>	Student's signature	<u>S. Saengkaew</u>
Field of study	<u>Chemical Engineering</u>	Advisor's signature	<u>V. Charinpanitkul</u>
Academic year	<u>2005</u>	Co-advisor's signature	<u>H. Vanisri</u>
		Co-advisor's signature	<u>Gerard Grehan</u>

Acknowledgements

First I would like to express my deepest appreciation to two important people Dr. Vanisri and Dr. Gréhan, my professors who open the chance for me to go to European country and give me a grateful experience. Let me know and learn the extensive world. Teach me to know another world which is opposite side with my country: **FRANCE**.

Thankfully Dr. Gréhan for his kindness to teach me another field which I never know before, let me know the beautiful, wonderful and interested subject: **Rainbow**. Thank for his patience to discuss endless about light scattering and rainbow which give me a great help.

Thankfully, Dr. Vanisri, one of the most important people for me, who not only teaches me the way to do research but also the way to be alive with happiness in the foreigner country.

Other two professors whose could not be forgotten: Associate Professor Charinpanitkul and Professor Gouesbet who also participate efficiently to the direction of my work.

Dr. Lavergne (Research director at ONERA, Professor at Sup Aéro, France) Dr. van Beeck (Assistant Professor at Von Karman Institut, Belgium) and Dr. Phumyos Vallikul (Assistant Professor at King Mongkut Institut of Technology North Bangkok, Thailand) deserve a special thank for their effort as a reviewer of this thesis.

Also special thank to all of my colleague in LESP. In particular to Guillaume, Camille and Gilles whose help me for PDA measurements. Thank to Annie who introduces me to the field of combustion and Loic for creating useful codes as Debye code. Henry who always helps me for computer problems. Muriel who organizes each time my travels and solve administration difficulties for me. Thank my best friend Ling Hong and also Yohann whose all the time helps me when I need help. All the mechanical technicians whose instruct and repair my ultrasonic nozzles. Philippe and Jean, the electrical workshop men whose save the life of the ultrasonic power supply and smile to me with kindness let me remind my country.

I would like to express my deepest appreciation to French Ministère délégué à la Recherche et aux Nouvelles Technologies in the framework of “co-tutelle de these” and to Thai Government for a Golden Jubilee Grant from the Thai Research Fund for their financial support throughout of my study.

Furthermore, my work has been also partially supported by the European Community programs Interreg III “the intelligent engine II” and the “MUSCLES G4RD-CT-2002-00644” program. This work would not be successful without being kindly supported for all of them.

Mostly, my thanks to my family, who always encourages and believes in me more than I do myself.

TABLE OF CONTENTS

Abstract in Thai		IV
Abstract in English		V
Acknowledgements		VI
Table of contents		VII
List of illustrations		X
List of tables		XVIII
Nomenclature		XX
Chapter I	Introduction	1
	1.1 Objective.....	5
	1.2 Scope of study.....	5
	1.3 Obtained benefit.....	6
Chapter II	Ultrasonic nozzle	7
	2.1 Developed ultrasonic nozzle.....	8
	2.2 Droplet size prediction.....	11
	2.3 Measurement of the spray characteristics.....	14
	2.4 Nozzle temperature measurements.....	31
Chapter III	Nussenzveig's theory and its improvement	33
	Preliminaries.....	35
	3.1 At forward angle.....	41
	3.2 At backward angle.....	42
	3.2.1 Comparison between Lorenz-Mie, Debye, Nussenzveig and Airy for $p=2$	42
	3.2.2 Comparison between Lorenz-Mie, Debye, Nussenzveig for $p = 0$	47
	3.2.3 Comparison between Lorenz-Mie, Debye, Nussenzveig for the interference between $p=0$ and $p=2$	48
Chapter IV	Rainbow principles and applications by using Nussenzveig's theory	49
	4.1 Forward region.....	49
	4.1.1 Geometrical optic formula analysis.....	49
	4.1.2 Nussenzveig's analysis.....	54
	4.1.3 Forward automatic processing based on Nussenzveig's theory.....	62
	4.2 Backward measurement (Rainbow refractrometry).....	67

	4.2.1 Rainbow by Geometrical optic.....	70
	4.2.2 Rainbow by Airy's theory.....	71
	4.2.3 Rainbow by Nussenzweig's theory.....	75
	4.2.4 Backward automatic processing based on Nussenzweig's theory.....	77
	4.3 Automatic dual processing of forward and backward signal.....	84
	4.3.1 Dual processing of simulated signal.....	84
	4.3.2 Dual processing of experimental signal.....	90
	4.4 Classical rainbow limitation.....	93
	4.4.1 Particles with radial gradients.....	93
	4.4.2 Deformed particles.....	102
Chapter V	Global rainbow principles and applications by using Nussenzweig's theory.....	105
	5.1 Global rainbow principle.....	105
	5.2 Global rainbow processing.....	110
Chapter VI	Experimental setup and results.....	125
	6.1 Experimental setup.....	125
	6.1.1 Optical alignments.....	125
	6.1.2 Calibration.....	129
	6.1.3 Image acquisition and processing.....	132
	6.2 Exemplifying results.....	136
	6.2.1 Spray temperature measurement at ambient temperature.....	136
	6.2.2 Bio-diesel spray temperature measurement in combustion.....	141
Chapter VII	Conclusion.....	163
References	165
Appendices	168
Appendix A	Theoretical tools for light scattering by spherical particle	169
	Lorenz-Mie Theory.....	170
	Debye Theory.....	172
	Airy Theory.....	174
	The Geometrical Optic.....	175
	• Direction of scattering.....	175
	• Prediction of intensity.....	176

• Phase.....	176
Appendix B Brent method.....	180
Appendix C Published and conference papers.....	182
Biography	238



สถาบันวิทยบริการ
จุฬาลงกรณ์มหาวิทยาลัย

LIST OF ILLUSTRATIONS

Figure		page
1.1	Biodiesel production process	2
2.1	(a) Capillary wave grid. (b) Disintegration mechanism.....	8
2.2	(a) Scheme of the ultrasonic nozzle. (b) Standing wave pattern in a typical nozzle.....	9
2.3	(a) The image of the studied nozzle. (b) Power supply by Spray Tech Company.....	10
2.4	The particle diameters versus the different parameters take into account by formula 2.2.....	12
2.5	Droplet diameter versus the liquid flow rate for water spray. Blue points are for D_{32} while red points are for D_{10}	15
2.6	Droplet diameter versus flow rate (at low liquid flow rate). Blue points are for D_{32} while red points are for D_{10}	15
2.7	The PDA measured size distribution. The flow rate is equal to 7.3 cc/min.....	16
2.8	The PDA measured size distribution. The flow rate is equal to 1.9 cc/min.....	17
2.9	The PDA measured size distribution. The flow rate is equal to 0.5 cc/min.....	17
2.10	Example of a pulsed spray for the flow rate of 0.047 cc/min. The time scale is in μ s.....	18
2.11	The PDA measured size distribution. The flow rate is equal to 0.038 cc/min.....	18
2.12	The PDA measured size distribution. The flow rate is equal to 0.047 cc/min.....	19
2.13	The PDA measured size distribution. The flow rate is equal to 0.066 cc/min.....	19
2.14	The comparison between the Rajan and Pandit prediction and the PDA measurement. The green triangles represent the D_{10} data while the blue triangles are for D_{32}	20
2.15	The diameter versus the excitation. The flow rate is equal to 1.9 cc/min and the frequency is equal to 45.3 kHz.....	22
2.16	The diameter versus the excitation. The flow rate is equal to 0.028 cc/min and the frequency is equal to 45.3 kHz.....	22
2.17	Size distribution measured for three different excitation powers for the flow rate equals to 1.9 cc/min.....	23
2.18	The measured power versus the power button position.....	23
2.19	Comparison between size distribution for water and ethanol.....	24
2.20	Diameter versus the flow rate with four products as parameter.....	25
2.21	Size distribution for diesel.....	26

Figure	page
2.22	Example of PDA measurement at 5 mm from the orifice..... 27
2.23	Processing of PDA temporal series. (a) number of particles versus time, (b) Longitudinal velocity and diameter versus time, (c) Transverse velocity versus longitudinal velocity, (d) diameter versus transverse velocity..... 28
2.24	ILIDS measurements. (a) Example of a recorded ILIDS image, (b) Size histogram obtained by analysing 50 ILIDS images..... 30
2.25	Example of a PIV/ILIDS map. The arrows give the velocities (direction and amplitude). From the fringes the size of the droplets could be extracted while the velocity is obtained from standard PIV software..... 30
2.26	(a) Maps of infrared emission for the nozzle just at the beginning of excitation and 15 minutes later. (b) Temperature at the nozzle orifice versus time..... 31
3.1	Definition of the impact parameter and van de Hulst's notation..... 35
3.2	The domain of application of the different Nussenzveig formulae for the rainbow ($p=2$)..... 38
3.3	Comparison between Lorenz-Mie, Debye and Nussenzveig for the interference between $p=0$ and $p=1$ 41
3.4	Comparison of the rainbow ray intensity predicted by Lorenz-Mie, Debye ($p=2$), Debye ($p=0$ and 2), Airy and Nussenzveig theories. The size parameter is equal to 50 and the refractive index is equal to 1.33. The incident wavelength is $0.6 \mu\text{m}$ 42
3.5	Comparison of the rainbow ray intensity predicted by Lorenz-Mie, Debye ($p=2$), Debye ($p=0$ and 2), Airy and Nussenzveig theories. The size parameter is equal to 500 and the refractive index is equal to 1.33. The incident wavelength is $0.6 \mu\text{m}$ 43
3.6	Comparison between rainbow predictions by Nussenzveig and Debye (with $p=2$) theories. The size parameter is equal to 500 and the refractive index is 1.33. The incident wavelength is $0.6 \mu\text{m}$... 44
3.7	Ratio of Debye normalized intensity over Nussenzveig normalized intensity for various particle sizes..... 45
3.8	Comparison of scattering diagrams obtained from the Debye and modified Nussenzveig predictions for various particle sizes..... 46
3.9	Contribution in the Alexander's dark band. Relative importance of the reflected light ($p=0$), one internally reflected ($p=2$) and twice internally reflected ($p=3$)..... 47
3.10	The main rainbow, including the ripple structure, for a size parameter of 500 and a refractive index of 1.33. Comparison between Lorenz-Mie, Debye ($p = 0 + 2$) and Nussenzveig ($p = 0 + 2$)..... 48

Figure	page
4.1	Scattered intensity distribution in the forward region computed by Lorenz-Mie theory for a droplet with the diameter equal to 50 μm and refractive index equal to 1.33 for a wavelength equal to 0.5145 μm 50
4.2	Fringe spacing as a function of droplet diameter. The parameter is the refractive index value..... 51
4.3	Fringe spacing as a function of droplet diameter. The parameter is the mean scattering angle..... 52
4.4	Fringes spacing versus the particle diameter corresponding to equation 3.18 with parameter is the average collecting angle..... 53
4.5	Angular patterns of horizontally (top) and vertically (bottom) polarized cross section for 40 μm droplets with different refractive indices computed by Lorenz-Mie theory..... 53
4.6	Scattering light distribution around the angle of 30°-60° for different values of refractive index..... 54
4.7	The forward scattering diagram for a water droplet ($N=1.33-0.0i$) with a diameter equal to 100 μm (figure 3.17a) and its associated FFT (figure 3.17b)..... 55
4.8	Index of the dominant spatial frequency component of the intensity light distribution as computed by the FFT versus particle diameter. Optical parameters; wave length 0.5145 μm , scattering angle between 25° to 45° and refractive index of 1.333..... 55
4.9	Index of the dominant spatial frequency component of the intensity light distribution as computed by the FFT versus particle diameter. Optical parameter; wave length 0.5145 μm , scattering angle between 27° to 33° and refractive index of 1.333..... 56
4.10	FFT and its spline versus diameter..... 57
4.11	Phase different between the scattered light by particle with diameter equal to 73 and 75 μm ($N=1.333$, $\lambda=0.5145 \mu\text{m}$, 2048 points)..... 57
4.12	The possible answers of size obtained from main frequency analysis for different assumed refractive index value..... 59
4.13	The possible particle diameter extracted by frequency processing versus the assumed refractive index value..... 59
4.14	Comparison of the forward scattered light computed by Lorenz-Mie and Nussenzveig theory and its associated FFT spectrum ($N=1.342$, $\lambda=0.5145 \mu\text{m}$, 2048 point)..... 60
4.15	The possible answers of size obtained from frequency and phase processing versus the refractive index..... 61
4.16	Convergence of the Brent method at forward only taking into account the frequency. The refractive index is assumed perfectly know..... 62
4.17	Scheme of the phase evolution and definition of d_{\min} and d_{\max} used in Brent method..... 63
4.18	Convergence of the Brent method at forward taking into account the frequency (in red) and the phase (in green). 64
4.19	Measured diameters versus nominal diameters with the refractive index as a parameter..... 65

Figure	Page	
4.20	Measured diameters versus nominal diameters. The parameter is the refractive index value. Periodicity of the phase has been taken into account.....	66
4.21	(a) Refractive index for hydrocarbon with different number j of carbon atom (b) Refractive index of a sulfuric acid-water mixture as a function of the mass fraction of sulfuric acid.....	67
4.22	The relationship between refractive index and the temperature for water and ethyl alcohol.....	68
4.23	Scattering diagram around rainbow angle simulated by Lorenz-Mie theory (for water $N=1.333$).....	68
4.24	Illustration of the scattering modes for first and second rainbows influencing the intensity in the rainbow region.....	69
4.25	Calculated first rainbow position as a function of refractive index according to geometrical optics. ($\lambda=0.5145 \mu\text{m}$).....	70
4.26	Calculated first rainbow position as a function of refractive index for different diameter according to Airy's theory.....	71
4.27	Scattering Diagram around rainbow angle for different diameters simulated by Airy Theory.....	72
4.28	Scattering Diagram around rainbow angle for different refractive indices simulated by Airy Theory.....	73
4.29	Influence of the ripple structure on the accuracy of refractive index determination in comparison to signals from pure second-order refraction.....	74
4.30	The comparison of the rainbow light distribution simulated by Lorenz-Mie and Nussenzveig theory ($d=50 \mu\text{m}$, $N=1.333$, $\lambda=0.5145 \mu\text{m}$ and 1000 points).....	75
4.31	The comparison of the rainbow distribution simulated by Lorenz-Mie and Nussenzveig theory. ($d=30 \mu\text{m}$, $N=1.33$, $\lambda=0.5145 \mu\text{m}$ and 2048 points).....	76
4.32	The comparison of the rainbow distribution simulated by Lorenz-Mie and Nussenzveig's theory. ($d=30 \mu\text{m}$, $N=1.38$, $\lambda=0.5145 \mu\text{m}$ and 2048 points).....	76
4.33	A backward signal. The diameter is equal to $100 \mu\text{m}$ and the refractive index is equal to 1.33.....	77
4.34	Test signals and associated correlations.....	78
4.35	Behaviour of the maximum of correlation for signals with ripple.....	78
4.36	Definition of the integral criteria.....	79
4.37	Comparison of a Lorenz-Mie signal with a test signal with a very bad evaluation of the refractive index and the associated correlation.....	80
4.38	Filtered signals and correlation.....	80
4.39	Series of iteration to determine the refractive index for a droplet with a diameter equal to $100 \mu\text{m}$ and a refractive index equal to 1.38.....	83

Figure	page
4.40	Iterations to find both the particle diameter and refractive index..... 84
4.41	Idem as figure 3.50 but only the iteration on the refractive index are plotted..... 85
4.42	Comparison of the scattering diagram computed by using Lorenz-Mie theory and Debye theory ($p=0,1$ and 2) for a diameter equal to $82.36 \mu\text{m}$ and a refractive index equal to 1.364 88
4.43	Comparison between Lorenz-Mie and Debye prediction for a particle with a diameter equal to $100 \mu\text{m}$ (a) for $N=1.364$, (b) for $N=1.38$ 88
4.44	The ONERA experimental setup..... 90
4.45	The dual ONERA signals..... 90
4.46	Comparison between experimental ONERA signals and the best Nussenzveig fit..... 91
4.47	Measured Refractive index versus measured diameter, from ONERA experimental results..... 92
4.48	Measured correlation refractive index/size..... 92
4.49	Examples of radial gradients. The parameter is the value of the coefficient b 93
4.50	Scattering diagram around the rainbow angle for a particle with radial gradient. The parameter is the number of layers..... 94
4.51	Scattering diagram in forward direction for a particle with radial gradient. The parameter is the number of layers..... 95
4.52	Effect of a gradient on forward scattering diagrams. Comparison between the forward scattering diagram for a homogeneous particle ($N=1.36$ and $d=100\mu\text{m}$) and non-homogeneous particle ($d=100 \mu\text{m}$, $N_c=1.36$, $N_s=1.328$ and $b=2$, $\lambda=0.5145 \mu\text{m}$). The frequency of the signal is essentially unaffected..... 96
4.53	Effect of a gradient on backward scattering diagrams. Comparison between the backward scattering diagram for two homogeneous particles ($d=100 \mu\text{m}$, $N=1.36$ or 1.328) and for a non homogeneous particle ($d=100 \mu\text{m}$, $N_c=1.36$, $N_s=1.328$ and $b=2$, $\lambda=0.5145 \mu\text{m}$). The rainbow is shifted, and for a positive value of b , the rainbow for the particle with gradient is not located between the rainbows for the two extreme refractive index values..... 96
4.54	The scattering diagrams show the effect of coefficient b on rainbow location. (for wavelength = $0.5145 \mu\text{m}$, particle diameter = $100 \mu\text{m}$, $N_c=1.36$ and $N_s=1.315$ for 100 Layers..... 97
4.55	The scattered light distribution for different values of the refractive index at the surface with a constant value at the center equal to 1.36 ($\lambda=0.5145\mu\text{m}$, particle $d=100 \mu\text{m}$, $N_c=1.36$, $b=2$ and 100 layers)..... 98

Figure	Page	
4.56	Comparison of the scattered light between Lorenz-Mie's computations for a multilayer particle ($d=100\ \mu\text{m}$, $N_c=1.36$ and $N_s=1.352$, $b=2$) and Nussenzweig's computation for a homogeneous particle ($d=100.07\ \mu\text{m}$, $N=1.361$) (a) in forward region (b) in backward region.....	99
4.57	Comparison of the scattered light at primary and secondary rainbows for non-homogeneous particle and equivalent homogeneous particle.....	99
4.58	The relationship between the equivalent particle refractive index and the real surface refractive index with different values of b	101
4.59	Effect of a non sphericity on the rainbow location. (a) original scattering diagrams (b) filtered scattering diagrams.....	102
4.60	Shift of the rainbow position versus ellipticity. (a) Position of the main rainbow peak (red circles) and of the two first supernumerary peaks versus ellipticity. (b) Comparison of the rainbow shift as numerically predicted by Moebius.....	103
5.1	An image and the scattered light of global rainbow.....	105
5.2	(a) Global rainbow signal with the number of particles as a parameter. (b) Number of particles by diameter. The size distribution parameters are identical for the three cases.....	106
5.3	Example of Global rainbow computation. The important fact is the differences at large scattering angles between corrected Nussenzweig's predictions and Airy predictions.....	107
5.4	(a) Comparison between global rainbow prediction by Lorenz-Mie's theory, Airy's theory and Nussenzweig's theory adding correcting coefficient and no coefficient. (b) The size distribution corresponding to the global rainbow patterns in figure 5.4(a).....	108
5.5	Behavior of the global rainbow signal simulated by Nussenzweig's theory. (a) displays three size distributions with the same width. (b) displays the associated global rainbow patterns. The main effect is the width of the first peak.....	109
5.6	Behavior of the global rainbow signal. (a) displays five size distributions with the same mean diameter ($50\ \mu\text{m}$). (b) displays the associated global rainbow patterns. The reduction of the Airy oscillations with width of the size distribution is clear.....	109

Figure	page	
5.7	Effect of a variation of the refractive index on the global rainbow pattern. (for a mean diameter equal to 50 μm with size distribution 400).....	110
5.8	Definition of the points used in the inversion algorithm.....	111
5.9	The flow chart of the inversion scheme based two singular points.....	112
5.10	Comparison between the measured of D_{airy_maxi} and D_{airy_inflec} versus number of filtered points from different mean diameters with the same size distribution and refractive index equal to 250 and 1.33 respectively.....	114
5.11	Comparison between the measured of N_{airy_maxi} and N_{airy_inflec} versus number of filtered points from different mean diameters with the size distribution and refractive index equal to 250 and 1.33 respectively.....	114
5.12	The Inversion code flowchart.....	118
5.13	The global rainbow inversion code interface.....	119
5.14	The extracted size distribution (histograms) compared to the initial size distribution (continuous lines).....	120
5.15	Case 1 (a) The original and reconstructed global rainbow signal (b) The original (in red) and extracted size distribution (in blue).....	121
5.16	Case 2 (a) The original and reconstructed global rainbow signal. (b) The original (in red) and extracted size distribution (in blue).....	122
5.17	Case 3 (a)The original and reconstructed global rainbow signal (b)The original (in red) and extracted size distribution (in blue).....	123
6.1	The experimental global rainbow set up realized.....	125
6.2	Schematic of the scattered light behaviour at the focus plane.....	126
6.3	The effect of diaphragm.....	127
6.4	Kappa CCD camera.....	127
6.5	The magnification of the microscope.....	129
6.6	Liquid jet image at the flow rate of 60 cc/min.....	129
6.7	Recorded signal by the liquid jet.....	130
6.8	Computed signal by the liquid jet.....	131
6.9	Relationship between pixels and scattering angles.....	131
6.10	The calibration code.....	132
6.11	Image of the scattered light by liquid jet used for calibration.....	133
6.12	Image of the scattered light by water spray.....	133
6.13	Original and filtered global rainbow signal with different dimensions of the integration zone.....	134
6.14	Original and filtered global rainbow signal with different position for the same dimension of the integration zone.....	135

Figure	Page	
6.15	The light scattered by a liquid jet for calibration. Comparison before and after the series of experiments.....	136
6.16	The calibration points and linear regression before and after the experiments.....	137
6.17	The recorded images of the scattered light by water and ethanol spray and their scattered light distribution.....	138
6.18	The figure from enlarging figure 6.17 to exemplify the filtering.....	138
6.19	Comparison between the original global rainbow, the filtered one and the recomputed with the extracted refractive index and size distribution. Case water 1 of table 6.2.....	140
6.20	The extracted size distribution for the water case 1 of table 6.2.....	140
6.21	Setup calibration for large refractive index range	142
6.22	Example of global rainbow and their processing.	144
6.23	Measurement of the refractive index on a large range of refractive index by using a unique optical configuration.....	145
6.24	Properties of the biodiesel sprays generated by the ultrasonic nozzle used for biodiesel experiments (working frequency 60 ± 1 kHz). Left column, size distributions, right column the longitudinal and transversal velocity versus the time, average on a temporal window equal to 1s	147
6.25	Comparison of the size distribution measured by global rainbow and PDA on a spray of biodiesel at 50%.....	148
6.26	A series of consecutively recorded global rainbow from a biodiesel 15% spray.....	149
6.27	The size distribution extracted from the global rainbow images of figure 6.26.....	150
6.28	Measured refractive index versus time.....	151
6.29	A side and a top schematic view of the burner.....	152
6.30	Scheme of the burner realized at Rouen University. Inside view.....	152
6.31	Photo of the burner: front view.....	153
6.32	Photo of the burner: backward view.....	153
6.33	View of a typical flame. The droplets of biodiesel 15% burn in air without adding other fuel.....	154
6.34	Snap-shot of biodiesel spray without air and combustion.....	155
6.35	Snap-shot of biodiesel spray with air but without combustion.....	156
6.36	Snap-shot of biodiesel spray with air and under combustion.....	157
6.37	Snap-shot of biodiesel spray with air and under combustion.....	158
6.38	Snap-shot of biodiesel spray with air and under combustion.....	159
6.39	The measured temperature versus the percentage of biodiesel.....	160

LIST OF TABLES

Table		page
2.1	The measurement of mean diameter of water spray for different conditions.....	16
2.2	The measurement of means diameter for water pulsed spray at low flow rate.....	21
2.3	The liquid properties.....	24
3.1	Coefficients of linear regressions for modified Nussenzweig's predictions.....	45
4.1	The measured diameters by using the developed automatic forward processing.....	64
4.2	The number of periods to extract the perfect diameter.....	66
4.3	The behaviour of the correlation integral.....	79
4.4	Effect of the filtering on the extracted refractive index value. The diameter is assumed to be perfectly known.....	81
4.5	The sensitivity of the backward procedure to the test diameter.....	82
4.6	Dual processing of signal.....	86
4.7	Study of ethanol measurement ($N=1.364$).....	87
4.8	Automatic processing of backward filtered signal with $j = 11$. The diameter is assumed perfectly known.....	88
4.9	Processing of signals computed for $N=1.364$ by Debye's theory for $p=0,1$ and 2. The average measured refractive index is equal to 1.364036 and the standard deviation is equal to $s=3.9e-5$	89
5.1	The extracted diameters and refractive index for different size distributions. The value of the refractive index used for the direct computation was 1.33.....	113
5.2	The extracted refractive indices from simulated signal by assuming the size distribution is the Gaussian distribution.....	120
5.3	The extracted refractive indices from simulated signal for arbitrary size distribution with the refractive index equal to 1.3333.....	123
6.1	The liquid jet diameter measured for the different liquid flow rates....	130

Table	page
6.2 The measured refractive index values of water and ethanol spray, for the two linear regressions, at close and long distance of the nozzle.....	139
6.3 The liquid properties of different biodiesel concentrations.....	141

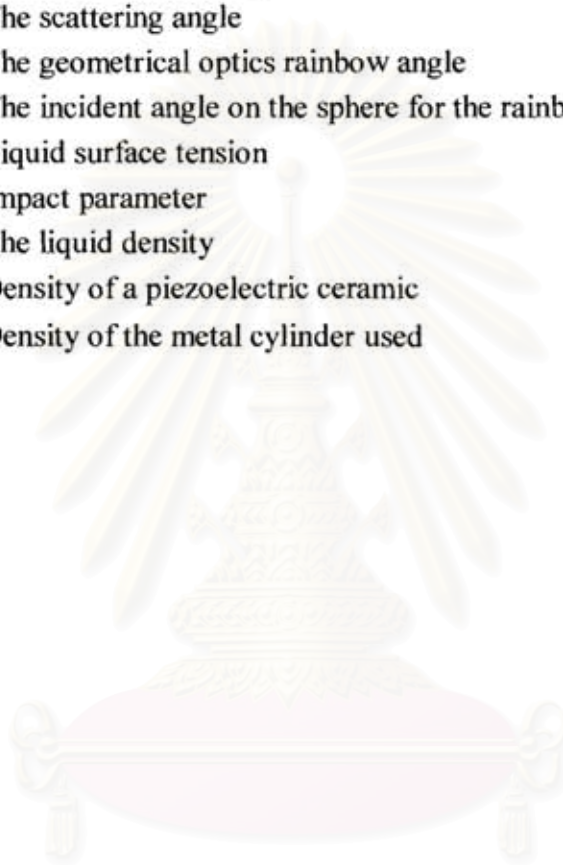


สถาบันวิทยบริการ
จุฬาลงกรณ์มหาวิทยาลัย

NOMENCLATURE

A	Nozzle area
A_c	Surface area of piezoelectric ceramic
A_i	Surface area of the metal cylinder used
Am	The amplitude of sound wave
Am_{crit}	The minimum amplitude of the sound wave to create droplets
a	Particle radius
b	Coefficient of the exponential law for gradient
C_c	Sound velocity in piezoelectric ceramic
C_i	Sound velocity in the metal cylinder used
D_{10}	The mean diameter
D_{32}	The Sauter diameter
d, d_p	Particle diameter
CAM	Complex Angular Momentum
f	Frequency of ultrasonic nozzle
$f_{reflexion}$	The complex amplitude function of reflection
$f_{refraction}$	The complex amplitude function of refraction
$f_{rainbow}$	The complex amplitude function for scattering angle close to the rainbow
f'_2, f''_2	The complex amplitude functions for scattering angle far enough from the rainbow angle
I_N	Dimensionless number
i	The angle of incidence of a ray on the particle
i	Complex ($i = \sqrt{-1}$)
ILIDS	Interferometric Laser Imaging Droplets Sizing
LDV	Laser Doppler velocimetry
LIF	Laser Induced Fluorescence
MDR	Morphology Dependent Resonances
N	The real part of the refractive index
N_c	The real part of the refractive index at the center of the particle
N_s	The real part of the refractive index at the surface of the particle
nls	Non-negative least square
Oh	The Ohnesorge number
PDA	Phase Doppler Anemometer
PIV	Particle Image Velocimetry
p	The ray name according to van de Hulst notation
Q	Liquid flow rate
r	The angle of refraction of a ray in the particle
x	The distance between a ray and the particle axis

We	The Weber number
α	The size parameter, $\alpha=\pi d/\lambda$
χ	Velocity of the sound in liquid
ε	The deviation from the rainbow angle
η	Liquid viscosity
λ	The incident wavelength
θ	The scattering angle
θ_R	The geometrical optics rainbow angle
θ_{iR}	The incident angle on the sphere for the rainbow ray
σ	Liquid surface tension
ρ	Impact parameter
ρ	The liquid density
ρ_c	Density of a piezoelectric ceramic
ρ_i	Density of the metal cylinder used



สถาบันวิทยบริการ
จุฬาลงกรณ์มหาวิทยาลัย

CHAPTER I

INTRODUCTION

Due to the increase of the petroleum cost, bio-energy is seen as one of the key options to mitigate greenhouse gas emissions and substitute fossil fuels. For example, over the past 10-15 years in the European Union, heat and electricity production from biomass increased with some 2% and 9% per year, respectively, between 1990 and 2000 and bio fuel production increased about eight-fold in the same period. Biomass contributed some two-third of the total renewable energy production in the European Union or 4% of the total energy supply in 1999. Given the targets for heat, power and bio fuels, this contribution may rise to some 10% in 2010 [1].

Biodiesel are fuels derived from vegetable, animal, waste oil, etc. Their life cycle is court so that this energy source is renewable. Although the use of vegetable oils in diesel engine was nearly as old as the diesel engine itself, the use of vegetable oil has not been developed because the petrol and its derivatives was very cheaper. However, nowadays the conjunction of the increase of petrol prices, the new pollution norms, the struggle with greenhouse effect, and the fact that bio mass is world width distributed make biodiesel becomes a promising alternative fuel. In Thailand, the interest for the use of biodiesel is also important, especially with biodiesel producing from palm oil or *Jatropha curas* Linn.

The production processes for biodiesel are well known. There are three basic routes to biodiesel production from oils and fats:

- base catalyzed transesterification of the oil;
- direct acid catalyzed transesterification of the oil;
- conversion of the oil to its fatty acids and then to biodiesel.

Most of the biodiesel produced today is done with the base catalyzed reaction for several reasons:

- it is low temperature and pressure;
- it yields high conversion (98%) with minimal side reactions and reaction time;
- it is a direct conversion to biodiesel with no intermediate compounds;
- no exotic materials of construction are needed.

The chemical reaction for base catalyzed biodiesel production is depicted below. One hundred pounds of fat or oil (such as soybean oil) are reacted with 10 pounds of a short chain alcohol in the presence of a catalyst to produce 10 pounds of glycerin and 100 pounds of biodiesel. The short chain alcohol, signified by ROH (usually methanol, but sometimes ethanol) is charged in excess to assist in quick conversion. The catalyst is usually sodium or potassium hydroxide that has already been mixed with the methanol. R', R'', and R''' indicate the fatty acid chains associated with the oil or fat which are largely palmitic, stearic, oleic, and linoleic acids for naturally occurring oils and fats.

The Biodiesel Reaction.

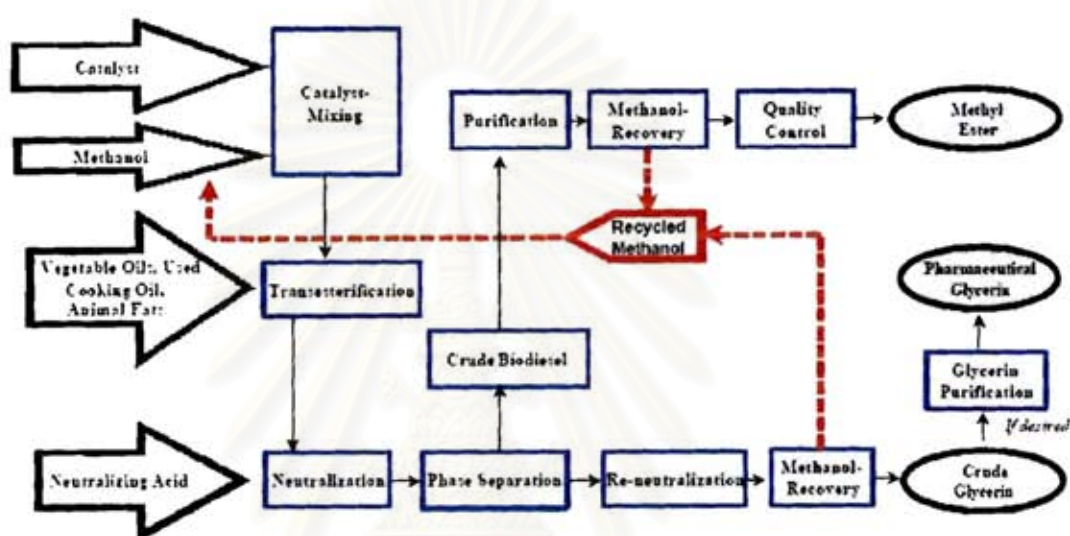
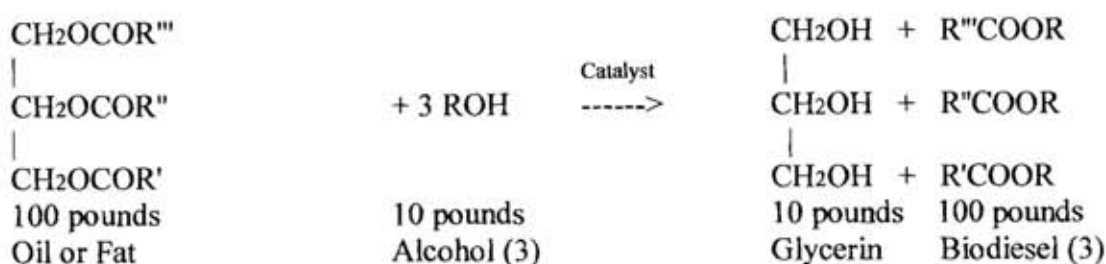


Figure 1.1 Biodiesel production process

Figure 1.1 shows an example of a simple biodiesel production flow chart. The base catalyzed production of biodiesel generally occurs using the following steps:

Mixing of alcohol and catalyst. The catalyst is typically sodium hydroxide (caustic soda) or potassium hydroxide (potash). It is dissolved in the alcohol using a standard agitator or mixer.

Reaction. The alcohol/catalyst mix is then charged into a closed reaction vessel and the oil or fat is added. The system from here on is totally closed to the atmosphere to prevent the loss of alcohol. The reaction mix is kept just above the boiling point of the alcohol (around 160 °F) to speed up the reaction and the reaction takes place. Recommended reaction time varies from 1 to 8 hours, and some systems recommend the reaction takes place at room temperature. Excess alcohol is normally used to ensure total conversion of the fat or oil to its esters. Care must be taken to monitor the amount of water and free fatty acids in the incoming oil or fat. If the free fatty acid level or water level is too high it may cause problems with soap formation and the separation of the glycerin by-product downstream.

Separation. Once the reaction is complete, two major products exist: glycerin and biodiesel. Each has a substantial amount of the excess methanol that was used in the reaction. The reacted mixture is sometimes neutralized at this step if needed. The glycerin phase is much denser than biodiesel phase and the two can be gravity separated with glycerin simply drawn off the bottom of the settling vessel. In some cases, a centrifuge is used to separate the two materials faster.

Alcohol Removal. Once the glycerin and biodiesel phases have been separated, the excess alcohol in each phase is removed with a flash evaporation process or by distillation. In others systems, the alcohol is removed and the mixture neutralized before the glycerin and esters have been separated. In either case, the alcohol is recovered using distillation equipment and is re-used. Care must be taken to ensure no water accumulates in the recovered alcohol stream.

Glycerin Neutralization. The glycerin by-product contains unused catalyst and soaps that are neutralized with an acid and sent to storage as crude glycerin. In some cases the salt formed during this phase is recovered for use as fertilizer. In most cases the salt is left in the glycerin. Water and alcohol are removed to produce 80-88% pure glycerin that is ready to be sold as crude glycerin. In more sophisticated operations, the glycerin is distilled to 99% or higher purity and sold into the cosmetic and pharmaceutical markets.

Methyl Ester Wash. Once separated from the glycerin, the biodiesel is sometimes purified by washing gently with warm water to remove residual catalyst or soaps, dried, and sent to storage. In some processes this step is unnecessary. This is normally the end of the production process resulting in a clear amber-yellow liquid with a viscosity similar to petrodiesel. In some systems the biodiesel is distilled in an additional step to remove small amounts of color bodies to produce a colorless biodiesel.

Nevertheless, the biodiesel channel is penalized by a small yield in the oil-yielding plants farming and by the generation of a by-product: glycerin. As previously mentioned, the glycerin could be used by cosmetic, pharmaceuticals and soap industries but the market is already saturated. As an increasing of the biodiesel production imposes an increasing of the glycerin production, new uses of glycerin must be found.

When produced, to obtain energy, the biodiesel must be burnt. This combustion necessitates the atomization of the liquid in a fog of droplets: the spray. Gas turbines, liquid rocket motors, and oil-fired furnaces utilize the spray combustion of continuously injected liquid fuels while IC engine are based on the spray combustion of pulsed injected liquid fuel. About the advantages of biodiesel combustion, the opinions are shared. Oxygen in methyl ester improves the lubrication of engines and help to have complete combustion. Biodiesel combustion does not reject SO_2 , rejects less CO and HC but produces more CO_2 and NOX. Furthermore, with pressure injectors as biodiesel viscosity is greater, the injected droplets are bigger. The combustion characteristics of a spray depend largely on the droplet diameter. Droplet diameter acts through the droplet inertia effect and the vaporization effect which depends on the droplet temperature. However, few systematic studies of droplet diameter effects on the spray combustion have been conducted. To study the combustion of spray, combustion diagnostics have to be used.

Combustion diagnostics have come a long way from visual inspection of a flame to detailed analysis of a combustion process with a multitude of sophisticated techniques, often using lasers. Light, or more generally, electromagnetic radiation, is the only way to “spy” on the fundamentals of combustion inside the chemically active flame front. Modern laser based diagnostics permit the study of combustion, even in the interior of engines, gas turbines, and large-scale combustors. Using spectroscopic and non-spectroscopic techniques it is now possible to measure gas phase velocity, pressure, temperature and species concentrations. However, some of these techniques are so complex that they are unsuitable for applications in actual spray environments.

In order to be able to design and develop efficient and stable spray combustors, it is essential that we first develop a complete understanding of the fundamental phenomena that influence and control the overall spray combustion process. In this regard, advanced diagnostics are essential not only for studying fundamental spray combustion processes in ideal laboratory conditions, but also for probing spray flames in realistic environments. Significant advances have been made over the years in the area of laser-based diagnostics for combustion application. In the area of the fuel droplet characterization, the development of the phase Doppler interferometers gives the possibility to measure the size and the velocity of individual droplets. These studies have contributed to an increased understanding of the behaviour of droplet dynamics and droplet-gas phase interactions in spray flames and of the effect of the fuel properties on the structure of the spray flame.

However, in order to gain a better understanding of the droplet heat-up process in spray flames, it would also be advantageous to measure the **fuel droplet temperature**. Another parameter that is of fundamental interest in the study of spray combustion is the fuel droplet evaporation rate. The study of this parameter is very important for understanding the complex heat transfer process that occurs in spray flames. Also, instantaneous droplets regression data obtained in the spray flame can be used to validate currently available spray combustion model. In spite of these needs, no instrument is currently available for in situ measurement of fuel droplet temperature and of fuel droplets regression rate in spray flames.

To overcome this lack of information, rainbow and global rainbow techniques have been developed. Rainbow and global rainbow techniques are based on the dependence of the absolute angular rainbow location with the refractive index therefore the temperature. These techniques have a strong potential but they are still under development. The main advantage of the rainbow techniques is that no additive is used (in opposition with fluorescence techniques), the only constraint is that the product must be transparent. Then rainbow techniques can be used at high temperature and pressure. The main problems are connected with the inversion procedure and the obligation to follow the shift of the rainbow induced by the change of the droplet properties. This last constraint is particularly critical with global rainbow for combustion studies where the changing of the refractive index can run from 1.5 to 1.3. Up to now, the published global rainbow configurations are limited to small angular ranges, inappropriate for combustion studies. In this thesis a large effort has been dedicated to the development of fast and accurate measurements of size and

temperature for one particle (classical rainbow refractometry) and for cloud of particles (global rainbow refractometry).

Moreover, in spray combustion, a critical point is the spray atomization. When using classical nozzles, the created spray is by nature poly-dispersed with large momentum differences between the small and large droplets. Then, with poly-dispersed spray, the evaporation study is complex because relatively large droplets passing through the group flame experience large inertia and longer vaporization time [2]. If the droplet is too large to heat up sufficiently and to vaporize vigorously even in a hot region of the flame, the droplet will fly off the group flame without burning. Then an ultrasonic nozzle, developed from the Chulalongkorn University, will be used because of its unique potential to create relatively highly mono-dispersed spray of droplets with the same low velocity.

Such ultrasonic nozzles produce continuously a spray of tiny droplets with a typical size running from 20 to 80 μm , a low initial velocity (less than 1 m/s), and flow rate of some cc/min. These properties are opposite to the properties of injectors used in internal combustion engines, where the liquid is injected at very high pressure (up to 2000 bar) during a very short time (typically 3 ms). These injection conditions permit not only to create tiny droplets but also, due to the high spray velocity (up to 600 m/s), to realize an appropriate mixing between the liquid vapour and the air to secure a good combustion. Here a good combustion is defined as one using the less as possible of fuel and producing the minimum quantity of pollutant for the same energetic efficiency.

On the contrary, the fact that ultrasonic nozzles produce a continuous mono-dispersed spray of small droplets is very attractive to develop an experimental set up where the basic properties of the droplets (without or under combustion) can be measured more easily than with classical injectors. The main reason of such a study is that droplet evaporation properties are not yet known, especially for multi-component products as biodiesel.

Then, this PhD thesis is a contribution to the combustion of biodiesel sprays, and more particularly of palm oil biodiesel, with the following objective:

1.1. Objective

The objective is to develop a global rainbow technique in order to determine the droplet temperature and size distribution in a free spray, before and during combustion. The spray will be created by an ultrasonic nozzle which is able to produce a relatively mono-dispersed spray. A special attention will be devoted to palm oil biodiesel sprays.

1.2. Scope

Optical techniques will be developed to accurately characterize sprays generated by an ultrasonic nozzle. Size distribution as well as temperature will be measured. PDA and global rainbow refractrometry will be mainly used and adapted in this work.

The capability of ultrasonic nozzles to atomize biodiesel oil will be investigated. The following issues will be taken into account.

- Characteristics of the spray such as: diameter and temperature, before and during combustion.
- Percentage of biodiesel oil in the fuel

1.3. Obtained Benefits

The expected benefits will be an accurate description of the characteristics of the biodiesel oil spray created by ultrasonic nozzles. Frontier optical techniques for characterizing sprays will be developed and established in Chulalongkorn University. Moreover, developed techniques to be discussed in this work could be applied to a large number of spray configurations for collecting information concerning operating parameters of atomisation.



สถาบันวิทยบริการ
จุฬาลงกรณ์มหาวิทยาลัย

CHAPTER II

ULTRASONIC NOZZLE

Introduction

In the combustion, a liquid fuel must be atomized, transformed into a fog of droplets. Atomizers are in charge of this transformation. The most common ones are based on the injection of the liquid to be atomized through a tiny aperture. The liquid can be injected alone or with air. In all cases the atomization results from the difference of velocity between the liquid and the air. The difference of velocity creates instabilities which develop up to the breaking of the liquid in droplets. The main limitation of this kind of atomizers is to create tiny droplets with a high velocity of the liquid. Then high injection pressure is necessary and the created spray also possesses a high velocity. Furthermore, the droplet size distribution obtained is often large: small and large droplets are simultaneously created which possess very different combustion properties.

In contrast, an ultrasonic nozzle uses ultrasonic vibration to generate the liquid atomization. It can produce very fine droplets with relatively uniform diameter without requirement of high air compressor or high pressure pump. As ultrasonic nozzles have unique properties, they have been used in many application fields such as pharmaceutical industry, paint coating, spray process, ignition process in a reactor and semi-conductor production process in a reactor. Complementary, the particularities of the spray created by an ultrasonic nozzle are adapted to fundamental studies due to narrow size distribution and low initial velocity, with the opportunity to adjust velocity and particle concentration.[3, 4, 5]

Here our interest is on the study of spray evaporation which is the key parameter to improve combustion processes. To perform accurate measurements with realistic sprays in terms of diameter, the spray must be composed of small droplets with a narrow size distribution. Then an ultrasonic nozzle has been selected to create a spray.

This chapter is devoted to the introduction to ultrasonic nozzles. The principle of an ultrasonic nozzle developed at Chulalongkorn university will be presented in section one. Section two proposes a correlation, assumed universal, to predict the particle size created by this kind of nozzle. Section three compiles the results corresponding to the experimental study of the developed nozzles by using classical optical techniques such as Phase Doppler Anemometry (PDA), Interferometric Laser Imaging Droplet Sizing (ILIDS), to measure the size and velocity of droplets. Temperature measurements by Infra Red camera will also be presented at the end of the chapter.

2.1 Developed ultrasonic nozzle

An ultrasonic nozzle uses piezoelectric ceramic to generate ultrasonic energy by transforming electrical energy to mechanical energy which could vibrate an atomizing surface. At the resonance frequency, which depends on the geometrical characteristics of the nozzle, the direction of vibration is perpendicular to the atomizing surface. When a liquid is introduced onto the atomizing surface, it spreads and forms a thin liquid film. The liquid film adsorbs a fraction of the vibration energy creating a unique wave pattern on the surface, known as capillary wave, see figure 2.1(a). When the amplitude of the underlying vibration is increased, the amplitude of the capillary wave increases correspondingly. Finally, when the critical amplitude is reached the height of the capillary wave exceeds that required to maintain its stability. The wave collapses and tiny drops of liquid are ejected from the top of the degenerating waves⁴. Figure 2.1(b) schematises this process.

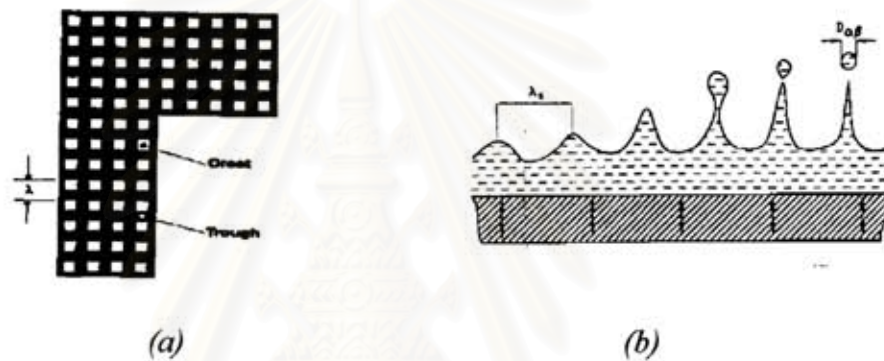


Figure 2.1: (a) Capillary wave grid³. (b) Disintegration mechanism⁴.

The design of an ultrasonic nozzle and its frequency depend mainly on nozzle length and on the speed of sound in the material used. Figure 2.2(a) shows an example of a design of an ultrasonic nozzle concerned in this study. It is an acoustically resonant device consisting of a pair of piezoelectric ceramic rings sandwiched between two metal cylinders called a backing piece (1) and a mechanical transformer (2). The length of each part can be determined by the following equation:

$$\frac{A_c \rho_c C_c}{A_i \rho_i C_i} = \tan(kl) \tan(kl_c) \quad i = 1, 2 \quad (2.1)$$

where

- A_c = surface area of piezoelectric ceramic;
- ρ_c = density of a piezoelectric ceramic;
- C_c = sound velocity in piezoelectric ceramic;
- A_i = surface area of the metal cylinder used;
- ρ_i = density of the metal cylinder used;
- C_i = sound velocity in the metal cylinder used.

$$k_c = \frac{2\pi f}{C_c} \quad \text{and} \quad k_i = \frac{2\pi f}{C_i}$$

When applying the electrical voltage to piezoelectric ceramic, the ceramic converts electrical energy to mechanical energy and transfers this energy to the two ends of the nozzle. The two ends of the nozzle are anti-nodes. The minimal vibrations (nodes) are located at an electrode and at the location of the transition from the large to the small diameter. As soon as the frequency of the applied voltage is equal to the nozzle frequency, which is known as the resonance frequency, the amplitude of vibration will reach the highest peak at these two ends of the nozzle as illustrated in figure 2.2(b).

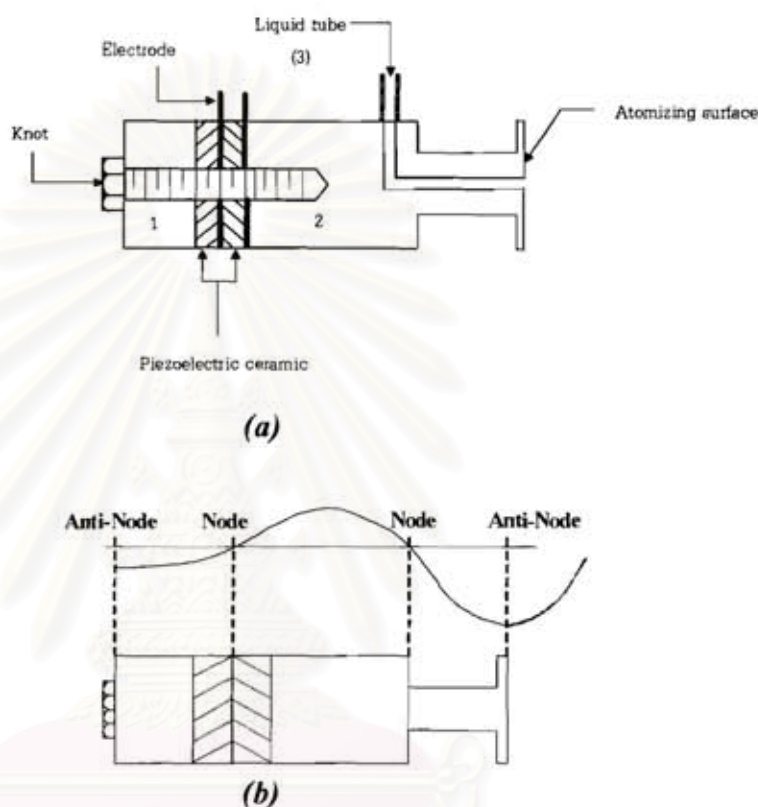


Figure 2.2: (a) Scheme of the ultrasonic nozzle. (b) Standing wave pattern in a typical nozzle.

The highest vibration occurring at the end of the backing piece will be reflected through the transformer and be amplified at the atomizing surface. The transforming part has a section of different diameter. The reason why the stem is smaller in diameter than the rest of the nozzle is that the amplitude of the vibration produced in the uniform diameter rod is insufficient to provoke atomization. Incorporating a small diameter stem, an amplified level of vibration in this part of the nozzle will take place and result in atomization at modest power levels.

Another factor regarding to the design of nozzle concerns the section diameter. In solids, waves other than longitudinal waves can be excited. In bars or rods, waves can be produced that travel radially, that is, perpendicular to the normal longitudinal waves. According to Mason[6] in order to suppress this kind of excitation, it is necessary to keep all diameters less than $\lambda/4$.

The developed ultrasonic nozzle used in this work is illustrated in figure 2.3(a). The piezoelectric ceramic ring of lead zirconate-titanate with 1 cm. in diameter and 0.2 cm. thickness is used. The backing piece made from stainless steel has high amplification capabilities. Aluminum alloy is used for the transformer part due to its resistance capacity. The two side faces of piezoelectric ceramic rings are mounted with an electrical conductive material, silver. To excite the piezoelectric ceramic, a power supply has been ordered from Spray Tech Company. The power supply automatically searches for the resonance frequency, depending on the geometrical characteristics of the nozzle, see figure 2.3(b).



(a)



(b)

Figure 2.3: (a) The image of the studied nozzle. (b) Power supply by Spray Tech Company

2.2 Droplet size prediction

The size of the droplets created by an ultrasonic atomizer depends on many parameters including the liquid properties and geometry of the atomizer. An accurate prediction of the size distribution is very difficult but various researchers have proposed different correlations. Among others, Rajan and Pundit [7] propose correlations which take into account the various physico-chemical properties of liquid, its flow rate, the amplitude and frequency of ultrasound and the area and geometry of the vibrating surface. According with the physical model used, three correlations have been proposed by Rajan and Pundit. In this thesis, only the most general model will be used.

$$d_p = \left(\frac{\pi\sigma}{\rho f^2} \right)^{0.33} \left[1 + A(We)^{0.22} (Oh)^{0.166} (I_N)^{-0.0277} \right] \quad (2.2)$$

where the Weber number is defined as follows involving the flow rate Q and the ultrasonic excitation frequency f :

$$We = \frac{fQ\rho}{\sigma} \quad (2.3)$$

in which ρ is the liquid density and σ its surface tension. The viscosity is taken into account by the Ohnesorge number, modified to:

$$Oh = \frac{\eta}{fAm^2\rho} \quad (2.4)$$

where η is the liquid viscosity and Am the amplitude of sound wave. The geometry of the vibrating surface and its area determine the intensity of ultrasonic power delivered. The dimensionless number I_N takes into account the effect of energy density on droplet size:

$$I_N = \frac{f^2 Am^4}{\aleph Q} \quad (2.5)$$

where \aleph is the velocity of sound in liquid medium.

This correlation gives the possibility to quantify the effect of each parameter, independently of the others. This approach is however difficult with experiments as the change of product often imposes the simultaneously change of several parameters. Figure 2.4 displays the droplet size predicted by formula 2.2 versus the seven parameters which can affect it.

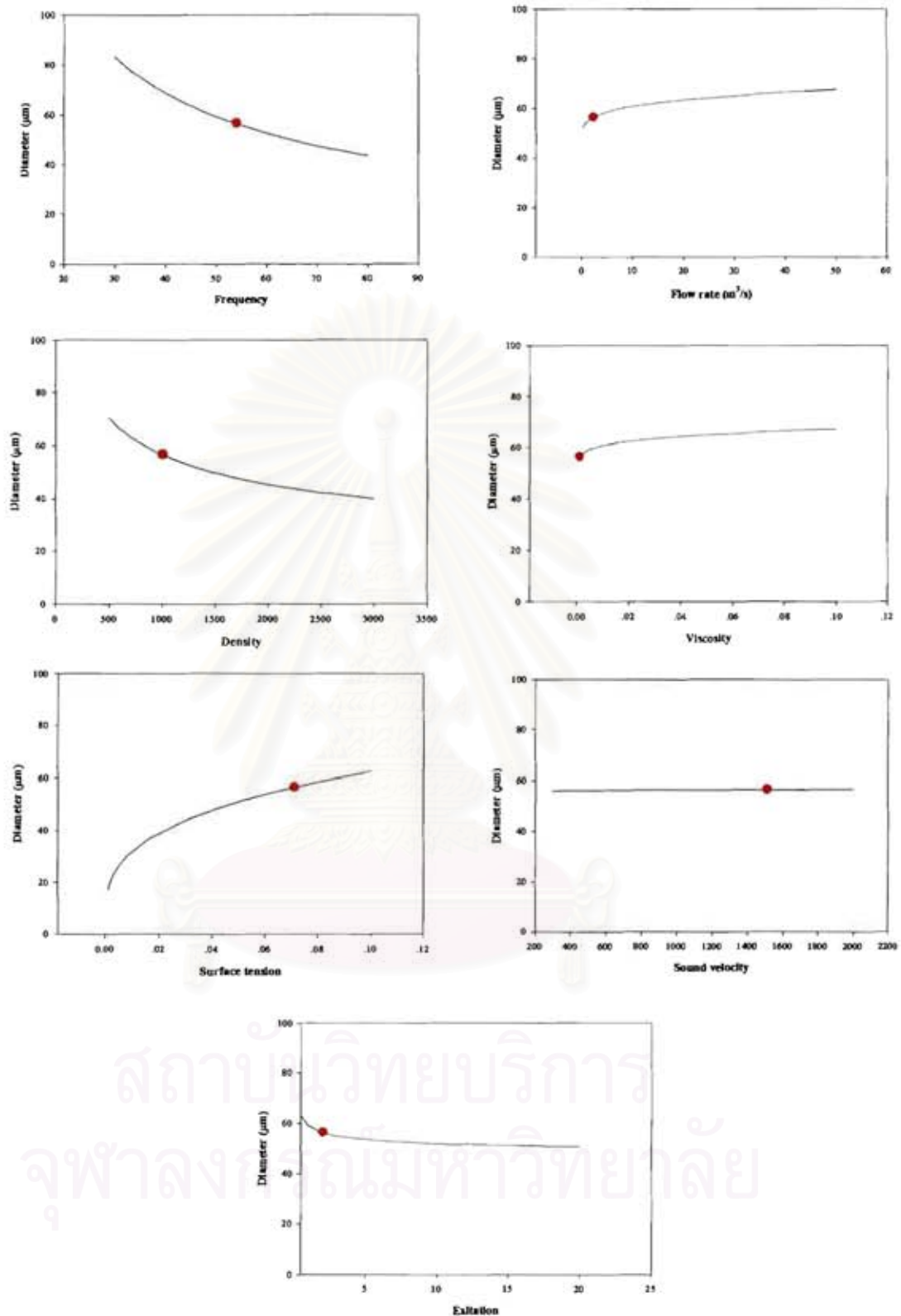


Figure 2.4: Particle diameters versus the different parameters taken into account by formula 2.2.

In figure 2.4 all computations have been carried out for the values of the parameters corresponding to water. For the following working conditions ($f = 54$ kHz,

amplitude = 2.02 μm , $Q=2.16 \times 10^{-8} \text{ m}^3/\text{s}$), a diameter equal to 56.43 μm is obtained, corresponding to the result by Rajan and Pandit. In the series of figure 2.4 only the parameter under study takes arbitrary values, and for each case, the value corresponding to water is noted with a red circle.

As some of these parameters are difficult to know accurately enough, it is interesting to observe that the sound velocity has no effect, that the excitation does not affect much the size when it is larger than about 2 μm . For this parameter, it is to be underlined that Rajan and Pandit give a critical value below which the liquid does not atomize. This critical value is given by:

$$Am_{crit} = \left(\frac{2\eta}{\rho} \right) \left(\frac{\rho}{\pi\sigma f} \right)^{0.333} \quad (2.6)$$

For water, it is found that the critical amplitude is equal to 0.8 μm , in agreement with authors such as Raco who mentioned that the minimum amplitude is less than 2 μm for most applications.

The other parameters are easier to be measured, and for biodiesel, the size is expected not to be too far than the one for water when atomising is successful. These predictions must now be experimentally validated.

2.3 Measurement of the spray characteristics

2.3.1 Size and velocity measurement close to the orifice of the nozzle by PDA

2.3.1.1 The effect of the liquid flow rate

The sensitivity of the droplet diameter with respect to the flow rate has been studied. An ultrasonic nozzle with frequency of 45.9 kHz is used in this investigation. The liquid is delivered to the nozzle by a medical syringe pump, giving the possibility to obtain accurate flow rates in a wide range (between 0.02 and 17 cc/min with a syringe of 100 cc i.e. a ratio equal to about 800 between the smallest and the largest flow rate). The size and the velocity of the droplets at 5 mm from the orifice on the axis of the canal orifice (see figure 2.3a) were measured by the commercial PDA. The PDA configuration used was the standard PDA configuration and the processing of the events was also carried out by using the Dantec PDA (58N80-58N81) and Dantec software.

Figures 2.5 and 2.6 display the particle diameters D_{10} and D_{32} versus the flow rate. In the liquid flow rate range of 0.02-17 cc/min, we first observe that the diameter is essentially constant, but the difference between the diameter D_{10} (about 40 μm) and the D_{32} diameter (about 65 μm) informs us that the size distribution is not mono-disperse. For example, figure 2.7 displays the size distribution corresponding to a flow rate equal to 7.3 cc/min while figure 2.8 and 2.9 display the size distribution corresponding to flow rates of 1.9 cc/min and 0.5 cc/min respectively. These figures show that the size distribution is essentially independent of the flow rate and that the size distribution is fundamentally constituted by one main peak at about 45 μm and a second small peak at about 110 μm . In this series of figures, the first peak is fitted by a Gaussian and a Log-normal law. Generally the Gaussian law is the best to fit the increasing part (from 0 to 40 μm) of the size distribution while the log-normal law is better to fit the decreasing part (from 40 to 120 μm) of the size distribution. All the experimental results corresponding to this series of experiments are compiled in table 2.1. The mean value of D_{10} is equal to 45 μm with a standard deviation equal to 1.5. These remarks are still valid for the low flow rates between 0.02-0.15 cc/min (in figure 2.6), where the mean size is still equal to about 39 μm (a change of about 10%) with a standard deviation equal to 3 and the size distribution is narrow independently from the fact that at such flow rates the spray is pulsed as exemplified in figure 2.10. The size distributions are displayed in figures 2.11 to 2.13. Table 2.2 compiles the experimental adjustments and results corresponding to this series of figures. The fact that at very low flow rates, the spray is pulsed can be explained as follows. At low flow rates the creation of a liquid film, with an appropriate thickness, on the atomising surface necessitates a given time t . When the liquid film is suitable for atomisation, all the film volume is transformed in droplets, then the atomisation stops, waiting for the liquid film thickness being again proper for atomisation.

It is experimentally found that the size distribution is very well fitted by a Gaussian curve with a mean diameter equal to about $40\ \mu\text{m}$. However, the fitting by a log-normal law is nearly identical for the main size and the width of the size distribution. Nevertheless, a small second peak is visible at about $120\ \mu\text{m}$.

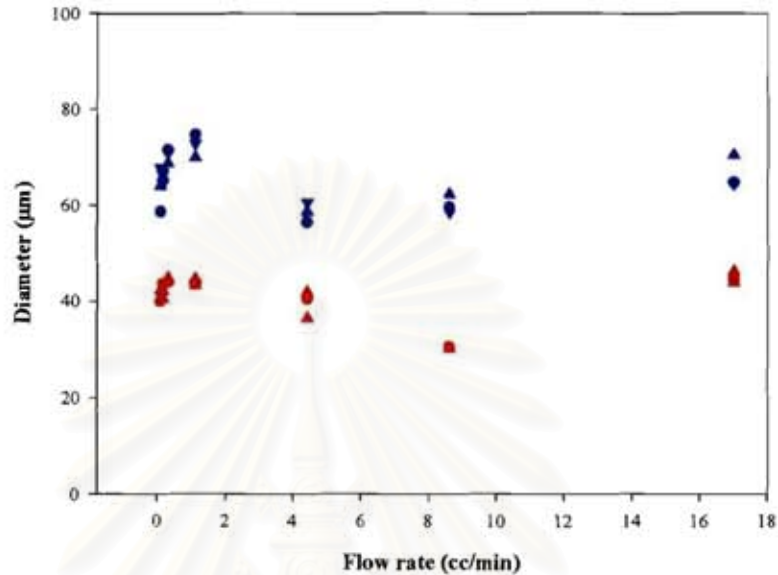


Figure 2.5: Droplet diameter versus the liquid flow rate for water spray. Blue points are for D_{32} while red points are for D_{10} .

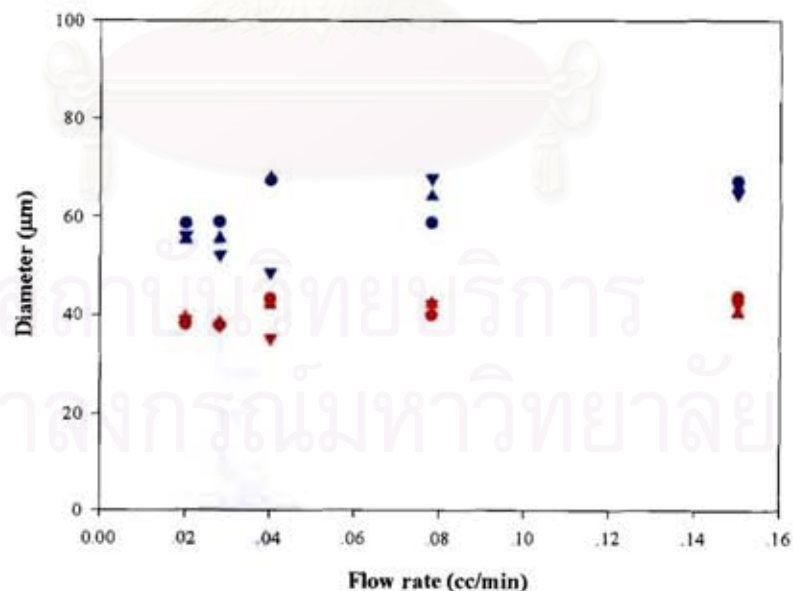


Figure 2.6: Droplet diameter versus flow rate (at low liquid flow rate). Blue points are for D_{32} while red points are for D_{10} .

Table 2.1 The measurement of mean diameter of water spray for different conditions.

Nozzle Frequency (KHz)	Liquid flow rate (cc/min)	Power	D ₁₀ (μm)	D ₃₂ (μm)
44.6	0.5	8	41.12	63.9
45.7	1.9	8	46.0	72.0
45.6	1.9	8	46.0	72.3
45.6	1.9	8	45.5	70.5
45.2	7.3	8	44.7	72.0
45.0	7.3	8	43.7	67.4
45.6	7.3	8	44.11	65.9
45.0	1.9	6	45.0	73.0
45.0	1.9	6	45.5	73.0
45.3	1.9	10	46.4	70.8
45.3	1.9	10	47.0	72.0

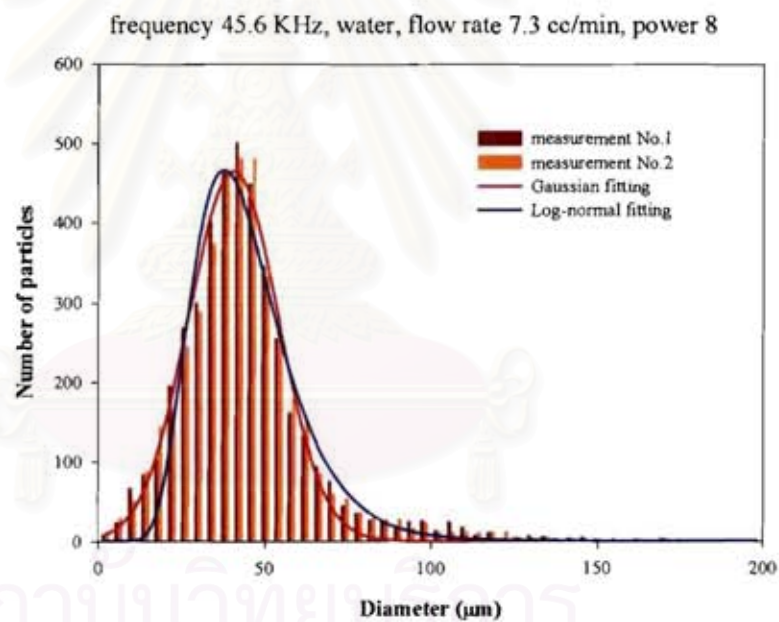


Figure 2.7: The PDA measured size distribution. The flow rate is equal to 7.3 cc/min.

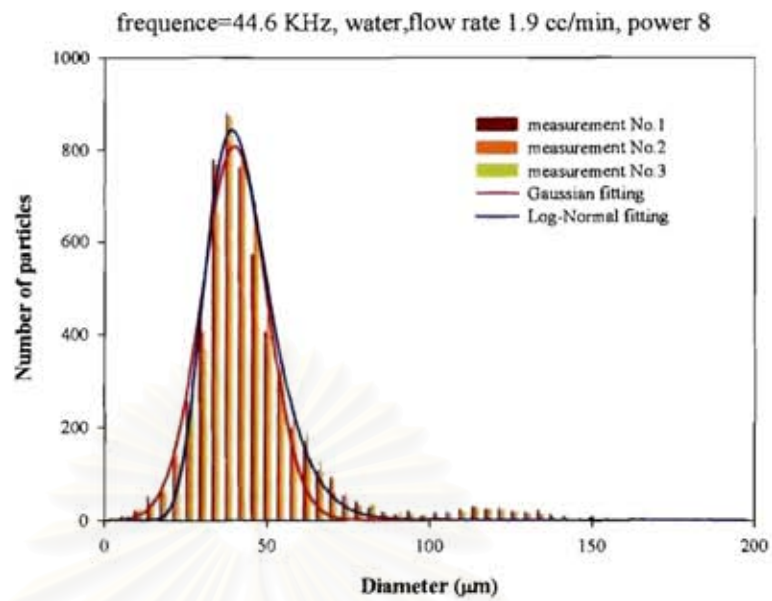


Figure 2.8: The PDA measured size distribution. The flow rate is equal to 1.9 cc/min.

file 20, frequency 44,6 KHz, water, flow rate 0.5 cc/min, power 8

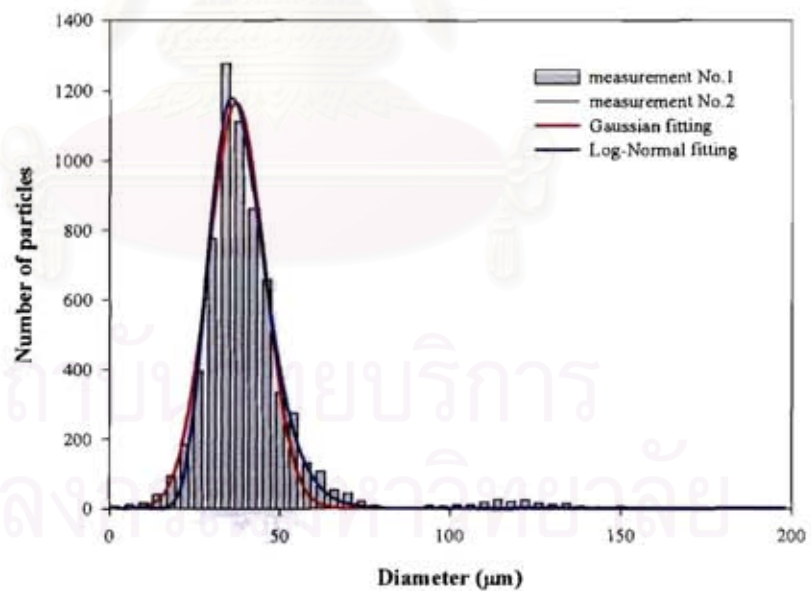


Figure 2.9: The PDA measured size distribution. The flow rate is equal to 0.5 cc/min.

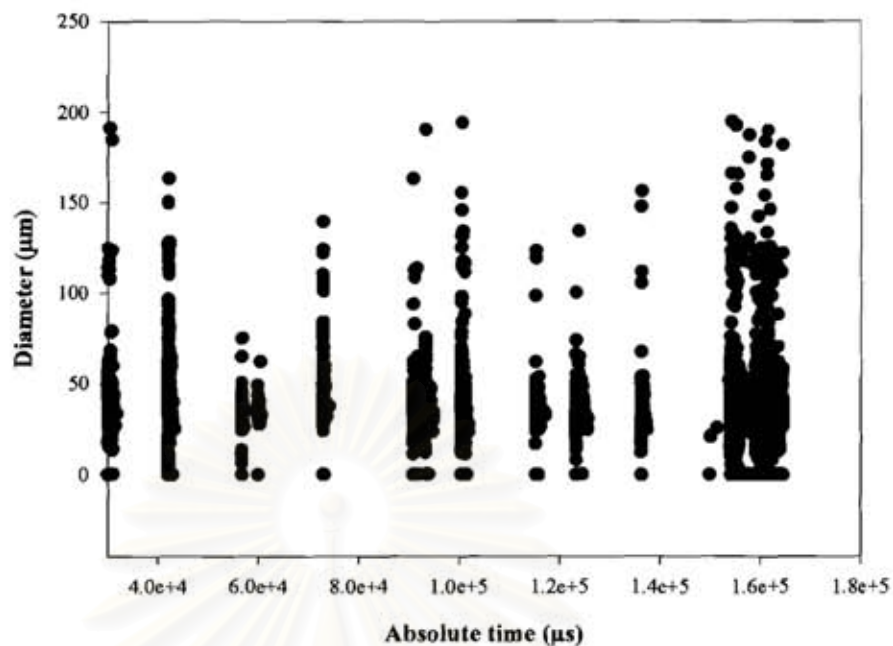


Figure 2.10: Example of a pulsed spray for the flow rate of 0.047 cc/min. The time scale is in μs .

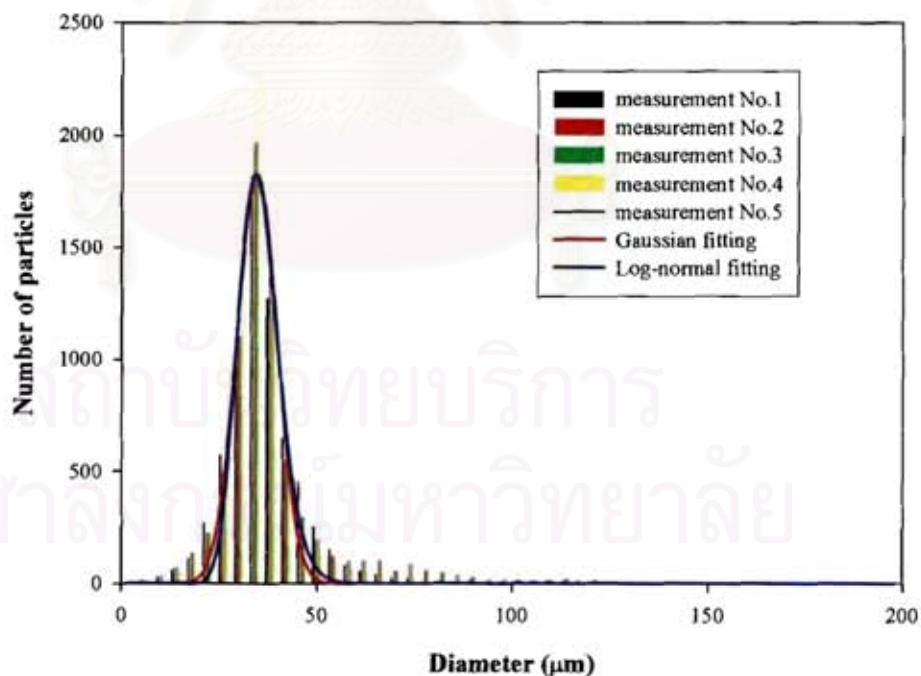


Figure 2.11: The PDA measured size distribution. The flow rate is equal to 0.038 cc/min.

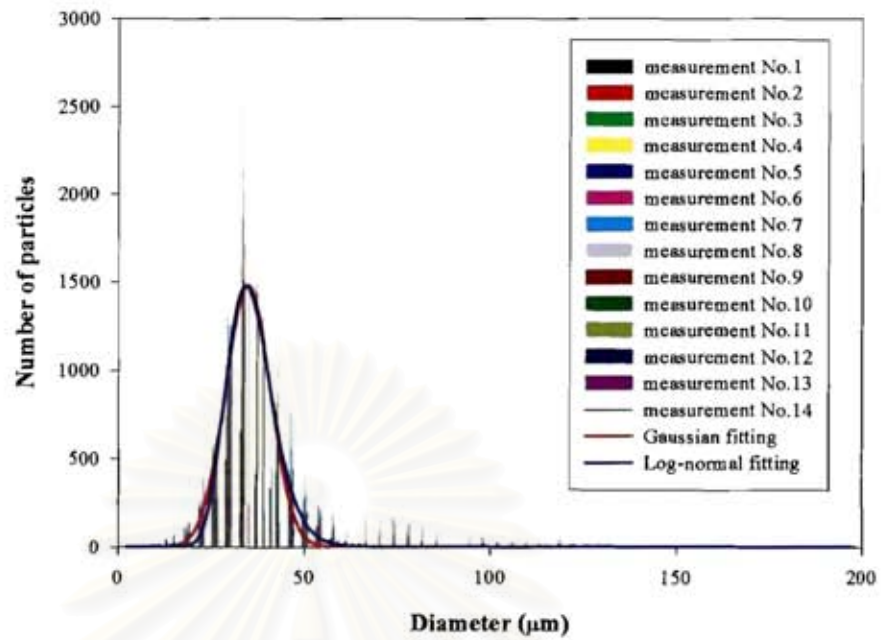


Figure 2.12: The PDA measured size distribution. The flow rate is equal to 0.047 cc/min.

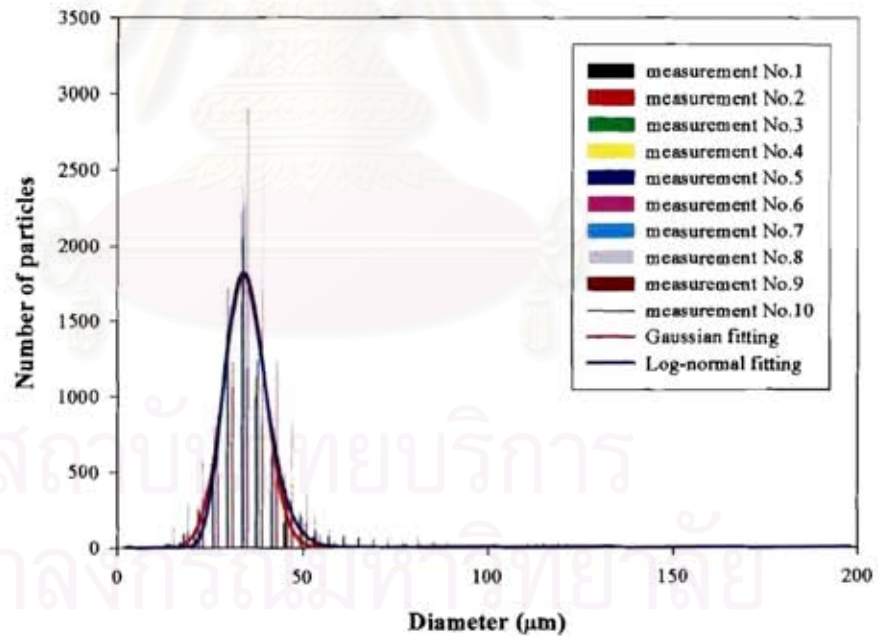


Figure 2.13: The PDA measured size distribution. The flow rate is equal to 0.066 cc/min.

Figure 2.14 compares the predictions of Rajan and Pandit with the experimental results of the diameters D_{10} and D_{32} measured by the PDA employed in this work. The red line corresponds to the prediction from (2.2) for our working conditions. These results show that the diameter is essentially independent of the liquid flow rate, in agreement with Rajan and Pandit correlation which predicts that the particle diameter increases just a little with the flow rate. Furthermore, the measured diameter and predicted diameter are in a good agreement, especially for the D_{32} diameter.

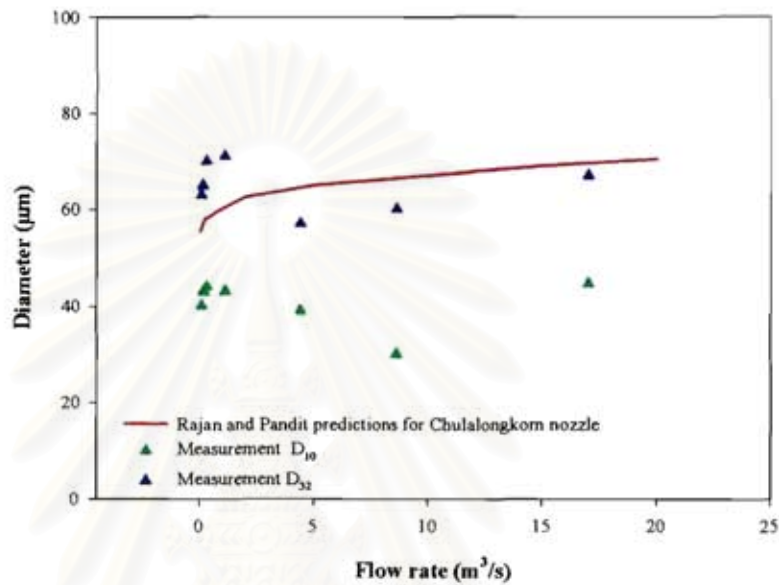


Figure 2.14: The comparison between the Rajan and Pandit predictions and the PDA measurements. The green triangles represent the D_{10} data while the blue triangles are for D_{32} .

สถาบันวิทยบริการ
จุฬาลงกรณ์มหาวิทยาลัย

Table 2.2 The measurement of mean diameter for water pulsed spray at low flow rates.

Frequency (kHz)	Flow rate (cc/min)	Power	D₁₀ (μm)	D₃₂ (μm)
45.9	0.038	8	37.95	58.56
46.3	0.038	8	36.11	46.71
45.6	0.038	8	39.25	55.27
46.0	0.038	8	38.8	55.99
45.8	0.066	8	43.15	67.23
45.8	0.066	8	42.05	67.78
45.5	0.066	8	37.80	65.95
46.0	0.066	8	42.7	69.10
46.2	0.066	8	38.66	59.60
45.4	0.066	8	37.70	52.67
45.5	0.066	8	34.24	41.73
45.9	0.066	8	35.80	45.20
46.1	0.047	8	37.73	58.80
46.4	0.047	8	38.20	55.40
46.2	0.047	8	37.60	51.00
45.4	0.047	8	37.20	52.60
45.6	0.047	8	44.70	69.70
46.0	0.047	8	40.83	63.40
46.1	0.047	8	44.00	67.30
46.0	0.047	8	39.40	57.99
46.0	0.047	8	44.08	69.00
47.3	0.047	8	36.70	73.60
47.0	0.047	8	41.90	69.50
46.0	0.047	8	40.30	59.90
46.2	0.047	8	38.50	54.40
45.6	0.047	8	35.20	52.51
45.6	0.047	8	34.90	61.50
45.9	0.047	10	38.90	57.90
45.9	0.047	10	33.20	40.33
45.9	0.047	6	34.60	47.66

2.3.1.2 The effect of input power

The dependence of the droplet diameter on the input power have been studied and displayed in figure 2.15 for a flow rate of 1.9 cc/min and in figure 2.16 for a flow rate of 0.028 cc/min. The mean diameters are essentially constant. This is particularly evident in figure 2.15 where Ajan and Pundit's predictions are added, showing the insensitivity of mean diameter to the excitation power. Figure 2.17 displays the size distribution for an excitation power running from 6 to 10. Here again the size distributions are essentially identical. There is no significant effect of the excitation power on the spray size distribution.

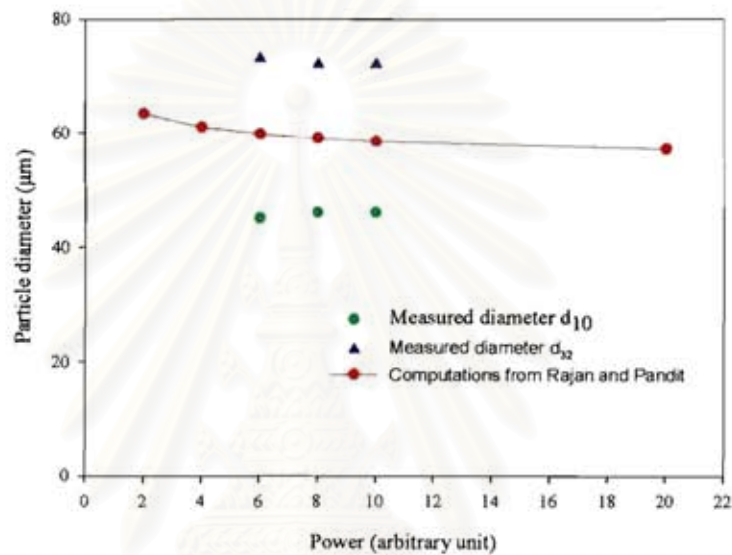


Figure 2.15: The diameter versus the excitation. The flow rate is equal to 1.9 cc/min and the frequency is equal to 45.3 kHz.

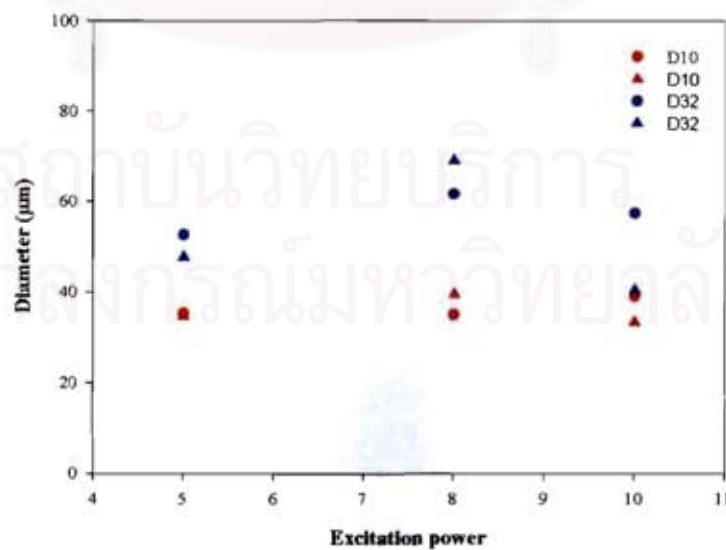


Figure 2.16: The diameter versus the excitation. The flow rate is equal to 0.028 cc/min and the frequency is equal to 45.3 kHz.

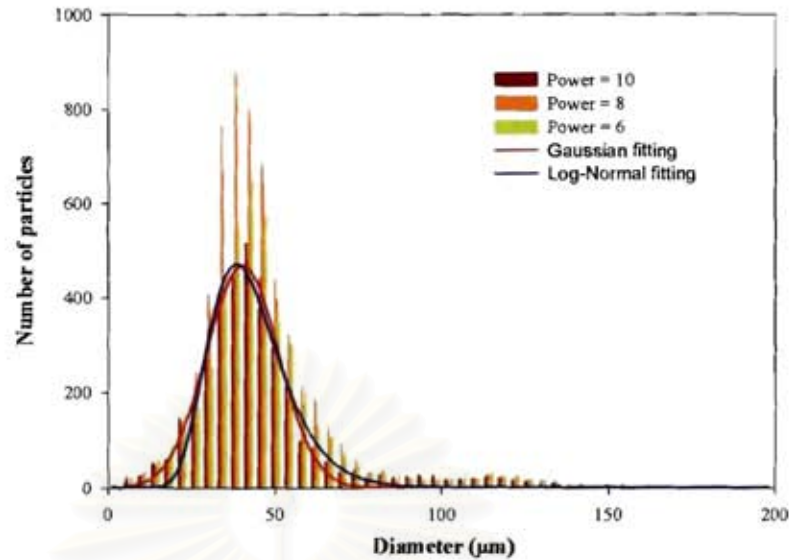


Figure 2.17: Size distribution measured for three different excitation powers for the flow rate equal to 1.9 cc/min.

Remark that to know the relationship between the power button position and the power supplying to the ultrasonic nozzle, tension and current temporal evolution have been recorded by using an oscilloscope. At each time step, the product of the instantaneous current by the instantaneous tension gives the instantaneous power. Figure 2.18 plots the maximum instantaneous power versus the power button position, for three different nozzles 45.3, 47 and 76 kHz.

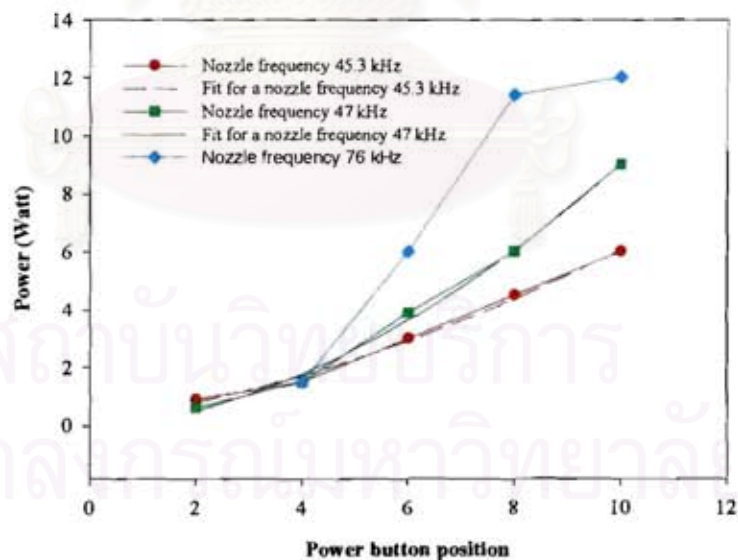


Figure 2.18: The measured power versus the power button position.

2.3.1.3 The effect of liquid properties (density, viscosity and surface tension)

From formula 2.2, the mean diameter produced by ultrasonic nozzles are not only frequency, flow rate and power input dependent, but is also affected by density, viscosity and surface tension. In practice, it is impossible to change continuously and independently these parameters, in contrast to the theoretical approach. Nevertheless, measurements have been performed for different products, which possess different physical properties. Table 2.3 displays the physical properties of liquid studied at 20°C. Figure 2.19 displays the size distributions measured for ethanol and for water.

Table 2.3 *The liquid properties.*

Liquid	Density (kg/m ³)	Surface tension (kg/s ²)	Viscosity (cp)
Water	1000	0.0728	1.02
Ethanol	790	0.0228	1.2
Silicone	970	0.0209	10
Diesel	860	0.0283	4

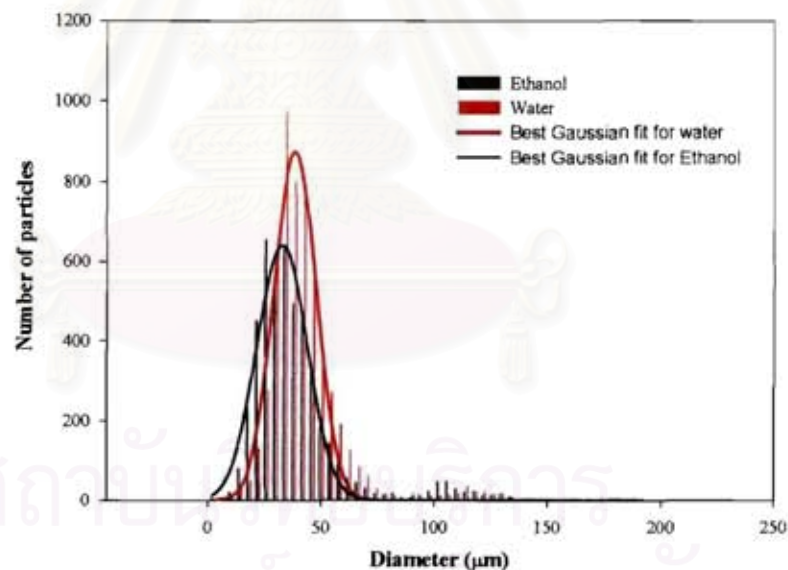


Figure 2.19: *Comparison between size distribution for water and ethanol.*

Figure 2.20 displays the mean diameter (D_{10}) versus the flow rate, with the kind of liquid as a parameter. Four liquids have been studied: water, ethanol, silicone and diesel. A first remark is that with silicone and diesel, due to the viscosity and the maximum power of the generator available, the maximum flow rate is limited to 2.2 cc/min. The evolution of the diameter with the flow rate is generally small but the following behaviors have been noted:

- For water, the diameter seems to increase linearly with the flow rate, but, for an increase of the flow rate by about 15, the diameter increases only by about 10%.

- For ethanol, the diameter reaches the smallest values of about 30 μm for a flow rate of 0.3 cc/min. The diameter of the ethanol droplets increases with the flow rate up to 2.2 cc/min and then decreases with the higher flow rate. Nevertheless, here again the change of diameter is in a range of about 10 %.

- For silicone, in spite of a significant dispersion measurement (about 10%), the increase in diameter with flow rate looks to be very strong: nearly 25% when the flow rate increases from 0.3 to 1.1 cc/min.

- For the diesel, the measurements are dispersed at low flow rates (0.3 and 1.1 cc/min), but less and less as the flow rate increases. The mean diameter is constant or decreases a little bit. Furthermore, as displayed in figure 2.21, the size distribution is clearly more log-normal than Gaussian, for the increasing part as well as for the decreasing part. For this product, a long tail in the size distribution exists. The mean size is always about 40 μm , but particles exist up to about 150 μm .

In summary, from this series of experiments, it can be concluded that the diameter changes with the liquid properties but is nearly independent with respect to the liquid flow rate under the range of study. Let us remark that the correlation of Rajan and Pundit predicts a large sensitivity of the droplet size with density, surface tension and viscosity. Our results are in agreement with these predictions at least qualitatively.

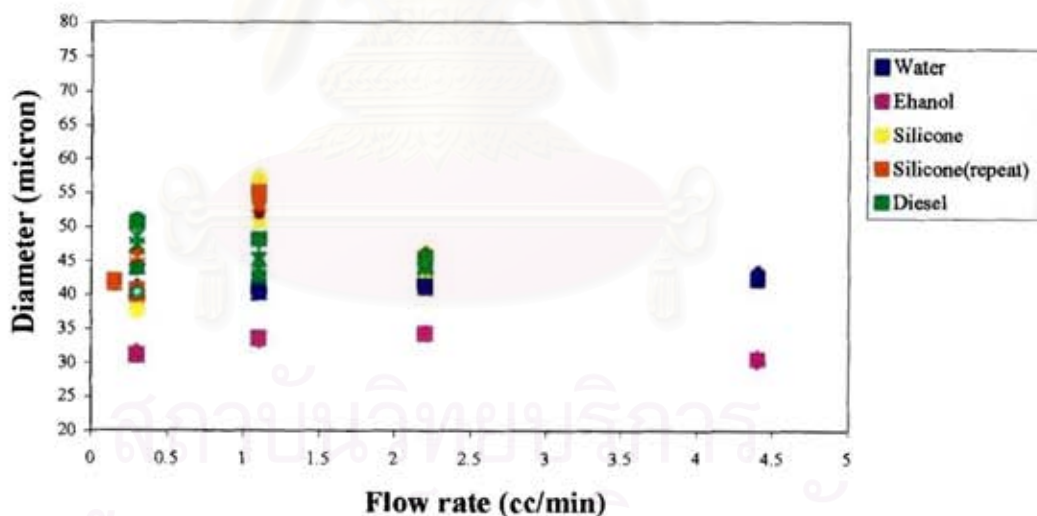


Figure 2.20: Diameter versus the flow rate with four products as parameter.

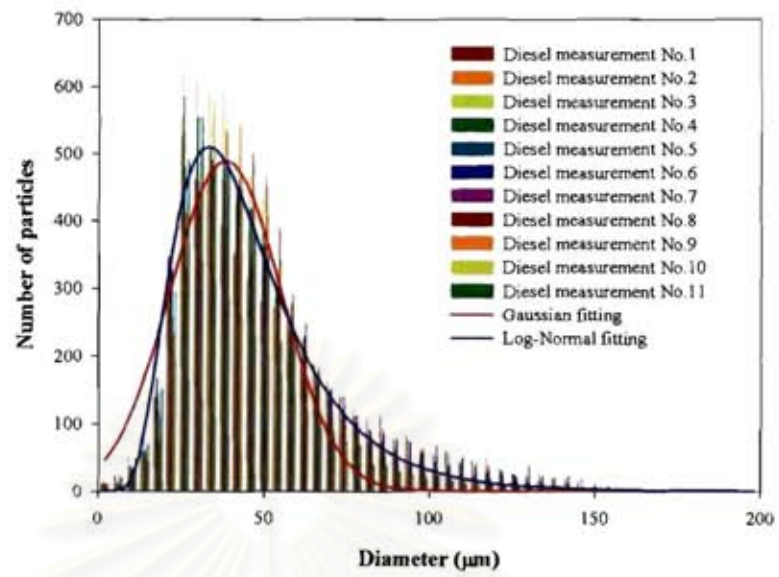


Figure 2.21: Size distribution for diesel.

สถาบันวิจัยบริการ
จุฬาลงกรณ์มหาวิทยาลัย

2.3.1.4 Temporal stability

The previous results have been obtained by measuring about 10 000 events with the PDA. To explore the stability of the nozzle versus time, a new series of experiments has been carried out. For this new series of experiments, the duration of the measurement was about 5 minutes for 500,000 events. It should be noted that the experiment starts with the excitation of the nozzle: the nozzle was at the room temperature when the experiment begins.

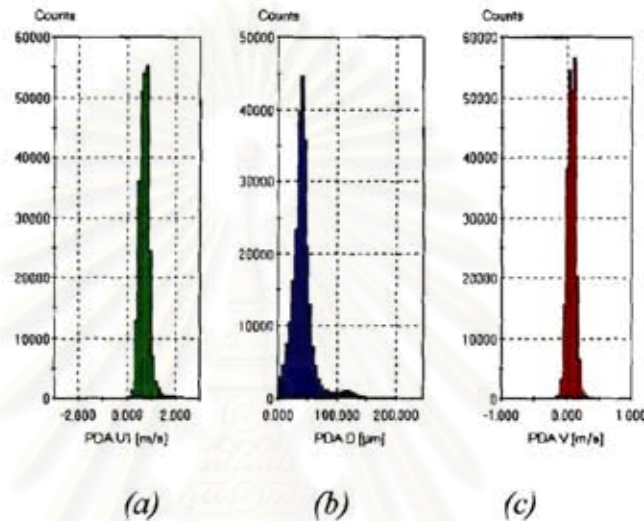


Figure 2.22: Example of PDA measurement at 5 mm from the orifice. (a) The longitudinal velocity Distribution, (b) the size distribution, (c) the transverse velocity distribution

Figure 2.22 displays histograms of longitudinal velocity, diameter and transverse velocity for a flow rate of $1.1 \text{ cm}^3/\text{min}$ and excitation frequency of 46 kHz, in the case of water. A nearly perfect Gaussian distribution of the particle size characterizes the spray. The spray parameters are $D_{10} = 46.68 \text{ }\mu\text{m}$ and $D_{32} = 63.9 \text{ }\mu\text{m}$. These values are in agreement with the previous results. To quantify the temporal evolution, the following post-processing has been applied to the measurement series:

1. The measurement series has been divided in windows of equal duration.
2. Each temporal window has a duration equal to 100 ms.
3. For each window, we compute and record: the number of particles, the average velocities (longitudinal and transverse), and the average diameter.

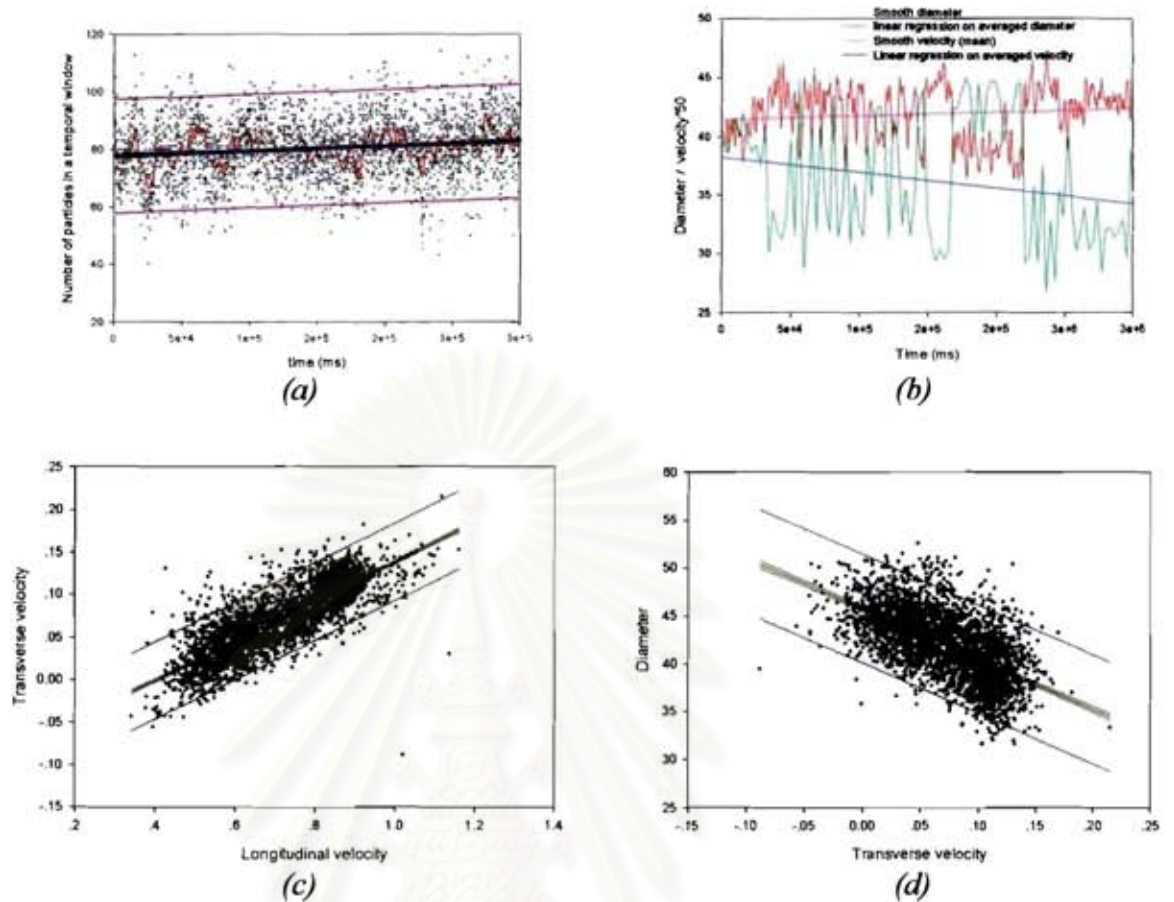


Figure 2.23: Processing of PDA temporal series. a) number of particles versus time, b) Longitudinal velocity and diameter versus time, c) Transverse velocity versus longitudinal velocity, d) diameter versus transverse velocity.

The experimental results of the measured values are plotted in figure 2.23. Figure 2.23(a) displays the number of measured particles versus time. From this figure, it is shown that the flow of particles is essentially constant at this location (about 80 particles every 100 ms). Figure 2.23(b) displays the average mean velocity (in green) and the average diameter (in red) versus time. From figure 2.23 (b) it can be concluded that:

1. the longitudinal velocity is small, about 60-80 cm per second;
2. a correlation between size and longitudinal velocity exists: the biggest the particles are, the smallest the longitudinal velocity is;
3. the correlation size/velocity evolves on a short time scale;
4. a continuous evolution at long time scale of the size and velocity appears (see the linear regressions)

In order to confirm these remarks, the transverse velocity versus the longitudinal velocity and the diameter versus transverse velocity have been plotted (see figures 2.23(c) and 2.23(d)). A strong correlation exists between the longitudinal and the transverse velocities as well as between the transverse velocity and the diameter. Figure 2.23(c) and 2.23(d) can be interpreted as the fact that, as the longitudinal velocity is small, the small transverse velocity is strong enough to affect the particle trajectories. The spray will then be organized as a juxtaposition of packet of particles with nearly the same momentum, as it will be confirmed by the ILIDS measurements (see page 30).

From these results it can be understood that the changes of size at short time scale is due to the effect of a transversally fluctuating flow, while long time evolution must have another origin. We postulate that this effect could be related to the change of the nozzle temperature due to the excitation. The study of this effect is the aim of the next section.

2.3.2 Size and velocity measurement far from the orifice of the nozzle by Interferometric Laser Imaging Droplets Sizing (ILIDS)

As the droplets are injected with a low velocity (about 0.7 m/s) rapidly they have the same velocity as the carried gas. Then at long distance away from the nozzle the PDA cannot be used because the probability for a particle to cross the optical probe is too small. To measure the characteristics of the spray far from the orifice, a suitable technique is ILIDS which has been introduced by Glover et al [8], and then studied and developed by several teams [9,10,11,12,13]. The measurement principle of ILIDS is based on the record of an off-axis, out-of-focus image. The size of the particle image is only a function of the lens aperture and of the magnitude of the out-of-focus. The size information is coded in the fringes created by the interferences between the light reflected and refracted by the droplets. To study the spray at 50 cm from the orifice, a classical PIV set up (it is a classical TSI PIV set-up and the PIV processing is carried out by Matlab toolbox) is used. The only difference between a classical PIV measurement and an ILIDS measurement is that the recording camera has to be moved towards the laser sheet (by 5 cm here) to obtain out-of focus configuration. The time between two pulses is equal to 600 μ s and the repetitiveness is of 10 couples of images by second. Figure 2.24(a) displays such a recording (one image of a couple). By analyzing such images with devoted software, the size distribution displayed in figure 2.24(b) has been obtained ($D_{10} = 50 \mu$ m). This size distribution compares well with the size distribution obtained by PDA as previously shown in figure 2.22. Furthermore, by applying a classical PIV processing to the out-of-focus couple of images it is possible to extract a map of velocities (the arrows in figure 2.25). The velocity is measured with in a range of about 0.1 m/s to 0.3 m/s which is in agreement with the free fall velocity for drops of this size, showing that the injection velocity is not longer dominating. Furthermore, from images as the one displayed in figure 2.24(a), it is clear that the particles are not uniformly nor randomly distributed but are organized in assemblies of drops with similar characteristics (velocity and size).

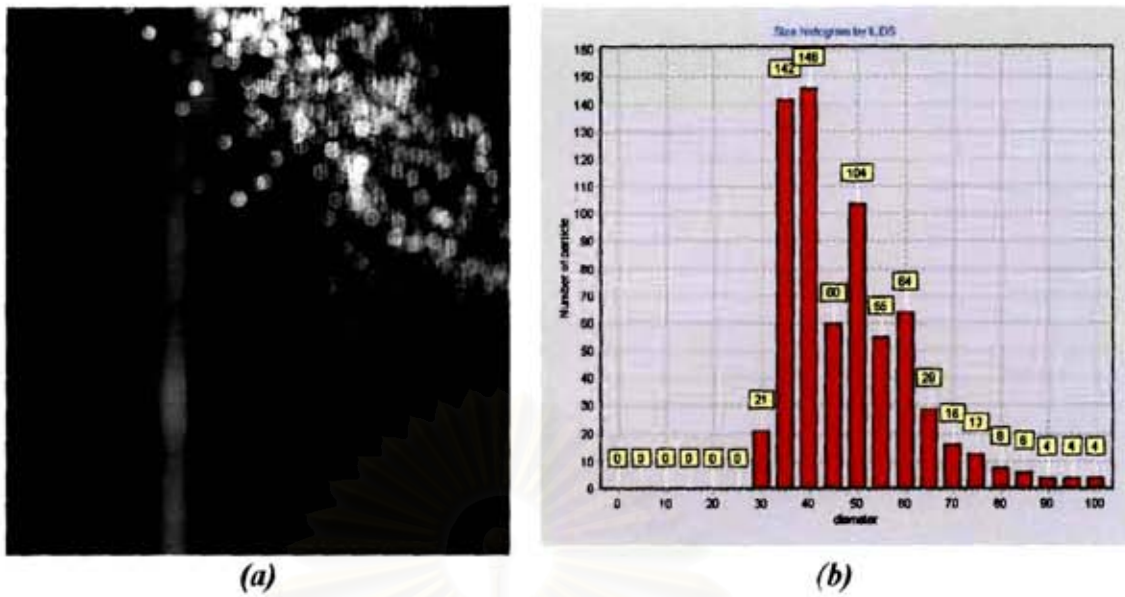


Figure 2.24: ILIDS measurements. (a) Example of a recorded ILIDS image, (b) Size histogram obtained by analysing 50 ILIDS images.

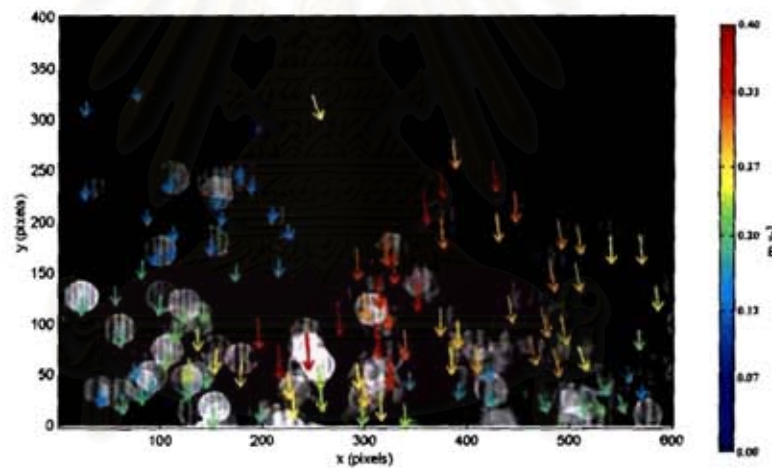


Figure 2.25: Example of a PIV/ILIDS map. The arrows give the velocities (direction and amplitude). From the fringes the size of the droplets can be extracted while the velocity is obtained from standard PIV software.

2.4 Nozzle temperature measurements

H.L. Berger reported that the temperature of an ultrasonic nozzle could increase when it is working. The self-heating of a nozzle is always present, since it is, after all, a power-producing device. The degree of self-heating is usually quite manageable since power consumption is usually on the order of a few watts. Furthermore, if the Curie temperature of zirconate-titanate (the most common material for piezoelectric ceramics) is in the range 300-350°C, no noticeable degradation of the ultrasonic nozzle has been recorded for temperatures up to 150°C. However, such a level of temperature can affect the liquid. This effect can be positive or negative, depending on the product and the application. For biodiesel, a high temperature will decrease the viscosity and then facilitates the atomisation process.

The temperature of the nozzle has been recorded by using an infrared camera (ThermalCAM PM595 LWB with objective of 24° from FLIR Systems). Figure 2.25(a) displays maps of the nozzle temperature at the beginning of the excitation and 15 minutes later while figure 2.25(b) displays the temperature at the nozzle orifice versus time.

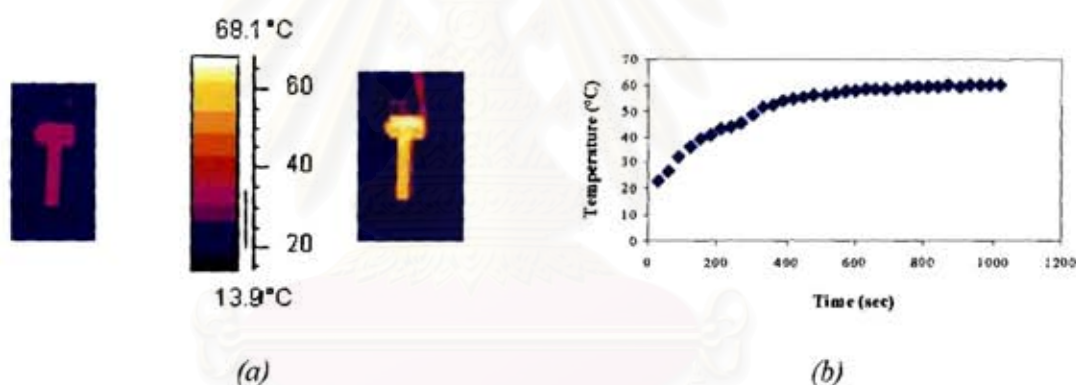


Figure 2.26: (a) Maps of infrared emission for the nozzle just at the beginning of excitation and 15 minutes later. (b) Temperature at the nozzle orifice versus time.

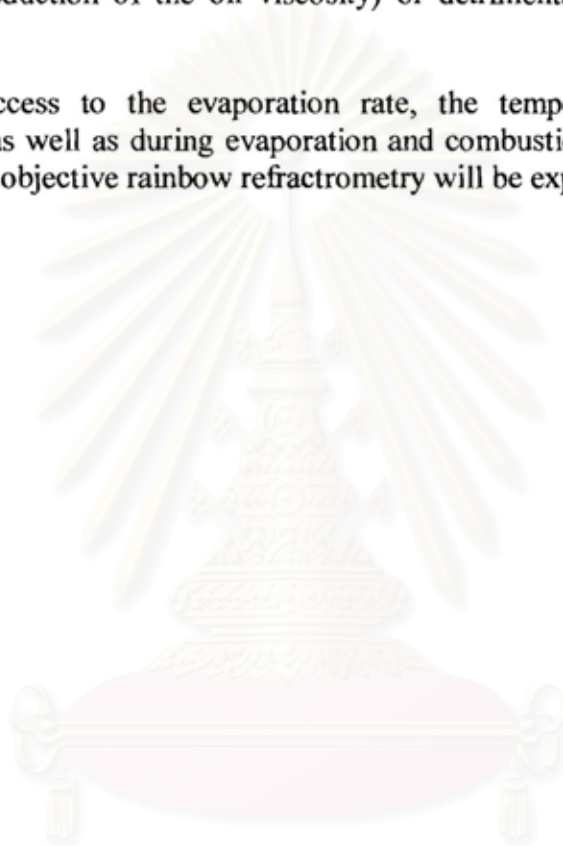
A strong increase of the nozzle temperature is observed. The increase of the nozzle temperature is estimated from the infrared images (after a calibration) to be of about 40°C. This temperature change of the nozzle will induce a temperature evolution of the liquid droplets. This slow evolution of the nozzle temperature is likely to be the cause of the continuous change of diameter remarked in figure 2.23(b).

Then to avoid the effect of nozzle temperature increasing on the droplet size, all the experiments presented in this book have been recorded 15 minutes after the beginning of the nozzle excitation.

Conclusion

The results presented in this chapter prove that ultrasonic nozzles are able to provide a spray of tiny droplets with a high uniformity in size and a very low initial momentum (low velocity), independently of the liquid flow rate under the range of study (from 0.02 to 17 cc/min). Then the dynamical properties of the droplet cloud will be principally due to the carrier gas flow. These unique properties are very attractive to realize oil burners to study the fundamental burning properties of oil as biodiesel from palm. Furthermore, the fact that an ultrasonic nozzle warms up can change the liquid properties. The heat-up of the liquid due to the nozzle can be beneficial (reduction of the oil viscosity) or detrimental if the product is thermo-sensitive.

To access to the evaporation rate, the temperature of the liquid after atomization as well as during evaporation and combustion phase must be measured. To reach this objective rainbow refractrometry will be explained in the next chapter.



สถาบันวิทยบริการ
จุฬาลงกรณ์มหาวิทยาลัย

CHAPTER III

NUSSENZVEIG'S THEORY AND ITS IMPROVEMENT

Before the advent of lasers, measurements in flames were made by inserting probes such as pitot tubes for velocity, suction pyrometers for temperature, and suction probes for gas concentration measurements. Particles were collected on filters inside suction probes for subsequent removal and size analysis. In the last decades, important developments have taken place in combustion diagnostic techniques. There has been a large-scale increase in the quantity of research that has been carried out in university, government and industrial laboratories, resulting in a much better understanding of fundamental processes in turbulent, reacting, high-temperature systems. Instead of relying on global measurements, instruments have been developed that probe into flames and combustion environments, allowing measurements to be made as a function of both space and time. The presence of particles of solid fuel, liquid drop and soot has created special difficulties. Interest developed in obtaining more information about these particles and led to a number of new concepts for particle characterization in size, concentration, temperature and composition measurements.

The velocity of the particles can be measured by using Laser Doppler Velocimetry (LDV) or Particle Image Velocimetry (PIV). LDV is used for measurement of local instantaneous velocity of particles suspended in the flow while PIV, using dual pulsed lasers with a pulse duration of several nanoseconds and an adjustable delay between the two pulses, permits to record a map of the velocity vectors. The size of the particles can be measured by using photography, holography, diffractometry, Interferometric Laser Imaging Droplets Sizing (ILIDS), Phase Doppler Anemometry (PDA), .etc.

These techniques give access to size and velocity information, and for some of them have been applied to analyse the behaviour of the sprays. But no information on the droplet temperature or composition can be obtained by using these techniques. However, in order to obtain a better understanding of the droplet heat-up process in spray flames, it would also be advantageous to measure the fuel droplet temperatures and the fuel droplet evaporation rate which are of fundamental interest in the study of spray combustion.

The measurement of droplets heat-up and evaporation flow rate is still a challenge which has found only partial solutions with limited domains of application. Among others, the following approaches have to be mentioned:

- **Morphology Dependent Resonance (MDR):** This approach is reviewed by Chen et al [14]. The principle is to identify in the scattering spectrum the contribution corresponding to light trapped inside the particle. From the properties of the spectrum peaks both the particle size and refractive index can be extracted. In practice, applied to line of perfectly spherical droplets, the technique gives the possibility to measure change of diameter as small as $a \times 10^{-5}$ where a is the particle radius, with a maximum diameter of about 80-100 μm .

- **Laser Induced Fluorescence (LIF):** LIF is based on the temperature dependent fluorescence. Among various implementations [15], the two colors laser-induced fluorescence technique [16] is particularly attractive. But a difficult problem with LIF technique is to know the fluorescence properties for the working condition (fuel species, working temperature and pressure).
- **Elastic scattering properties:** these techniques are based on the temperature dependence of the real part of the refractive index. The measured quantities are a section of the scattering diagram which can be in forward region as suggested by Massoli et al [17] or at the rainbow region. The most of the work has been carried out at the rainbow region, and without being exhaustive, we must mention the contribution of Anders et al [18], van Beeck [19], Sankar et al [20]. Nevertheless, in spite of some significant progresses, important breakdowns limit the development and application of this emerging technique that has shown potential for the non intrusive measurement of fuel droplet temperature. The rainbow refractometry possesses the unique advantage to depend directly on the refractive index then no addition of fluorescence product has to be realized: it is really a **non intrusive technique**. The present chapter is a contribution to the development and application of rainbow techniques to spray temperature.

All the previously mentioned techniques are based on the interaction between light (a laser beam) and droplets which can be assumed, at least in first approximation, to be spherical. Then the understanding of the interaction between one particle and light is essential. The physics and associated mathematics are described in several textbooks [21]. The level of sophistication of the different theories is connected to the associated numerical difficulties and computational times. The basic principle behind the main theories used in this thesis are compiled in appendix A. The interferometric aspect leads to Airy theory while the wavy aspect leads to Lorenz-Mie and Debye theories. Nevertheless, some key notions and definitions will be introduced to facilitate the understanding of this chapter. These notions are essentially issued from geometrical optics which is the less sophisticated of the optic theory of particle approach but cannot be ignored due to its pedagogic power. These four theories, which can be considered as tools and are the ones used in this thesis, are described, with the associated codes, in appendix A. A special attention is dedicated to the Nussenzweig's theory because it will be proved that, by adding correcting coefficients, predictions as accurate as Lorenz-Mie theory can be achieved for a computing time equivalent to Airy theory: a fundamental improvement for inversions in real time.

Then Chapter 3 is organized as follows. Section **Preliminaries** recalls the most important notions necessary to read this chapter and introduces in details the Nussenzweig's key formulae to be used and improved in this work. Section 3.1 compares the Nussenzweig's predictions to more classical theories at forward angle. Section 3.2, for the backward angles, starts with the comparison of predictions obtained from the different theories (Lorenz-Mie, Debye, Nussenzweig and Airy) and later introduces correcting coefficients at Nussenzweig's theory to obtain fast and accurate predictions of the light scattered at the rainbow angle.

Preliminaries:

To describe the interaction of light with a spherical object, two approaches are essentially possible:

1. Approximate the incident beam by a series of rays and follow the path of each ray in agreement with the laws of geometrical optics. That is to say, we use the Descartes –Snell and Fresnel laws to compute the direction and intensity of the reflected and refracted rays each time that a ray impinges on an interface.
2. Rigorously solve the Maxwell's equations with the appropriate boundary conditions

When the incident beam is divided in rays, it is enough to study their progression in a plane, exemplified in figure 3.1. A key parameter is the impact parameter defined as the ratio of the distance between a ray and the common axis to the particle radius ($\rho = \frac{x}{a}$), where a is the particle radius. When the impact parameter is equal to 0, the incident ray is perpendicular to the particle surface and the refracted ray crosses the particle along a diameter. When the impact parameter is equal to 1, the incident ray is parallel to the particle surface. To facilitate the discussion the rays leaving the particle are named according to the van de Hulst's notation:

- $p = 0$ for the externally reflected ray
- $p = 1$ for the ray refracted twice
- $p = 2$ for the ray experimenting one internal reflection and two refractions,
- $p = 3$ for the ray experimenting two internal reflections and two refractions,
- $p = n$ for the ray experimenting $n-1$ internal reflections and two refractions.

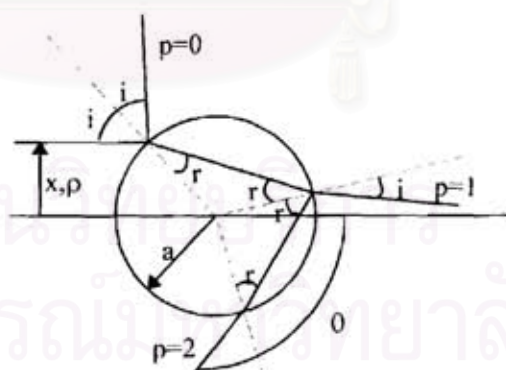


Figure 3.1: Definition of the impact parameter and van de Hulst's notation.

At each impact of a ray with the droplet surface, new directions are computed by using the Descartes-Snell's laws (1623) and the associated intensity by using the Fresnel's laws (1820). A fundamental limitation of the geometrical optics approach is the impossibility to predict the characteristics of the light at points corresponding to the crossing of two rays of the same kind, such as at a focus point. Then rainbows, which correspond to the extremum of deviation for rays experimenting a given

number of internal reflections, cannot be described by geometrical optics. The Airy's theory (1836), which starts from the wave front obtained by ray tracing inside the particle and then applies the Huygens' principle, permits a quantified description of the rainbow, taking into account the finite size of the droplet.

The rigorous solving of Maxwell's equations leads to the Lorenz-Mie (1890, 1908) theory which gives a solution under the form of infinite series where all the kinds of interactions are mixed together. A rigorous analytical post processing of the Lorenz-Mie theory leads to the Debye (1909) theory, which also gives a solution under the form of infinite series but where each kind of interaction can be independently quantified. These two complementary approaches are extremely accurate but very time consuming. An alternative approach is the complex angular momentum theory (CAM theory) developed by Nussenzveig (1969). This theory starts from the Debye's theory. But by using heavy mathematics, series are transformed in integrals which are analytically solved by introducing various approximations depending on the angular region under study and on the kind of ray of interest. Nussenzveig claims that "it is hoped that they provide useful quantitative information down to a size parameter as small as 100 (diameter of about 15 μm in visible) and at least qualitative information down to a size parameter as small as 10 (diameter of about 1.5 μm in visible)".

In this thesis, the interest is limited to the forward and first rainbow regions, where the main contribution in forward are the rays $p=0$ and $p=1$, and at the first rainbow region where the principal contribution is due to the rays $p=0$ and $p=2$ essentially but the role of $p=3$ has to be understood.

$p = 0$: To describe the reflected ray, Nussenzveig introduces one formula which can be applied at forward and backward regions. The notations are schematized in figure 3.1. The complex amplitude of the light externally reflected by the spherical particle is given by Nussenzveig [22] as ([22], formula 4.35):

$$f_{\text{reflexion}}(\alpha, \theta) = -d \left(\frac{\sqrt{N^2 - \cos^2(\theta/2)} - \sin(\theta/2)}{\sqrt{N^2 - \cos^2(\theta/2)} + \sin(\theta/2)} \right) \exp(-2i\alpha \sin(\theta/2)) \left\{ 1 + \frac{i}{2\alpha} \left[\frac{1}{\sin^2(\theta/2)} - \frac{2N^2 - \cos^2(\theta/2)}{(N^2 - \cos^2(\theta/2))^{3/2}} + O(\alpha^{-2}) \right] \right\} \quad (3.1)$$

where α is the size parameter equal to $\alpha = \frac{\pi d}{\lambda}$, d is the particle diameter and λ is the wavelength of the incident beam. θ is the scattering angle defined in figure 3.1, and N is the real part of the refractive index.

$p = 1$: To describe the twice refracted ray in the framework of the CAM theory, Nussenzveig introduces one formula. The complex amplitude of the light purely refracted by a spherical particle is given by Nussenzveig as ([22], formula 5.49):

$$f_{refraction}(\alpha, \theta) = -\frac{d}{2} \frac{2N^2}{(N^2 - 1)^2} \frac{[(N \cos(\theta/2) - 1)(N - \cos(\theta/2))]^3 \exp(2i\tau\alpha)}{(\cos(\theta/2))^{1/2} \tau^2}$$

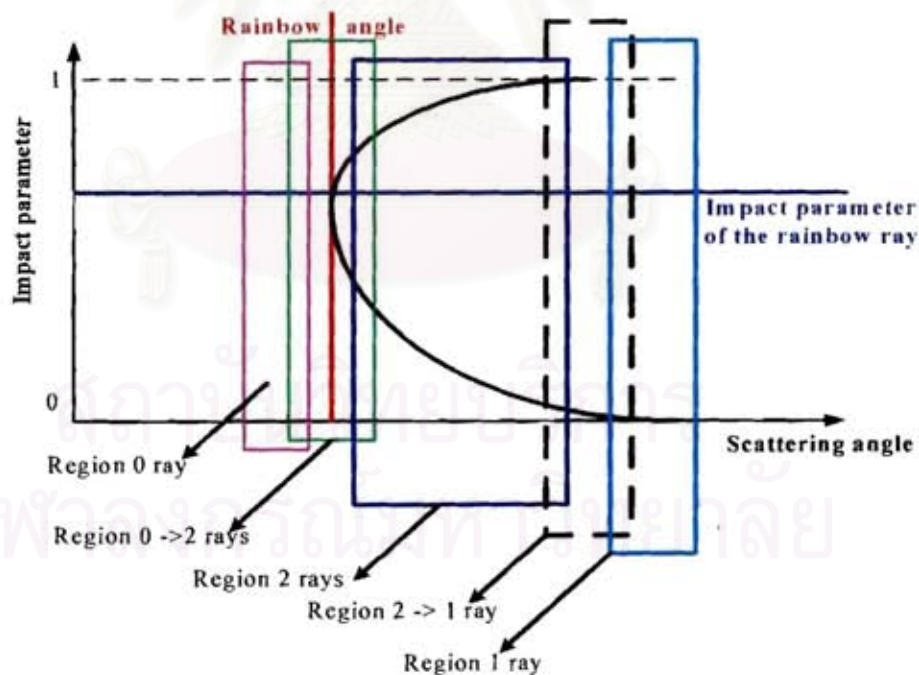
$$\left\{ 1 - \frac{i\tau}{16\alpha(N \cos(\theta/2) - 1)} \left[\frac{2(N \cos(\theta/2) - 1)}{N \sin(\theta/2)} \left(\cot \theta - \frac{(N \cos(\theta/2) - 1)(N - \cos(\theta/2))}{2\tau^2 \sin(\theta/2)} \right) \right. \right.$$

$$\left. \left. - \frac{9}{1 - \chi} + 15\chi - 6 + 8(\chi - 1) \left(\chi^2 + \frac{5}{8}\chi + 1 \right) \frac{N^2 \sin^2(\theta/2)}{(N \cos(\theta/2) - 1)^2} \right] + O(\alpha^{-2}) \right\}$$

(3.2)

where τ is given by $\tau = (1 - 2N \cos(\theta/2) + N^2)^{1/2}$ and χ by $\chi = \frac{N \cos(\theta/2) - 1}{N(N - \cos(\theta/2))}$.

$p = 2$: To describe the first rainbow ($p=2$) the situation is much more complex and, Nussenzveig introduces 5 formulae according with the angular region of interest as schematized in figure 3.2. In figure 3.2, the different rectangles schematise the domain of application of the five Nussenzveig formulae for the rainbow and voluntarily partially superimpose them to visualize the imprecision in the definition of them. However, for the practical aspect of this thesis only angular regions close and larger than the rainbow angle are of interest. Then only the formulae corresponding to cases 0-2 rays and 2 rays have been studied.



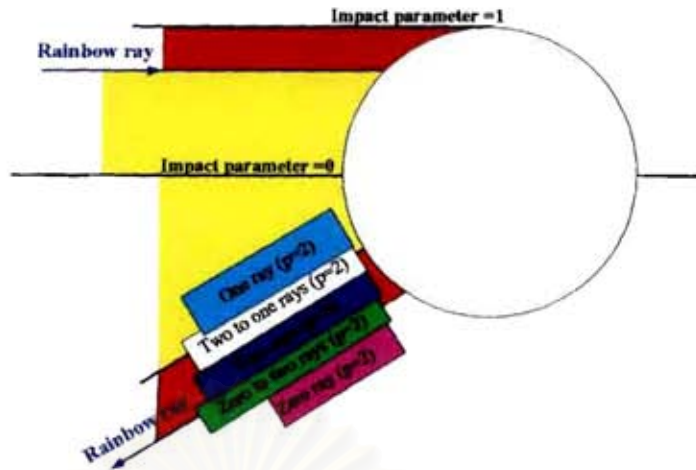


Figure 3.2: The domains of application of the different Nussenzveig formulae for the rainbow ($p=2$).

In the region $0 \rightarrow 2$ rays, the complex amplitude of the light experimenting one internal reflection is given by Nussenzveig [23] as ([23], formula 3.45):

$$\begin{aligned}
 f_{rainbow}(\alpha, \theta) = & \frac{d}{2} \cdot \frac{16e^{-i\pi/4}}{27\sqrt{3}} \left(\frac{\pi}{\sin \theta} \right)^{\frac{1}{2}} c(6s\alpha)^{\frac{1}{6}} \exp[6ic\alpha + is\alpha\epsilon + iA\alpha\epsilon^2 + O(\alpha\epsilon^3)] \\
 & \left\{ [1 + O(\epsilon) + O(\alpha^{-1})] A_1 \left[-\frac{c(2\alpha)^{\frac{2}{3}} \epsilon (1 + B\epsilon + O(\epsilon^2))}{(3s)^{\frac{1}{3}}} \right] \right. \\
 & \left. - \frac{iC}{(2\alpha)^{\frac{1}{3}}} \left[1 + O\left(\epsilon^{\frac{1}{2}}\right) + O(\alpha^{-1}) \right] A_1 \left[-\frac{c(2\alpha)^{\frac{2}{3}} \epsilon (1 + B\epsilon + O(\epsilon^2))}{(3s)^{\frac{1}{3}}} \right] \right\}
 \end{aligned} \tag{3.3}$$

with ([23], formula 3.46):

$$A = \frac{c(11c^2 - 15)}{36s^2} \tag{3.4}$$

and ([23], formula 3.47):

$$B = \frac{875c^6 - 1257c^4 + 657c^2 + 45}{8640(sc)^3} \tag{3.5}$$

and ([23], formula 3.48):

$$C = \frac{28 - 31s^2}{4c(3s)^{\frac{4}{3}}} \tag{3.6}$$

with ([23], formula 2.35):

$$s = \sin \theta_{1R} = \left(\frac{4 - N^2}{3} \right)^{\frac{1}{2}} \quad (3.7)$$

$$c = \cos \theta_{1R} = \left(\frac{N^2 - 1}{3} \right)^{\frac{1}{2}} \quad (3.8)$$

where θ_{1R} is the incident angle on the sphere for the rainbow angle, and ε verify $\theta = \theta_{1R} + \varepsilon$.

In the region 2 rays, for larger scattering angles, Nussenzveig proposes to write the scattered amplitude as the sum of two elementary amplitudes: $f(\alpha, \theta) = f_2'(\alpha, \theta) + f_2^*(\alpha, \theta)$, each elementary amplitude corresponding to a “geometrical optics ray” ([23], formulae 3.41 and 3.42).

$$f_2'(\alpha, \theta) = i \frac{d}{2} \left\{ \left(\frac{\sin \theta_1}{\sin \theta} \right)^{\frac{1}{2}} \frac{(2N \cos \theta_1 \cos \theta_2)^{\frac{3}{2}} (N \cos \theta_2 - \cos \theta_1)}{(N \cos \theta_2 - 2 \cos \theta_1)^{\frac{1}{2}} (N \cos \theta_2 + \cos \theta_1)^{\frac{3}{2}}} \exp[2i\alpha(2N \cos \theta_2 - \cos \theta_1)] \right. \\ \left. \left[1 - \frac{iG(\theta, \theta_1)}{64\alpha \cos \theta_1} \right] \right\} \quad (3.9)$$

$$f_2^*(\alpha, \theta) = -\frac{d}{2} \left\{ \left(\frac{\sin \theta_1}{\sin \theta} \right)^{\frac{1}{2}} \frac{(2N \cos \theta_1 \cos \theta_2)^{\frac{3}{2}} (N \cos \theta_2 - \cos \theta_1)}{(2 \cos \theta_1 - N \cos \theta_2)^{\frac{1}{2}} (N \cos \theta_2 + \cos \theta_1)^{\frac{3}{2}}} \exp[2i\alpha(2N \cos \theta_2 - \cos \theta_1)] \right. \\ \left. \left[1 - \frac{iG(\theta, \theta_1)}{64\alpha \cos \theta_1} \right] \right\}_{\sin \theta_1 = z'} \quad (3.10)$$

with:

$$G(\theta_1, \theta) = 8 \cot \theta_1 \left[\cot \theta + \frac{\cot \theta_1}{2(2\chi - 1)} \right] \\ + 6(9\chi - 11) - \frac{15}{2\chi - 1} - \frac{9}{(2\chi - 1)^2} \\ + \tan^2 \theta_1 \left[56\chi^3 - 3\chi^2 + \frac{39}{2}\chi - \frac{79}{2} - \frac{33}{2(2\chi - 1)} - \frac{51}{4(2\chi - 1)^2} - \frac{15}{4(2\chi - 1)^3} \right] \quad (3.11)$$

where:

$$\chi = \frac{\cos \theta_1}{\cos \theta_2} \quad (3.12)$$

The angle of incidence on the sphere (θ_1) and the angle of refraction inside the sphere (θ_2) are related by the following relations, where θ is the deviation angle (or scattering angle):

$$2\theta_2 - \theta_1 = (\pi - \theta)/2, \quad \sin \theta_1 = N \sin \theta_2 \quad (3.13)$$

which can be rewritten as (see A5 of Ref [23]):

$$z^4 - 2mdz^3 - 4m(1-m)z^2 + 4m^2dz + m^2d^2 = 0 \quad (3.14)$$

by setting:

$$z = \sin \theta_1, \quad d = 2 \cos\left(\frac{\theta}{2}\right), \quad m = \frac{N^2}{4} \quad (3.15)$$

The roots of equation (3.14) correspond to two incident angles for one scattering direction. The smaller root corresponds to a ray with an impact parameter smaller than the rainbow ray while the larger root corresponds to a ray with an impact parameter larger than the rainbow ray. Next sections are related to the comparison of the numerical predictions obtained by using these formulae with predictions from other theories (Lorenz-Mie, Debye and Airy theories).

3.1 At forward angle

At forward angle the scattered light is mainly dominated by the interference between external reflected light ($p=0$) and refracted light ($p=1$). Figure 3.3 displays scattering diagrams computed between 27° and 33° with 2048 steps. The computations have been carried out for a refractive index equal to 1.333 and a particle diameter equal to $100\ \mu\text{m}$. The scattered diagrams are simulated by Lorenz-Mie theory, which takes into account all the effects together, Debye and Nussenzveig's theories which take into account only the interference between $p=0$ and $p=1$. The comparison shows that Nussenzveig's theory is able to predict well the forward scattered light in terms of frequency and phase. This is the important key point to be used for the sizing measurement by analysis of the forward scattered light which will be described in detail later in chapter 4. The differences in intensity are due to higher order rays.

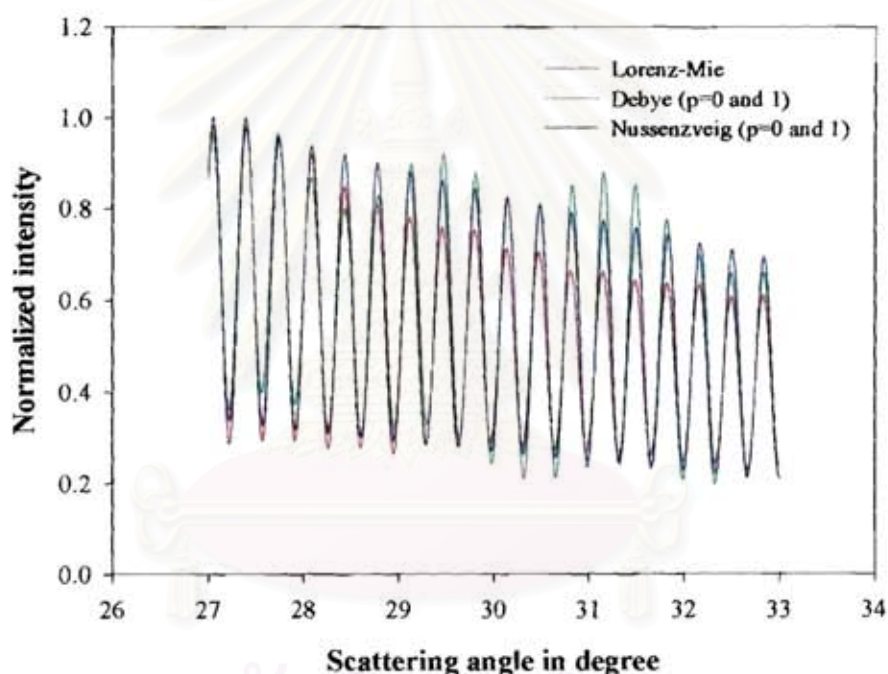


Figure 3.3: Comparison between Lorenz-Mie, Debye and Nussenzveig for the interference between $p=0$ and $p=1$.

3.2 At backward angle

3.2.1 Comparison between Lorenz-Mie, Debye, Nussenzveig and Airy for $p=2$

Few results have been published comparing the light around the rainbow angle predicted by the CAM theory and other approaches. Here the predictions of Khare and Nussenzveig [24] have been compared and discussed

To the best of our knowledge, Khare and Nussenzveig are the only ones to provide a comparison between the CAM theory and other approaches for light scattering, close to the rainbow angle, in the range from 135° to 142° . In rainbow for small particle and global rainbow technique, the collecting angle can be larger while other previous works generally concentrate on the lower range of scattering diagrams. Therefore, in this work, we shall especially focus our attention, while still considering smaller angles, on the angular range from 142° to 150° . Figures 3.4 and 3.5 display the normalized intensity versus the scattering angle for a large angular range between 135° and 150° . The normalization has been defined in such a way that the maximum of the Debye predictions with $p = 2$ is equal to unity. The same normalization factor has been afterward applied to the other approaches.

From figure 3.4, considering the main peak of primary rainbow, we observe a significant difference between Lorenz-Mie and Debye predictions (with $p = 0$ and 2) to be attributed to interactions of higher order rays which cannot be negligible for the case of small enough particles (the size parameter is equal to 50). Predictions from Debye (with $p=2$), Airy and Nussenzveig approaches perform more poorly. Although Nussenzveig and Airy predictions are in good agreement, they underestimate the scattered light intensity compared with Debye theory results within the angular range 136° - 142° and overestimate within the angular range 145° - 150° .

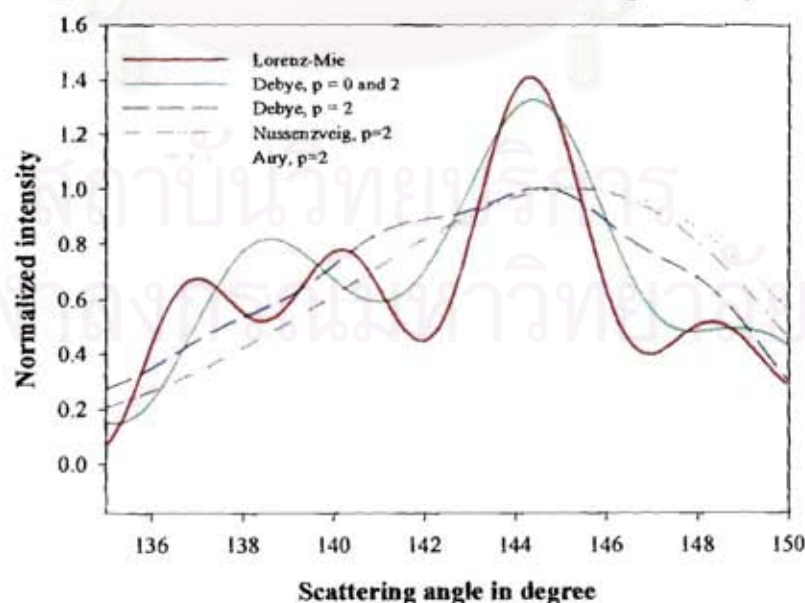


Figure 3.4: Comparison of the rainbow ray intensity predicted by Lorenz-Mie, Debye, Airy and Nussenzveig theories. The size parameter is equal to 50 and the refractive index is equal to 1.33. The incident wavelength is $0.6 \mu\text{m}$.

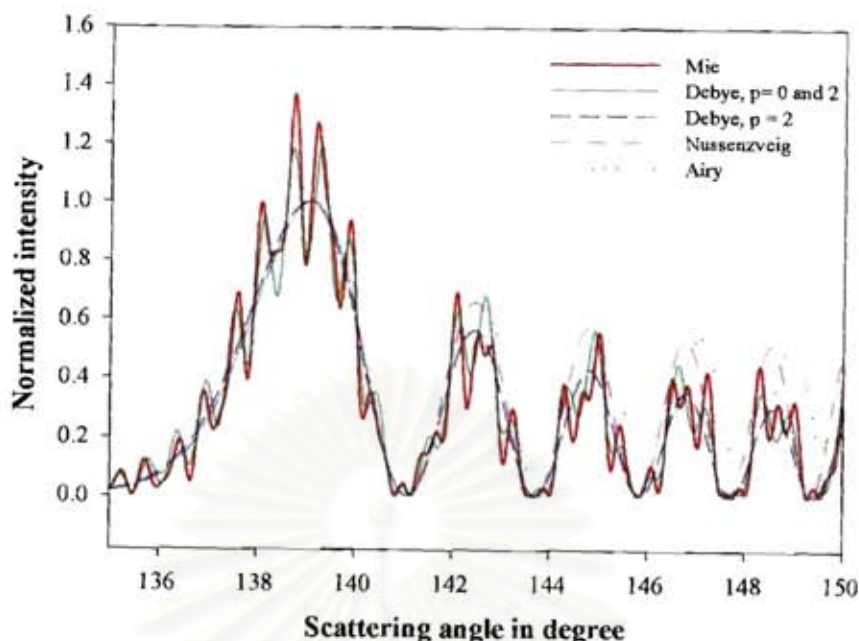


Figure 3.5: Comparison of the rainbow ray intensity predicted by Lorenz-Mie, Debye, Airy and Nussenzveig theories. The size parameter is equal to 500 and the refractive index is equal to 1.33. The incident wavelength is $0.6 \mu\text{m}$.

For the case of a larger particle with a size parameter equal to 500 (about $95 \mu\text{m}$), figure 3.5 illustrates that the Airy and Nussenzveig (formula 3.3) predictions are identical and close to the Debye prediction (with $p=2$) for the main peak of the primary rainbow. Conversely, for the supernumerary bows both theories display intensities which are significantly larger than for Debye and Lorenz-Mie predictions (approximately twice for the fourth supernumerary bow). Concerning the peak locations, Nussenzveig predictions are nearly in phase with Debye predictions while Airy predictions progressively shift to higher angular values. These observations have been confirmed by a large number of computations for different sizes of particle and refractive index values. This leads to the conclusion that Nussenzveig predictions are more accurate than Airy predictions especially when one considers supernumerary peak locations.

However, in order to obtain more accurate predictions for the light scattered far from the rainbow, a deeper discussion relying on Nussenzveig's equations (3.9) and (3.10) must be carried out, especially for the case when the scattering angle is larger than the geometrical optics rainbow angle. Figure 3.6 compares the results obtained by using equations (3.9) and (3.10) with results from Debye theory with $p = 2$. It is observed that, for the increasing part of the main rainbow peak (scattering angle up to 139°), Nussenzveig's predictions exhibit significant differences with respect to Debye predictions. For higher scattering angles, an accurate enough prediction can be obtained but remains limited to a rather small computational domain. In the range from 139° to 151° , the predictions based on equations (3.9) and (3.10) are more accurate than from equation (3.3). The locations of the supernumerary bows are very satisfactorily predicted but the intensity is underestimated by about 5%. Nevertheless, limitations towards high values of the

scattering angle can be a penalty to accurately enough fit experiments in a large angular domain.

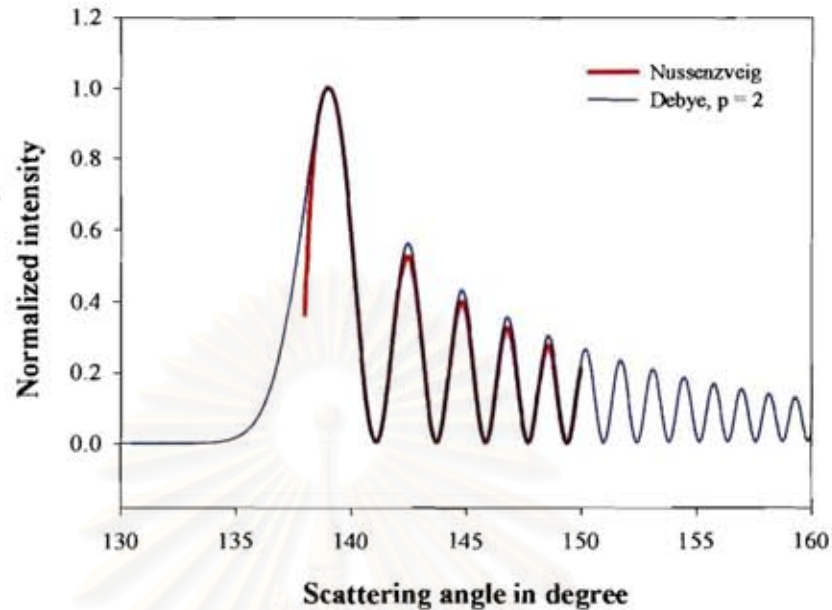


Figure 3.6: Comparison between rainbow predictions by Nussenzveig and Debye (with $p=2$) theories. The size parameter is equal to 500 and the refractive index is 1.33. The incident wavelength is $0.6 \mu\text{m}$.

Relying on these observations, correction coefficients for intensity predictions by using formula (3.3) of Nussenzveig's theory are evaluated by using the following procedure:

- Compute normalized scattering diagrams for particle sizes ranging from 10 to 100 microns in the framework of Debye theory ($p = 2$) and with equation (3.3) of Nussenzveig's theory.
- Then, compute the argument z of the Airy function (see appendix A, formula A8) as a function of the incident wavelength, particle diameter, particle refractive index and scattering angle.
- Plot the normalized scattered intensities obtained from Debye and Nussenzveig predictions versus z .
- Finally compute the ratio of the Debye normalized intensity over the Nussenzveig normalized intensity, when the Debye intensity is larger than a critical value: here selected to be equal to 0.3. The result is an empirical correction coefficient.

Figure 3.7 displays the ratio of scattering intensity predicted by the Debye theory over Nussenzveig normalized intensity against z with particle size as a parameter. For these computations, the material is water with N equal to 1.33. Coefficients of linear regressions to be used for modified Nussenzveig predictions are displayed in Table 3.1.

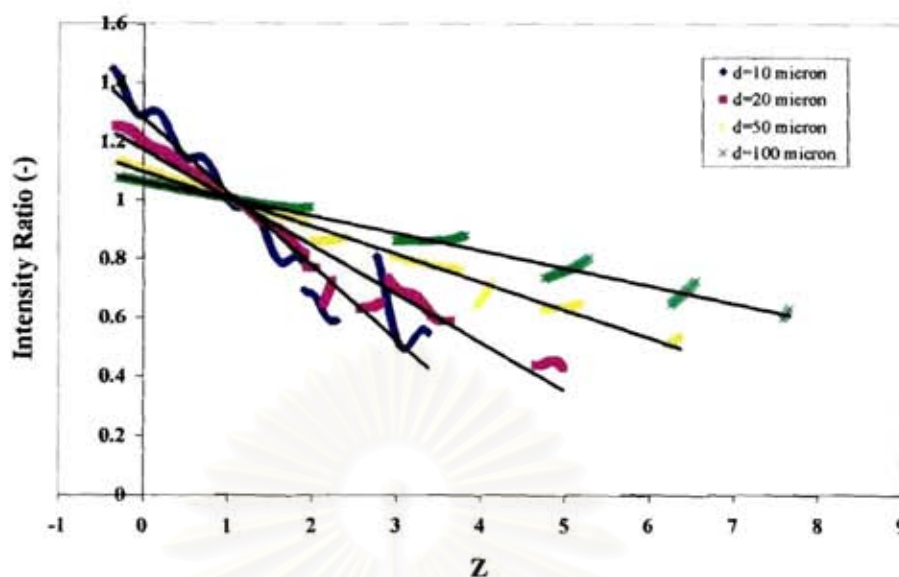


Figure 3.7: Ratio of Debye normalized intensity over Nussenzveig normalized intensity for various particle sizes.

Table 3.1 Coefficients of linear regressions for modified Nussenzveig's predictions.

Particle Size	Linear Regression
$d < 15 \mu\text{m}$	$y = -0.2523z + 1.2807$
$15 \mu\text{m} \leq d < 30 \mu\text{m}$	$y = -0.1642z + 1.1722$
$30 \mu\text{m} \leq d < 75 \mu\text{m}$	$y = -0.0946z + 1.0982$
$75 \mu\text{m} \leq d < 125 \mu\text{m}$	$y = -0.0593z + 1.0639$

After insertion of the empirical coefficients into Nussenzveig approach, it can be observed from Figure 3.8 that the modified Nussenzveig predictions lead to scattering diagrams which are in excellent agreement with the ones from Debye theory with ($p = 2$) for all investigated particle sizes. Although not shown here, computations carried out for different refractive indices between 1.3 and 1.4 confirm that the insertion of the correcting coefficients is efficient to quantitatively predict the rainbow structure within the angular domain from 130° to 160° . Also, sensitivity tests have been carried out at boundaries between correcting coefficient domains. For instance, Nussenzveig predictions for $d=14.9 \mu\text{m}$ and $15.1 \mu\text{m}$ depart of about 10% from Debye predictions for $15 \mu\text{m}$.

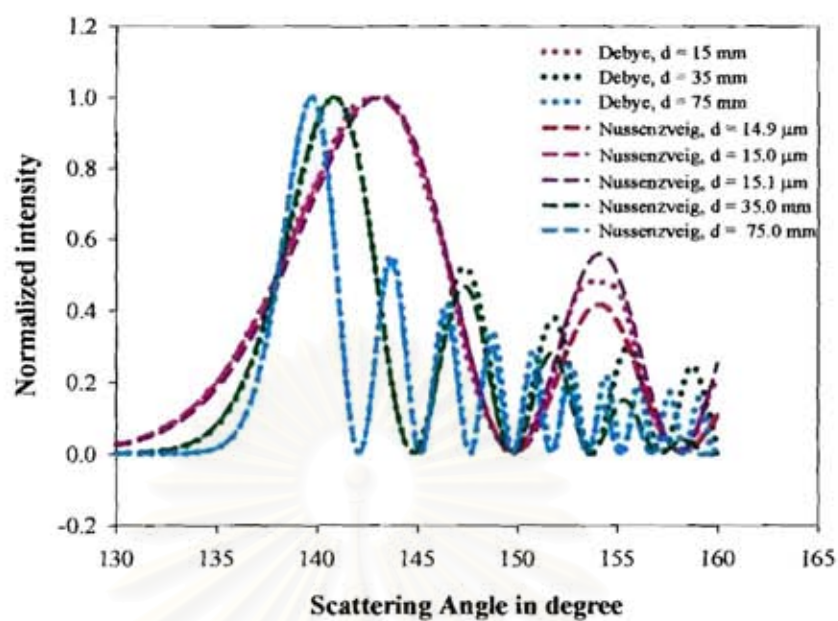


Figure 3.8: Comparison of scattering diagrams obtained from the Debye and modified Nussenzweig predictions for various particle sizes.

สถาบันวิทยบริการ
จุฬาลงกรณ์มหาวิทยาลัย

3.2.2 Comparison between Lorenz-Mie, Debye, Nussenzveig for $p = 0$

On the side of the Alexander's dark band, the intensity predicted by Airy and Nussenzveig (limited to $p=2$) approaches decreases very fast, faster than an exponential according to Nussenzveig. But also the externally reflected light possesses a nearly constant intensity in this angular range, and fast gives a contribution more important than the $p = 2$ one (see the continuous pink and dashed dark red curves). Then approaches limited to $p = 2$ cannot describe the collected intensity in this region, as exemplified in figure 3.9. Figure 3.9 displays the scattered intensity, in logarithm scale, versus the scattering angle in the angular range 130 to 140°.

In logarithm scale the fast decrease of the intensity due to $p = 2$ rays in the Alexander's dark band (scattering angle smaller than 134.5°) is very noticeable (see the blue curve, Debye for $p = 2$ and the dashed black curve, Nussenzveig for $p = 2$) but it is also remarkable that the contribution of the second rainbow is much more important than the one of the externally reflected light. This fact is illustrated by the green (Debye for $p = 0$ and 2) and the red (corresponding to full Lorenz-Mie theory) curves. The result of this analysis is that taking into account the reflected light could be useful in the case of measurement technique based on the rainbow for individual particles and when the details of the ripple are recorded. For the global rainbow, especially when applied to sprays of small particles ($d < 100 \mu\text{m}$), taking into account the reflected light will only give a small correction to the intensity predicted at large angles. To improve the description of the light scattered below the rainbow angle, the second rainbow must be included.

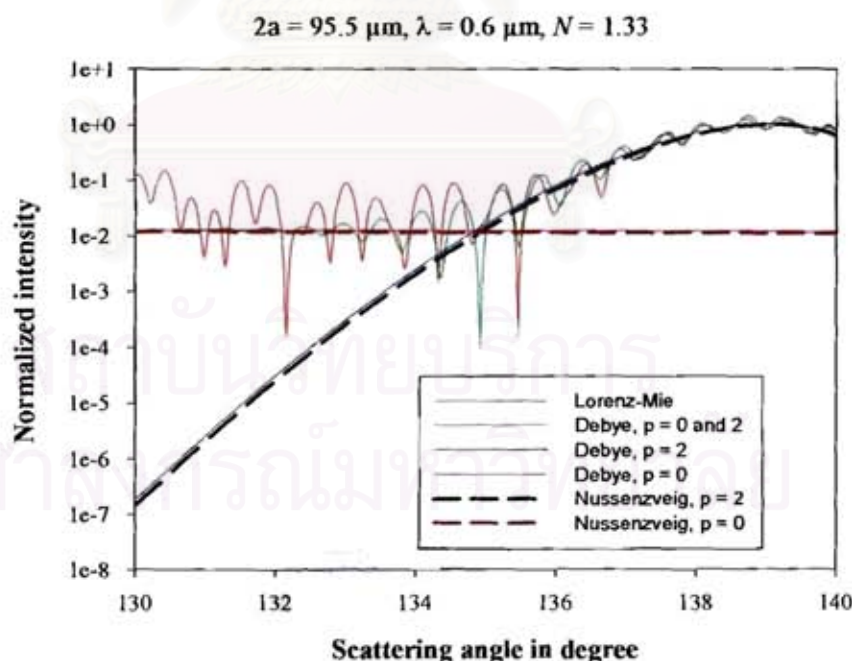


Figure 3.9: Contribution in the Alexander's dark band. Relative importance of the reflected light ($p=0$), one internally reflected ($p=2$) and twice internally reflected ($p=3$).

3.2.3 Comparison between Lorenz-Mie, Debye, Nussenzweig for the interference between $p=0$ and $p=2$

To compute the rainbow, incorporating the ripple structure, the complex amplitude given by equations (3.1) and (3.3), with correcting coefficients, are summed up together. The complex square of this quantity gives the scattered intensity. Figure 3.10 displays results of such a computation for a size parameter of 500 and a refractive index of 1.33 (same configuration than for figure 3.5). A first remark is that the interferences create strong fringes on the Airy bows, the ripple structure. A second remark is that the agreement between Nussenzweig and Debye for $p = 0 + 2$ is nearly perfect up to about 154° . The agreement with the Lorenz-Mie theory is not so perfect (due to higher order processes in full Lorenz-Mie predictions) but still good.

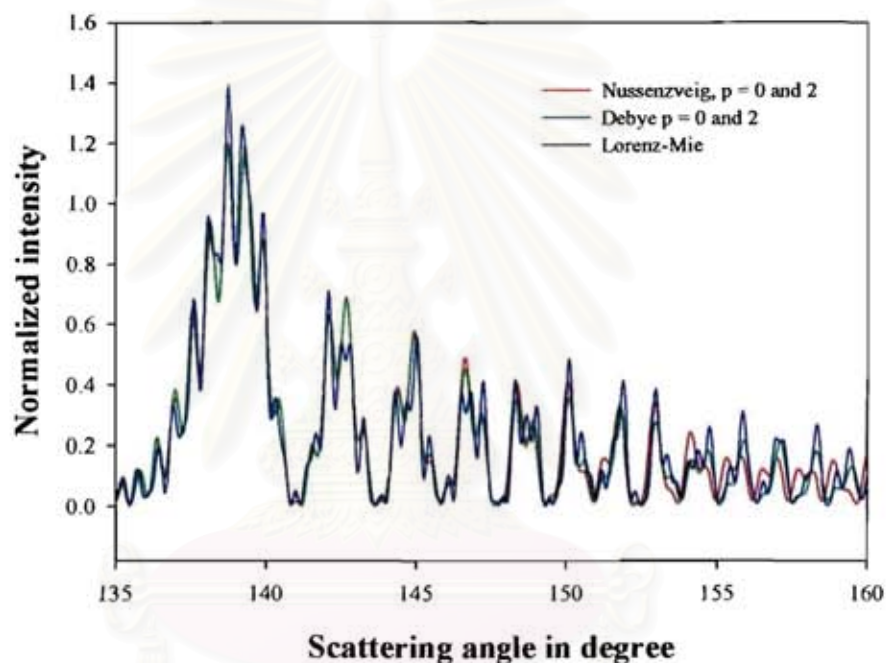


Figure 3.10: The main rainbow, including the ripple structure, for a size parameter of 500 and a refractive index of 1.33. Comparison between Lorenz-Mie, Debye ($p = 0 + 2$) and Nussenzweig ($p = 0 + 2$).

In summary, the Nussenzweig approach, for $p = 0$ and 1 at forward and for $p = 0$ and 2 with correcting coefficients at backward, is able to perfectly enough describe the scattering diagrams, including the ripple structure, in a large angular domain for individual small particles.

In the next chapters these tools will be applied to sizing and refractive index (temperature) measurements of individual and clouds of particles.

CHAPTER IV

RAINBOW PRINCIPLES AND APPLICATIONS BY USING NUSSENZVEIS'S THEORY

When we were interested by spray evaporation (e.g., the combustion of liquid fuel, including bio diesel), the precise measurement of the physical characteristics of the droplets is necessary. That is to say we have to deal with the very accurate measurement of the droplet size, temperature and composition. The refractive index is sensitive to temperature and composition; its measurement is a measure of the temperature and/or of the composition of the droplet. Then it is essential to perfectly understand the dependence of the scattering diagrams with the size and refractive index (temperature) for individual droplets.

According with these objectives, this chapter is dedicated to recall basic physic underlying the measurements technique, to criticize classical approaches, and to introduce an alternative approach. Section 4.1 is devoted to the measurement of the size by analyzing the forward scattered light and follows by an automatic analysis. Section 4.2 is devoted to the measurement of the refractive index by analyzing the backward scattered light around the rainbow angle and its automatic processing. Section 4.3 aims to introduce an automatic dual version based on these approaches, including the presentation of the processing of real experiments. Section 4.4 is a discussion of the classical rainbow limits: homogeneous and spherical particles.

4.1 Forward region

When working with one individual particle, the accurate measurement of the particle diameter is critical for all techniques (rainbow, LIF, MDR,). This paragraph is devoted to the discussion of classical approaches to measure the diameter. Often the measurement of the size is carried out by analyzing the light scattered in the forward direction, i.e. the scattering angle is smaller than 90° . Two main reasons support this choice: (i) the forward scattered light is easy to analyze because it is assumed to be essentially composed only of externally reflected light ($p=0$) and purely refracted light ($p=1$), (ii) the forward scattered light is reputed to be of little dependence on the refractive index value. These two facts are now discussed.

4.1.1 Geometrical optics formula analysis

In the forward direction, the scattered light can be essentially represented as regular fringes generated by the interferences between $p=0$ and $p=1$ rays, as shown in figure 4.1. In figure 4.1, it is clear that the scattered intensities of the two largest particles are markedly greater than the scattered intensity of the smallest one. Moreover, for a given refractive index, the number of fringes is also a function of the size; the bigger the particle is, the greater the number of fringes is. This relation can be viewed as an increase in *spatial frequency* of the scattered pattern. As the relationship between the number of fringes and the particle diameter has been established, a well-known and rapid technique for droplet sizing would simply be to count the number of observed fringes and convert it to the diameter. However, such a

method is limited in accuracy. A small change in diameter, ex. about 0.5 microns at 50 microns, creates the same number of fringes over a 20° collection angle as shown in figure 4.1.

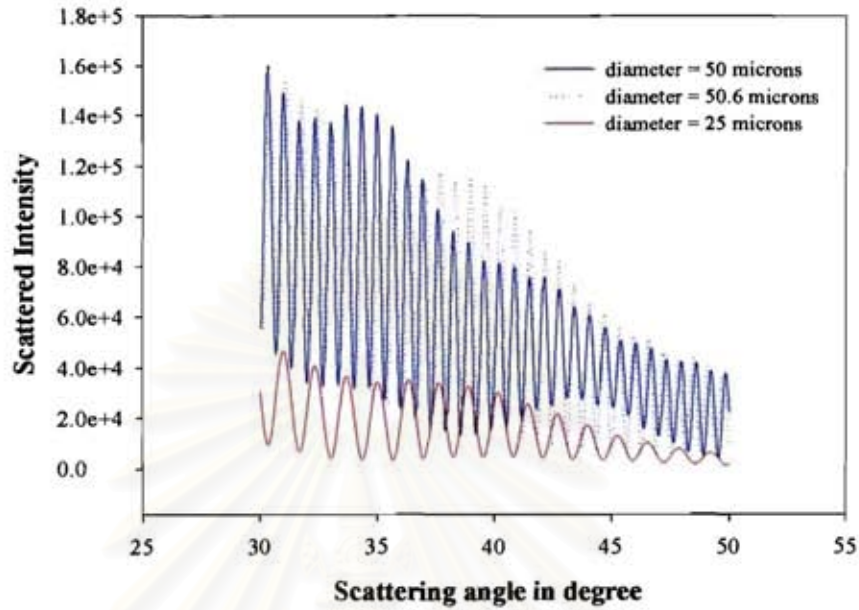


Figure 4.1: Scattered intensity distribution in the forward region computed by Lorenz-Mie theory for a droplet with the diameter equal to $50 \mu\text{m}$ micron and refractive index equal to 1.33 for a wavelength equal to $0.5145 \mu\text{m}$.

To compute the scattered light at forward region different approaches can be used. Lorenz-Mie theory can predict the exact scattered light but requires a complex numerical procedure which is time consuming. So it is worthwhile to approximate forward light scattering by ray optics.

From geometrical optic, the angular distance between two consecutive fringes can be easily computed. From appendix A, formula A.17 gives the difference of paths between a ray reflected in direction θ and a reference path, while formula A.31 gives the difference of paths between a ray refracted in direction θ and the same reference path. Then the difference of paths between the reflected and refracted light is given by:

$$\delta\phi_{p1-p0} = \sqrt{(2a)^2 \left(1 + N^2 - 2N \sin\left(\frac{\theta}{2}\right) \right)} + a \sin \frac{\theta}{2} \quad (4.1)$$

Between two scattering angles θ_1 and θ_2 , to have a consecutive fringe, the path difference must be equal to the wavelength

$$\lambda = 2a \left[\sqrt{1 + N^2 - 2N \sin\left(\frac{\theta_1}{2}\right)} + \sin \frac{\theta_1}{2} - \sqrt{1 + N^2 - 2N \sin\left(\frac{\theta_2}{2}\right)} - \sin \frac{\theta_2}{2} \right] \quad (4.2)$$

This can be approximated by:

$$\Delta\theta_f = \frac{\lambda}{a \left[\cos(\theta_m / 2) + \frac{N \sin(\theta_m / 2)}{\sqrt{1 + N^2 - 2N \cos(\theta_m / 2)}} \right]} \quad (4.3)$$

The previous formula is used by a lot researchera to measure the particle size. Nevertheless, this formula is based on different approximation to be now discussed. The angle between two interference fringes $\Delta\theta_f$ depends only on particle size (a), the real part of refractive index (N), and slightly on scattering angle which is defined here as a mean scattering angle (θ_m). The sensitivity of the predicted fringe spacing versus the size, with the refractive index as a parameter and the mean scattering angle is shown in figures 4.2 and 4.3.

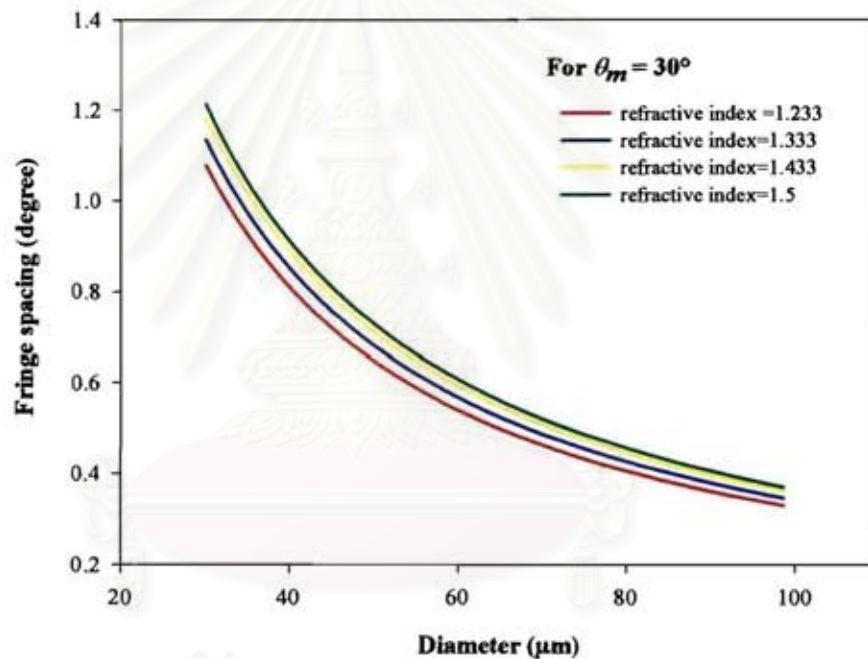


Figure 4.2 Fringe spacing as a function of droplet diameter. The parameter is the refractive index value.

As the angular distance between fringes is the function of droplet radius, it is obvious that, if the scattering angle and the refractive index are known, the measurement of the angular distance between fringes, the spatial frequency, is a measurement of the particle diameter [25].

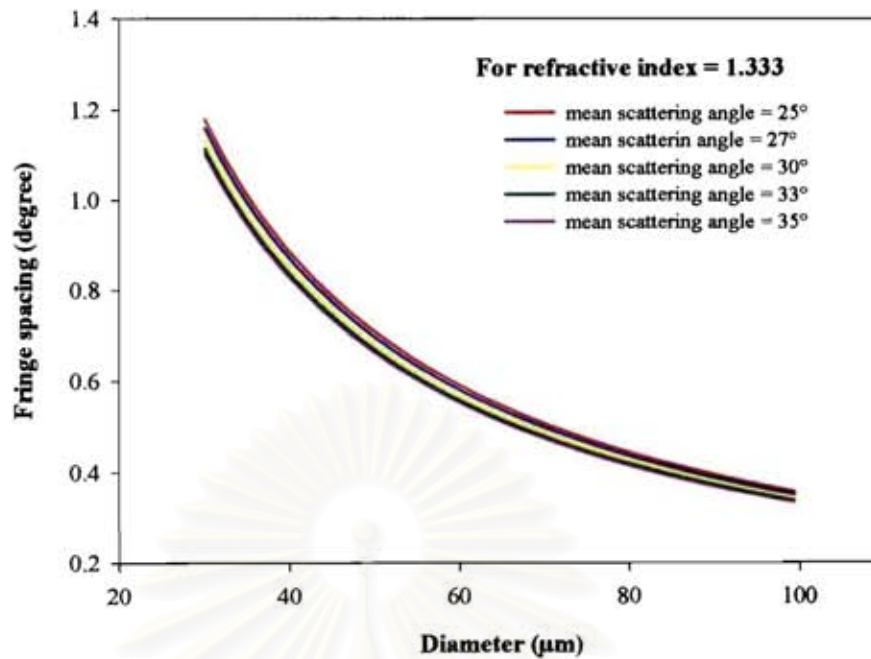


Figure 4.3 Fringe spacing as a function of droplet diameter. The parameter is the mean scattering angle.

Moreover to obtain equation 4.3 it has been assumed that angular distance between two interference fringes is constant in the collection solid angle. This can be true just only for a small solid angle. The definition of the solid angle has an effect on the accuracy of size measurement.

As an example, figure 4.4 shows the fringe spacing as a function of diameter for different mean scattering angles. Although the scattered light in the forward region could be seen as essentially regular fringes, figure 4.4 shows that for a given particle size, the angular distance between two interference fringes is not exactly the same along the forward scattering angle. In case we use the average scattering angle, with the same mean scattering angle, about 30° , but different solid angles equal to 10° (solid angle between 25° - 35°) and 5° (solid angle between 27° - 33°) could not give the same answer in terms of accuracy. The accuracy is about 8% and 4% for solid angles of 10° and 5° respectively. Then by using average scattering angle to extract the particle size a few microns error could occur.

Furthermore, Massoli et al [26] have claimed that the scattered light distribution in the forward angle (about 33° for diameter equal to 40 microns) is almost independent of the refractive index. This result has been obtained not for one individual particle but by summing the contribution of particles in the range 40 ± 0.26 microns with a step of 0.008 micron, and integrating over an angular aperture of $\pm 2.4^\circ$ to smooth the scattering diagram. Figure 4.5, extracted from Massoli et al paper, exemplify this result.

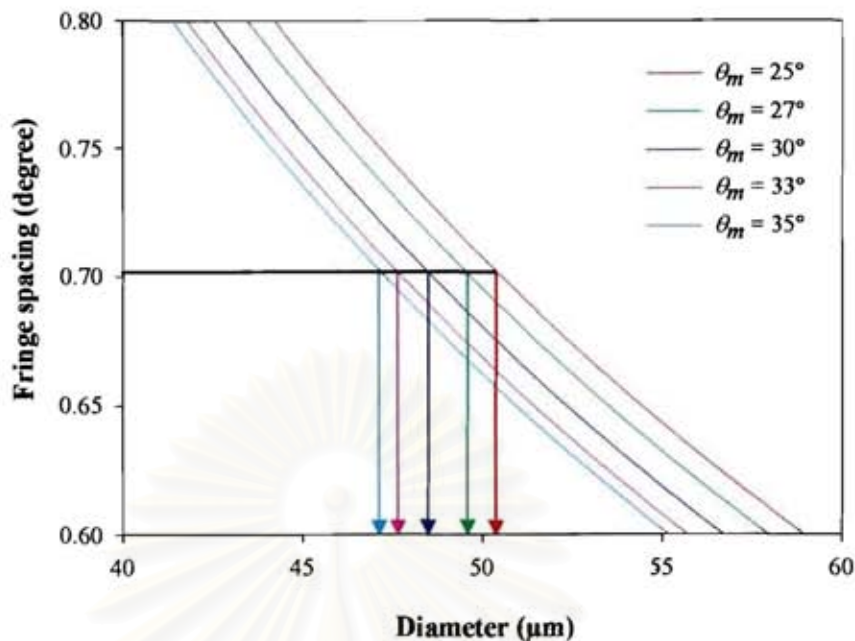


Figure 4.4: Fringe spacing versus the particle diameter corresponding to equation 3.18. The parameter is the average collecting angle.

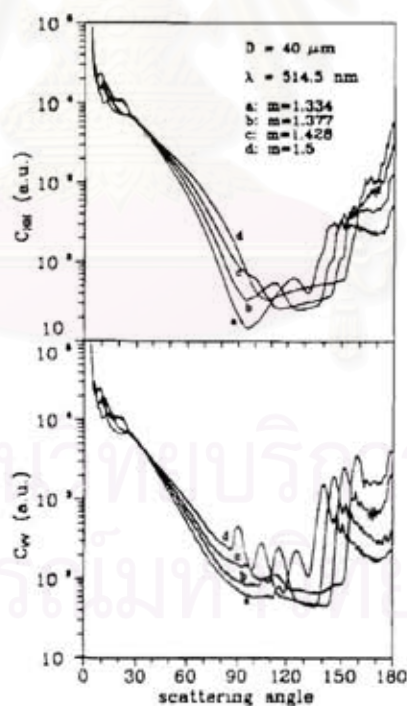


Figure 4.5: Angular patterns of horizontally (top) and vertically (bottom) polarized cross section for 40 micron droplets with different refractive indices computed by Lorenz-Mie theory.

Figure 4.6 displays the scattering diagram between 30° to 60° for one particle of 40 microns without any integration on size and scattering angle. The intensity and angular distance between fringes are close but not equal. For example, between 30° and 40° degrees there are 11 or 12 oscillations for refractive index of 1.5 and 1.334 respectively. Then even though the refractive index has little effect on the scattered light in the forward region, it is enough to decrease the measurement accuracy.

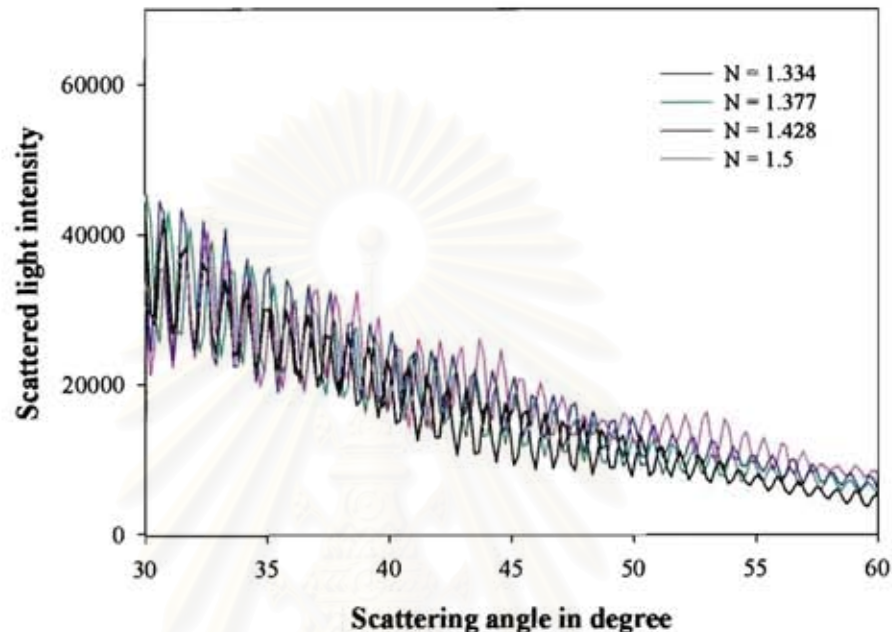
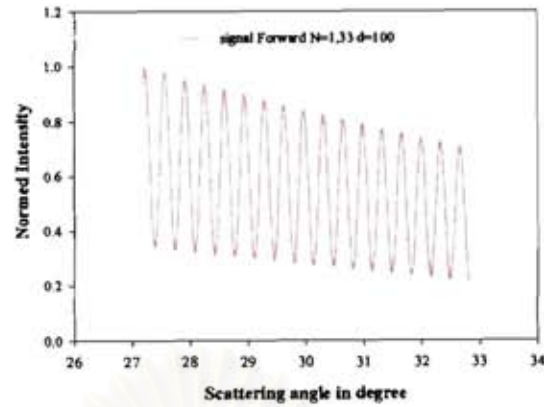


Figure 4.6: Scattering light distribution in the range angle of 30° - 60° for different values of refractive index.

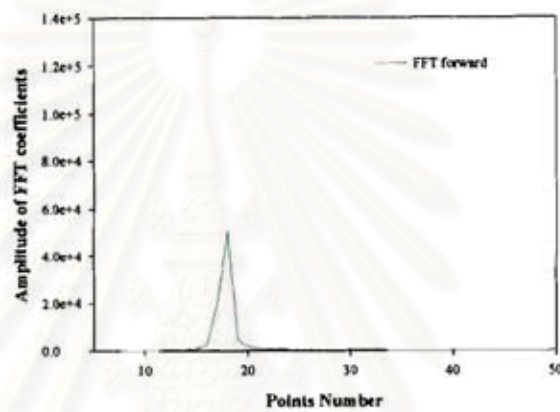
4.1.2 Nussenzveig's analysis

To improve the measurement in the forward region one possibility is to use the Lorenz-Mie theory to fit an experimental scattering diagram in frequency and phase as Min and Gomez [27] did but this approach is very time consuming. An alternative is to use the Nussenzveig's approach introduced in chapter 3, which is as accurate as Lorenz-Mie but as fast as geometrical optics. The strategy is to calculate the light distribution for an arbitrary size and refractive index, and then to compare it with the simulated/recorded profile. A satisfactory return can be obtained when the location, shape and amplitude of the peak and trough match together.

However, it is difficult to compare directly and accurately the simulated/recorded with computed/measured scattering diagrams but it is easy to compare the frequency components of both signals by computing the associated Fast Fourier Transforms (FFT). Figure 4.7a and 4.7b display the forward scattering diagram for a particle of 100 microns and $N=1.333$ and its associated FFT spectrum.



(a)



(b)

Figure 4.7: The forward scattering diagram for a water droplet ($N=1.33-0.0 i$) with a diameter equal to 100 microns (figure 4.7a) and its associated FFT (figure 4.7b).

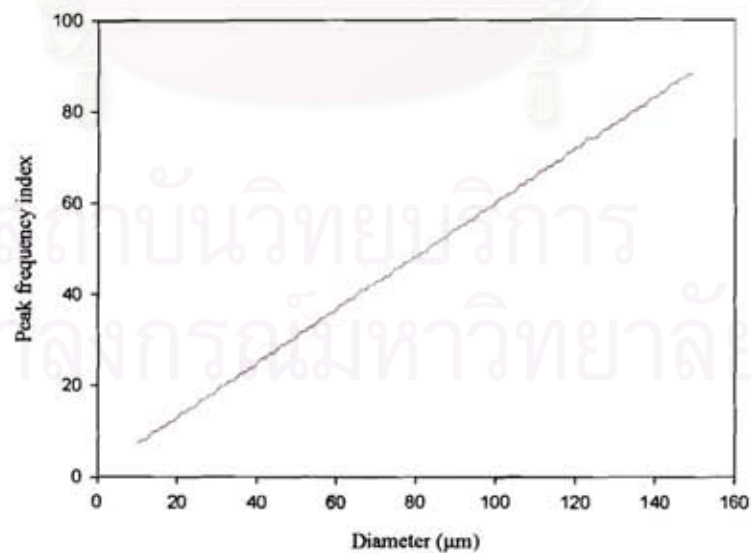


Figure 4.8: Index of the dominant spatial frequency component of the intensity light distribution as computed by the FFT versus particle diameter. Optical parameters: wave length 0.5145 micron, scattering angle between 25° and 45° and refractive index of 1.333.

Figure 4.8 displays the position of the maximum of the Fourier transform (more accurately Fast Fourier Transform: FFT), computed on the angular range between 25-45° with 2048 points, versus the particle diameter for a refractive index equal to 1.33. As the angular frequency is the inverse of the angular distance, this curve gives the same information as figures 4.2, 4.3 and 4.4. In figure 4.8, the peak index looks to be a monotonic function of particle size over a fairly large range of size.

By applying FFT with the scattering distribution, the larger the scattering angle range is the higher the accuracy is. However, in the practical way, the solid angle cannot be larger than about 10° due to the limitation of the optics configurations. Figure 4.9 shows the relationship between peak frequency and diameter with the same liquid properties as the computations in figure 4.8 but a different optics configuration. The used optics configuration is the same as the Onera's configuration, which measures the scattered light between 27-33°.

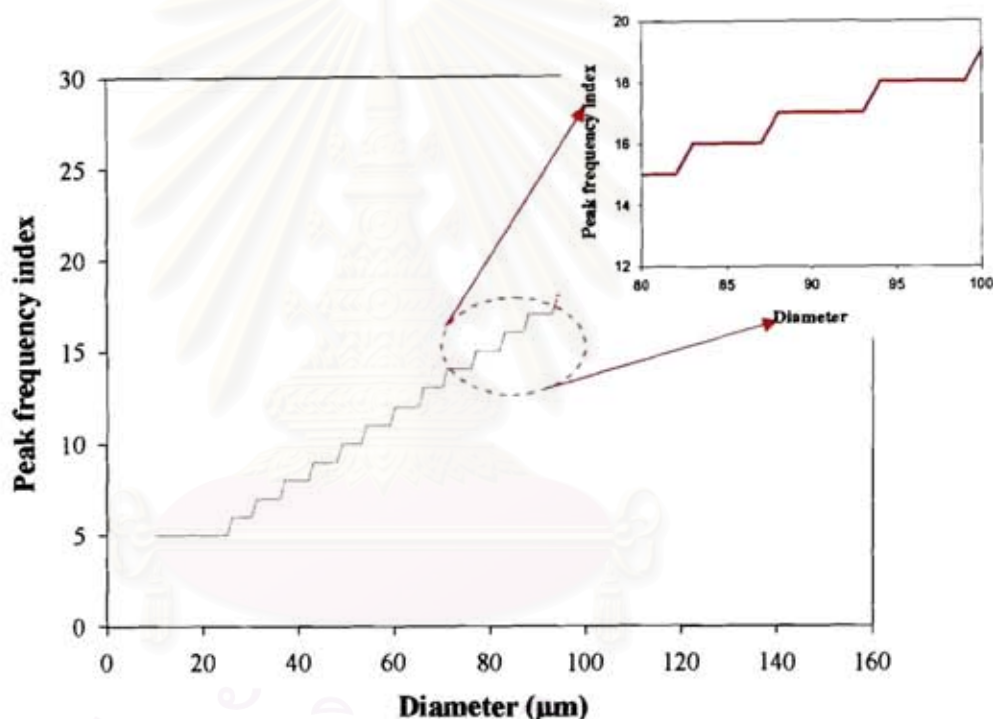


Figure 4.9: Index of the dominant spatial frequency component of the intensity light distribution as computed by the FFT versus particle diameter. Optical parameters: wave length 0.5145 micron, scattering angle between 27° to 33° and refractive index of 1.333.

The location of the peak frequency is given with steps due to the digitalization. At the same FFT maximum position corresponds to a range of possible diameters. As shown in figure 4.9, for example, it is clear that by measuring only discrete locations of the FFT maximum, the accuracy on the measured diameter is equal to about 4%.

To improve the accuracy of the diameter measurements, a first step is to improve the localization of the FFT maximum by using a spline method. A spline method is based on the fitting of the maximum point and its neighbours by a spline

curve. Then the angular fringe frequency can be measured much more accurately. This procedure permits to measure the diameter with accuracy equal to about 2-3% for a diameter of about 100 microns as shown in figure 4.10.

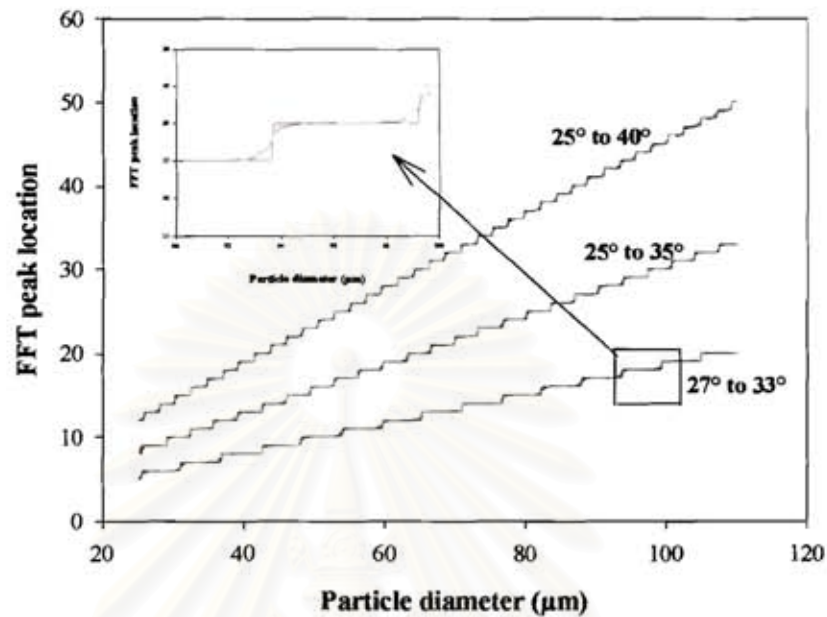


Figure 4.10: FFT and its spline versus diameter.

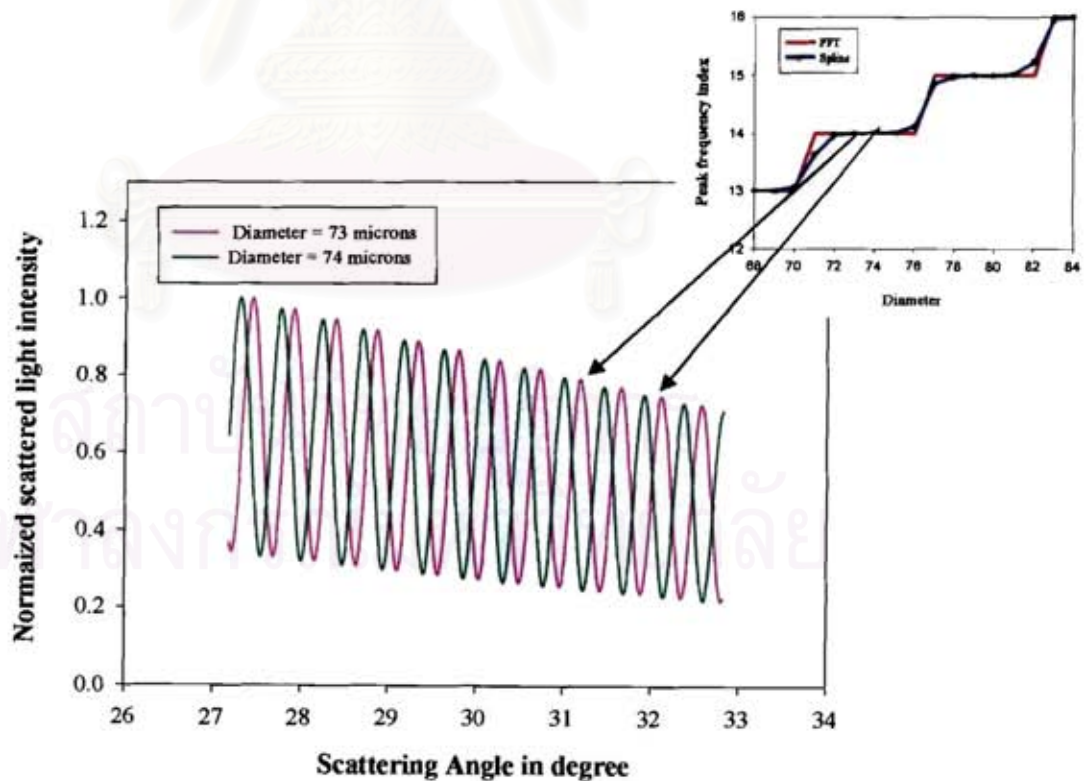


Figure 4.11: Phase difference between the scattered light by particles with diameter equal to 73 and 75 microns ($N=1.333$, wave length=0.5145 micron, 2048 points).

Even if the range of possible diameters has been reduced, there is still a significant undetermination. Nevertheless, as exemplified in figures 4.1 or 4.11, two particles with different diameters but with the same associated spatial frequency can be discriminated by using the spatial location of the fringes.

Then, to refine the accuracy of the measurements, the absolute location of the fringes (the phase) must be taken into account. To quantify the phase shift between the recorded signal and the computed signal by Nussenzveig a cross FFT technique is used. A cross FFT is a useful result, calculated by the FFT, that is often neglected, perhaps because of its somewhat unintuitive nature. Because our interest has been narrowed to a single frequency bin of the power spectrum, the phase extracted from the complex form of FFT at the peak frequency index corresponds directly to the observed shift of the original scattering function over the fixed window. The most apparent change between the two profiles pertaining to the 50 microns and 50.6 microns droplets shown in figure 4.1 is the difference in the position of the extrema, which are interpreted by FFT as a phase shift of the dominant frequency component. The phase lag computed by the FFT is 80° . This sensitivity of the phase to small change in particle diameter can be displayed by overlaying the computed phase at each particle size with the peak frequency index, as shown in figure 4.11. To 360° of phase corresponds a change of the particle diameter of about $0.7 \mu\text{m}$. Although phase alone does not satisfy the requirement of a one-to-one correspondence with diameter, this variable, when coupled with the peak frequency index, appears piecewise monotonic across each frequency step for calculated resolution if the collection angle is large enough. The use of frequency and phase information in the signal collected over a finite, and possibly broad, collection angle thus provides a single-valued, concise and accurate indicator of droplet size.

The next paragraph is devoted to an example of size measurement by analyzing the scattered light at the forward angle using FFT, spline method and phase information as described above.

The recorded signal from the particle with the diameter equal to 104 microns and the refractive index equal to 1.342 illuminated by the incident wave with the wavelength equal to 0.5145 micron is computed by Lorenz-Mie theory. The optics configuration used is the same configuration as in the real experiments in ONERA which measures the scattered light in the range $27-33^\circ$. The Nussenzveig's theory has been used to compute and compare with the recorded profile.

By applying FFT and spline method to the recorded and computed forward scattered light and comparing the frequency component of both signals a continuous range of returns is obtained for a given refractive index. Even if the forward scattered light depends strongly on the droplet size, the refractive index however still has an effect. In case when the refractive index is unknown, other possible size ranges are also obtained as function of the refractive index value. The size range increases with the refractive index value as shown for example in figures 4.12 and 4.13.

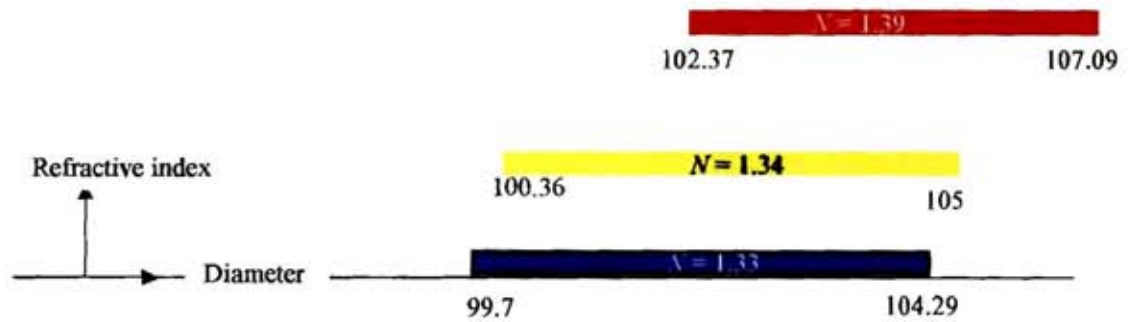


Figure 4.12: Possible sizes obtained from main frequency analysis for different assumed refractive index values.

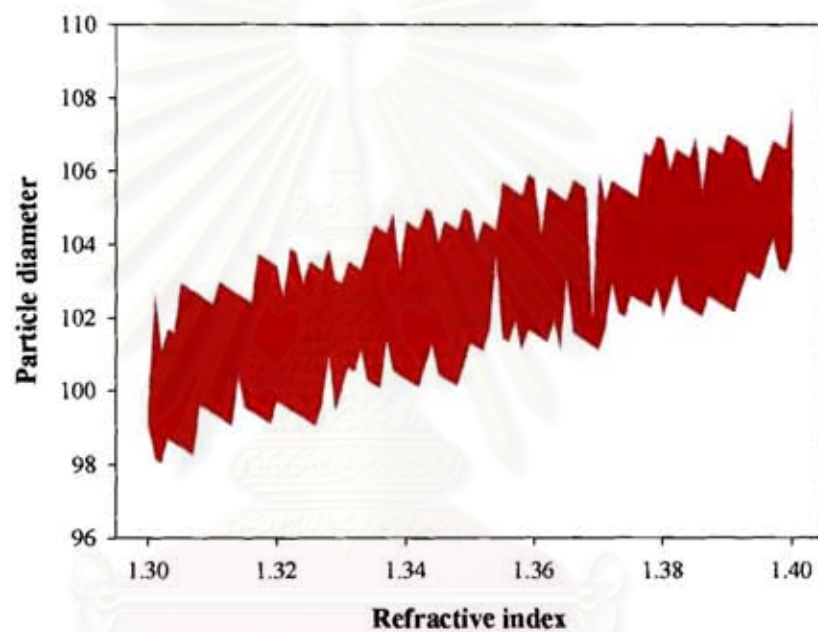


Figure 4.13: Possible particle diameters extracted by frequency processing versus the assumed refractive index value.

Figures 4.12 and 4.13 show the possible returns for the size range versus the refractive index of the droplet which scatters light with the same spatial frequency as the measured signal. The possible diameter sizes, for example, can run from 99.7 up to 104.29 microns for a refractive index equal to 1.33. In case when the refractive index is known to be equal to 1.342, the continuous range of possible sizes runs between 100.5 and 104.35 (accuracy of about 4-5%) In this possible range of sizes, only some particles will possess a scattering diagram in phase with the measured signal as shown in figure 4.14. Figure 4.14 compares the forward scattered light and its associated FFT spectrum between recorded signals simulated by Lorenz-Mie as a red line and Nussenzveig's computed signal as a blue line.

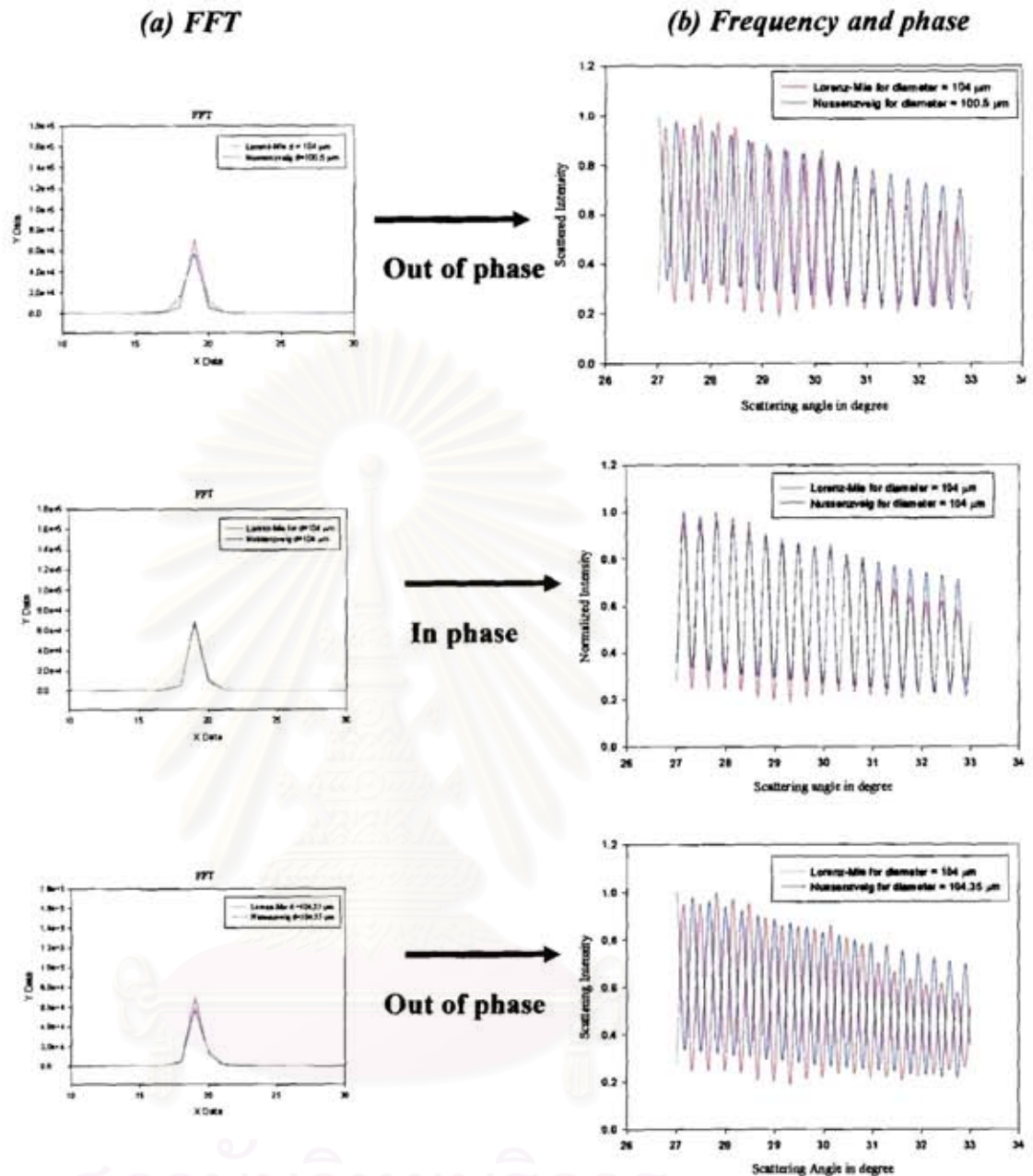
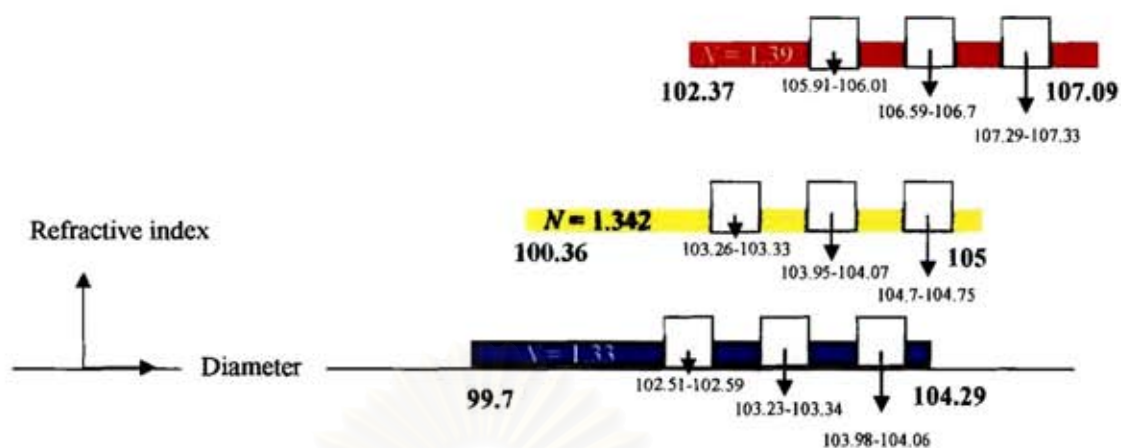


Figure 4.14: Comparison of the forward scattered light computed by Lorenz-Mie and Nussenzveig theory and its associated FFT spectrum ($N=1.342$, $\lambda=0.5145$ micron, 2048 points).

Taking into account the phase (the recorded signal and the computed signal must have maxima and minima at the same location), the number of possible returns is reduced. The continuous return is transformed to several continuous returns: for $N=1.33$ only 3 small ranges of diameters are possible; 102.55-102.6, 103.21-103.34, 103.95-104.06 microns.

From the smallest to the largest of the possible diameters, we obtain an accuracy of 2%, and for each range of possible diameters the accuracy is better than 0.1%.



All the possible solutions for a phase difference smaller than 2°

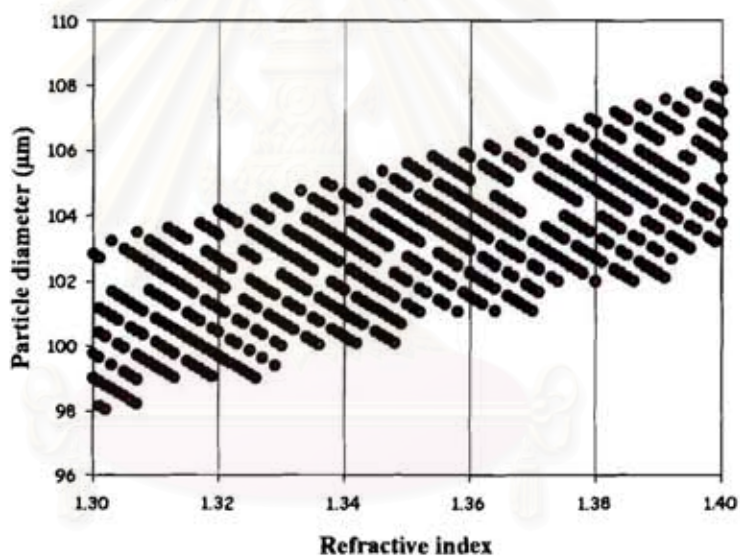


Figure 4.15: The possible returns of size obtained from frequency and phase processing versus the refractive index.

4.1.3 Forward automatic processing based on Nussenzweig's theory

Our aim now is to automatically process forward signals. In this section we will assume that the refractive index is perfectly known. Only the accuracy of the inversion for the diameter will be studied.

The processing will be performed in two steps. The first step is on frequency which gives an approximate value of the diameter, the second step is on phase which will refine the evaluation of the diameter.

The algorithm is discussed below for a test particle with a diameter equal to 100 microns and a refractive index equal to 1.36.

4.1.3.1 Frequency processing:

As described before, the frequency of the forward signal is a monotonic function of the particle diameter. The larger the particle diameter is, the higher the associated angular frequency is. Then we propose to use the Brent algorithm (see Appendix B) by defining the function $F(x)$ as the difference between the frequency of the simulated signal and the frequency of the computed signal: $F(x) = f_{\text{simulated}} - f_{\text{computed}}$.

This function is positive when the computed frequency is smaller than the simulated frequency, and negative for the opposite case.

The boundaries of the study domain can be arbitrarily selected. For example, figure 4.16 displays the series of iterations when the boundaries of the study domain are selected to be 50 μm and 130 μm , with an accuracy for the solution as small as 0.01 μm . The convergence is obtained in only 7 iterations with a measured size equal to 100.24 microns

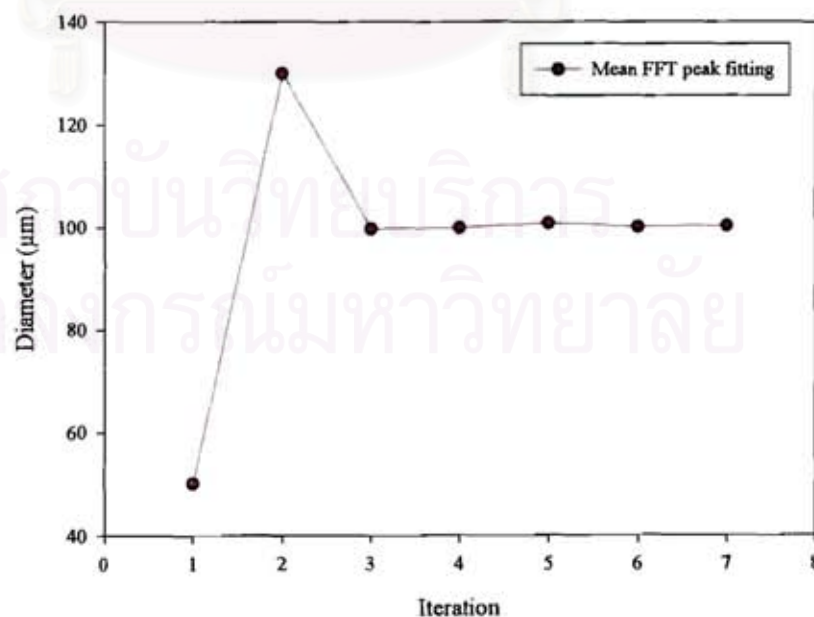


Figure 4.16: Convergence of the Brent method at forward only taking into account the frequency. The refractive index is assumed to be perfectly known.

4.1.3.2 Phase processing:

The phase is a non uniform function of the diameter, then the study domain for the Brent method must be carefully defined. The first step is to compute the phase between the possible diameters coming from the frequency processing step and the simulated signal. Then by using the fact that the phase periodicity is about $0.7 \mu\text{m}$, a study domain is defined according with figure 4.17.

If the phase (p) is positive: $d_{max} = d_{frequency}$ and $d_{min} = d_{frequency} - 0.7*(150+p)/360^\circ$

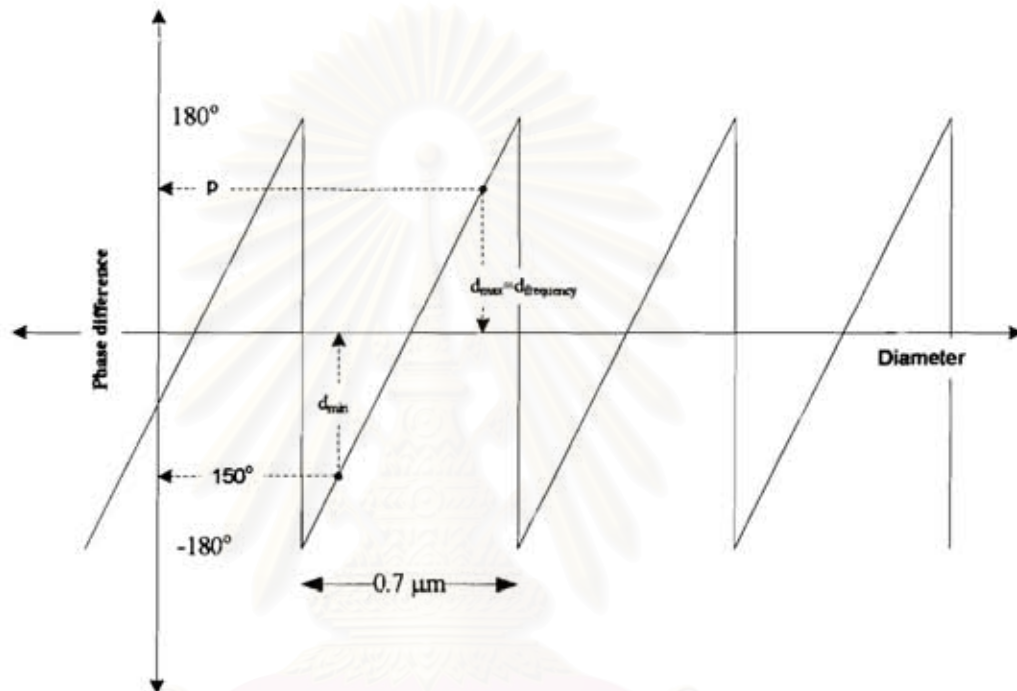


Figure 4.17: Scheme of the phase evolution and definition of d_{min} and d_{max} used in Brent method.

If the phase (p) is negative: $d_{min} = d_{frequency}$ and $d_{max} = d_{frequency} + 0.7*(150-p)/360^\circ$

This definition of the Brent domain warrants us to have only one solution in the study domain. Then in this domain, the Brent method is applied to a function defined as the phase difference between the simulated signal and the computed signal. When this function is null both signals are in phase. For the case under study, figure 4.18 displays the full series of iterations (frequency and phase). The convergence for the phase is obtained in only 4 steps as shown in green, and the final measured size is equal to 100.007 microns.

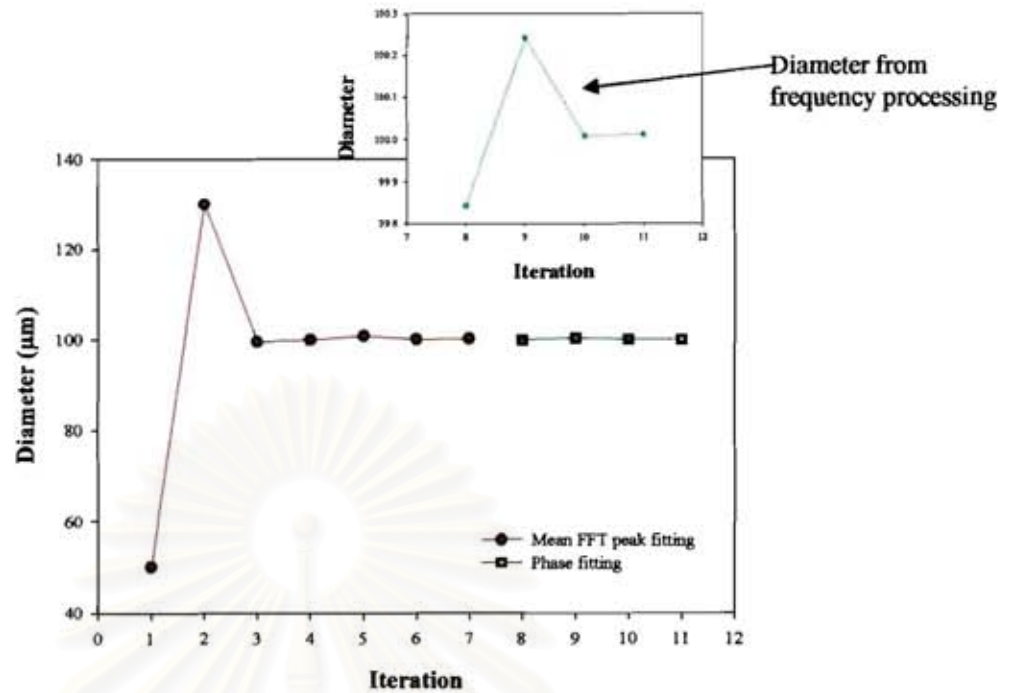


Figure 4.18: Convergence of the Brent method at forward taking into account the frequency (in red) and the phase (in green). The refractive index is known.

Then by taking into account frequency and phase, for a diameter of 100 microns, an accuracy of about 1/10 000 is obtained.

To further test the validity of this approach, different signals have been simulated by using Lorenz-Mie theory, for diameters running from 30 µm to 100 µm and for refractive indices running from 1.3 to 1.4 by step of 0.02. The measured diameters are compiled in table 4.1 and plotted in figure 4.19

Table 4.1 The measured diameters by using the developed automatic forward processing.

Refractive index \ Diameter	1.30	1.32	1.34	1.364	1.38	1.40
30 µm	29.98	30.002	29.98	30.71	30.04	27.98
40 µm	39.999	39.27	40.03	41.41	39.98	42.03
50 µm	50.01	52.23	50.01	50.70	49.97	50.01
60 µm	60.00	59.98	59.98	59.99	60.68	60.008
70 µm	69.99	70.00	70.73	70.00	70.68	70.00
80 µm	80.00	79.27	80.73	79.31	80.00	80.01
90 µm	89.24	90.00	90.00	90.02	90.02	90.00
92 µm	91.99	92.00	91.27	90.60	92.68	92.00
94 µm	94.00	94.00	94.71	94.00	92.61	92.65
96 µm	93.72	96.74	95.29	96.02	96.66	96.00
98 µm	98.00	98.00	96.57	96.61	99.37	98.00
100 µm	99.24	99.99	100.69	100.00	99.33	100.00

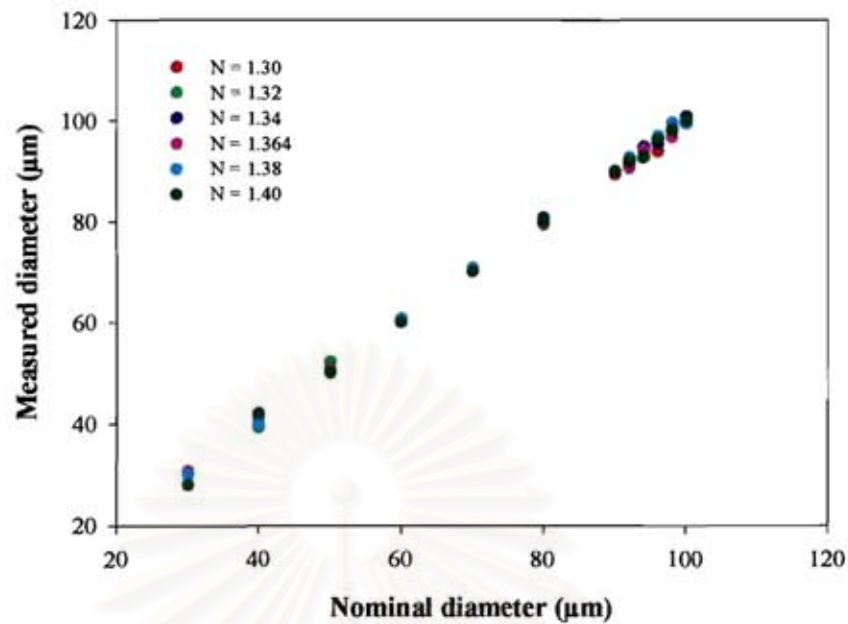
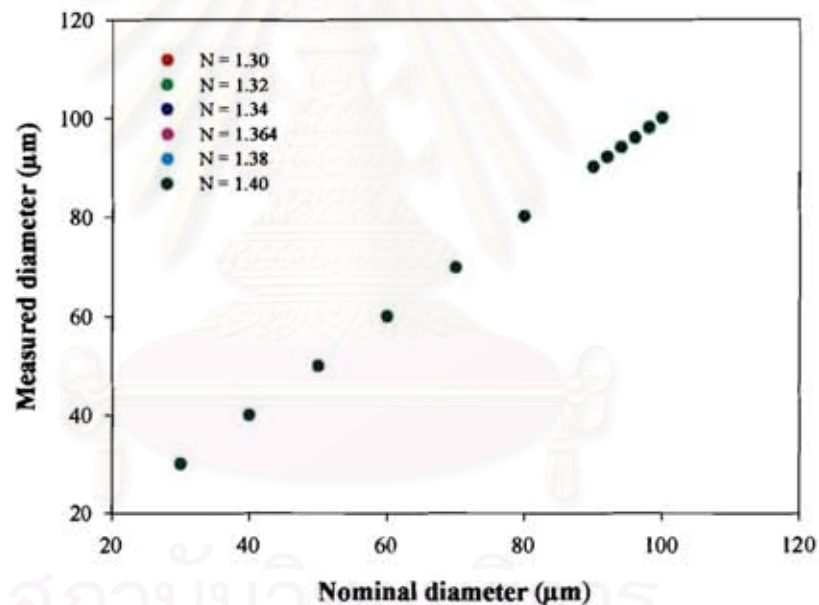


Figure 4.19: Measured diameters versus nominal diameters with the refractive index as a parameter.

The diameters are relatively well measured. Nevertheless, a close attention shows that some diameters are not perfectly enough measured. These values are highlighted in table 4.1. For example, the particle with a diameter equal to 96 μm and a refractive index value of 1.30 is measured as 93.72 μm . This is due to the non-unicity of the frequency with the diameter for the configuration under study as described in figures 4.10 and 4.11. Other diameters, with the same frequency, are in phase agreement. These diameters, according with the periodicity of the phase function, are located at $\approx \pm I 0.7 \mu\text{m}$ where I is an integer. Table 4.2 compiles the number of periodicities used to find the perfect return in diameter. The + symbol means that the diameter has been increased by about 0.7 μm , while the - symbol means that the diameter has been decreased by about 0.7 μm . The number of symbols represents the number of times the operators (+ or -) have been applied. Figure 4.20 displays these measured diameters versus the nominal diameters. The agreement is perfect for all cases under study with an absolute accuracy better than 0.01 μm .

Table 4.2 The number of periods to extract the perfect diameter.

Refractive index Diameter	1.30	1.32	1.34	1.364	1.38	1.40
30 μm				-		+++
40 μm		+		--		---
50 μm		---		-		
60 μm					-	
70 μm			-		-	
80 μm		+	-	+		
90 μm	+					
92 μm			+	++	-	
94 μm			-		++	++
96 μm	+++	-	+		-	
98 μm			++	++	--	
100 μm	+		-		+	

**Figure 4.20:** Measured diameters versus nominal diameters. The parameter is the refractive index value. Periodicity of the phase has been taken into account.

The conclusion is that a fast, robust and accurate algorithm, based on the Nussenzweig's theory, has been written which ensures a size measurement with an absolute accuracy of about 0.01 μm in a large domain of size and refractive index, when the refractive index is known. The next step is to measure the refractive index by assuming that the particle diameter is known.

4.2 Backward measurement (Rainbow refractrometry)

The temperature and composition are key parameters in the combustion field. The refractive index is a function of the liquid density as shown in figure 4.21(a). For this reason the determination of the refractive index allows one to distinguish between different liquids. Measurement of refractive index allows one to determine concentration in a mixture of liquids, as can be seen in the example of figure 4.21(b).

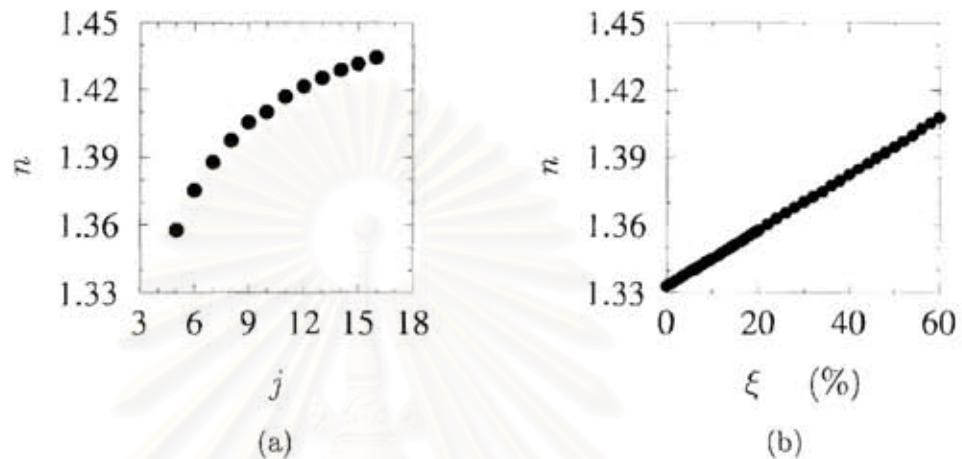


Figure 4.21: (a) Refractive index for hydrocarbon with different number j of carbon atoms
(b) Refractive index of a sulfuric acid-water mixture as a function of the mass fraction of sulfuric acid.

Moreover, an increase of temperature results normally in a decrease of density. The knowledge of the refractive index allows one therefore to determine the temperature, as can be seen in figure 4.22. Figure 4.22 shows the dependence of the refractive index on the temperature for water and ethyl alcohol. It should be mentioned that for temperature measurements with accuracy of a few degrees, the refractive index has to be measured with a very high accuracy. For example, to a change of 1°C for a water droplet corresponds a refractive index change of 0.0002 at about 20°C or 0.0006 at 100°C .

To measure the refractive index, the most promising approach is based on the measurement of the rainbow location. This technique has been first investigated by Roth et al [28], who exploited the dependence of the angular position of the rainbow on the real part of the refractive index.

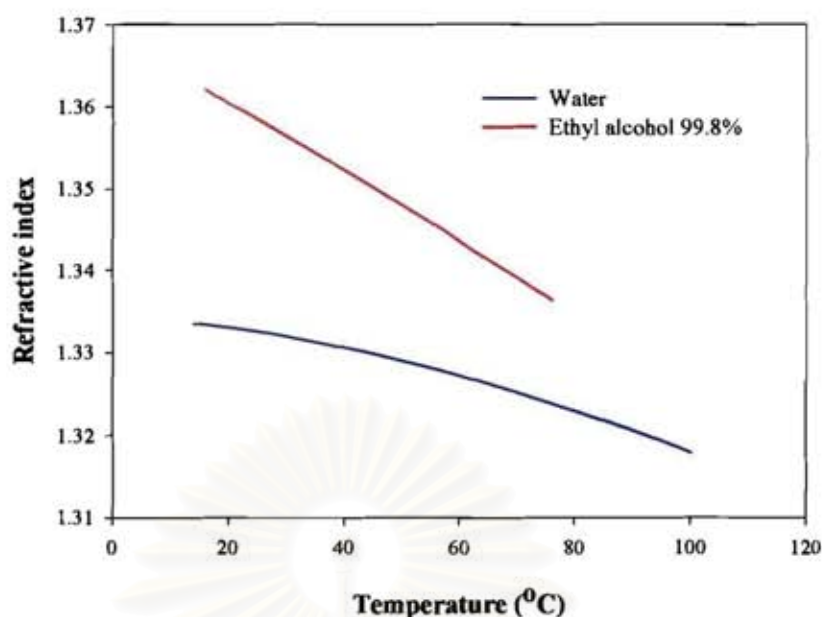


Figure 4.22: The relationship between refractive index and the temperature for water and ethyl alcohol.

The rainbow is a very common natural phenomenon, which can be observed when rain and sun are present together. It is one of the most beautiful phenomena in the nature, which has inspired art and mythology in all people. Rainbow is created by the “rays” experiencing one internal reflection which is very sensitive to the value of the refractive index of the particles. This sensitivity to the refractive index explains the beauty of the natural rainbow [29]. As the refractive index of a product changes with its temperature, the possibility to extract the refractive index and the particle size from the characteristics of the light scattered around the rainbow angles has attracted a lot of researchers.

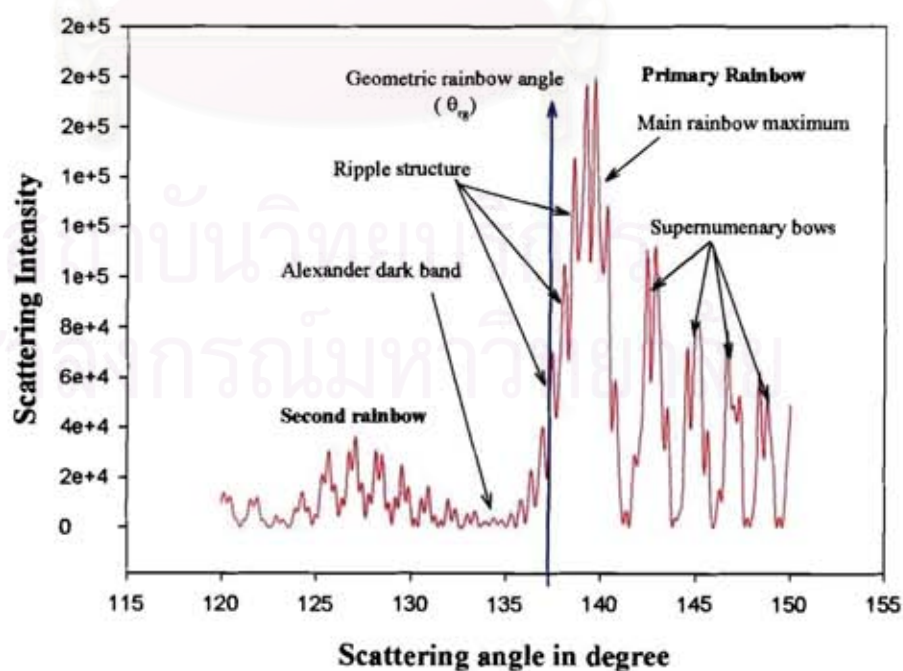


Figure 4.23: Scattering diagram around rainbow angle computed by Lorenz-Mie theory (for water $N=1.333$).

The exact scattered light around rainbow angle can be computed by Lorenz-Mie theory. Figure 4.23 shows the angular scattered-light distribution between 120° - 150° according to Lorenz-Mie theory for a wavelength of 0.6 micron. The scatterer is a spherical droplet with a refractive index equal to 1.333 and a diameter equal to 100 microns. Two zones of high intensity can be easily defined. The primary rainbow, resulting from the interference between first internal reflections ($p=2$), corresponds to angles larger than 137° . The second rainbow is created by the second internal reflection ($p=3$) and corresponds to angles smaller than about 130° . The gap between these two rainbows is called Alexander's dark band where the intensity is very small in comparison with the first and second rainbows and mainly dominated by external reflection. In the first and second rainbows can be distinguished oscillations of low and high frequencies. The lower frequency oscillations are created by the interference between the rays with one (or two) internal reflection. For first rainbow, the first oscillation which has the highest intensity is called Main rainbow maximum and the other supernumerary bows (or Airy fringes). The high frequency fringes are called "ripple structure", superimposed on the Airy fringes. These fringes are the signature of interferences between the light directly reflected at the surface of the particle and the light internally reflected. The rainbow position predicted by geometrical optic is noted " θ_{rg} ". The paths of the different rays which create a rainbow are shown in figure 4.24

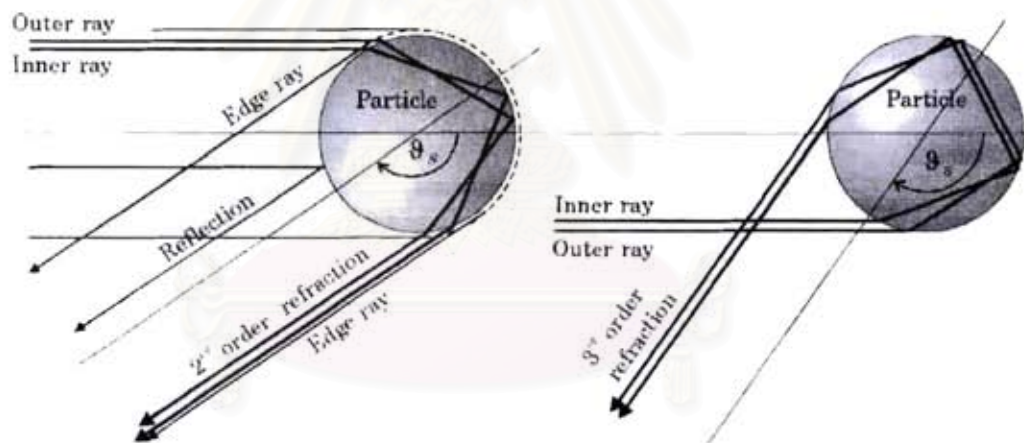


Figure 4.24: Illustration of the scattering modes for first and second rainbows influencing the intensity in the rainbow region.

4.2.1 Rainbow by Geometrical optics:

According to Descartes' theory of rainbows, the angular position θ_{rg} of the first rainbow is given by the minimum scattering angle of the rays of order two. In figure 4.24 the limit ray with minimum deflection or minimum scattering angle is shown. In addition neighboring incident rays are shown with larger scattering angles. In the vicinity of the ray with minimal deflection the density of the rays is higher, which results in higher intensity near the rainbow. It is found that minima of the scattering angle are obtained only for rays with order number $p \geq 2$. The rainbows from rays with higher order numbers, however, have fainter intensities. The second rainbow, which consists of rays of order three, can be observed in nature under favorable conditions. Scattering angles of the limit ray of order p can be calculated with equation 4.4. According to the theory of Descartes the angular position of the different rainbows are given by the relation:

$$\theta_{rg} = 2 \left\{ p \cos^{-1} \left(\frac{1}{N} \sqrt{1 - \frac{N^2 - 1}{p^2 - 1}} - \sin^{-1} \sqrt{\frac{N^2 - 1}{p^2 - 1}} \right) \right\} \quad (4.4)$$

where N is the refractive index of the droplet liquid and p is the order number of the scattered rays contributing to the rainbow. In nature the first and second rainbows can be observed. The position of the first and second rainbows is obtained for $p = 2$ and $p = 3$. Descartes' theory is based on ray path and therefore independent of droplet size.

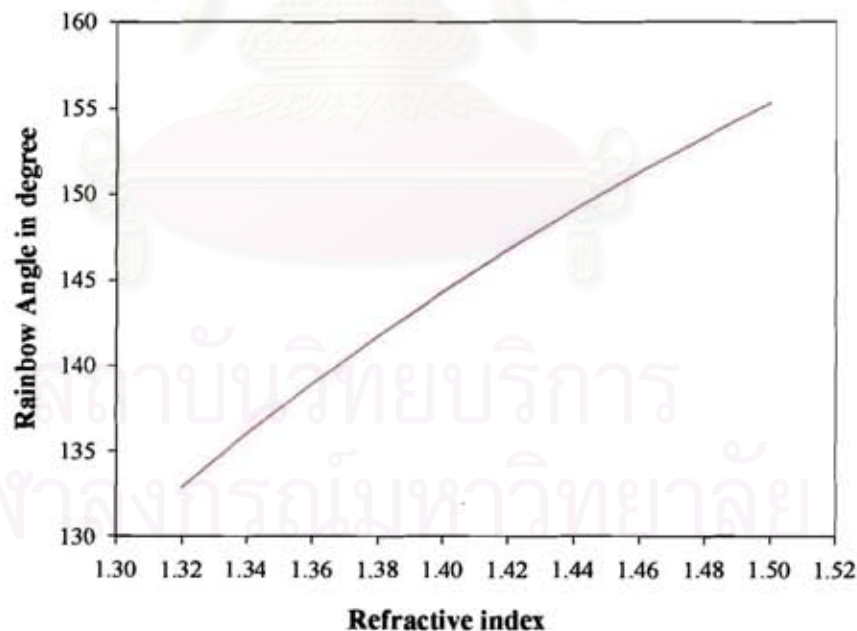


Figure 4.25: Calculated first rainbow position as a function of refractive index according to geometrical optics. ($\lambda = 0.5145$ micron).

The dependence of the geometrical optics rainbow position on the refractive index is shown in figure 4.25. Here the first rainbow location is computed by using geometrical optics (Descarte's law): the rainbow position is independent on

the size. The refractive index runs from 1.3 to 1.5. Changing the refractive index of about 0.001 (typically 10°C) moves the position of rainbow of about 0.146°, for water. Then the measurement of the rainbow position determines the refractive index with a high accuracy and therefore the temperature and /or composition of the liquid droplet.

4.2.2 Rainbow by Airy's theory:

The theory of Descartes describes the rainbow position with sufficient accuracy in the range of a millimeter or larger diameter. However, detailed measurements of the angular position of the rainbow show that for smaller droplets deviation from Descartes' theory occurs. The smaller the droplet is the larger the deviation is. The angular position of the rainbow maxima increases with decreasing droplet size.

In 1838 George B. Airy developed an extension of Descartes' theory, which accounts for the effect of the droplet radius. The rainbow position according to Airy's theory is given by:

$$\theta_{ra} = \theta_{rg} + \frac{1.0845}{\sqrt{(N^2 - 1)/(p^2 - 1)}} \left[\lambda^2 \frac{\sqrt{1 - (N^2 - 1)/(p^2 - 1)}}{64 a^2} \right]^{1/3} \quad (4.5)$$

where θ_{rg} represents the rainbow position according to Descartes' theory, which is given by equation 4.5, λ is the wavelength and a is the droplet radius. The theory of Airy includes Huygens' principle and curved wave fronts of the light scattered in the direction of the rainbows.

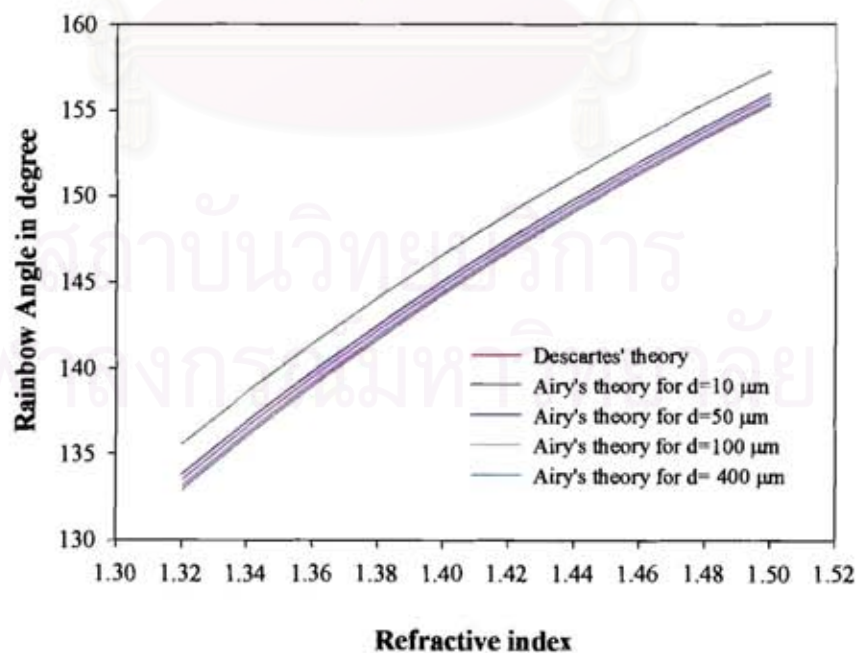


Figure 4.26: Calculated first rainbow position as a function of refractive index for different diameters according to Airy's theory.

The dependence of the angular position of the first rainbow on the refractive index given by equations 4.4 and 4.5 according to Descartes and Airy's theory respectively are displayed in figure 4.26. The influence of droplet size on the position of first rainbow is small for large particle. For increasing droplet diameter the rainbow position θ_{ra} approaches θ_{rg} and the influence of the droplet size becomes negligible. For smaller droplets (smaller than 200 μm) the size dependence becomes more and more important

Van Beeck and Reithmuller [30, 31] try to measure the refractive index and size of individual droplets by using Airy's theory. The method is based on the fact that a change of diameter corresponds to a change in angular distance between neighbouring rainbow maxima according to Airy's theory (see figure 4.27) while a change of the refractive index corresponds to a shift of the rainbow position (figure 4.28).

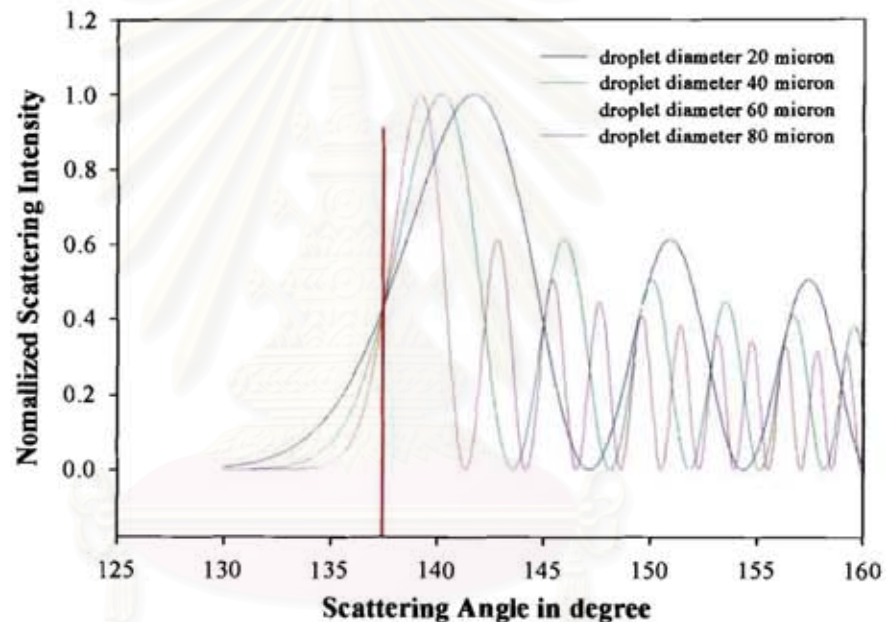


Figure 4.27: Scattering diagram around rainbow angle for different diameters simulated by Airy Theory.

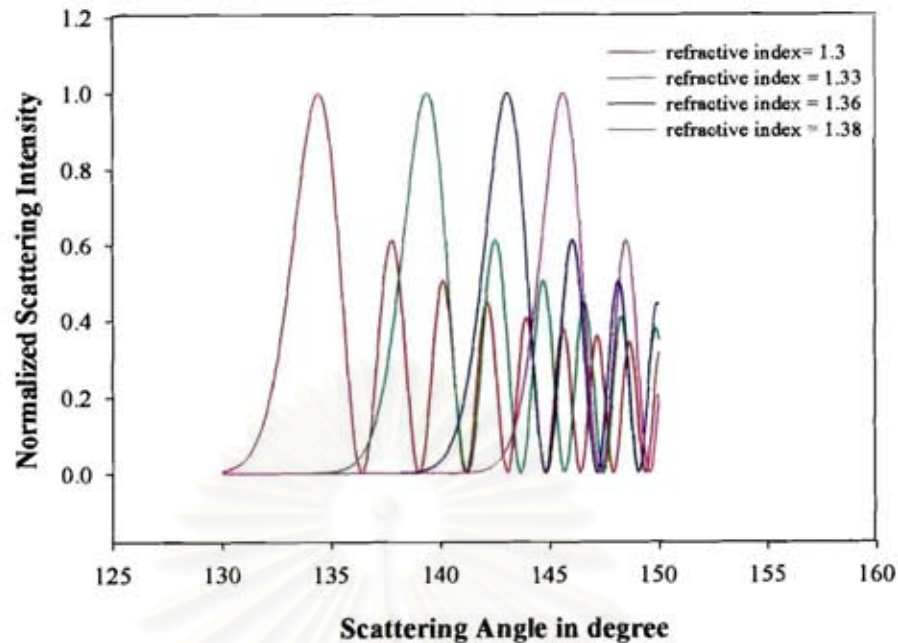


Figure 4.28: Scattering diagram around rainbow angle for different refractive indices simulated by Airy Theory.

The scattering intensity depends on the power $7/3$ of diameter. Then, in order to compare the scattering light distribution for different diameters, the curves have been normalized to be 1 at the maximum. The comparison of scattering light distributions for different sizes of droplet is shown in figure 4.27. It is obvious that the rainbow pattern is changed with the particle size. The bigger the particle is, the narrower the curve of the first main peak is, and also the smaller the angular distance between neighbouring Airy peaks is. One important thing to be noticed is that all the curves have a common point which corresponds to the Geometrical optics rainbow and which is also very close of the inflection point of the Airy curve in the Alexander dark band side.

The refractive index change induces a shift of the rainbow location as shown in figure 4.28. Then the conclusion is that the absolute measurement of rainbow position is a measurement of the refractive index while the relative angular distance between supernumerary bows is a measurement of the particle diameter.

However, the Airy theory does not describe all the rainbow structure. By comparing the exact scattered light computed by Lorenz-Mie theory in figure 4.23 and the previous Airy predictions it is clear that the high frequency oscillations are missing. These high frequency oscillations (ripple structure) are created by the interferences between the externally reflected light and the once internally reflected light. Then to measure the size and the refractive index by applying Airy's theory, the measured intensity distribution has to be filtered in order to eliminate the ripple structure. But the filtering process induces a modification of the Airy fringes, which perturbs the measurements as exemplified in figure 4.29 in agreement with Damaschke [32].

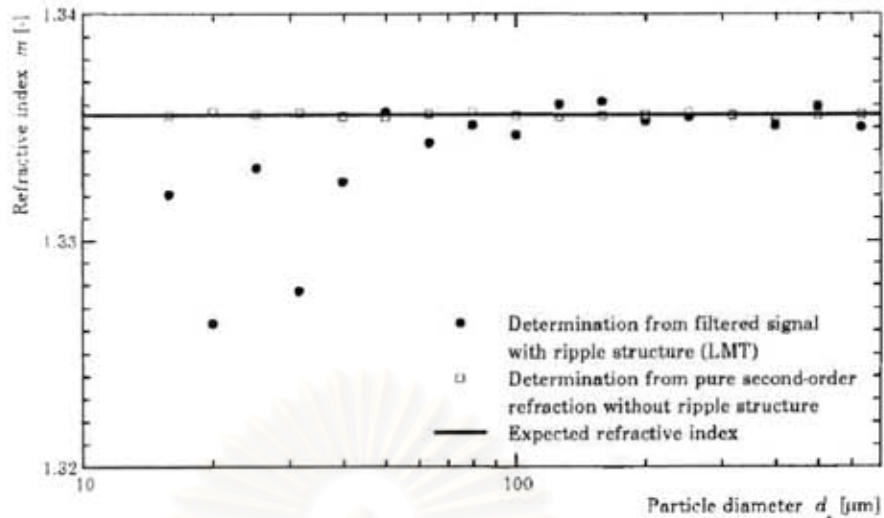


Figure 4.29: Influence of the ripple structure on the accuracy of refractive index determination in comparison to signals from pure second-order refraction.

The deviations from the expected refractive index are shown in figure 4.29. The continuous line is the refractive index value used to compute the exact rainbow distribution, by using Lorenz-Mie theory. The full points correspond to the extracted refractive index from filtered Lorenz-Mie signal process by Airy's theory. The empty points correspond to the extracted refractive index from Debye signal ($p=2$) process by Airy's theory. The deviation increases rapidly for smaller particle, especially smaller than 100 microns. This is due to the ripple structure which has higher sensitivity for smaller droplets. In the rainbow signal, especially for small particles, the ripple structure prevents the exact determination of the rainbow maxima and reduces the accuracy of the refractive index measurement.

The ripple can be computed by using Lorenz-Mie or Nussenzveig's theory. Our strategy is to analyze the rainbow distribution with its full structure ($p=0$ and $p=2$) computed as fastly as by Airy and as accurately as Lorenz-Mie, by using Nussenzveig's theory.

สถาบันวิทยบริการ
จุฬาลงกรณ์มหาวิทยาลัย

4.2.3 Rainbow by Nussenzveig's theory:

As it has been described and shown in chapter 3, the Nussenzveig's theory, taking into account $p=0$ and $p=2$ and adding correcting coefficients, is able to perfectly enough describe the rainbow pattern including the ripple structure for small particles.

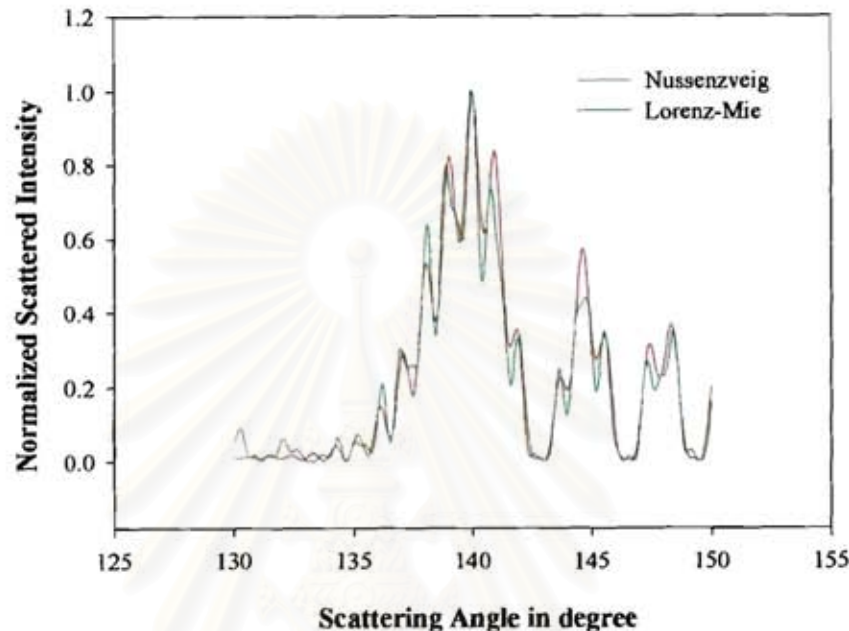


Figure 4.30: The comparison of the rainbow light distributions simulated by Lorenz-Mie and Nussenzveig theory ($d=50$ microns, $N=1.333$, $\lambda =0.5145 \mu\text{m}$ and 1000 points).

Figure 4.30 shows an example of comparison between full rainbow distributions simulated by Lorenz-Mie theory and Nussenzveig theory taking into account the interferences between first internal reflection ($p=2$) and external reflection ($p=0$) for a particle with a diameter equal to 50 microns with a refractive index equal to 1.333. As can be seen, Nussenzveig approach can predict rainbow pattern incorporating the ripple structure in good enough agreement with Lorenz-Mie theory even for small particles. The differences in intensity are due to the higher order rays in full Lorenz-Mie theory. In addition, when the refractive index is small the first rainbow is moved to smaller angles. The distance between first and second rainbows becomes smaller. Then the first rainbow distribution is not created only by the interferences between external reflection ($p=0$) and once internal reflection ($p=2$) but also from two internal reflections ($p=3$). For example, when the refractive index is equal to 1.31, the first and second rainbows are superposed. Furthermore, when the particle size decreases, the effect of $p=3$ on the primary rainbow is the reason why the prediction of the scattered light by Nussenzveig's theory is not in perfect agreement with Lorenz-Mie theory, as shown in figure 4.31. In contrast, when the particle has higher values of the refractive index the primary rainbow is moved to larger angles. The primary and secondary rainbows are completely separated. In this case the secondary rainbow ($p=3$) has no effect on the scattered light of the primary rainbow. Then using Nussenzveig's theory taking into account $p=0$ and $p=2$ is sufficient

enough to predict the scattered light around the rainbow angle, as shown in figure 4.32.

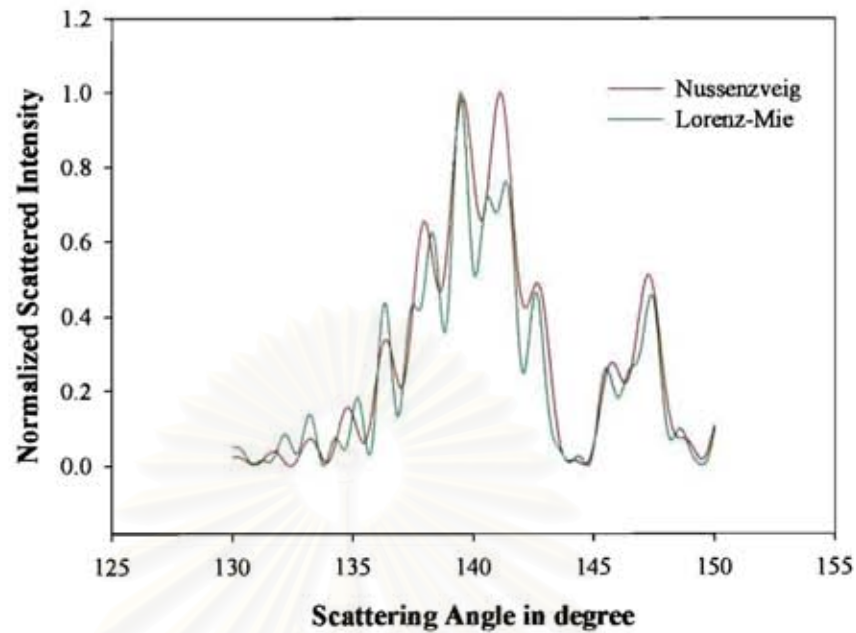


Figure 4.31: The comparison of the rainbow distributions simulated by Lorenz-Mie and Nussenzveig theories. ($d=30$ microns, $N=1.33$ $\lambda=0.5145$ μm and 2048 points).

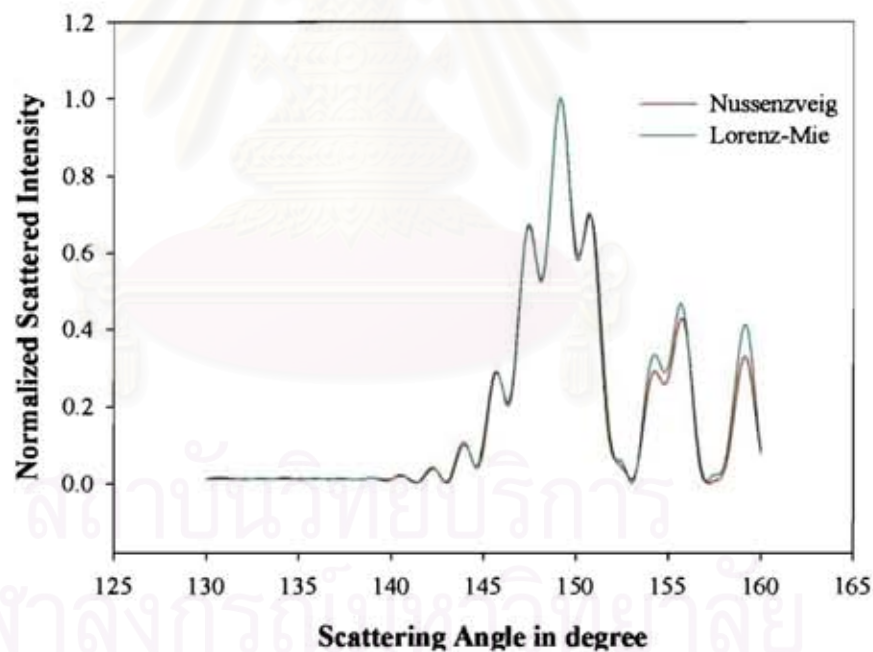


Figure 4.32: The comparison of the rainbow distributions simulated by Lorenz-Mie and Nussenzveig's theories. ($d=30$ microns, $N=1.38$ $\lambda=0.5145$ μm and 2048 points).

The previous results show that Nussenzveig's theory could be efficiently used to predict rainbow including the ripple structure when the $p=0$ and $p=2$ contributions are dominating. A particular attention will be paid to size and refractive index value when this condition is not satisfied. The Nussenzveig's predictions will be introduced in algorithm for automatic inversion. This is the aim of the next paragraph where the accuracy of the approach will be quantified.

4.2.4 Backward automatic processing based on Nussenzveig's theory:

The processing of the backward signals is related to the research of the refractive index value, by finding the best fit of a recorded/simulated signal by Lorenz-Mie with a computed signal by Nussenzveig's computation.

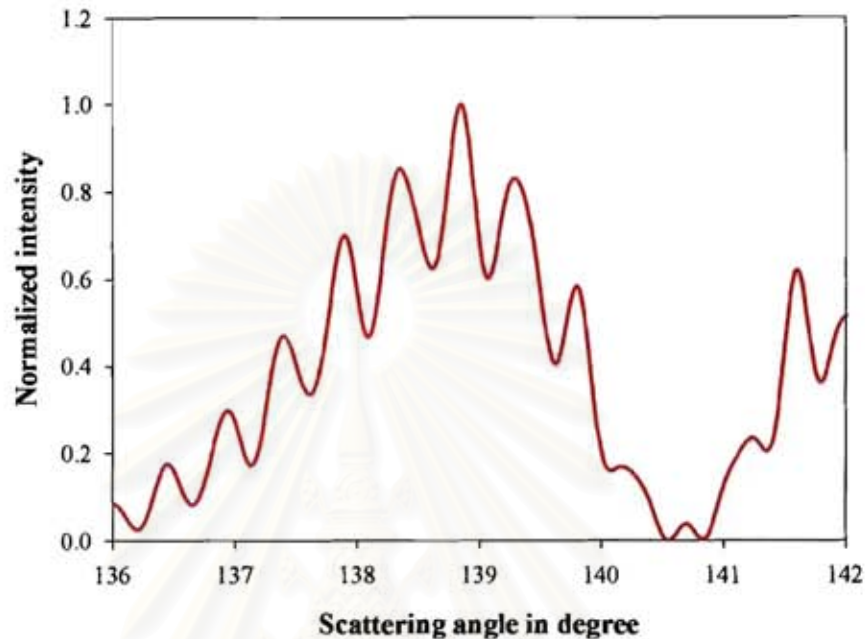


Figure 4.33: A backward signal. The diameter is equal to $100 \mu\text{m}$ and the refractive index is equal to 1.33.

The simulated signal is essentially characterized by a main rainbow peak (see figure 4.33). Then a way to characterize it is to compute its correlation with a computed signal. Figure 4.34 displays one Lorenz-Mie signal, three test signals with the three associated correlations. The simulated signal has been computed in the Lorenz-Mie framework for a diameter equal to $100 \mu\text{m}$ and a refractive index equal to 1.33. The test particle scattering diagrams have been computed in the framework of Nussenzveig's theory ($p=0$ and 2) for diameters equal to $100 \mu\text{m}$ and refractive index equal to 1.32662, 1.33 and 1.33662 respectively. When the test refractive index is equal to the researched refractive index the rainbows are located at the same angle (see figure 4.34(a)) and the maximum of the correlation is located at point 1024 for a signal digitalized in 2048 points (see figure 4.34(b)). When the refractive index value under test is larger than the researched refractive index, the rainbow peak is shifted toward larger angles (see figure 4.34(a)) while the maximum of the correlation is shifted toward lower points (see figure 4.34(b)).

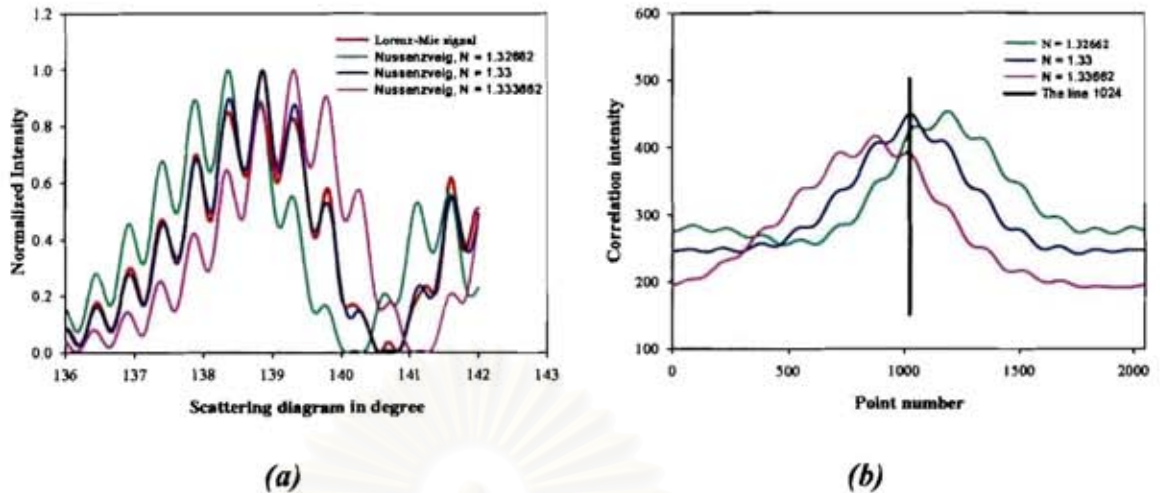


Figure 4.34: Test signals and associated correlations.

Then, at first sight, the location of the maximum of the correlation looks to be a good candidate to be the $f(x)$ function in the Brent method. Nevertheless, as exemplified in figure 4.35, due to the ripple structure, the location of the maximum of the correlation is not a monotonic and continuous function of the refractive index. For example, when the refractive index value is larger than 1.33, we expect to have a maximum of correlation located below 1024 (see figure 4.34) but for $N = 1.33084$ and $N = 1.33095$ in figure 4.35, the maximum of correlation appears for points larger than 1024 (1047 and 1051, respectively). Then for a small increase of the refractive index it jumps to the other size of the target line, as exemplified for $N=1.33096$ with a maximum of correlation located at 919. This “jumping” behaviour is a general characteristic of the correlation of signals with ripple as also exemplified by the jump from 990 to 845 when the refractive index evolves from 1.33292 to 1.33293.

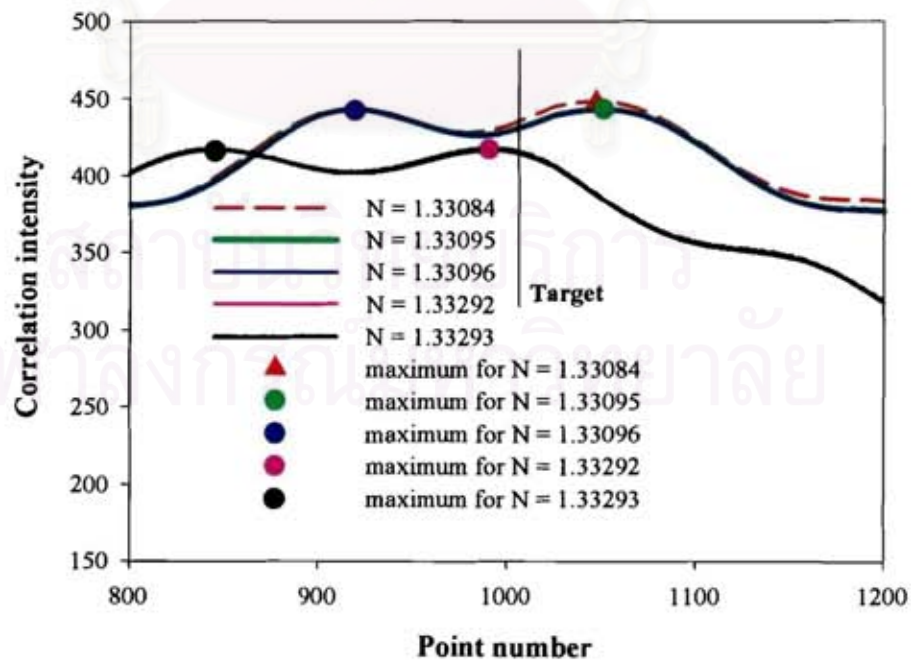


Figure 4.35: Behaviour of the maximum of correlation for signals with ripple.

This approach fails relatively often and finally cannot be used. A second way is to compute the integrals of the correlation before and after the maximum of the autocorrelation (here between 1-1024 and 1024-2048). These integrals correspond to the area in red and blue in figure 4.36.

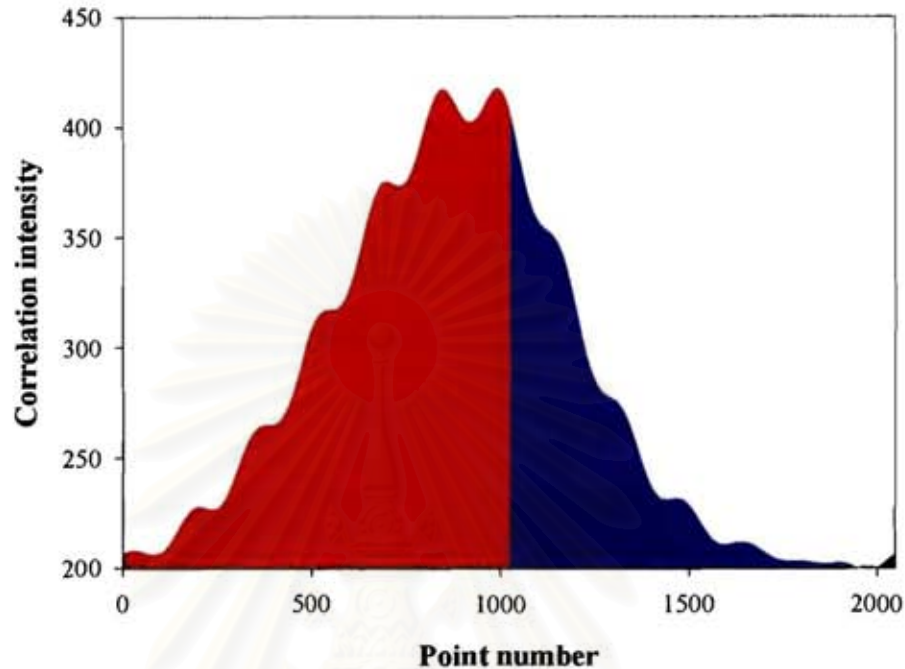


Figure 4.36: Definition of the integral criterion.

With this criterion, for the example of figure 4.35, the values obtained are compiled in table 4.3. Monotonicity and continuity are now satisfied. Then the integral of the correlation is a better candidate than the maximum of the correlation to be the $f(x)$ function in the Brent method, $f(x) = \text{Area of the correlation [1 to 1024]} - \text{Area of the correlation [1024 to 2048]}$.

Table 4.3 The behaviour of the correlation integral.

Refractive index	Blue integral	Red integral
1.33	0.501	0.499
1.33084	0.514	0.486
1.33101	0.517	0.483
1.33286	0.554	0.446
1.33298	0.557	0.443

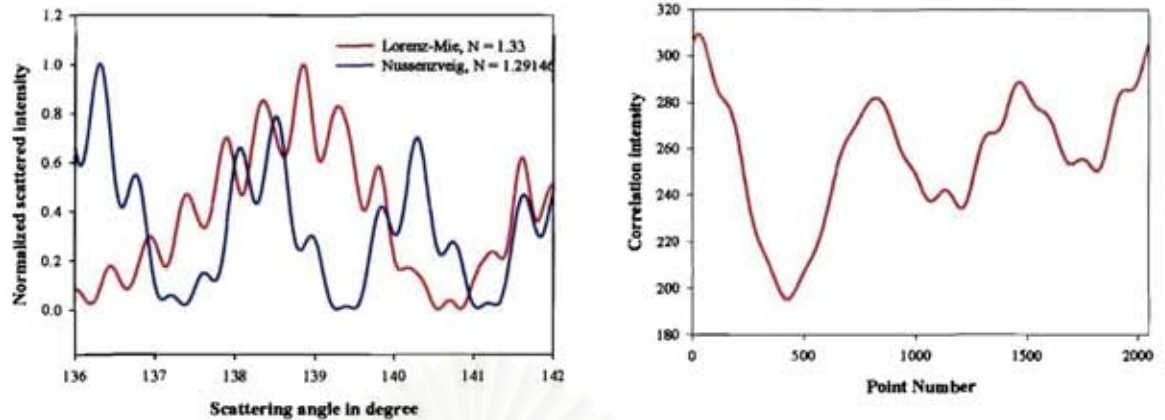


Figure 4.37: Comparison of a Lorenz-Mie signal with a test signal with a very bad evaluation of the refractive index and the associated correlation.

Nevertheless, if the test value for the refractive index is too far from the target value some disagreements can appear as illustrated in figure 4.37 where the integral criterion is also equal to 0.5. As a consequence, the range of refractive index is selected as the refractive index value corresponding to the geometric rainbow at the maximum of the no filtered rainbow minus 0.03.

The convergence problem looks to be solved, but a refined analysis displays some residual oscillations expectedly coming from the ripple structure.

Another step is then to reduce the ripple structure by a FFT filtering (the same filter will be applied to the signal and to the test), and afterward to apply the correlation integral procedure.

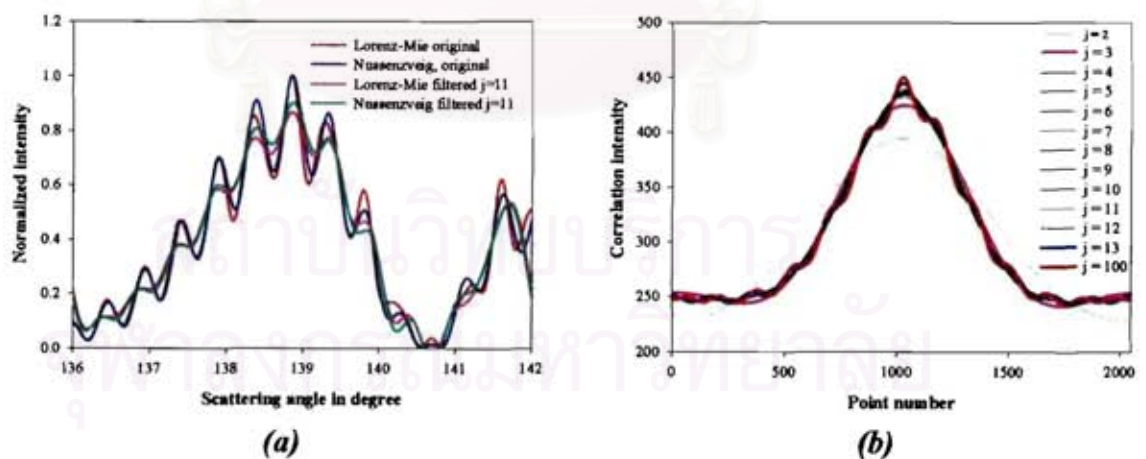


Figure 4.38: Filtered signals and correlation.

This procedure is exemplified in figure 4.38. The original signal corresponds to a droplet with a diameter equal to $100\ \mu\text{m}$ and a refractive index equal to 1.33, computed with 2048 points. For these values, the original automatic backward processing fails. Figure 4.38(a) displays the same original signal with and without a filtering. The corresponding correlations, for different degrees of filtering, are plotted in red in figure 4.37(b). The filtering reduces the ripple in the scattering diagram with the consequence to reduce it in the correlation. The signal is successfully processed for integer frequency (j) limits lower than 13. Table 4.4 compiles the refractive index values extracted by integral procedure on filtered signal. The stability of the returns as well as their validity is impressive.

Table 4.4: Effect of the filtering on the extracted refractive index value. The diameter is assumed to be perfectly known.

Filtering	Refractive index by integral
J=13	impossible
J=12	1.32993
J=11	1.32992
J=10	1.32992
J=9	1.32992
J=8	1.32992
J=7	1.32992
J=6	1.32992
J=5	1.32992
J=4	1.32992
J=3	1.32991
J=2	1.32990

A next step is to test the sensitivity of the algorithm with respect to the value of the particle diameter. The same data files have been processed but for different possible diameters. The effect of an inaccuracy of the diameter on the refractive index measurement is illustrated by table 4.5.

Table 4.5 *The sensitivity of the backward procedure to the test diameter.*

Original diameter	Backward guest diameter	Backward measured refractive index
99.6	99	1.38016
93.28	93	1.38059
84.94	85	1.38000
103.4	103	1.37958
95.2	95	1.38036
104.72	105	1.37991
110.86	111	1.37994
91.74	92	1.38038
82.36	82	1.37958
84.82	85	1.38036
94.56	95	1.37951
94.92	95	1.38068
102.06	102	1.38000
90.84	91	1.37987
88.18	88	1.37990
101.44	101	1.38007
79.98	80	1.38019
83.81	84	1.38000
100.92	101	1.38027
100.22	100	1.37962

Then the series of iterations is displayed in figure 4.39. The procedure converges in 24 steps which can be sorted in two groups. The first group, marked with triangles, corresponds to the first 13 iterations, determines a range of refractive index in agreement with the lower and larger recorded angles while the second group, marked with circles corresponds to the processing of the first rainbow peak by integral of the correlation (in blue).

สถาบันวิทยบริการ
จุฬาลงกรณ์มหาวิทยาลัย

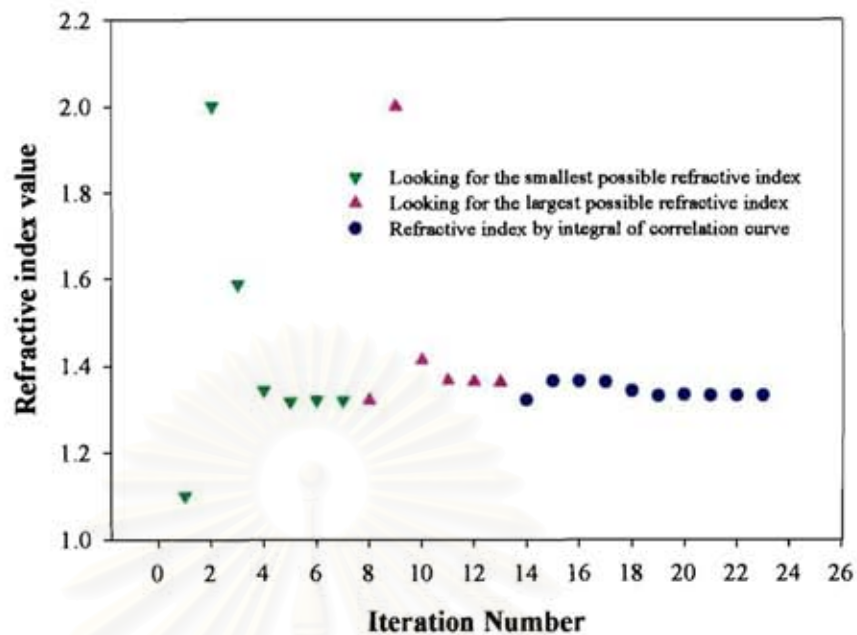


Figure 4.39: Series of iterations to determine the refractive index for a droplet with a diameter equal to $100 \mu\text{m}$ and a refractive index equal to 1.38.

In conclusion, when the particle diameter is known, the refractive index can be measured by predicting the rainbow in the Nussenzweig's framework. With a processing based on equalizing the two partial integrals of the correlation, the accuracy of the refractive index measurements achieves the fourth decimal place.

A next step is to simultaneously measure the size and the diameter by processing a dual signal i.e. a couple of signals corresponding to a forward and a backward recording. It is the aim of the next section.

สถาบันวิทยบริการ
จุฬาลงกรณ์มหาวิทยาลัย

4.3 Automatic dual processing of forward and backward signals.

4.3.1 Dual processing of simulated signal

The automatic dual processing is fundamentally the succession of the algorithms developed to process the forward and backward signals. It aims to finding the best fit of a recorded/simulated signal by Lorenz-Mie's theory with computed signal by Nussenzveig's theory for both sides of the scattering region. Starting from a guest value of the refractive index, a first estimation of the diameter is carried out by using the frequency/phase algorithm described in section 4.1. This value of the diameter is used by the backward correlation algorithm described in section 4.2 to obtain a first estimation of the refractive index. The procedure is repeated up to the convergence of diameter and refractive index values with the requested accuracy. The succession of iterations is exemplified in figures 4.40 and 4.41 for a particle with a diameter equal to 100 μm and a refractive index equal to 1.38. Figure 4.41 displays only iterations on the refractive index. Three loops have been necessary to converge to a measured diameter equal to 99.99 μm and a measured refractive index equal to 1.3802, corresponding to about 50 iterations.

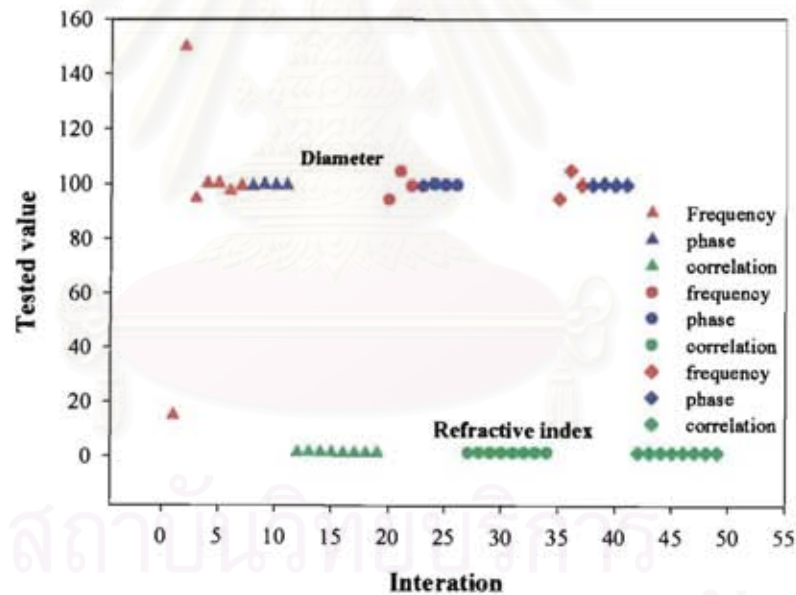


Figure 4.40: Iterations to find both the particle diameter and refractive index.

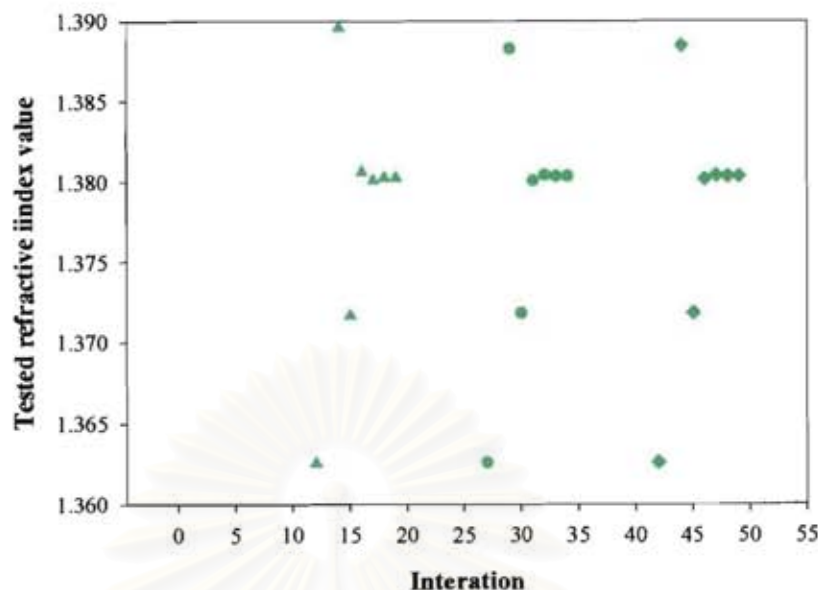


Figure 4.41: *Idem as figure 3.50 but only the iterations on the refractive index are plotted.*

To validate the dual processing algorithm and quantify its accuracy, dual signals have been computed by using the Lorenz-Mie theory for a refractive index equal to 1.38 and diameter randomly generated. The results are compiled in table 4.6. Table 4.6 possesses 3 columns. The first column corresponds to the diameter used for the Lorenz-Mie computations. The second and third columns compile the measured diameter and refractive index obtained by the dual algorithm without assumption. As for Table 4.2, the – and + correspond to an extra “jump” of about 0.7 μm .

A first observation is that the measured refractive index by the dual algorithm is as accurate as the refractive index measured with only the backward algorithm (size assumed to be known). This observation can be quantified as follows: to backward processing (column 3, table 4.5) corresponds an average refractive index equal to 1.38005 with a standard deviation $s=3.2e-4$ while at the dual processing (column 3, table 4.6) corresponds an average refractive equal to 1.38005 with a standard deviation equal to $s= 3.2e-4$, i.e. for the same values .

The simultaneous determination of the diameter and of the refractive index has no effect on the refractive index measurement quality.

A second observation is that the diameter can be measured with an extremely high accuracy as demonstrated by the comparison between the value of column 1 and column 4.

Table 4.6 *Dual processing of signal.*

Original diameter (μm)	Forward and backward measured diameter	Forward and backward measured refractive index
99.6	99.60 (+)	1.38024
93.28	93.28 (++)	1.38019
84.94	84.96	1.37982
103.4	103.45	1.3796
95.2	95.15 (-)	1.3804
104.72	104.76	1.37992
110.86	110.85 (+++)	1.38006
91.74	91.71	1.38031
82.36	82.39	1.37966
84.82	84.83	1.38035
94.56	94.63	1.37944
94.92	94.83	1.38077
102.06	102.03	1.38012
90.84	90.83 (-)	1.38005
88.18	88.19 (+)	1.37981
101.44	101.45 (+)	1.38008
79.98	79.97	1.38018
83.81	83.81	1.38006
100.92	100.90	1.38027
100.22	101.24 (-)	1.37964

This method is therefore found to be robust, and then it will be used in the full procedure of inversion where both parameters (the size and the refractive index) have to be simultaneously determined.

Nevertheless, in reason of the large number of evaporation experiences carried out with ethanol, for example at ONERA-Toulouse, a special attention will be dedicated to this product. Table 4.7 compiles the results of dual inversion carried out on a series of particles. The original diameter series is the same as for table 4.6 and the original refractive index was equal to 1.364.

Table 4.7 Study of ethanol measurement ($N=1.364$).

Original diameter (μm)	Forward and backward measured diameter	Forward and backward measured refractive index
99.6	99.58	1.36418
93.28	93.29 +	1.36453
84.94	85.03	1.36299
103.4	103.38 -	1.36432
95.2	95.19	1.36430
104.72	104.72	1.36399
110.86	110.87	1.36375
91.74	91.82 --	1.36314
82.36	82.31	1.36504 **
84.82	84.88	1.36296
94.56	94.63	1.36298
94.92	94.91	1.36441
102.06	102.03 -	1.36386
90.84	90.82 --	1.36376
88.18	88.14	1.36397
101.44	101.38	1.36494
79.98	80.00 +	1.36413
83.81	83.76	1.36523
100.92	100.88	1.36471
100.22	100.22 +	1.36447

The average measured refractive index is equal to 1.364083 with a standard deviation equal to $6.8\text{e-}4$. The shift from the expected value is more important than for the other cases (water 1.33 and fuel 1.38) as well as the standard deviation. The cause of this 'mistake' is to be researched from a deep understanding of the scattering process. Figure 4.42 compares the scattering diagram computed by using the Lorenz-Mie theory and the Debye theory (limited at $p=0, 1, 2$) for a particle with a diameter equal to $82.36 \mu\text{m}$ and a refractive index equal to 1.364. The difference between the two predictions is larger than for the other cases (see figure 4.42 for an other example). The origin of this difference of behaviour could be attributed to the effect of higher order rays. Indeed for a refractive index equal to 1.364 the first rainbow is located at 142.22° but the $p=6$ and $p=11$ rainbows are located very close to 145.26° for the fifth rainbow and 142.22° for the $p=11$ rainbow. This assumption is supported by table 4.8 which compiles measured refractive index, for different particle diameters and refractive indices. The first column corresponds to ethanol ($N=1.364$) but the scattering diagrams to process have been computed in the framework of Lorenz-Mie theory or Debye theory for p up to 2 or 11. The sensitivity of the measured refractive index to the number of terms in the Debye series confirms the assumption of an effect of rainbows of high order on the scattering diagram. The analysis of the results compiled in table 4.9 gives the same conclusion.

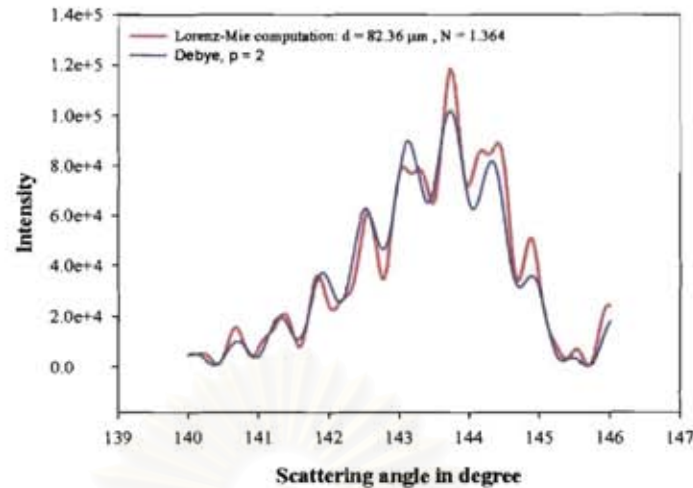


Figure 4.42: Comparison of the scattering diagram computed by using Lorenz-Mie theory and Debye theory ($p=0, 1$ and 2) for a diameter equal to $82.36 \mu\text{m}$ and a refractive index equal to 1.364 .

Table 4.8: Automatic processing of backward signal filtered with $j = 11$. The diameter is assumed perfectly known.

Refractive index Diameter(μm)	1.364 (Lorenz-Mie)	1.364 (Debye, $p=2$)	1.364 (Debye, $p=11$)
100	1.3643	1.3640	1.3644
98	1.3644	1.3640	1.3638
96	1.3640	1.3640	1.3639
94	1.3640	1.3640	1.3639
92	1.3641	1.3640	1.3640
90	1.3640	1.3640	1.3604

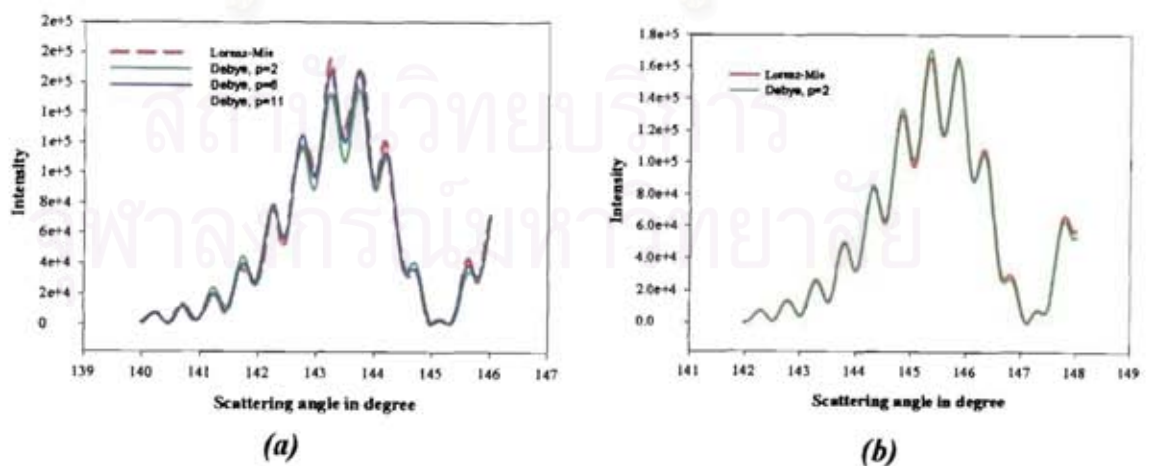


Figure 4.43: Comparison between Lorenz-Mie and Debye predictions for a particle with a diameter equal to $100 \mu\text{m}$ (a) for $N=1.364$ (b) for $N=1.38$.

Table 4.9: Processing of signals computed for $N=1.364$ by Debye's theory for $p=0, 1$ and 2 . The average measured refractive index is equal to 1.364036 and the standard deviation is equal to $s=3.9e-5$.

Original diameter (μm)	Forward and backward measured diameter (μm)	Forward and backward measured refractive index	Phase
99.60	99.60	1.36404	-3.0
93.28	93.29	1.36402	-0.3
84.94	84.95	1.36399	-4.0
103.40	104.80	1.36408	-4.0
95.20	95.20	1.36403	-4.0
104.72	104.73	1.36405	0.6
110.86	110.85	1.36407	6.7
91.74	93.15 +	1.36410	3.0
82.36	82.37	1.36398	-5.0
84.82	84.83	1.36400	-4.0

The possibility to process computed dual signals to extract the couple diameter/refractive index is proved by the results presented before.

The next step is to process real experimental signals. It is the aim of the next section.

สถาบันวิทยบริการ
จุฬาลงกรณ์มหาวิทยาลัย

4.3.2 Dual processing of experimental signals.

ONERA-Toulouse provides us with series of experimental data recorded on their setup. The measurements have been carried out on lines of droplets created by a monodisperse generator. Figure 4.44 is a view of the experimental set up.

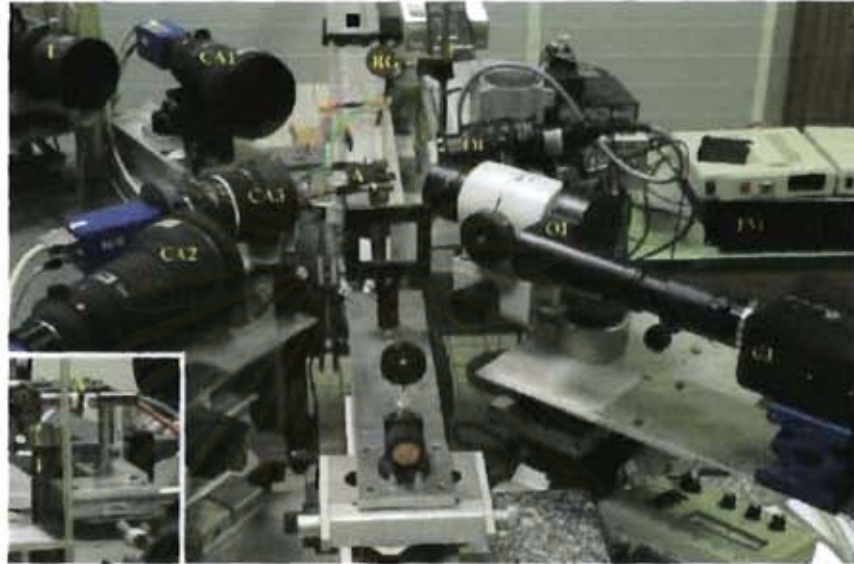


Figure 4.44: *The ONERA experimental setup.*

The important fact is that the forward scattering diagram and backward scattering diagram are recorded for individual particles with a good quality, as exemplified in figure 4.45.

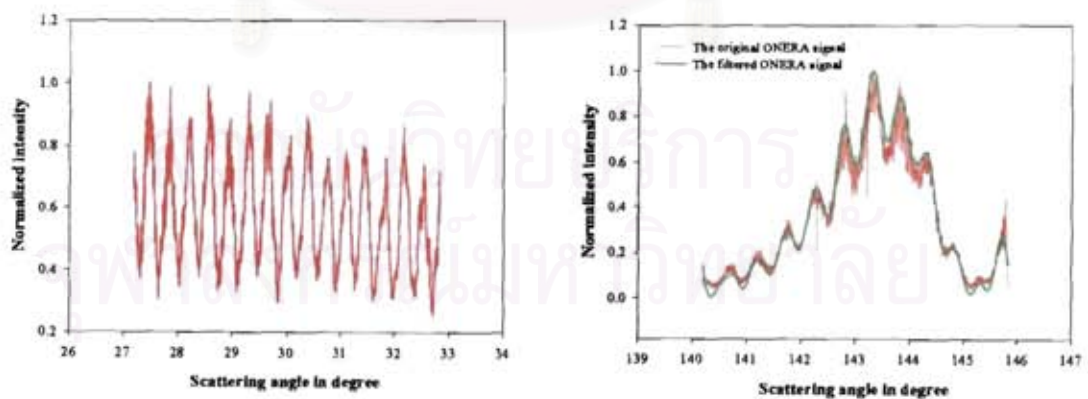


Figure 4.45: *The dual ONERA signals.*

Then the dual algorithm introduced in the previous section was applied to the original forward signal and to the filtered backward signal. An example of agreement between the dual original signal and the Nussenzveig test dual signals is displayed in figure 4.46.

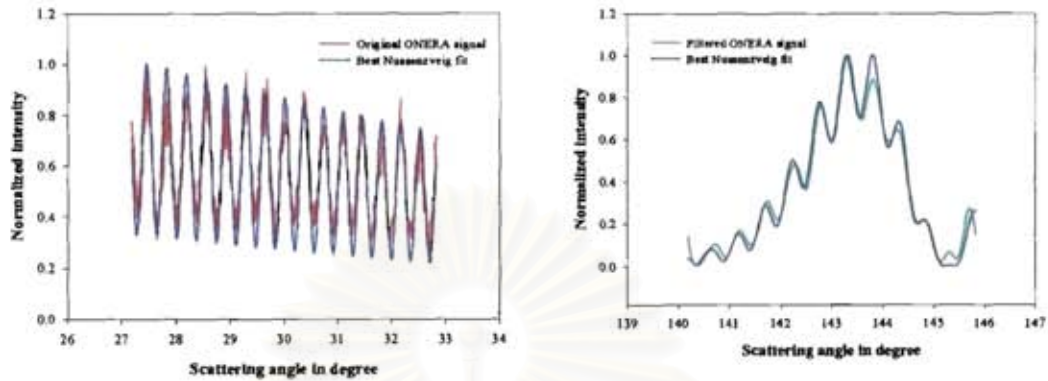


Figure 4.46: Comparison between experimental ONERA signals and the best Nussenzveig fit.

The procedure has been applied at five series of 50 individual measurements. Each series corresponds to a given distance from the orifice of the monodisperse droplet generator. The liquid temperature at injection was equal to 22°C while the air temperature was equal to 23°C. The measurements have been carried out at 30, 35, 40, 45 and 50 mm from the orifice.

Figure 4.47 plots the measured refractive index versus the measured diameter. The two returns with the closest distance to the experimental recording have been selected. This multiple return is due to the non unicity of the frequency and phase relatively to the diameter for this experimental configuration as extensively explains before. Nevertheless, this fact has no real influence on the quality of the experimental results. A first remark is that all points, excepted one are perfectly aligned. A second remark is that the two series of points are perfectly parallel then they give the same information, and we can claim that the measurement of the refractive index versus the diameter is possible on a range corresponding to a modification of the diameter smaller than 0.2 μm and for an evolution of the refractive index of about 0.002, as shown in figure 4.48 which is only an arbitrary selection of a part of figure 4.47.

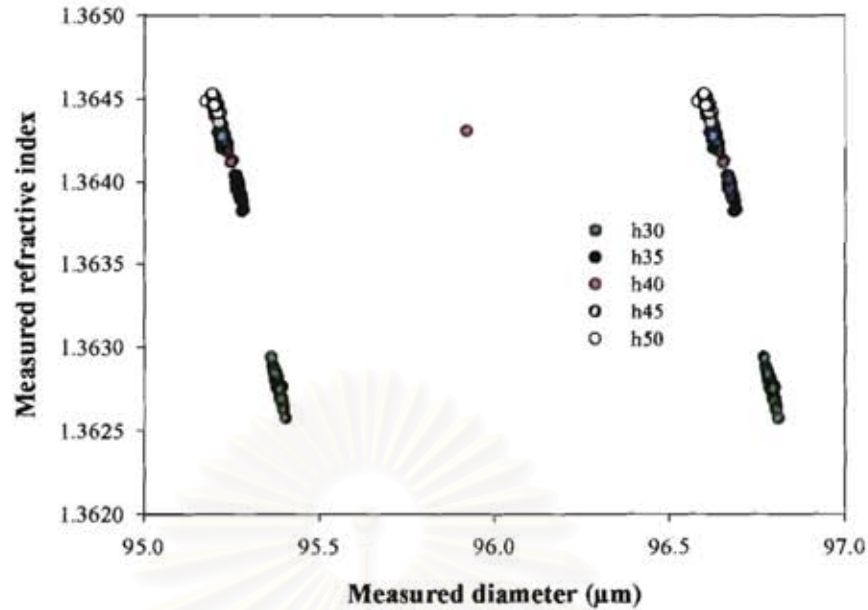


Figure 4.47: Measured refractive index versus measured diameter, from ONERA experimental results.

For ethanol, the refractive index information can be transformed to temperature information via the following law:

$$N = 1.371526 - 3.7976 \cdot 10^{-6} T \quad (4.6)$$

For the case of ethanol spray, the droplet temperature has been measured with cooling process from 23°C at 30 mm apart from the orifice to 18°C at 50 mm apart from the orifice. These data permit a measurement of the evaporation rate of the droplets.

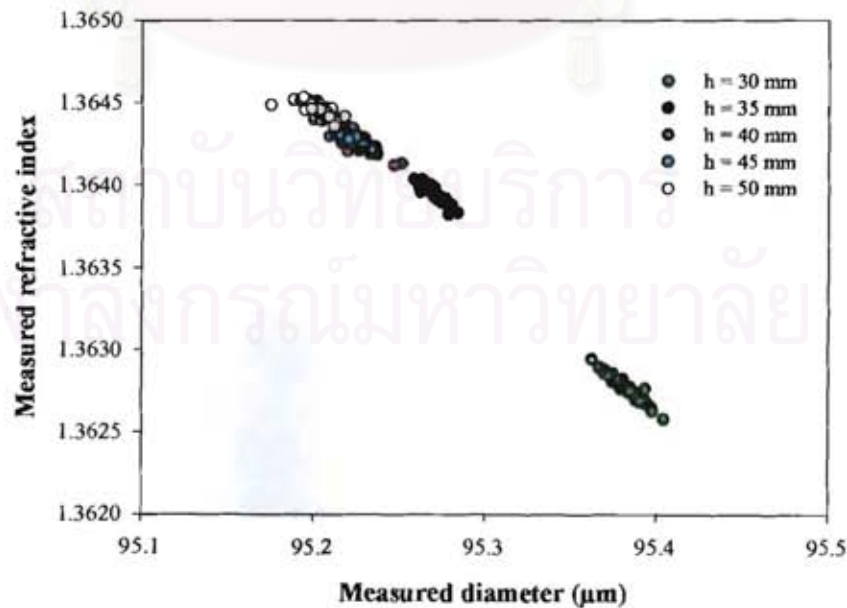


Figure 4.48: Measured correlation refractive index/size.

4.4 Classical rainbow limitations

The previous section is based on the assumption that the droplets are perfectly homogeneous and spherical. This section discusses what happens when this assumption is not satisfied.

4.4.1 Particles with radial gradients.

To evaluate the effect of a non-homogeneous and non uniform distribution of the refractive index inside a particle, a theoretical model must be used, which must give the possibility to compute the scattered light for a range of size of interest (typically from 50 to 200 μm). In this paper, the reference computations will be carried out in the framework of the Lorenz-Mie theory for multilayered spheres. The computational algorithms have been previously described by Wu et al [33].

The refractive index inside the particle is defined by the refractive index at the particle center, N_c , at the particle surface, N_s , and by a transitional law between these two points. In this paper, the following law is used:

$$N(x) = N_c + (N_s - N_c) \times \frac{e^{bx} - 1}{e^b - 1} \quad (4.7)$$

where x is the dimensionless distance from the particle center. The parameter b governs the bent of the function. It depends mainly on the nature of the experiments (heating or cooling), and usually evolves during a process.

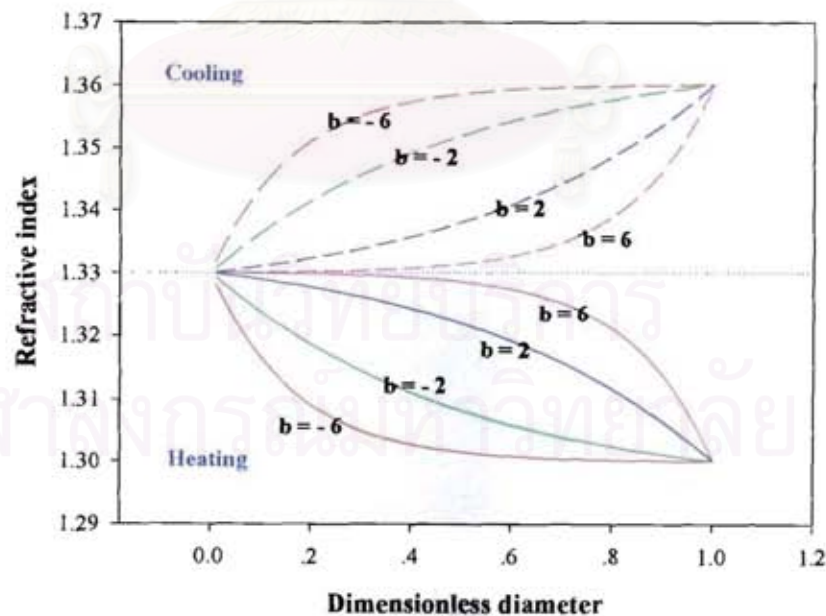


Figure 4.49: Examples of radial gradients. The parameter is the value of the coefficient b .

Figure 4.49 displays the radial profiles of refractive index for different values of the parameter b . When b is positive the gradient is strong at the surface while when b is negative the gradient is strong at the center. The slope of the gradient is directly proportional to the modulus of b . Specifically, relying on several simulations from an evaporation model [34], b is set to 1.9, in the case of a droplet cooling (injection temperature 51°C, ambient temperature 20°C) which are realistic values when the measurements are carried out at a sufficient distance from the injector.

In order to determine the number of layers required to simulate a continuous gradient, computations have been carried out for a 100 μm diameter particle with N_c equal to 1.33, N_s equal to 1.36 and b equal to 2. The number of layers has been varied from 10 to 1280. Figure 4.50 displays the scattering diagrams around the rainbow angle predicted from a Lorenz-Mie multilayer code while figure 4.51 displays the scattering diagram for the same case, but in the forward direction. From these two figures, it is concluded that 100 layers are sufficient to predict accurately enough the scattering diagrams both in forward and backward directions, including the rainbow ripple structure in frequency and phase. The low frequency evolution of the intensity is not investigated in this paper because it is more difficult to experimentally record.

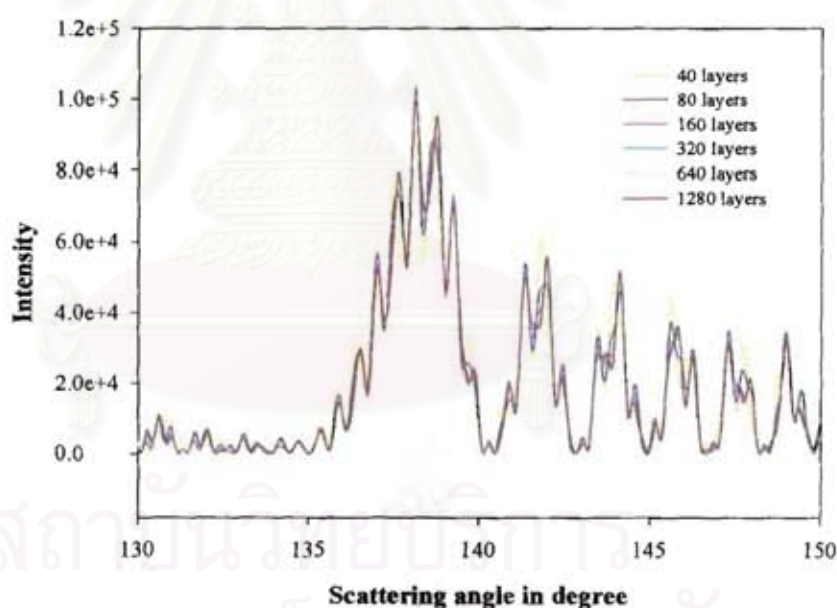


Figure 4.50: Scattering diagram around the rainbow angle for a particle with radial gradient. The parameter is the number of layers.

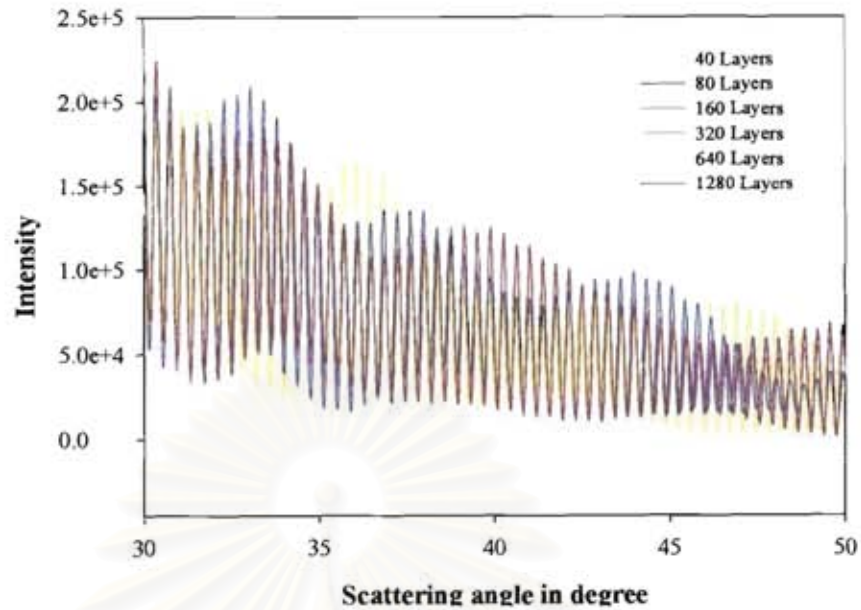


Figure 4.51: Scattering diagram in forward direction for a particle with radial gradient. The parameter is the number of layers.

Figures 4.52 and 4.53 compare the scattering diagram for a homogeneous particle and for a non-homogeneous particle, in forward and backward regions respectively. The computation parameters are: a particle diameter equal to 100 microns illuminated by a plane wave with an incident wavelength of 0.5145 micron, a refractive index of 1.36 for homogeneous particle or N_c equal to 1.36 and N_s equal to 1.328 with b equal to 2 for non-homogeneous particle. Both cases have been computed in the framework of the Lorenz-Mie theory for multilayer spheres. In figure 4.52, the frequencies of the signal for the two cases are nearly identical, but the phase between them and the intensity are modified. Figure 4.53, in backward, around the rainbow angle, shows that the signal is shifted. The intensity and location of the ripple fringes are also modified. An important fact is that, when b is positive, the position of the rainbow corresponding to the particle with a gradient is not between the position of the rainbows for the minimum and maximum of refractive index values but larger than the position of the rainbow for the maximum refractive index. On the opposite, let us mention that, when b is negative, the position of the rainbow corresponding to the particle with a gradient is between the position of the rainbow for the minimum and the maximum of refractive index values. Naturally, the rainbow position is a function of the refractive index at the center, at the surface and of the gradient shape (coefficient b in this paper).

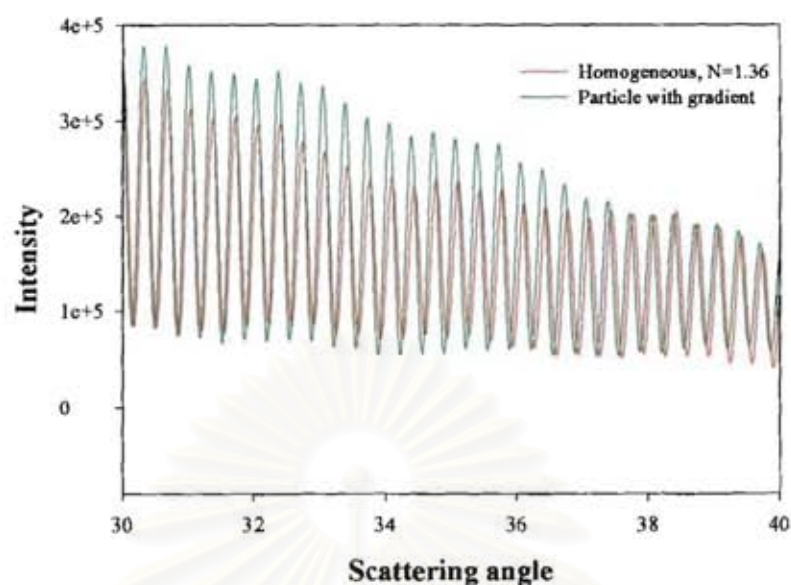


Figure 4.52: Effect of a gradient on forward scattering diagrams. Comparison between the forward scattering diagram for a homogeneous particle ($N=1.36$ and $d=100\mu\text{m}$) and non-homogeneous particle ($d=100\mu\text{m}$, $N_c = 1.36$, $N_s = 1.328$ and $b=2$). The incident wavelength is equal to $0.5145\mu\text{m}$. The frequency of the signal is essentially unaffected.

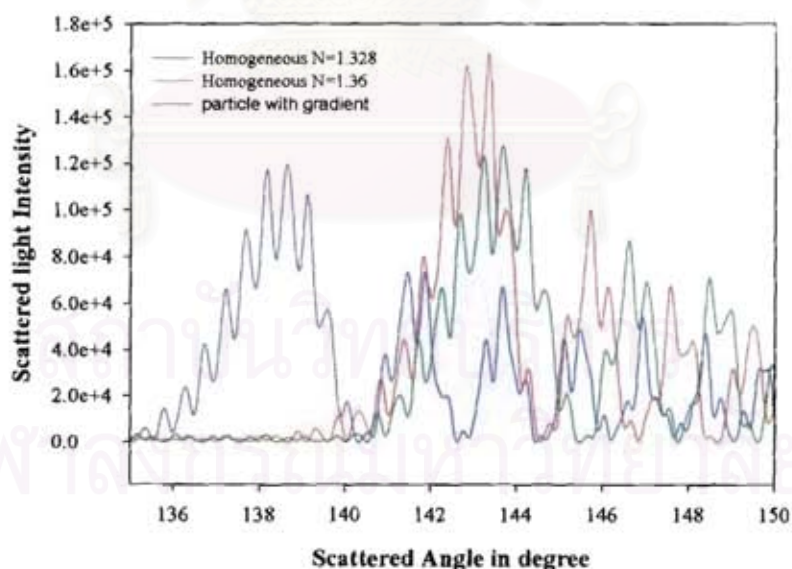


Figure 4.53: Effect of a gradient on backward scattering diagrams. Comparison between the backward scattering diagram for two homogeneous particles ($d=100\mu\text{m}$, $N=1.36$ or 1.328) and for a non homogeneous particle ($d=100\mu\text{m}$, $N_c = 1.36$, $N_s = 1.328$ and $b=2$). The incident wavelength is equal to $0.5145\mu\text{m}$. The rainbow is shifted, and for a positive value of b , the rainbow for the particle with gradient is not located between the rainbows for the two extreme refractive index values.

Figures 4.54 and 4.55 exemplify the sensitivity of the rainbow location with respect to the refractive index gradient. Figure 4.54 is devoted to the effect of coefficient b on the rainbow location while the effect of surface refractive index value, for a constant value of b equal to 2, is shown in figure 4.55. In figure 4.54, all the computations correspond to a particle with a diameter equal to 100 microns illuminated by a plane wave with an incident wavelength equal to 0.5145 micron. The refractive index at the center is the largest and is equal to 1.36 while, at the surface, the refractive index is equal to 1.315. The coefficient b runs from -4 to 6. As b increases from -4 to 4, the first rainbow location is shifted to larger angles (from 138° to 148°) while the second rainbow is shifted to smaller angles (from 132° down to 115°). Let us note that for $b=6$ the light distribution is essentially the same as for $b=4$.

Figure 4.55 displays computations for a particle with a diameter equal to 100 microns and the beam incident wavelength is equal to 0.5145 micron. The value of b is a constant equal to 2. The refractive index at the center is fixed to 1.36, while the refractive index at the surface is equal to 1.36 (homogeneous case), 1.356, 1.315 and 1.296 respectively. When the difference between refractive indices at the center and at the surface is increased, for b positive, the primary rainbow location is shifted to larger angles. The second rainbow is shifted to smaller scattering angles. The stronger the gradient is, the larger the shift is. In contrast, when b is negative, the primary rainbow location is shifted to lower angles.

In cases when the refractive index at the surface is larger than the refractive index at the center, the rainbow location for non-homogeneous particles will be smaller than the rainbow location corresponding to the refractive index at the center (minimum refractive index), for positive values of b , while for negative values of b , the rainbow location for non-homogeneous particles will be between the location of the rainbow for the minimum and for the maximum of refractive index values.

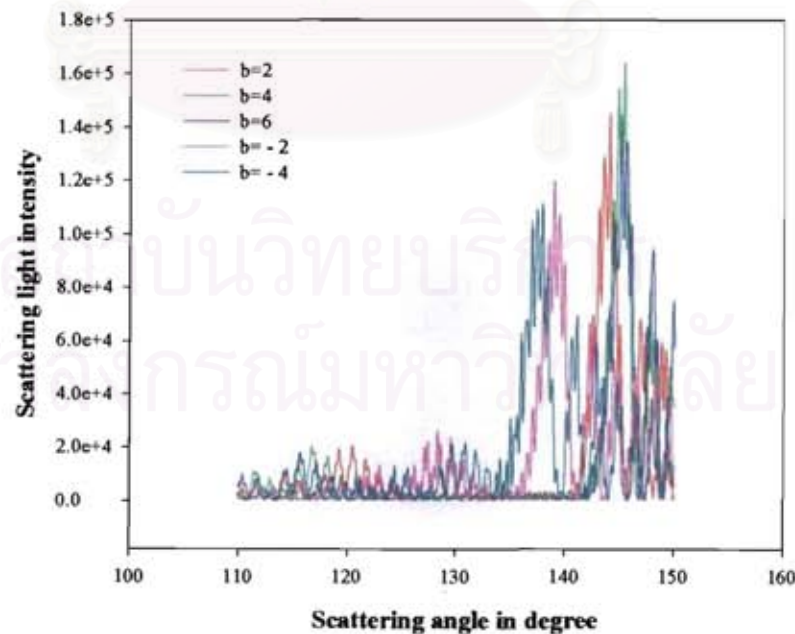


Figure 4.54: The scattering diagrams show the effect of coefficient b on rainbow location. (For wavelength=0.5145 micron, particle diameter=100 microns, $N_c=1.36$ and $N_s=1.315$ for 100 layers).

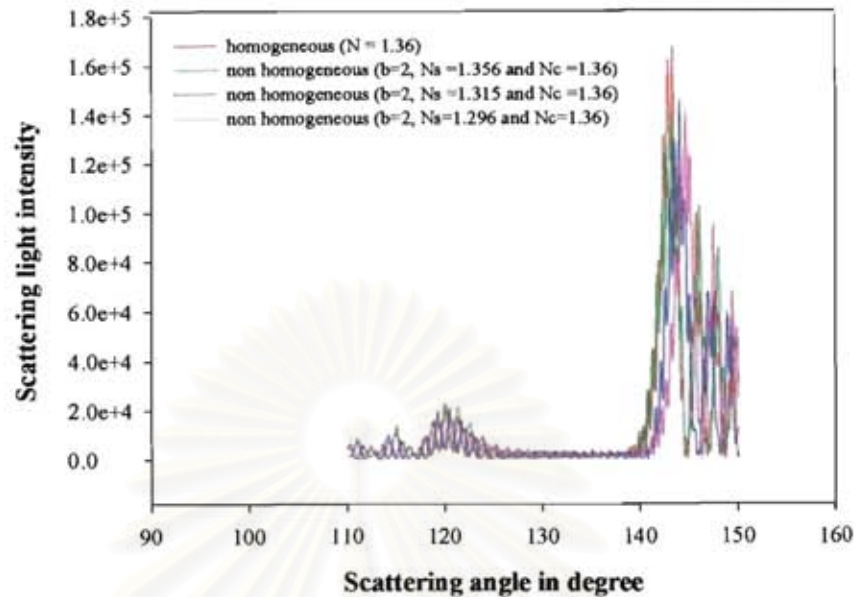


Figure 4.55: The scattered light distribution for different values of the refractive index at the surface with a constant value at the center equal to 1.36 (wave length =0.5145 micron, particle diameter=100 microns, $N_c=1.36$, $b=2$ and 100 layers).

Search for an equivalent particle

In the case of homogeneous particles it has been shown that the Nussenzweig's theory can satisfactorily predict the scattered light in agreement with Lorenz-Mie theory by taking into account the external reflected light ($p=0$), the refracted light ($p=1$) and one time internal reflected light ($p=2$) (see previous sections or [35]). In the case of non-homogeneous particles, a challenge is to exhibit an equivalent homogeneous particle with identical scattered light properties (if this equivalent particle exists).

In order to find the refractive index and the particle size of the equivalent homogeneous particle which possesses a scattering diagram close to the one for a non-homogeneous particle, the intensity distribution from the particle with gradient is simulated by Lorenz-Mie's theory for multilayered particles and then compared to the intensity distribution from a homogeneous particle, simulated by the Nussenzweig's theory, in forward and backward regions. The processing scheme is the dual processing introduced in section 4.3 which is recalled as follows.

Firstly: For an arbitrary refractive index, the Fast Fourier Transforms (FFT) of the forward scattering diagram (between 30-50°) for homogeneous and non-homogeneous particles are compared. The diameter of the homogeneous particle is adjusted to obtain the same frequency contribution as for the non-homogeneous particle under study. This process provides a relatively large range of admissible particle diameters.

Secondly: For the admissible diameter range, the refractive index is adjusted to obtain the same location of the main rainbow peak as for the non-homogeneous particle.

Thirdly: The particle diameter and refractive index are adjusted to obtain an agreement in frequency and phase [3,36] in forward and backward regions, including the ripple structure.

Figure 4.56 is an example of scattering diagrams computed by Lorenz-Mie's theory for a multilayer sphere ($d=100\ \mu\text{m}$, $N_c=1.36$, $N_s=1.352$, $b=2$) and by Nussenzveig's theory at forward angles (in figure 4.56(a)) and around rainbow angle (in figure 4.56(b)). The scattered light for the non-homogeneous case can be satisfactorily fitted by the scattered light from a homogeneous particle in terms of frequency and phase. The equivalent particle diameter is found to be equal to 100.07 microns and the equivalent refractive index is found to be equal to 1.361.

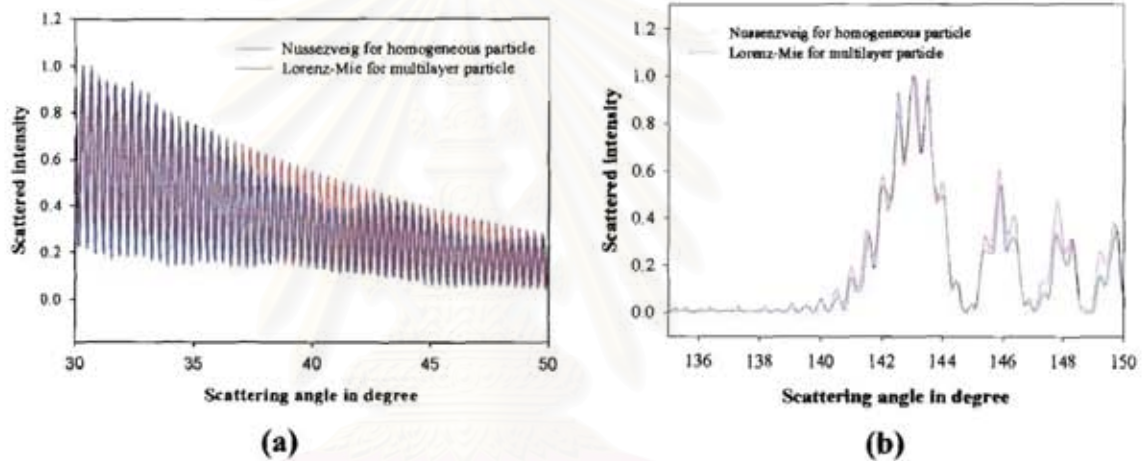


Figure 4.56: Comparison of the scattered light between Lorenz-Mie's computations for a multilayer particle (diameter=100 microns, refractive index at the center=1.36 and at the surface=1.352, $b=2$) and Nussenzveig's computation for a homogeneous particle (diameter=100.07, refractive index=1.361) (a) in forward region (b) in backward region.

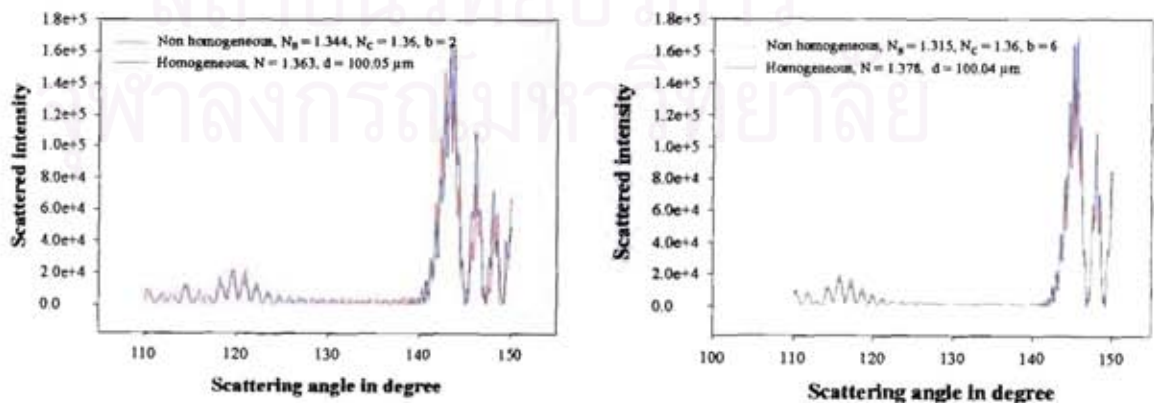


Figure 4.57: Comparison of the scattered light at primary and secondary rainbows for non-homogeneous particle and equivalent homogeneous particle.

Figure 4.57 compares the scattered light around rainbow angle computed by Lorenz-Mie's theory for multilayered spheres for non-homogeneous particles and by Lorenz-Mie's theory for homogeneous spheres with the parameters (size, refractive index) describing the equivalent particle in the Nussenzveig's theory. Two cases of non-homogeneous particles having the same diameter (100 microns) and refractive index at the center (1.36) have been studied. For one case, the particle has the refractive index at the surface equal to 1.344 with b equal to 2. For the other case, the particle has the refractive index at the surface equal to 1.315 with b equal to 6. The results show that even when the gradient is stronger at the surface or the evolution faster (higher value of b) we can find a scattered light distribution of an equivalent homogeneous particle fitting well enough the scattered light distribution for non-homogeneous particles. Moreover, not only the primary rainbow of a non-homogeneous particle can be fitted by the one of a homogeneous particle but the statement remains true for the secondary rainbow. Then the second rainbow provides the same information as the first rainbow.

The aforementioned procedure has been applied to different multilayered particles. In this study, the refractive index at the center is set to a constant value equal to 1.36. Refractive indices at the surface are taken to be 1.359, 1.358, 1.356, 1.352, 1.344, 1.328, 1.315, 1.305 and 1.296. Also the coefficient b is assigned the values: -4, -2, 1.5, 2, 2.5, 3, 4, 6, i.e. 60 cases are studied. For each case, couples of equivalent refractive index and diameter for homogeneous particles are extracted.

Let us first note that the diameter of the equivalent particle is nearly constant (about equal to 100 μm), nearly independently of the gradient amplitude and shape. Therefore only the equivalent refractive index is studied. The results are compiled in figure 4.58 where the equivalent refractive index is plotted versus the real surface refractive index N_s .

The results in figure 4.58 can be sorted in two families depending on the value of the parameter b . When b is positive, the equivalent refractive index is always larger than the largest real refractive index (1.36) while, when b is negative, the value of the equivalent refractive index is intermediary between the values at surface and at center. Furthermore, the relationship between the equivalent refractive index and the surface refractive index is essentially linear, with the slope coefficient depending on b .

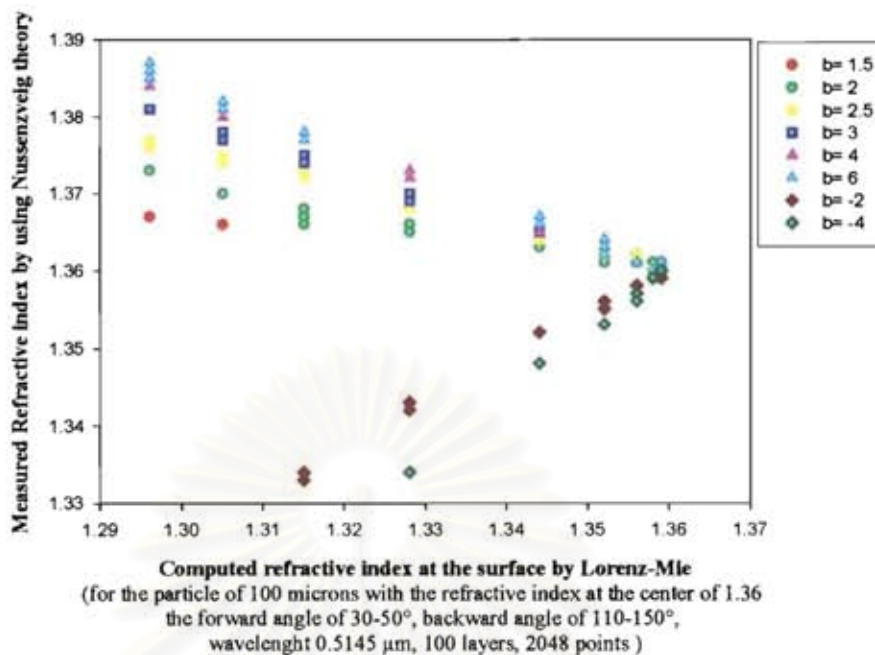


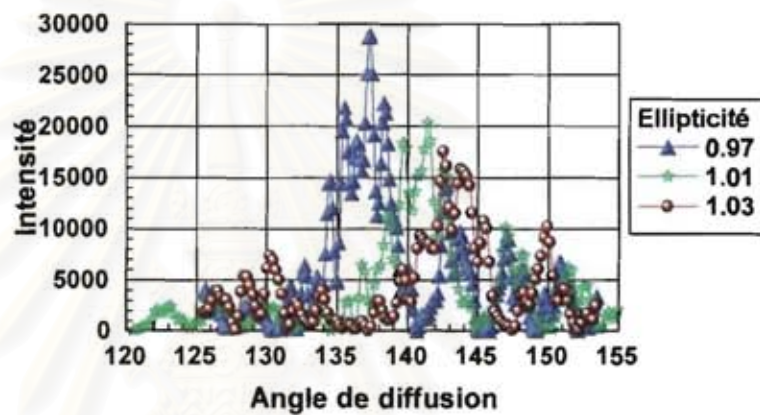
Figure 4.58: The relationship between the equivalent particle refractive index and the real surface refractive index with different values of b .

In conclusion, when rainbow refractrometry is applied to particles having a radial gradient an equivalent refractive index is measured. The equivalent refractive index is a function of the refractive difference between the refractive index at particle center and the refractive index at its surface, including the evolution law between the surface and the center. To extract the gradient complementary techniques have to be used as Laser Induced Fluorescence (sensitive mainly on the center) and infrared technique (sensitive only to the surface).

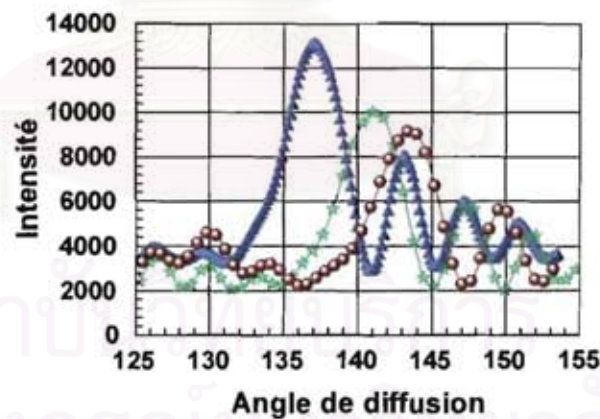
สถาบันวิทยบริการ
 จุฬาลงกรณ์มหาวิทยาลัย

4.4.2 Deformed particles.

In complement of the ripple structure, a strong limitation of the classical rainbow technique is that the scattering particles are assumed to be perfectly spherical but a small non-sphericity can dramatically modify the rainbow location, that is to say the temperature (composition) measurement. The computation of the light scattered by non-spherical particles is more difficult than for spheres. Nevertheless, during these last years advances have been realized which permit to compute the scattering of light by spheroids with relatively large size [37,38]. For example figure 4.59 displays scattering diagrams for a particle with a diameter of about $40\ \mu\text{m}$ and with the ellipticity as a parameter. Three cases have been studied corresponding to an ellipticity equal to 0.97, 1.01 and 1.03. The major effect of a non-sphericity is to shift the rainbow position.



(a)

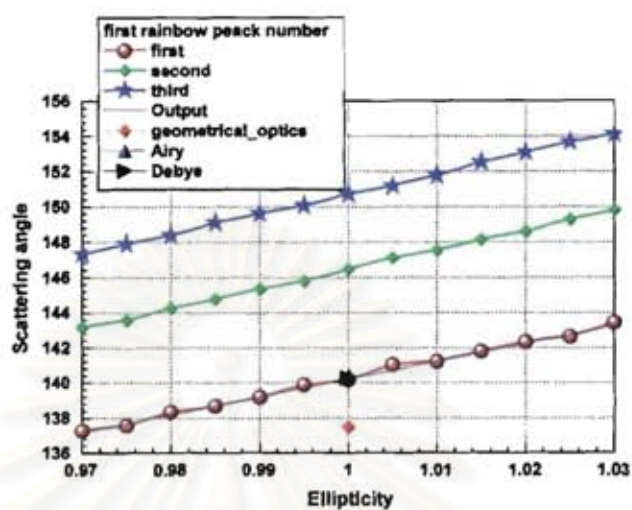


(b)

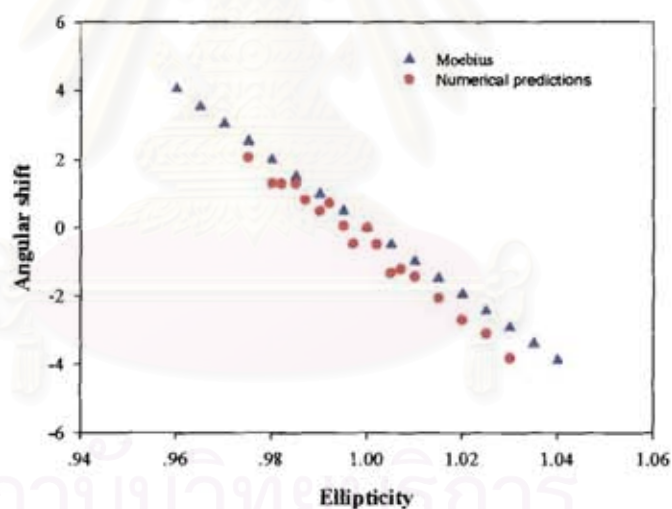
Figure 4.59: Effect of a non sphericity on the rainbow location.
(a): original scattering diagrams, (b): filtered scattering diagrams.

Figure 4.60 displays a study of the behaviour of the shift versus the ellipticity for a particle with a diameter equal to about $40\ \mu\text{m}$. Figure 4.60(a) displays the location of the mean rainbow peak and of the first two supernumerary peaks versus the ellipticity while figure 4.60(b) compares the shift of the mean rainbow peak, extracted from the rigorous numerical results displayed in figure 4.60 (a), with the predictions of the Moebius's theory, which is an approximate theory developed in

the framework of geometrical optics for large particles. The conclusion of these studies is that the Moebius theory is an appropriate tool to understand the major effects of non sphericity on the rainbow of small particles.



(a)



(b)

Figure 4.60: Shift of the rainbow position versus ellipticity.

(a): Position of the main rainbow peak (red circles) and of the two first supernumerary peaks versus ellipticity.

(b): Comparison of the rainbow shift as numerically predicted by Moebius.

To eliminate non-sphericity effects, the global rainbow technique has been introduced by van Beeck et al in 1999 [39]. This technique is introduced in the next paragraph.

While, when the gradient is strong at the surface of the particle, the measured refractive index is always higher than the maximum refractive index value any where inside the particle. This effect is a clear signature of the presence of a gradient.

The complete characterization of the gradient will ask for complementary information which could be obtained from numerical codes or other experiments as LIF which is more sensitive to the center of the particle or Infra-red imaging which is only sensitive to the surface temperature of the particle.

In the case of cloud of droplets, only backward scattered light is processed. By using non-negative least square method (nnls) with scattered light computed by Nussenzweig's theory and minimizing the distance between the recorded and the computed global rainbow distribution, a mean refractive index and a size distribution are extracted. The inversion time is smaller than 1 s, giving the possibility to follow the temperature evolution of a section of spray under combustion for example. From the numerical simulations, the accuracy of the refractive index measurement is of about 0.001 to 0.0001, the extracted size distribution is not perfect but good enough to display the main characteristics of the spray.

The next step is to develop an experimental global rainbow set up to measure temperature and size distribution. It is the aim of the next chapters.



สถาบันวิทยบริการ
จุฬาลงกรณ์มหาวิทยาลัย

CHAPTER V

GLOBAL RAINBOW PRINCIPLES AND APPLICATIONS BY USING NUSSENZVEIG'S THEORY

In the previous section, the improvement of rainbow signal processing permits to accurately measure the size and refractive index of mono-disperse droplets. Then the evaporation rate is obtained. However, in a real spray, the spray is not created as a line of droplets. Then the previous approach cannot be used. Therefore, the global rainbow technique has been applied to measure the temperature and mean size of the droplets in the spray which is the key parameter in the combustion field.

5.1 Global rainbow Principle.

The global rainbow technique is based on the analysis of the light scattered around the rainbow angle due to an assembly of particles. Generally, this technique uses the same physical principle as rainbow refractrometry. Nevertheless, the recorded light is not issued from one particle but correspond to collaborative scattering of a large number of particles. The global rainbow pattern is characterized by a main peak and followed by a tail as displayed in figure 5.1. The location of the main peak depends essentially on the refractive index value while its shape depends on the size distribution. The main advantages of the global rainbow technique are:

1. Suppression of the ripple structure: for spheres, as the ripple structure is very sensitive to the particle size, adding the contribution of a large number of particles removes this structure.
2. No effect of non spherical particles: for non spherical particles, according with the Moebius theory, if the orientation of the particles in the spray can be assumed to be described by a random law, the contribution will be only a uniform background.

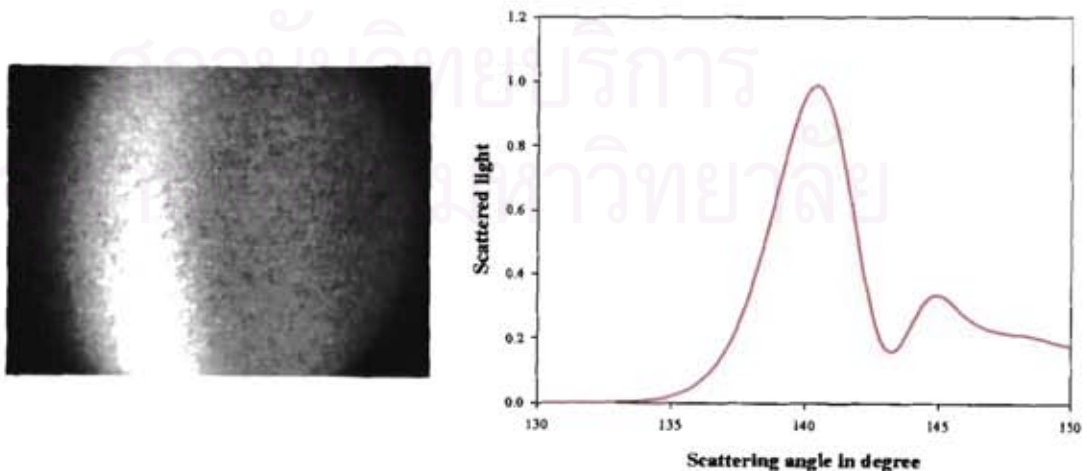


Figure 5.1: An image and the scattered light of global rainbow.

The global rainbow pattern is obtained by adding together several amounts of scattered light by individual droplets. To compute global rainbow diagrams in the framework of the Lorenz-Mie theory, the procedure is to compute a series of individual scattering diagrams, here for size distributions defined by a Gaussian random law and then to sum up the contributions. To obtain a smooth curve it is necessary to sum up about 1000 individual particles. Figure 5.2 exemplifies this process.

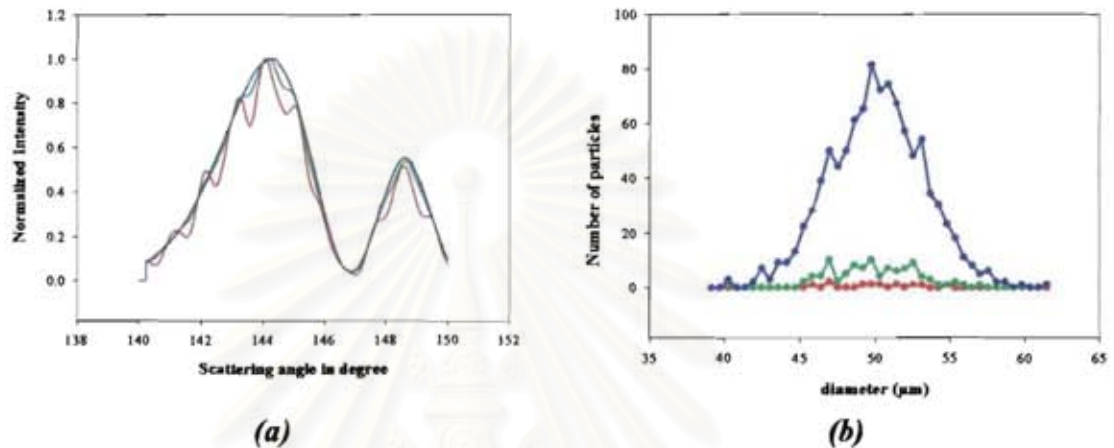


Figure 5.2: (a) Global rainbow signal with the number of particles as a parameter (red 20, green 100, blue 1000).
 (b) Number of particles by diameter. The size distribution parameters are identical for the three cases.

As previously described, the Lorenz-Mie theory is the most rigorous theory but it is also the most time consuming. For practical applications it is important that we are able to compute global rainbow patterns with the same accuracy as by using Lorenz-Mie theory but about 500 times faster by using Nussenzveig theory. Then a code to predict the global rainbow patterns has been written in DELPHI, based on the corrected Nussenzveig's theory.

Figure 5.3 displays the code interface consisting in three main parts:

1. The inputs for computations
2. The outputs: direct visualization and saving in files for later use
3. Some numerical flags to check the applicability of the Nussenzveig's theory.

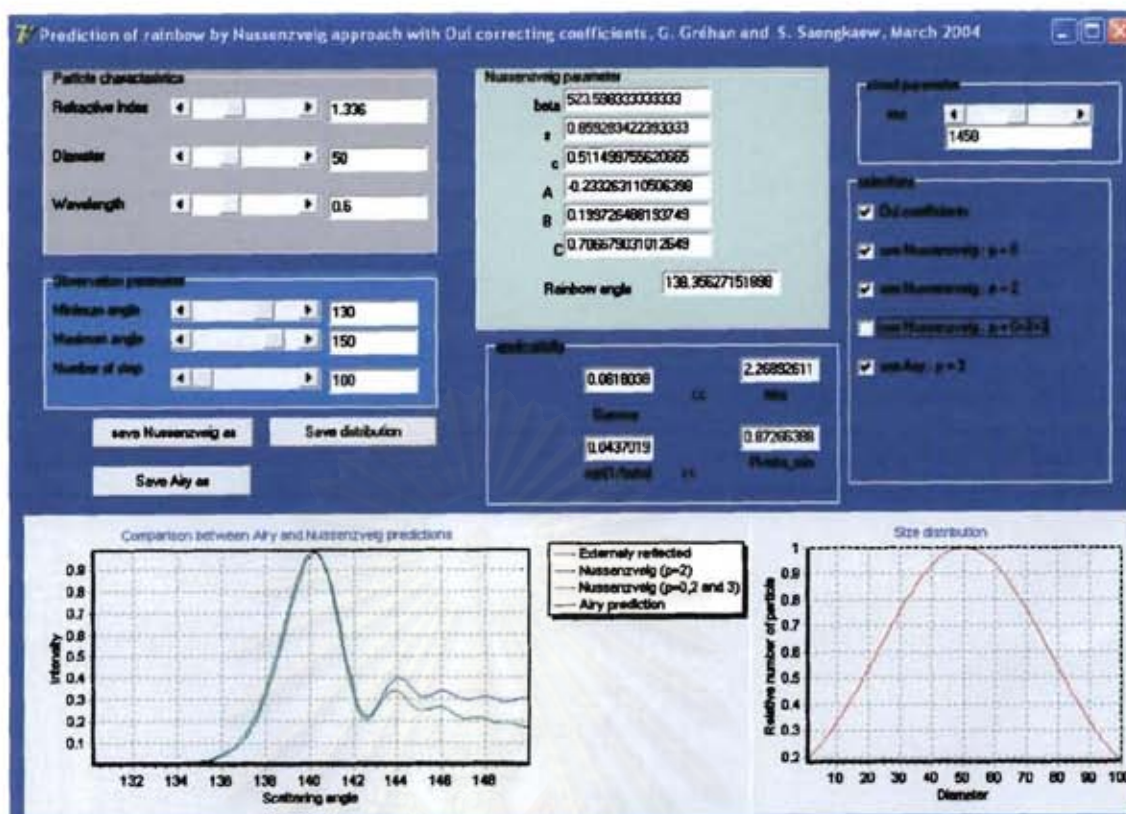


Figure 5.3: Example of global rainbow computation. The important fact is the differences at large scattering angles between corrected Nussenzweig's predictions and Airy predictions.

Figure 5.4(a) displays the predicted global rainbow patterns computed by Nussenzweig theory and by Lorenz-Mie theory for the size distribution shown in figure 5.4(b), for water droplets ($N=1.33-0.0i$). In figure 5.4(a), 3 regions can be defined:

1. scattering angle smaller than 136°
2. scattering angle between 136° and 143° ,
3. scattering angle larger than 143° .

Within the central region, for scattering angle from 136° to 143° , the agreement between the different curves is essentially perfect. It reveals that Lorenz-Mie's predictions, Airy's prediction's and Nussenzweig's predictions with or without correcting coefficients are in agreement. For larger scattering angles, Airy's predictions and Nussenzweig's predictions without correcting coefficients exhibit consistent scattered intensity but higher than that of the Lorenz-Mie theory. On the contrary, Nussenzweig's predictions with correcting coefficients agree perfectly with Lorenz-Mie's predictions. In the third region representing the scattering angles smaller than 136° , the disagreement between Lorenz-Mie's predictions and Airy-Nussenzweig's predictions is large because this region is essentially dominated by the second rainbow. The Nussenzweig theory can also predict the light scattered by higher order rainbows. Then the same procedure to find correcting coefficient as introduced in chapter 3 can be applied for the second rainbow to obtain an accurate and fast description of the light scattered at these angles.

However, in this thesis, we are interested in products having high values of refractive index in which the first and second rainbows are completely separated. As a consequence, the prediction and analysis of global rainbow patterns can be carried out in the framework of Nussenzveig's theory with correcting coefficients taking into account only $p=2$ rays.

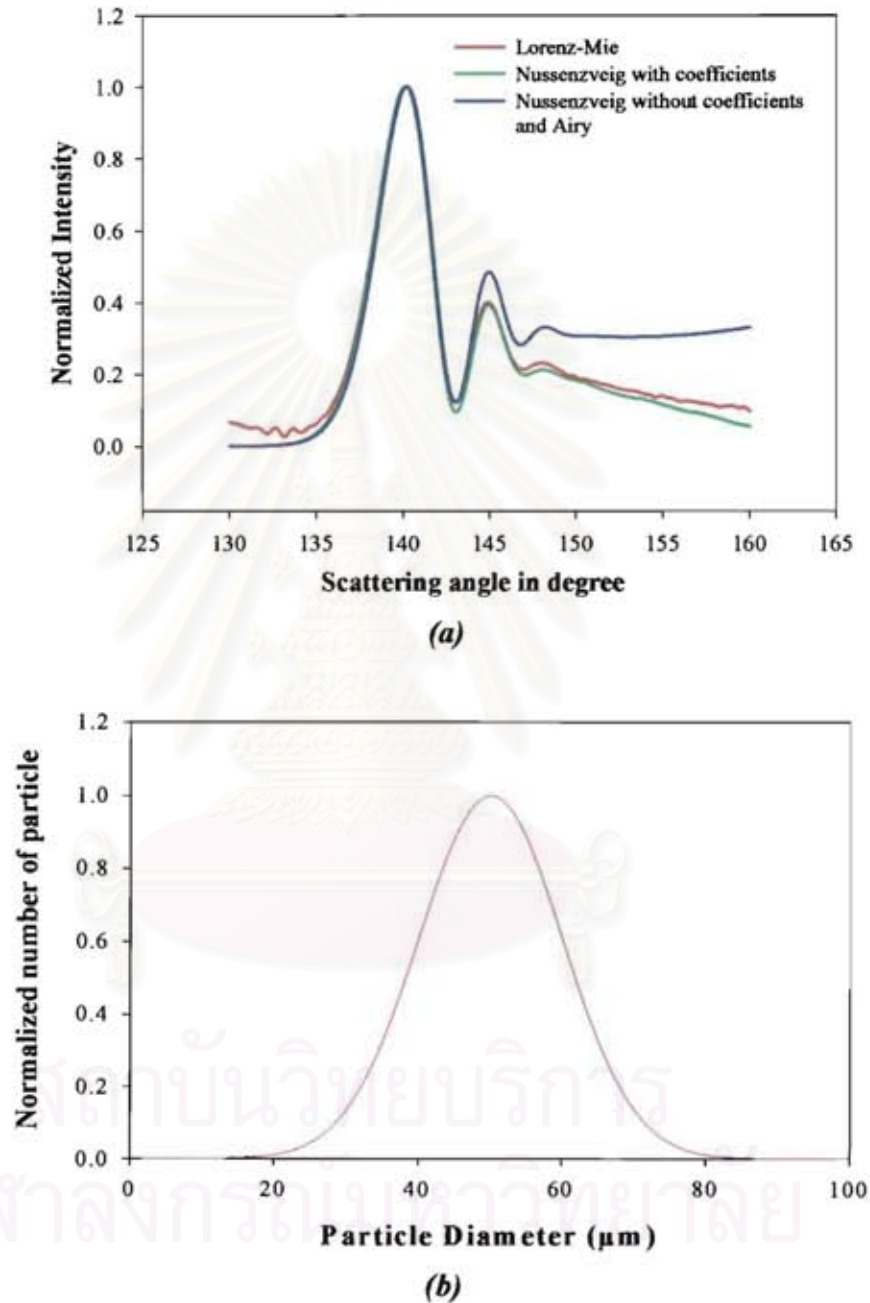


Figure 5.4: (a) Comparison between global rainbow prediction by Lorenz-Mie's theory, Airy's theory and Nussenzveig's theory adding correcting coefficients and without any correcting coefficients.

(b) The size distribution corresponding to the global rainbow patterns in figure 5.4(a).

As for the rainbow for one particle (see section 4.2) the global rainbow pattern also depends on mean diameter, size distribution and the refractive index. Figure 5.5 presents the effect of mean diameter on the global rainbow pattern, while figure 5.6 shows the effect of size distribution. It is evident that global rainbow pattern is changing with the mean size and size distribution. In figure 5.5, the change of mean diameter mainly affects the width of the first peak. The larger the mean diameter is, the narrower the width of first peak is. On the contrary, in figure 5.6 the change of size distribution mainly affects the tail of the global rainbow pattern, and has little effects on the first peak. Finally, figure 5.7 displays the effect of refractive index on the global rainbow pattern. An increase of the refractive index value translates the global rainbow pattern to larger scattering angles.

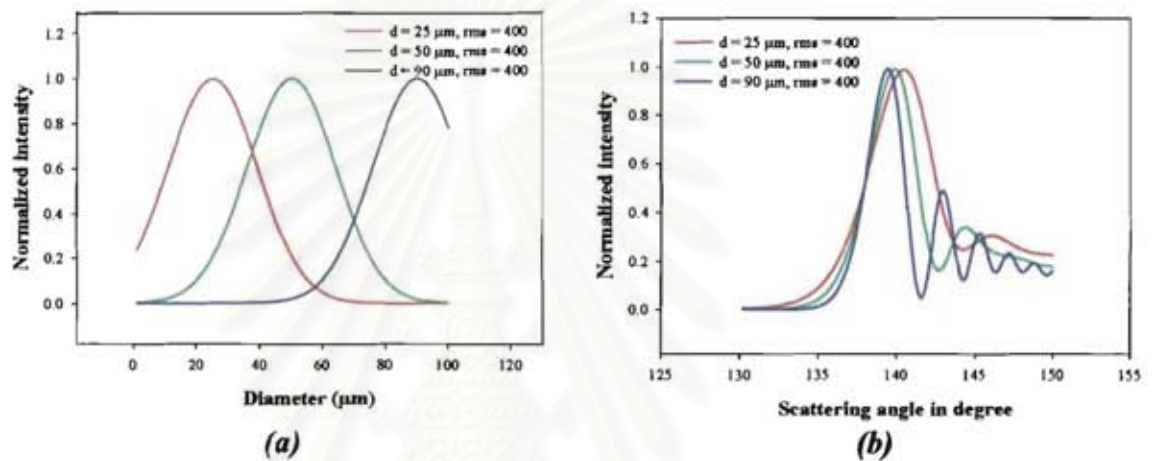


Figure 5.5: Behavior of the global rainbow signal simulated by Nussenzveig's theory. (a): displays three size distributions with the same width. (b): displays the associated global rainbow patterns. The main effect is the width of the first peak.

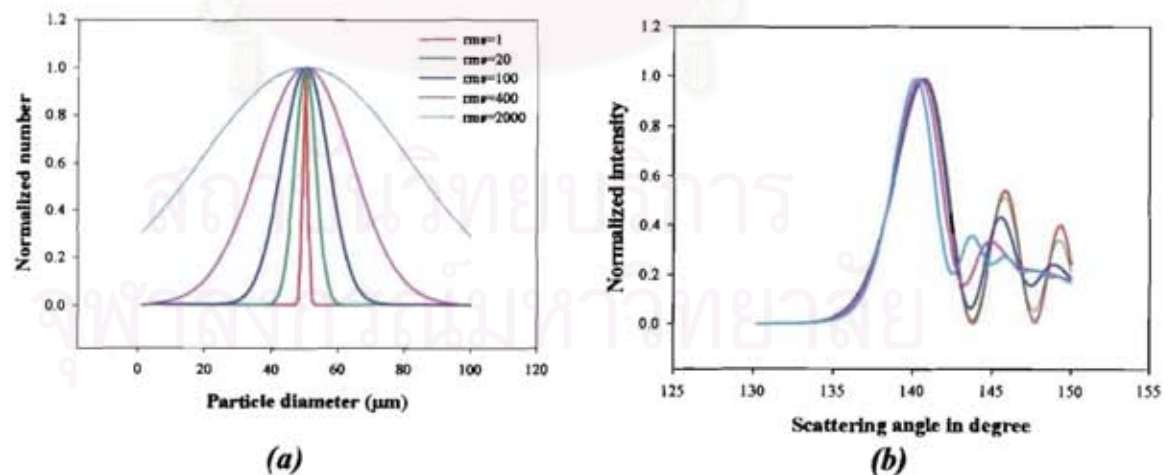


Figure 5.6: Behavior of the global rainbow signal. (a): displays five size distributions with the same mean diameter ($50 \mu\text{m}$). (b): displays the associated global rainbow patterns. The reduction of the Airy oscillations with width of the size distribution is clear.

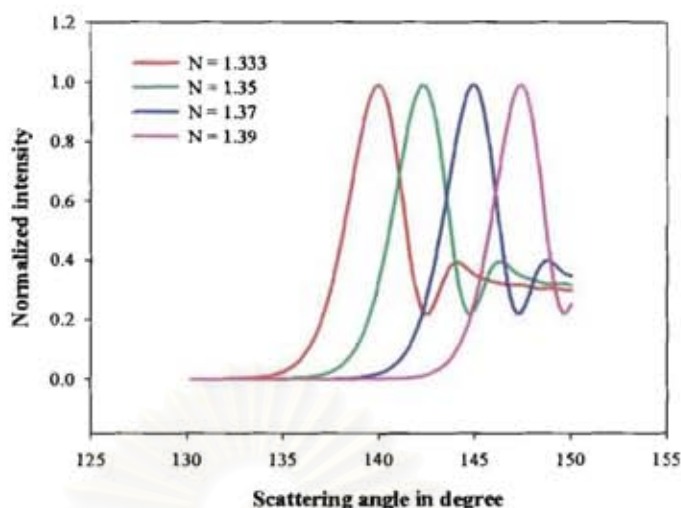


Figure 5.7: Effect of a variation of the refractive index on the global rainbow pattern (for a mean diameter equal to 50 microns with an rms equal to 400).

The sensitivity of the global rainbow patterns to the refractive index and to the particle size can be used to develop a technique in order to extract the information from a recorded global rainbow. It is the aim of the next paragraph.

5.2 Global rainbow processing

Firstly van Beeck et al [40] propose a fast inversion of the global rainbow based on the Airy theory and on the assumption that the size distribution is Gaussian. As the global rainbow signal depends on both the droplet temperature and droplet size, both must be simultaneously solved. Moreover it has been shown that the distance between the rainbow fringes obtained with the Airy theory is *a priori* independent of the droplet temperature [41]. Therefore the droplet size can be obtained from any fringe spacing without knowing the droplet temperature. Following this idea, van Beeck and Riethmuller [42] arrived at equation (5.1) in which the droplet diameter can be obtained from the distance between two characteristic points, i.e., scattering angles θ_i and θ_j , of the global rainbow pattern:

$$D_{Airy} = \frac{\lambda}{4} \left(\frac{\cos \tau_{rg}}{\sin^3 \tau_{rg}} \right)^{0.5} \left(\frac{z_i - z_j}{\theta_i - \theta_j} \right)^{1.5} \quad (5.1)$$

where z_i and z_j are the non-dimensional Airy factors corresponding to θ_i and θ_j respectively. The couple of points of the rainbow pattern that have been used are the first two inflection points or the first two maxima, as defined in figure 5.8. By use of these characteristic points of the global rainbow pattern, the previous equation can be rewritten as:

$$D_{Airy_max i} = 1016,175\lambda(\theta_{M2} - \theta_{M1})^{-1.5} \quad (5.2)$$

$$D_{Airy_inflec} = 531.555\lambda(\theta_{inf12} - \theta_{inf11})^{-1.5}$$

From the values of the Airy diameters the width of the size distribution can be estimated by comparison with Airy diameters computed for an assumed size distribution law (see figure 4 of reference 40).

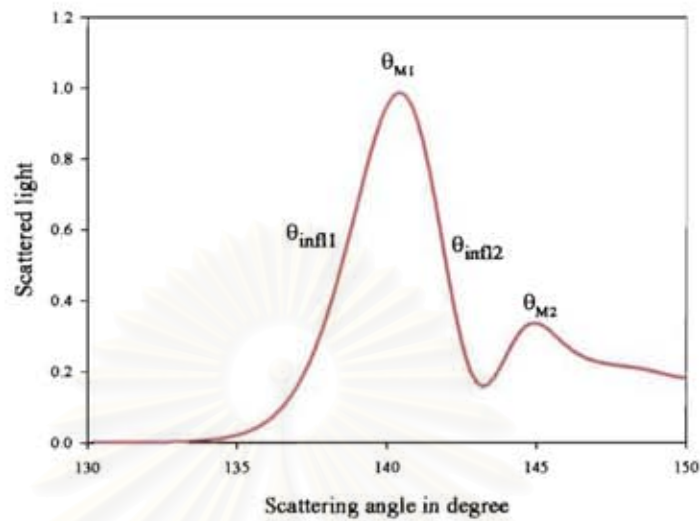


Figure 5.8: Definition of the points used in the inversion algorithm.

Then the droplet temperature is obtained from the Airy diameter by solving the equation:

$$\cos \frac{\theta_{rg}}{2} = \frac{\left(\sqrt{\frac{4 - N^2}{3}} \right)^3}{N^2} \quad (5.3)$$

with:

$$\theta_{rg_max\ i} = \theta_{M1} - 46.15 \left(\frac{\lambda}{D_{Airy_max\ i}} \right)^{2/3} \quad (5.4)$$

Figure 5.9 shows the flow chart of data inversion algorithm according to the basic concept as described above.

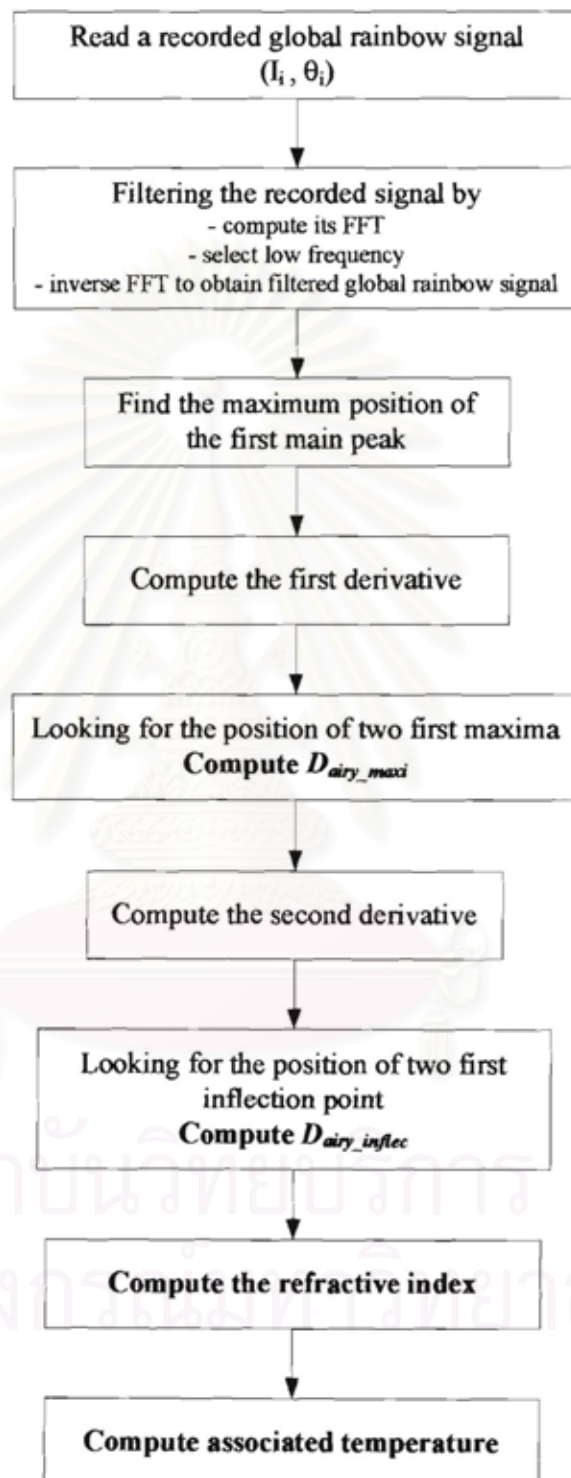


Figure 5.9: The flow chart of the inversion scheme based on two singular points.

This inversion procedure has been applied to simulated global rainbow patterns computed in the framework of the Nussenzweig's theory. Examples of the extracted results from the global rainbow signal with different mean diameters and standard deviations have been compiled in the following table.

Table 5.1: *Extracted diameters and refractive index for different size distributions. The value of the refractive index used for the direct computation was 1.33.*

Mean diameter	rms	D_{Airy_maxi} (μm)	D_{Airy_infl} (μm)	N_{Airy_maxi}	N_{Airy_infl}
25 μm	250	39.76	38.12	1.3304	1.3294
25 μm	1400	73.40	70.53	1.3312	1.3294
34 μm	250	45.58	44.79	1.3300	1.3290
34 μm	1400	71.6	75.32	1.3301	1.3302
50 μm	250	58.96	58.00	1.3299	1.3295
50 μm	1400	85.29	77.48	1.3312	1.3297
80 μm	250	85.96	85.65	1.3300	1.3301
80 μm	1400	89.86	84.61	1.3304	1.3297

Table 5.1 shows that the measurement of the refractive index is quite good. On the contrary the measurement of the mean diameter is less satisfactory especially for small mean diameters and large size distributions. The size distribution affect on the measured mean diameter, the larger the size distribution is, the larger the measured mean diameter is.

From the data inversion procedure, the filtered signal using FFT method is applied to keep only low frequency signal used to extract the refractive index and mean size information. As this method mean diameter and refractive index computed from a few characteristic points of global rainbow pattern. Then any change on filtered global rainbow signal according to the number of filtered points affects the extracted information.

Figures 5.10 and 5.11 display the sensitivity of the extracted mean diameter for D_{airy_maxi} and D_{airy_inflec} and refractive index for N_{airy_maxi} and N_{airy_inflec} to the filtering process. The conclusion is that the information extracted from the inflection point (size and refractive index) is very sensitive to the filtering process.

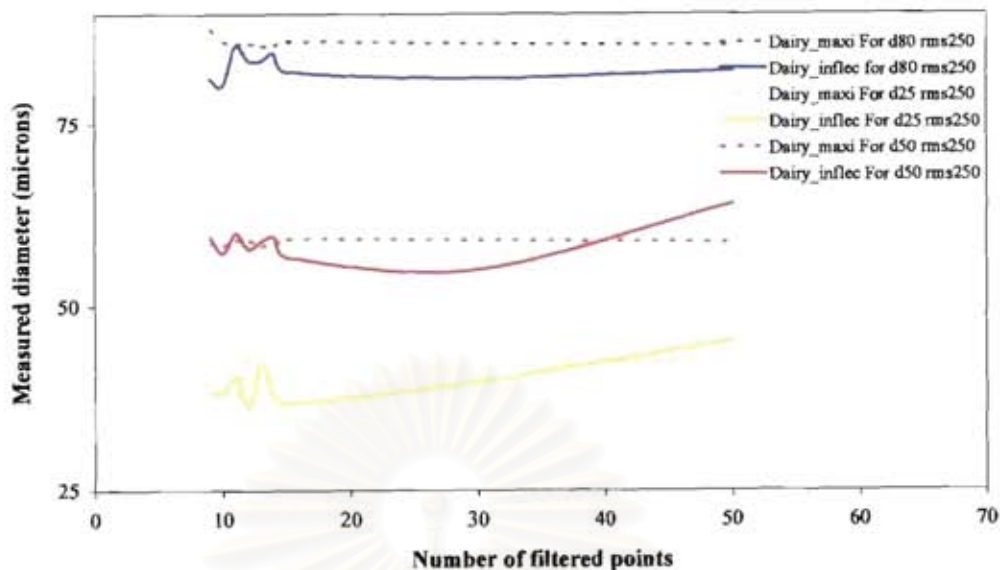


Figure 5.10: Comparison between the measurements of D_{airy_maxi} and $D_{airy_infllec}$ versus number of filtered points for different mean diameters with the same size distribution and refractive index equal to 250 and 1.33 respectively.

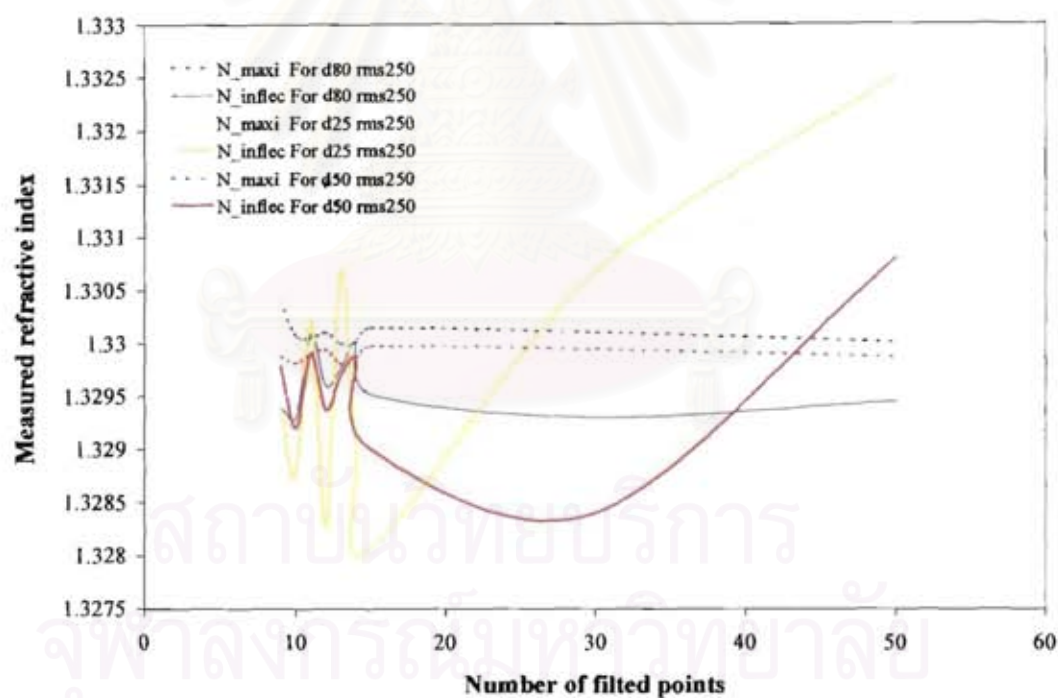


Figure 5.11: Comparison between the measurements of N_{airy_maxi} and $N_{airy_infllec}$ versus number of filtered points for different mean diameters with the size distribution and refractive index equal to 250 and 1.33 respectively.

Moreover, in the practical way, D_{airy_maxi} is not simple to determine because the second peak of global rainbow is difficult to record especially for small particles and large size distributions. Then another procedure to inverse global rainbow signals is introduced.

The global rainbow pattern can be seen as a vector I of dimension m which describes the collected intensity for each pixel (collecting angles). This vector is equal to the product of a matrix A by a vector B . The vector B , of dimension n , represents the size distribution histogram in n classes while the matrix A , of dimension $m.n$ represents the scattering of the particles. The lines of A correspond to a scattering direction while the columns of A correspond to one particle size class. Then the elements A_{ij} represents the scattered intensity in the direction θ_i of the particle of size d_j . Then the following equation represents a measurement:

$$A * B = I \quad (5.5)$$

or

$$\begin{bmatrix} A(\theta_1, d_1) & A(\theta_1, d_2) & A(\theta_1, d_3) \dots A(\theta_1, d_{nb_point}) \\ A(\theta_2, d_1) & A(\theta_2, d_2) & A(\theta_2, d_3) \dots A(\theta_2, d_{nb_point}) \\ A(\theta_3, d_1) & A(\theta_3, d_2) & A(\theta_3, d_3) \dots A(\theta_3, d_{nb_point}) \end{bmatrix} * \begin{bmatrix} b(d_1) \\ b(d_2) \\ b(d_3) \end{bmatrix} = \begin{bmatrix} I_1 \\ I_2 \\ I_3 \end{bmatrix}$$

M M M M M M

$$A(\theta_{nb_angular_point}, d_1) \quad \dots \quad A(\theta_{nb_angular_point}, d_{nb_dia_point}) * b(d_{nb_dia_point}) = I_{nb_angular_point}$$

The elements of the matrix A can be computed by any light scattering theory, particularly by using the Nussenzveig's theory with correcting coefficients. As A and I are known, by solving the previous equation, the size distribution can be extracted. If A is a square matrix, a naive way is to multiply the two sides of equation (5.5) by A^{-1} . This approach suffers from grave numerical difficulties. A better approach is to multiply by the transposed matrix A^T . This operation permits to reduce the set of equations to be solved to n by n .

$$(A^T.A).B=A^T.I \quad (5.6)$$

But here again, the direct solving of this equation (called *normal equation*) by using directly classical methods as Gauss-Jordan elimination, LU decomposition, SVD decomposition, etc., is not acceptable because although the obtained solution B exactly satisfies $I=AB$, the values of at least some of the elements of B are not physically possible (number of particles negative).

Then the equation (5.6) must be solved with some additional constraints. The principal constraint is that the number of particles in a class must be null or positive, and a secondary constraint asks for the continuity of the size distribution.

In the case of third derivative

$$H = \begin{bmatrix} 1 & -3 & 3 & -1 & 0 & 0 & 0 \\ -3 & 10 & -12 & 6 & -1 & 0 & 0 \\ 3 & -12 & 19 & -15 & 6 & -1 & 0 \\ -1 & 6 & -15 & 20 & -15 & 6 & -1 \\ 0 & -1 & 6 & -15 & 20 & -15 & 6 \\ 0 & 0 & 0 & 0 & 0 & 0 & 0 \\ 6 & -15 & 20 & -15 & 6 & -1 & 0 \\ -1 & 6 & -15 & 20 & -15 & 6 & -1 \\ 0 & -1 & 6 & -15 & 19 & -12 & 3 \\ 0 & 0 & -1 & 6 & -12 & 10 & -3 \\ 0 & 0 & 0 & -1 & 3 & -3 & 1 \end{bmatrix}$$

3. The value of σ is assumed to be given, in agreement with Numerical Recipes, by:

$$\sigma = \frac{\text{Tr}(A^T \cdot A)}{\text{Tr}(H)} \quad (5.8)$$

This approach has been implemented in a DELPHI code, according to the following flow chart (figure 5.12).

สถาบันวิทยบริการ
จุฬาลงกรณ์มหาวิทยาลัย

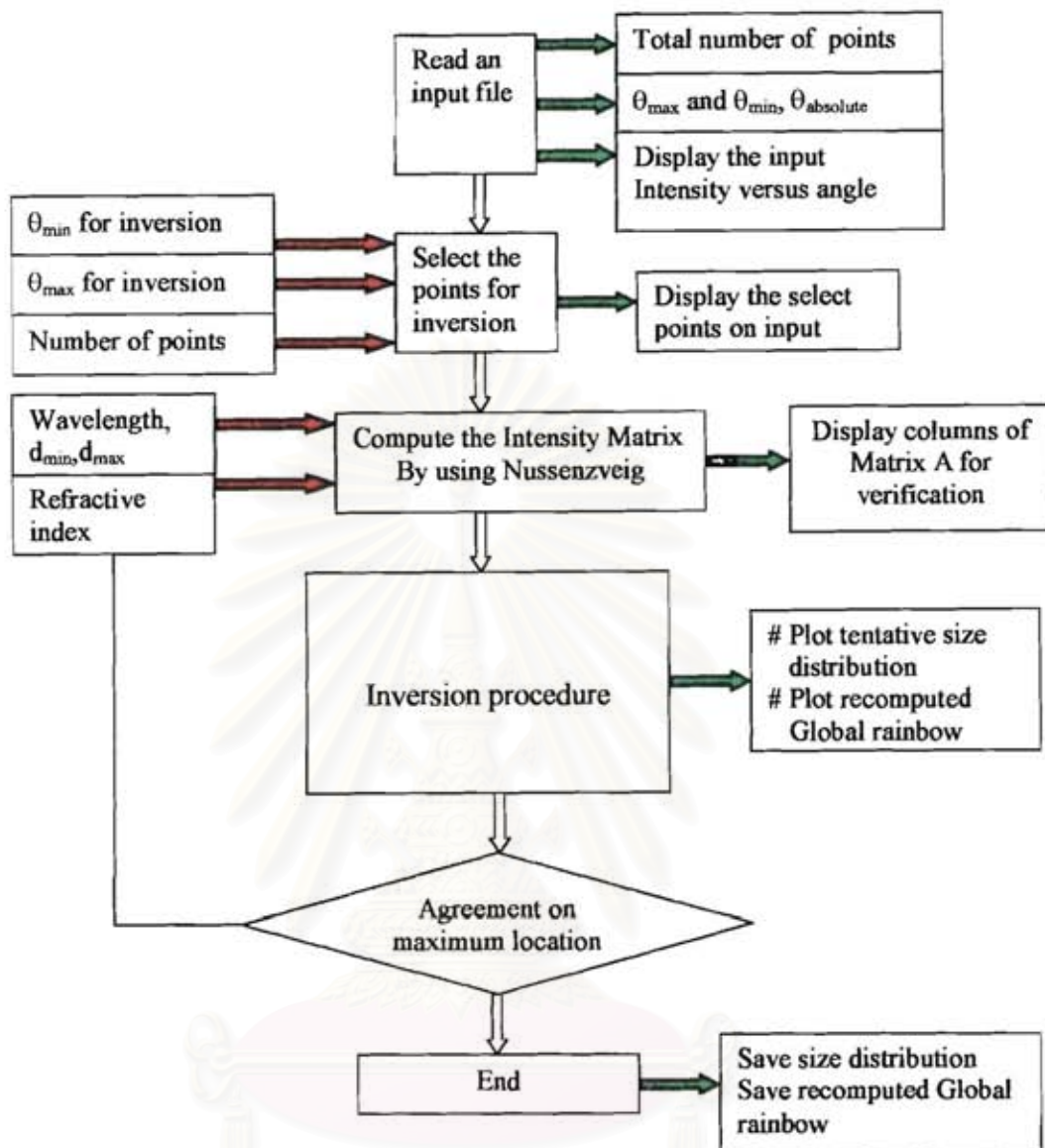


Figure 5.12: The Inversion code flowchart.

Figure 5.13 displays a view of the code interface. The quality of the inversion procedure has been tested by inverting computed global rainbow patterns. The global rainbow patterns recomputed from the results of the inversion (refractive index and size distribution in a finite number of classes) always correspond satisfactory with the original one. Figure 5.14 compares some original distributions with the ones extracted with the non negative least square code. It is critical to note that the inversion procedure is carried out in less than 1sec., opening the possibility of real time measurements of particle temperature and size distribution.

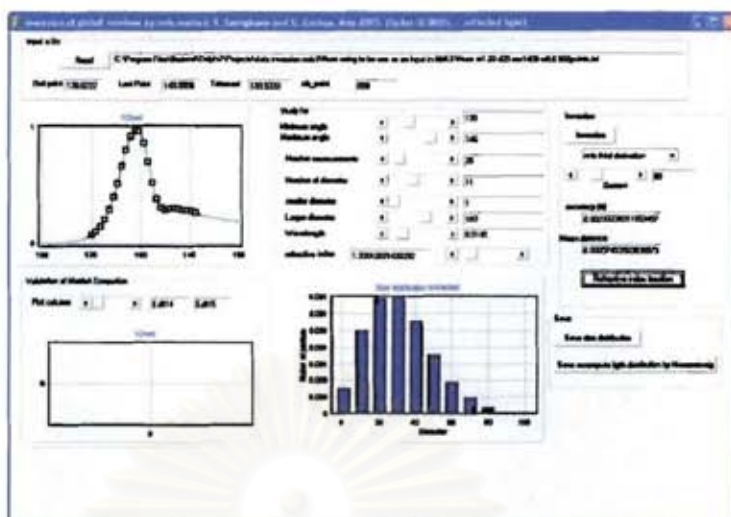
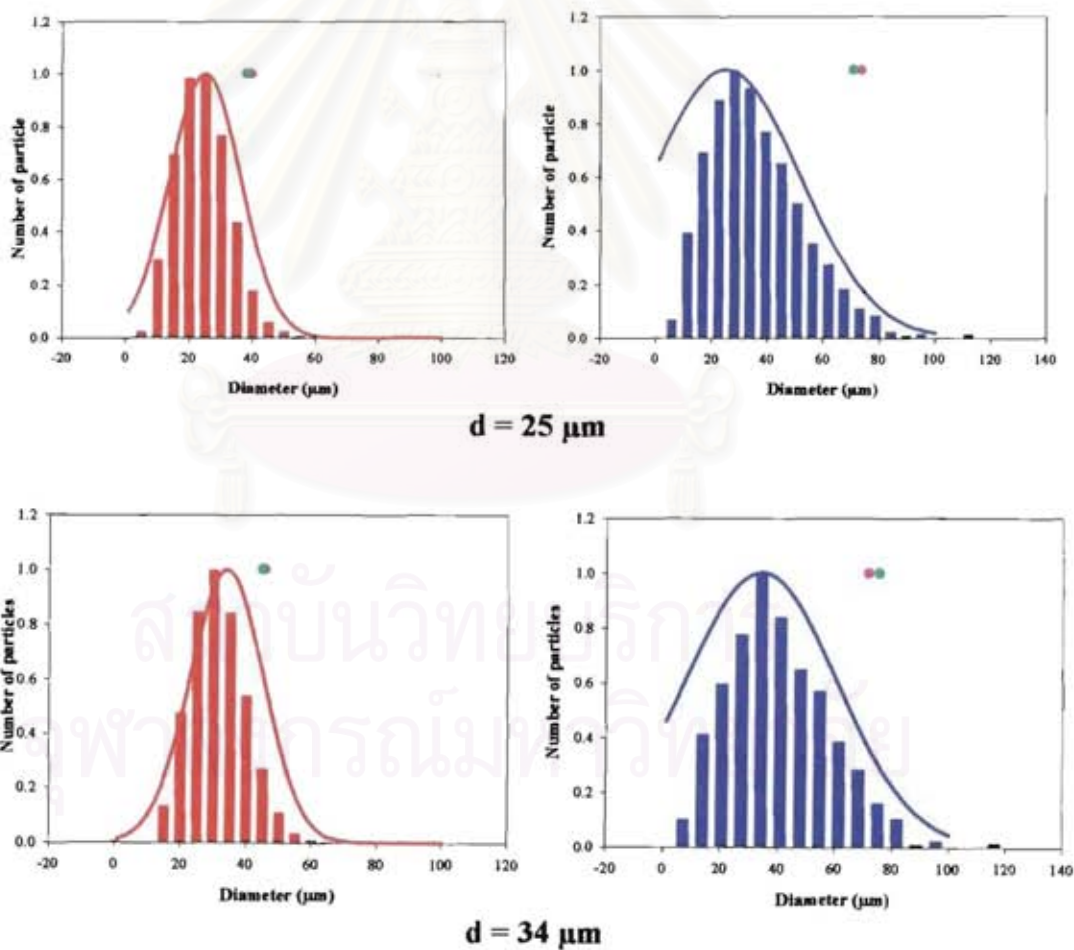


Figure 5.13: The global rainbow inversion code interface.



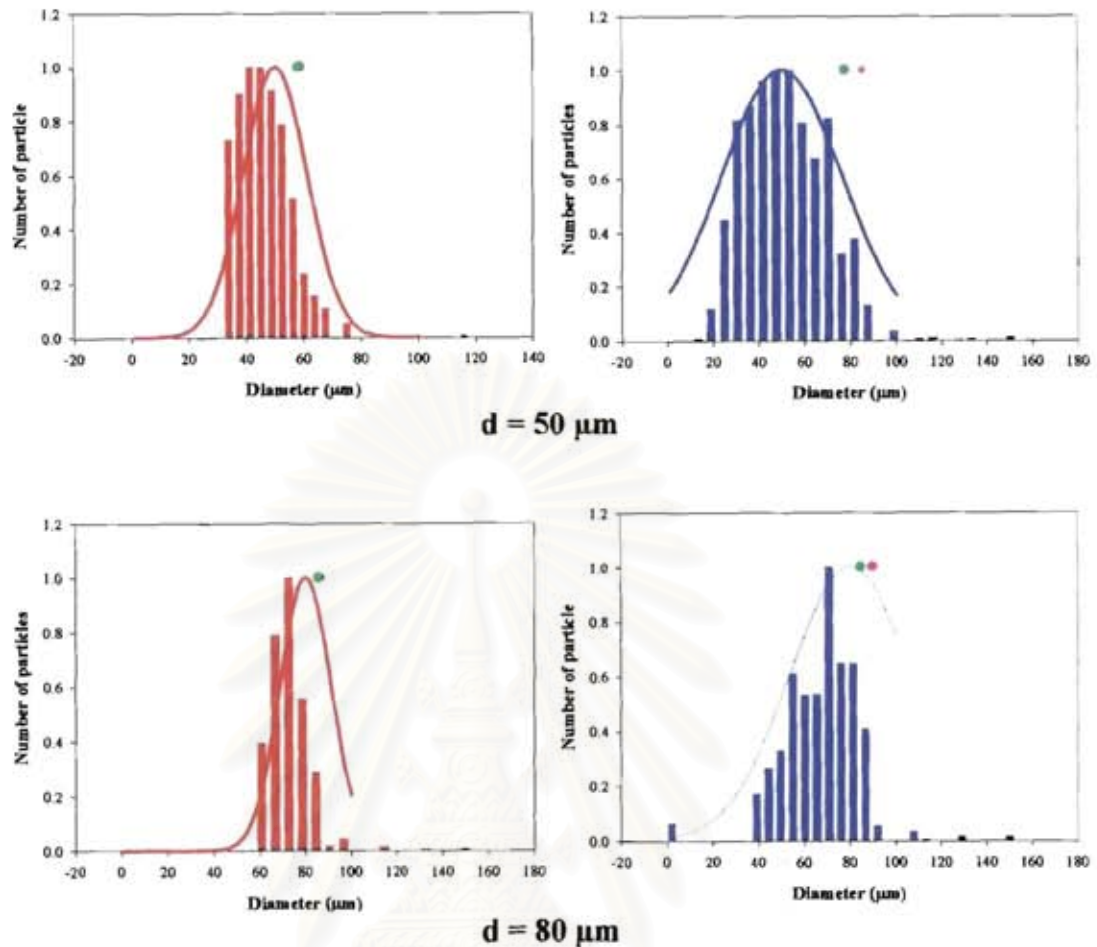


Figure 5.14: The extracted size distribution (histograms) compared to the initial size distribution (continuous lines).

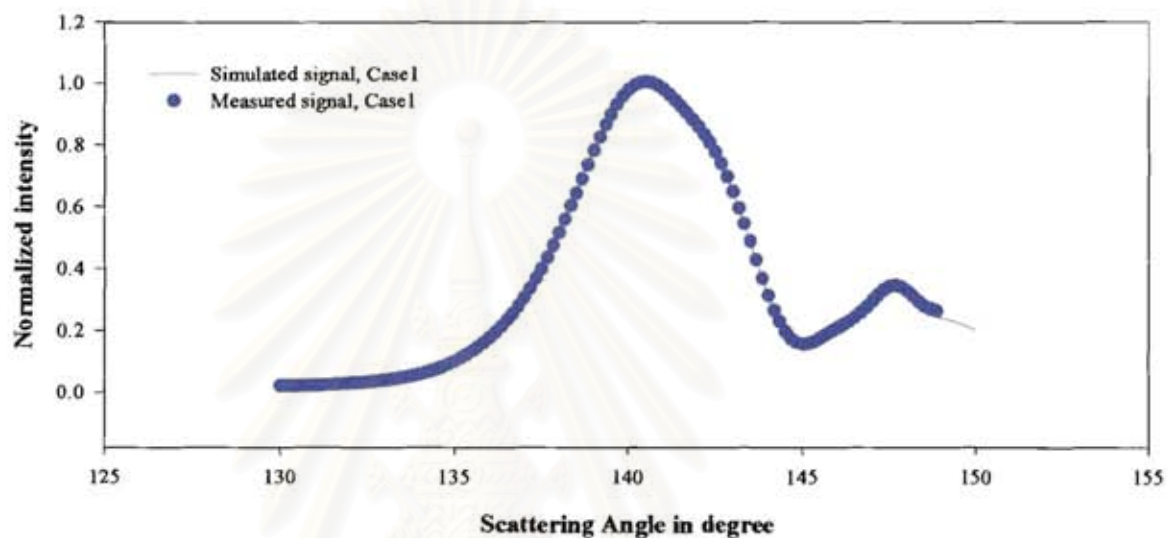
Figure 5.14 compares the extracted size distributions, represented by histograms, with the initial size distributions, represented as continuous lines. The general behaviours are well obtained but the extracted size distribution underestimate the initial size distributions. The points correspond to extracted mean diameters based on two singular points as described in the previous section. The green point corresponds to D_{Airy_infl} while the pink one corresponds to D_{Airy_maxi} . Table 5.2 compiles the refractive indices extracted for the different size distributions.

Table 5.2 The extracted refractive indices from simulated signal by assuming that the size distribution is the Gaussian distribution.

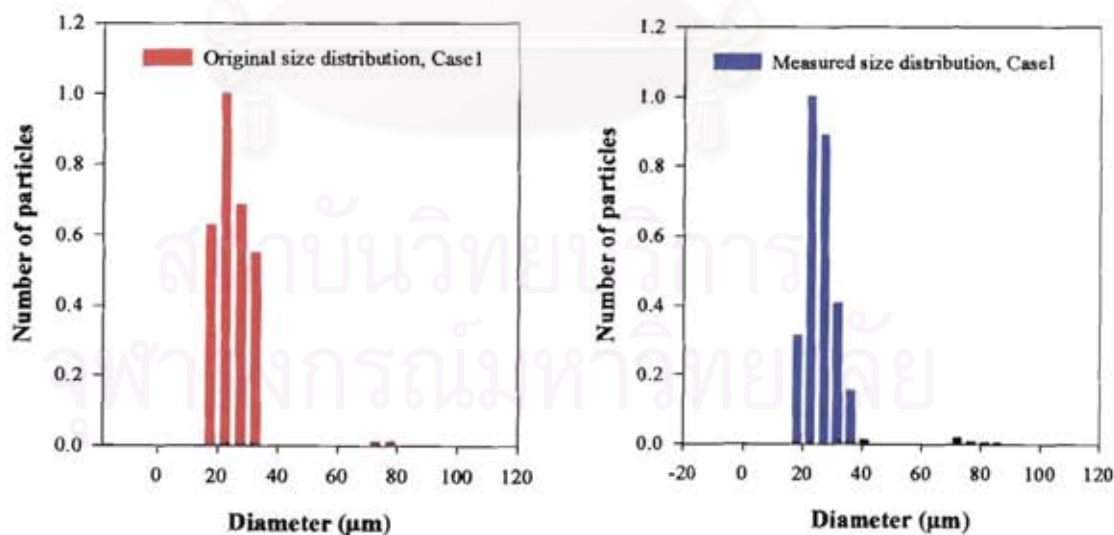
Mean size	rms	Refractive index
25 μm	250	1.3308
25 μm	1400	1.3302
34 μm	250	1.3304
34 μm	1400	1.3308
50 μm	250	1.3306
50 μm	1400	1.3305
80 μm	250	1.3308
80 μm	1400	1.3307

The same study has been carried out but for arbitrary distributions (no Gaussian law). The objective was to estimate the potential of the inversion procedure to inform on the presence of multimodal distributions, and more particularly on the presence of a few big droplets.

Global rainbows have been computed for different arbitrary size distributions. The examples given in the next three figures demonstrate that, with our algorithm, it is possible to characterize sprays with complex size distributions. Table 5.3 compiles the extracted values of the refractive indices, which are also in good agreement with the original values.

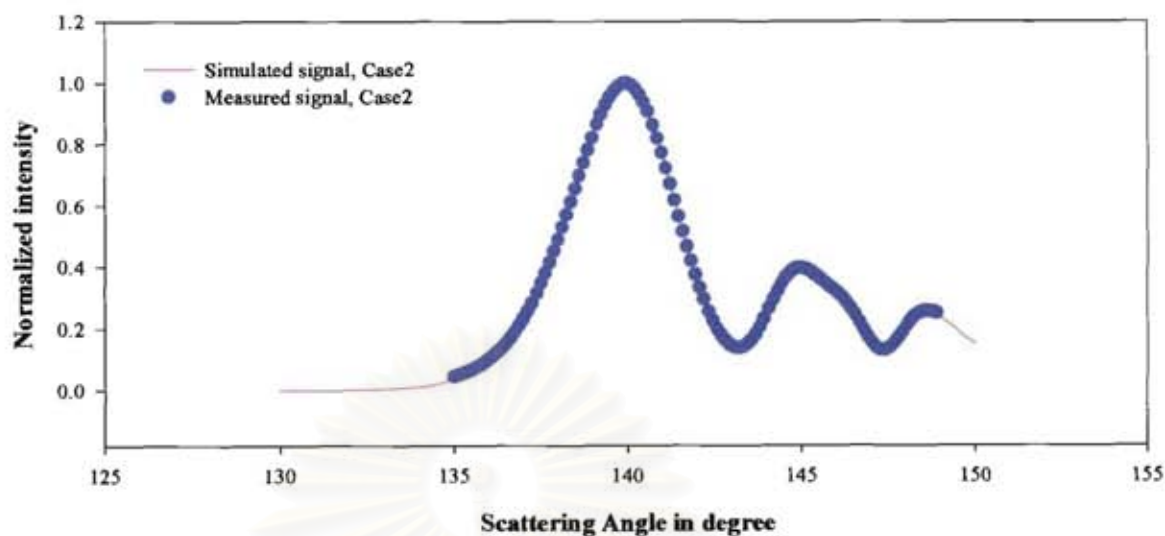


(a)

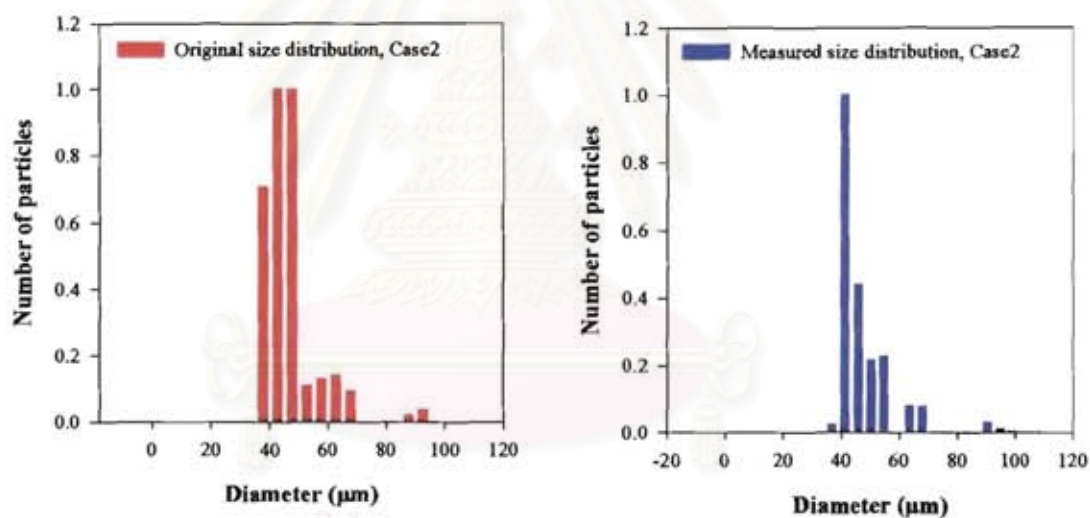


(b)

Figure 5.15: Case 1 (a) The original and reconstructed global rainbow signal
(b) The original (in red) and extracted size distribution (in blue)

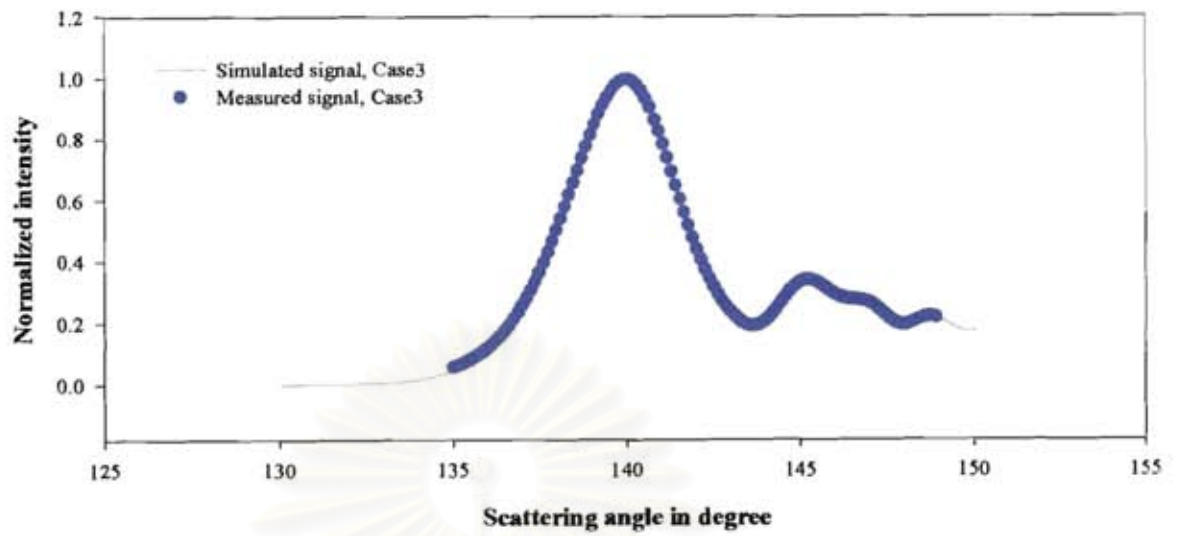


(a)

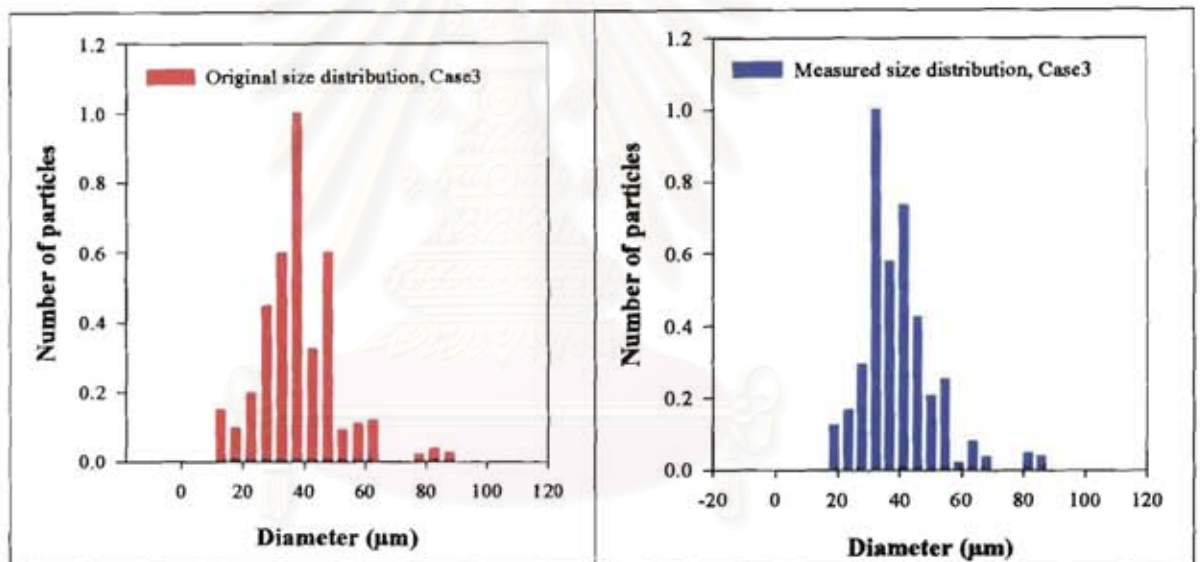


(b)

Figure 5.16: Case 2 (a) The original and reconstructed global rainbow signal. (b) The original (in red) and extracted size distribution (in blue).



(a)



(b)

Figure 5.17: Case 3 (a) The original and reconstructed global rainbow signal.
(b) The original (in red) and extracted size distribution (in blue).

Table 5.3 The extracted refractive indices from simulated signal for arbitrary size distribution with the refractive index equal to 1.333.

Study case	Extracted refractive index
Case No.1	1.33313
Case No.2	1.33328
Case No.3	1.33317

Conclusion

It has been shown that Nussenzveig's theory has high potential to predict the scattered light as accurate as Lorenz-Mie's theory for forward and backward angles. By adding correcting coefficients for predictions at backward region, the range of application of the Nussenzveig's formulae has been increased. Moreover, the computation time is very fast: as fast as Airy's theory, about 300 times faster than Lorenz-Mie's theory. This fact gives the possibility of inverse computations. Then Nussenzveig's theory has been used to fit scattered light by one individual droplet and cloud of droplets.

In the case of individual droplets, the size and refractive index are extracted from dual signals corresponding to a section of the scattering diagram in the forward region (typically between 27 and 33°) and to a section of the section of the scattering diagram in the backward region (typically between 140 and 146°).

For homogeneous particle, it is been proved that the size is measured with an absolute accuracy equal to about 0.01 μm while the refractive index is measured with an accuracy equal to about 0.0001.

For non-homogeneous particle, with a radial gradient, an equivalent particle is measured with the same accuracy. The equivalent particle is a homogeneous particle having the same scattering diagram, in term of frequency and phase (angular position of oscillations) as the particle with radial gradient, including non processed regions as the second rainbow one. Furthermore, when the particle has the gradient strong at the center the measured refractive index can be seen as an average refractive index. While, when the gradient is strong at the surface of the particle, the measured refractive index is always higher than the maximum refractive index value anywhere inside the particle. This effect is a clear signature of the presence of a gradient.

The complete characterization of the gradient will ask for complementary information which could be obtained from numerical codes or other experiments as LIF which is more sensitive to the center of the particle or Infra-red imaging which is only sensitive to the surface temperature of the particle.

In the case of cloud of droplets, only backward scattered light is processed. By using non-negative least square method (nnls) with scattered light computed by Nussenzveig's theory and minimizing the distance between the recorded and the computed global rainbow distribution, a mean refractive index and a size distribution are extracted. The inversion time is smaller than 1 s, giving the possibility to follow the temperature evolution of a section of spray under combustion for example. From the numerical simulations, the accuracy of the refractive index measurement is of about 0.001 to 0.0001, the extracted size distribution is not perfect but good enough to display the main characteristics of the spray.

The next step is to develop an experimental global rainbow set up to measure temperature and size distribution. It is the aim of the next chapters.

CHAPTER VI

EXPERIMENTAL SETUP AND RESULTS

This chapter is dedicated to the realization and to the validation of an experimental global rainbow setup. This chapter is divided in two parts. The first part is devoted to the design of the experimental set up and the calibration, while the second part compiles experimental results. In the first part, the first sub-section presents the elementary optical pieces used, describing the effect of each element and how to align them in order to obtain a good quality for the images to process. The second sub-section describes in detail the calibration procedure which is a key to perform good measurements. The third sub-section discusses the image acquisition and processing. In the second part, the first sub-section is devoted to measurement at ambient temperature of water and ethanol droplets while the second sub-section is devoted to biodiesel measurements without and with combustion.

6.1 Experimental setup

6.1.1 Optic alignments

The global rainbow system is shown in figure 6.1. The experimental setup mainly consists in two parts, emitting part and receiving part. The different components constituting the emitting and the receiving parts of the experimental setup will be explained in the following sections.

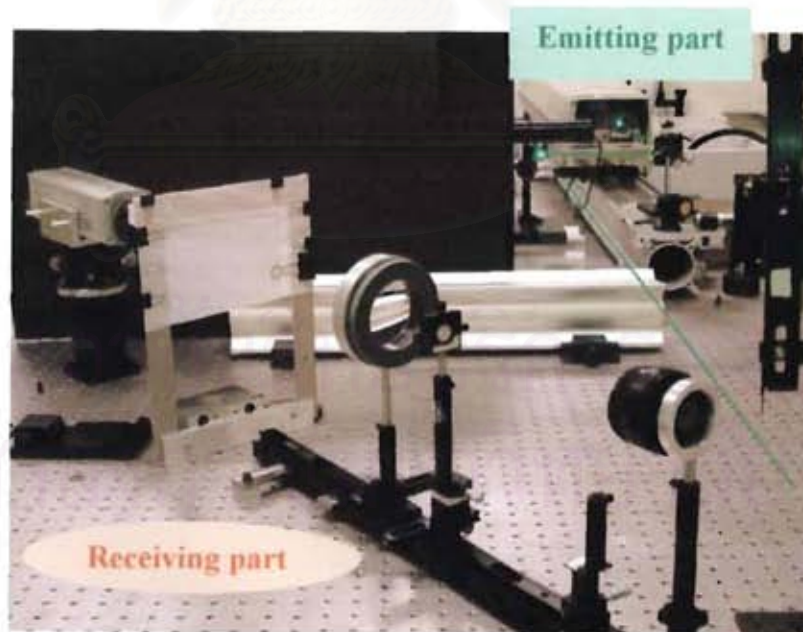


Figure 6.1: *The experimental global rainbow set up realized.*

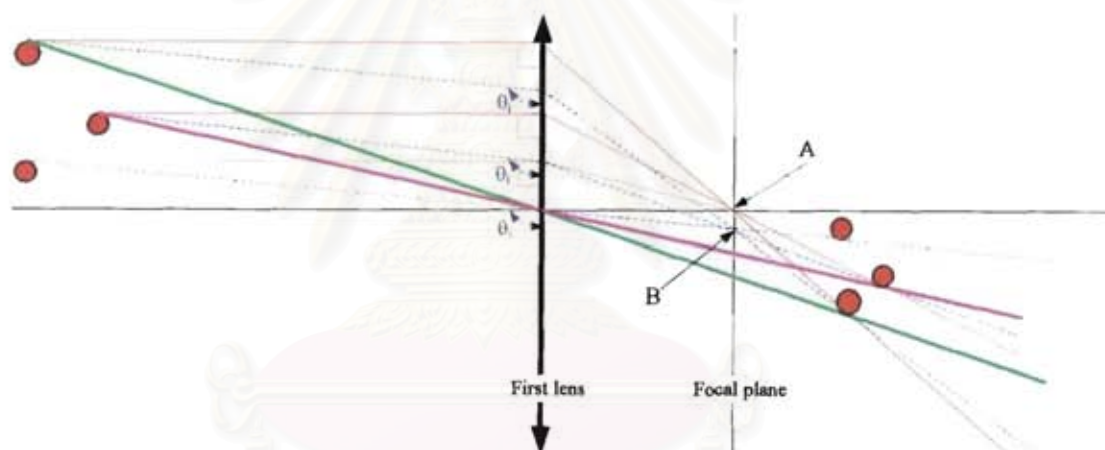
- **Emitting part** : A continuous wave Argon laser is used: spectra physics 2016. The laser emits a beam with a diameter equal to 1.6 mm and a wavelength equal to 0.5145 micron. The power is equal to about 1 Watt. To direct the laser beam in the proper direction mirrors are used.

➤ **Receiving part** : The receiving part consists of a compound of two spherical lenses, a diaphragm and CCD camera.

The compound lens

The compound lens combines a camera objective (focal length $f=50$ mm, diameter $d=20$ mm) with a plane-convex lens (focal length $f=150$ mm, diameter $d=100$ mm).

A camera objective is used to collect the scattered light in the solid angle sustained by an angular range of about 20 degrees. The second lens conjugates the image focal plane of the first lens on the observation screen. Each position at the focal plane corresponds to a definite incident angle on the lens. For different particles, the scattered light impinging on the lens with the same angle is located at the same position on the focal plane as shown in figure 6.2. Taking an image at this position is just only one way to measure the global rainbow signal because for all other positions the signal will be deformed due to the mixing of different light coming from different scattering angle.



Point A => corresponding to the scattered light from every particles which impinging on the lens with the angle of 90°

Point B => corresponding to the scattered light from every particles which impinging on the lens with the angle of θ_1°

Figure 6.2: Schematic of the scattered light behavior at the focus plane.

In addition, when measuring a spray, the rainbow position can move according with the location of the particles in the laser beam, even though all of the droplets have the same properties. This can make a mistake or misunderstanding for interpretation. To prevent this problem a diaphragm is used to select a part of the spray. Furthermore, the fact to select only a part of the spray permits to have particles with close properties (size and refractive index) and to measure the evolution of these properties inside of the spray.

A diaphragm

A diaphragm is used to select and define the measurement volume. This will let only the selected scattered light from the measurement volume pass and lock

undesirable ambient light as shown in figure 6.3. The diaphragm is located at the image plane of the camera objective. The diameter of a diaphragm is equal to 2 mm.

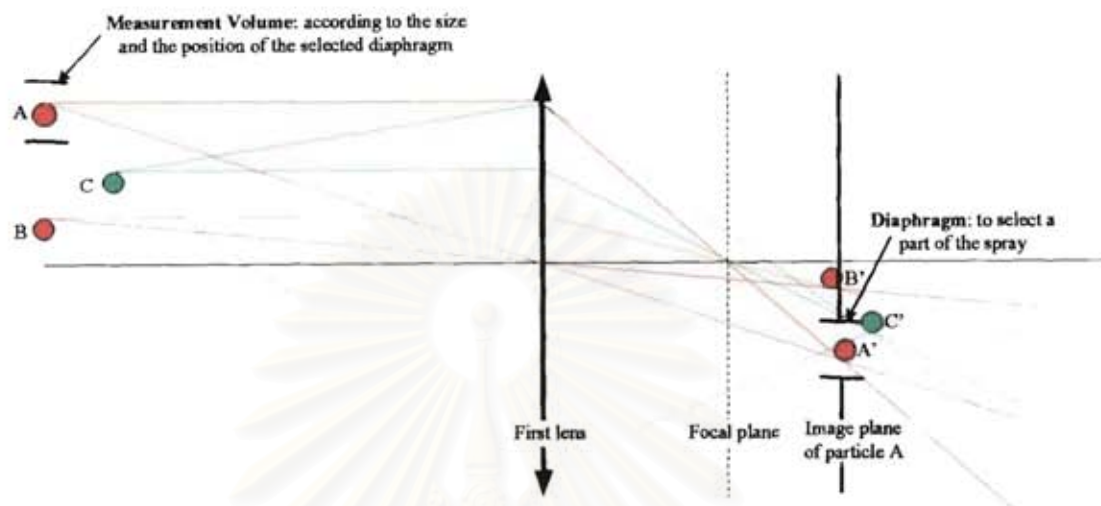


Figure 6.3 The effect of diaphragm.

CCD camera

The global rainbow patterns are recorded by a Kappa CCD camera: 2h20, black and white with 1400 pixels by line and 1050 lines (figure 6.4). The intensity is recorded with 12 bits. The exposure time can be adjusted between 110 μs and 4000 sec. The camera is connected with the PC by 1394 connector to acquire and process the images. The image processing is carried out by homemade software developed under Delphi. The software will be described in a next section.



Figure 6.4: Kappa CCD camera.

When the adjustment is finished the next step is to calibrate the experimental setup, that is to say find the relationship between pixels and absolute scattering angles which is the objective of the following paragraph.

How to do the alignment?

The alignments are made by carrying out the following operations;

1st: laser beam adjustment: adjust the laser beam to horizontality at the good working level by using the water level.

2nd: adjust the collection solid angle: the first lens is placed at the position which permits to record the scattered light on the solid angle sustained by an angular range of about 20° around the rainbow angle.

3rd: finding the focal plane of the first lens: with the parallel white light source located at far as possible from the first lens and a semi transparent screen, the focal plane is located. The focal plane corresponds to the position of the screen for which the spot is the smallest and the brightest.

4th : realize the image of the focal plane on the screen: the second lens is placed at the position in which it conjugates the semi transparent screen (which materializes the focal plane) and the final screen. After the adjustment the semi transparent screen is removed.

5th: adjust the liquid jet verticality: Adjust the liquid jet to be perpendicular to the laser beam by observing the scattered light. The scattered light around the particle will be at the same level when the liquid jet is perpendicular to the incident beam.

6th : put the diaphragm at the image plane of the first lens: the liquid jet is backlighted by the white light. The image plane corresponds to the clearest image; at this position the image does not move if the white light source is moved.

7th : Camera location: the CCD camera with the objective $f=50$ mm is located in order to record the full rainbow image. A special care is that the lines of the camera must be parallel to the scattering plane. If it is not the case, the recorded intensity/pixel function will not be a simple function of the scattering angle.

จุฬาลงกรณ์มหาวิทยาลัย

6.1.2 Calibration

As the rainbow technique is based on the measurement of the absolute location of the light scattered around the rainbow angle, it is essentially to know the absolute angular location of each pixel of the camera. To do the calibration, one way is to record the light scattered by a liquid jet which is assumed to be perfectly characterized in size and refractive index. After that the scattered light is computed for the same size and refractive index. Then the relationship between pixels and angles is obtained by identifying the position of the maximum intensity of each Airy peak.

➤ **Characterization of the liquid jet:** To create the liquid jet, a cylindrical metallic pipe with the inner diameter of about 0.6 mm and the length of about 30 cm is used. The liquid flow rate can be controlled by flow meter. A far field microscope (infinity) is used to measure the size of the liquid jet. Figures 6.5 and 6.6 display the magnification scale and an example of the liquid jet image recorded by microscope respectively.

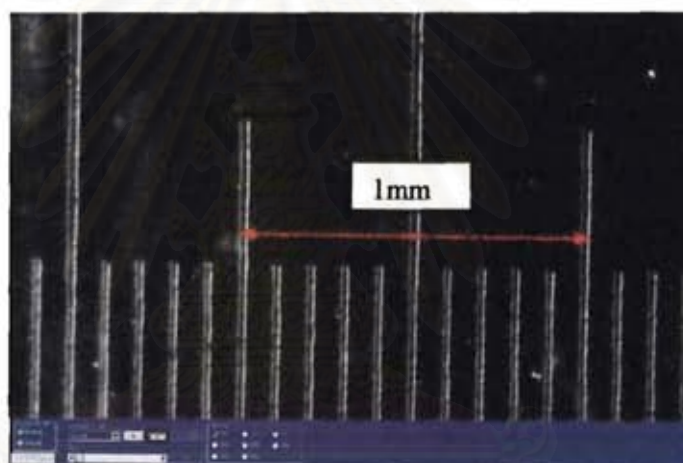


Figure 6.5: The magnification of the microscope.

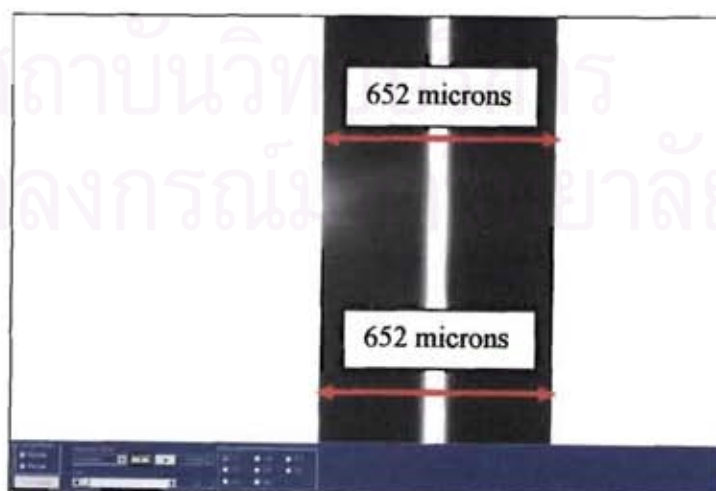


Figure 6.6: Liquid jet image at the flow rate of 60 cc/min.

Figure 6.6 shows that the liquid jet has a constant diameter along the measured range.

The size of the liquid jet is a function of the liquid flow rate as shown by the results in table 6.1.

Table 6.1: The liquid jet diameter measured for the different liquid flow rates.

Flow rate	Liquid jet Diameter (For scale of 6.9 cm: 1mm)
55 cc/min	645 μm
60 cc/min	652 μm
65 cc/min	652 μm
70 cc/min	659 μm
75 cc/min	659 μm
80 cc/min	659 μm
85 cc/min	666 μm
90 cc/min	666 μm

➤ **Relationship between pixels and angles:** The experiment has been realized under the following conditions:

Calibration conditions

- Liquid: Water
- Liquid flow rate: 60 cc/mm corresponds to the diameter: 652 μm
- The liquid temperature: 20°C corresponds to the refractive index: 1.333

The light distribution scattered by the liquid jet has been recorded as shown in figure 6.7. The red line is the raw recorded scattered light signal, while the green line is the filtered signal used to facilitate the localization of the maximum of each Airy peak as displayed by the yellow points. The computed scattered light distribution with the same properties as the liquid jet has been determined as shown in figure 6.8.

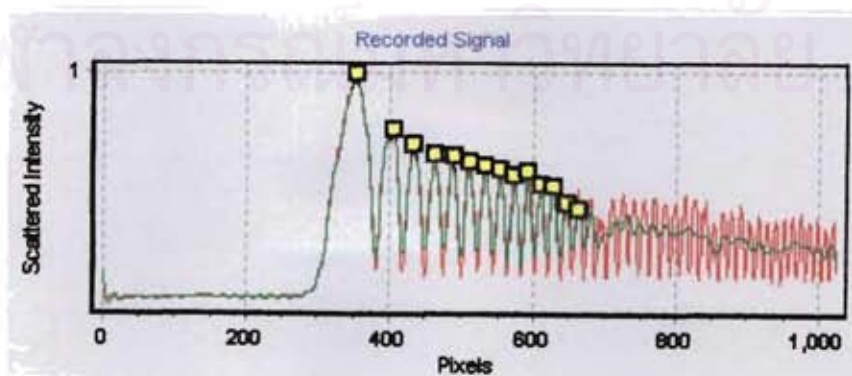


Figure 6.7: Recorded signal from the liquid jet.

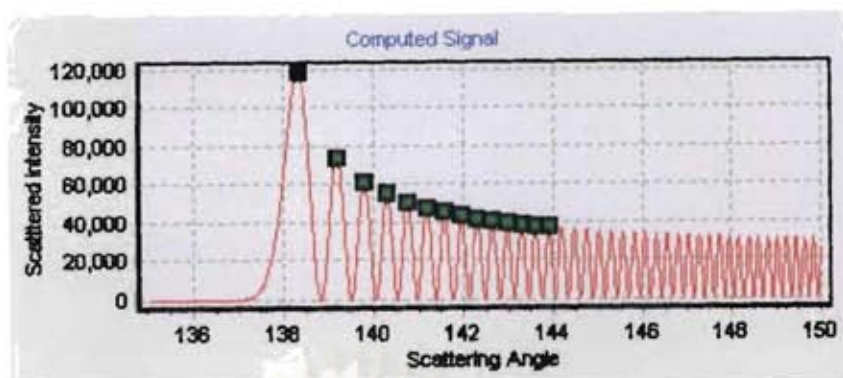


Figure 6.8: Computed signal by the liquid jet.

By identifying the position of the maximum intensity of each Airy peak from the recorded and computed signals, the relationship between pixels and angles is obtained as shown in figure 6.9.

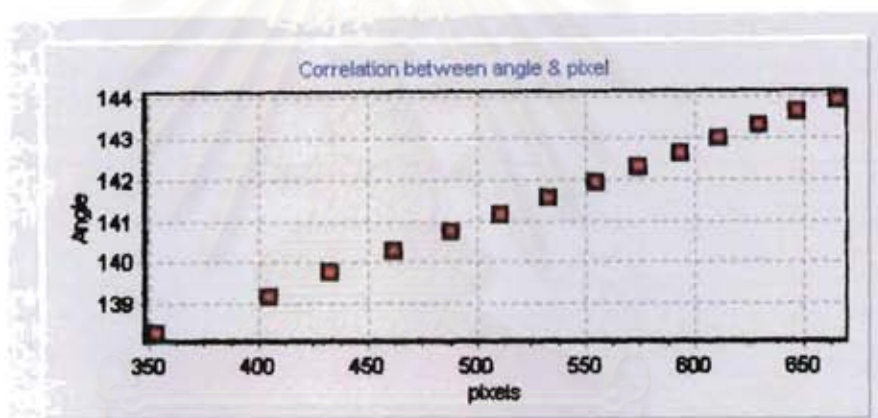


Figure 6.9: Relationship between pixels and scattering angles.

The calibration curve gives the linear relationship between pixels and scattering angles. For this case, the correlation is given by;

$$\text{Angle} = 131.966 + 0.018 * \text{pixel}$$

This optical configuration is able to collect the scattered light from 131.985° to 154.301° (for 1400 pixels).

As the rainbow refractrometry is based on the absolute angular measurement its accuracy depend on the quality of the calibration. Then the calibration must be done for each experiment. As the consequence a code has been dedicated for this task which now can be run in less than 1 minute. Figure 6.10 displays the screen of the calibration code.

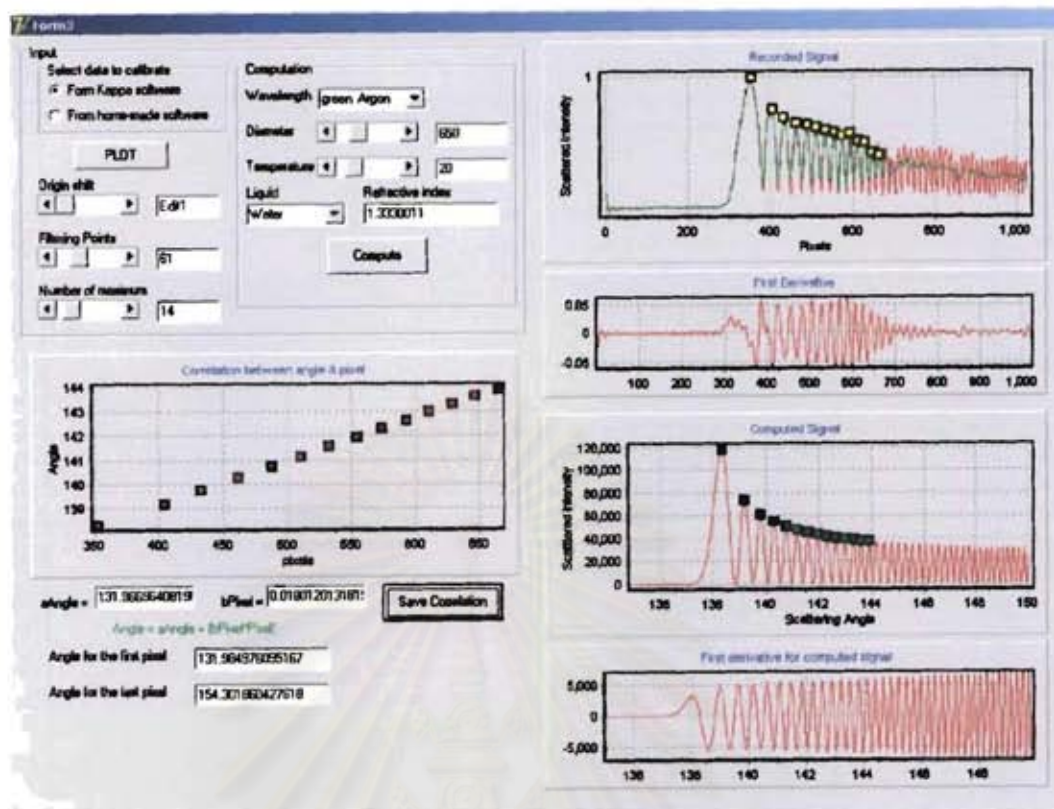


Figure 6.10: The calibration code.

6.1.3 Image acquisition and processing

Now we have to record an image with the good parameters, transform the recorded image to a global rainbow pattern, and extract the information on size distribution and refractive index from the recorded global rainbow pattern.

Image acquisition: the connection 1394 permits the communication between the camera and the computer. The camera accepts input from the computer which gives the possibility to adjust: the exposure time, the gain, the binning and the region of interest. Two programs are used: One is “Data image” from Kappa, another is the homemade code.

- Data image software records image of 1250 pixels by 1050 lines. This software is essentially used to record images which are processed to quantify the effect of the integration on the global rainbow signal.
- The homemade software reads image of 1400 pixels by an user selected number of lines and directly plot and save intensity versus pixel. This recorded light distribution is directly processed to obtain the size distribution and the refractive index.

In all cases, the camera gives an image which is basically the intensity recorded by each elementary pixel. Such an image can be seen as a matrix where the value of element ij is the intensity of the pixel at the j^{th} line, i^{th} column. When the

camera is well adjusted, all the pixels of the i^{th} column record light scattered at the same scattering angle. Then these elements can be added together, defining an integration zone, to obtain the rainbow pattern. Nevertheless, the assumption that the pixels of a column collect light scattered at the same scattering angle can be valid only on a finite domain. The experimental definition of this domain is carried out in the next section.

Definition of the optimum integration zone.

By using data image software, the images of the light scattered by liquid jet and spray have been recorded as shown in figure 6.11 and 6.12 respectively.



Figure 6.11: Image of the scattered light by liquid jet used for calibration.

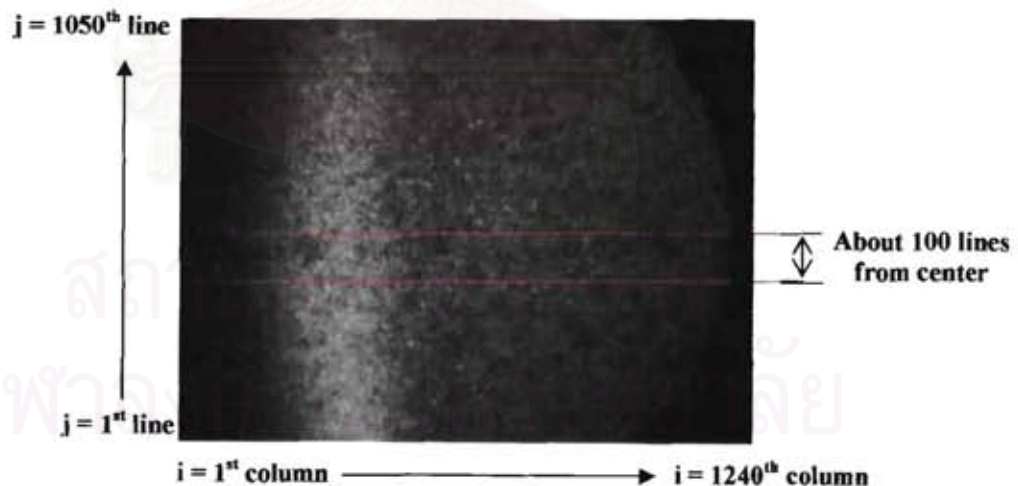


Figure 6.12: Image of the scattered light by water spray.

In order to be able to process accurately the recorded images it is necessary to know the optimum integration zone which will produce signals with the minimum of noise and with the maximum of visibility. A special attention will be given to the effect of the curvature of the first fringes, clearly visible in figure 6.12 and on the behavior of the fast increasing part of the global rainbow because of the sensitivity of the measured refractive index to it.

Images in figure 6.11 and 6.12 have been recorded from the same optical configurations. The study of image in figure 4.11 shows that the line 510 is the most intense. First, we study the effect of increasing the number of lines used for integration symmetrically around line 510th. Figure 6.13 displays the results of different sizes of integration zone running from 20 to 640 lines. For an integration zone of 20 lines, the scattering diagram is characterized by a high level of noise. When the number of lines increases the noise level decreases but the visibility of the second peak (around pixel of about 600-700) decreases. This can be see clearly in figure 6.13 (b) where the noise has been suppressed by FFT filtering. An optimum integration can be defined to have between 80 to 160 lines centered on the liquid jet diagram (line 510 in this example). Next, we study the effect of the position of the integration zone in the image. Figure 6.14 (a) displays three curves, corresponding to the global rainbow patterns extracted from lines 1-81, 470-550 and 944-1024 respectively. Figure 6.14 (b) represents the filtered signals. The location of the maximum of intensity is essentially not affected; but the increasing part of the rainbow pattern is shifted to large scattering angles for the 1-81 and 944-1024 zones. Furthermore the tail of the rainbow pattern (between pixels 500-1000) is strongly affected. The strong decrease of the intensity after pixel 1100 for the 1-81 and 944-1024 zones is due to the lens.

These facts confirm that the integration zone must be centered on the position of the liquid jet rainbow and limited in its dimension. In this thesis an integration zone of 100 lines centered on the position of the liquid jet rainbow is used to obtain global rainbow patterns.

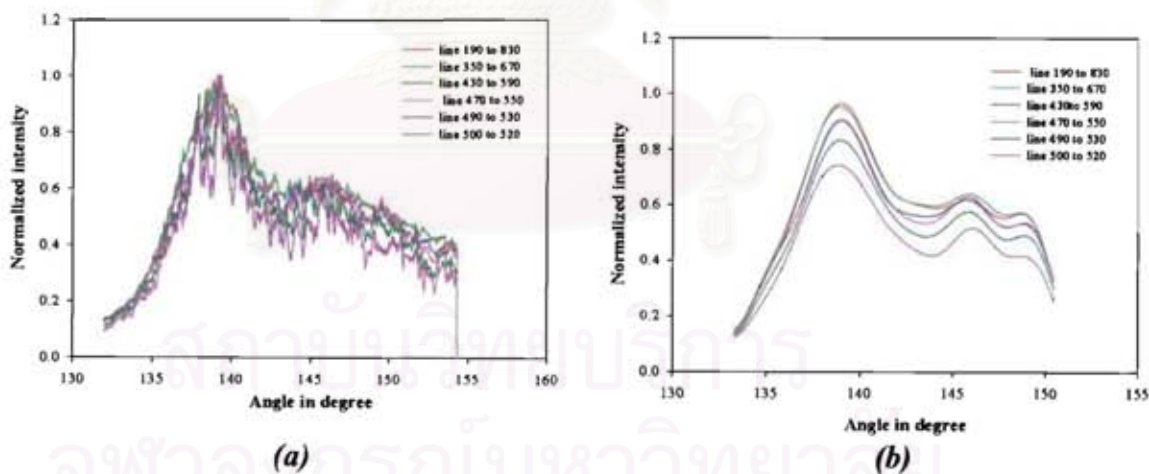


Figure 6.13: Original and filtered global rainbow signals with different dimensions of the integration zone.

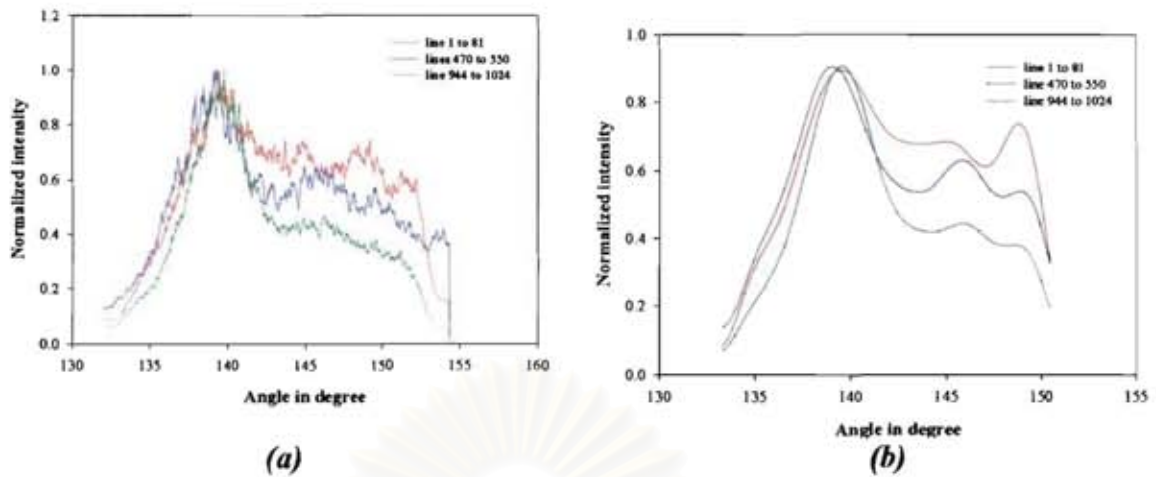


Figure 6.14: Original and filtered global rainbow signals with different positions for the same dimension of the integration zone.

The global rainbow patterns can be transferred to the inversion code as introduced and explained in section 5.2 to extract the refractive index value and the size distribution.

สถาบันวิทยบริการ
จุฬาลงกรณ์มหาวิทยาลัย

6.2 Exemplifying results

6.2.1 Spray temperature measurement at ambient temperature

The liquid jet with the flow rate equal to 60 cc/min and the temperature equal to 20°C is used to calibrate the experiments. Figure 6.15 displays two images of the scattered light by the liquid jet, taken before and after the experiments. The two signals look nearly identical.

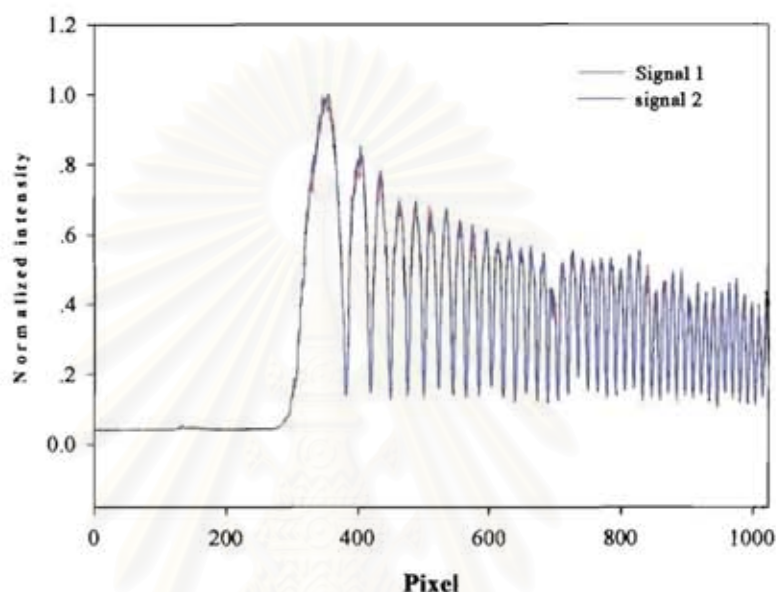


Figure 6.15: The light scattered by a liquid jet for calibration. Comparison before and after the series of experiments.

Nevertheless, when doing the calibration procedure, some slight differences appear due to the high frequency noise. For the first signal, the sixteen first maxima can be used for the calibration while for the second signal only the 13 first maxima can be used for the calibration. Figure 6.16 displays the two series of points used for the calibration with a linear regression. The two series of points are very close and well fitted by the linear regression. The location of geometrical optics rainbows for water and ethanol are materialized by arrows.

สถาบันวิทยบริการ
จุฬาลงกรณ์มหาวิทยาลัย

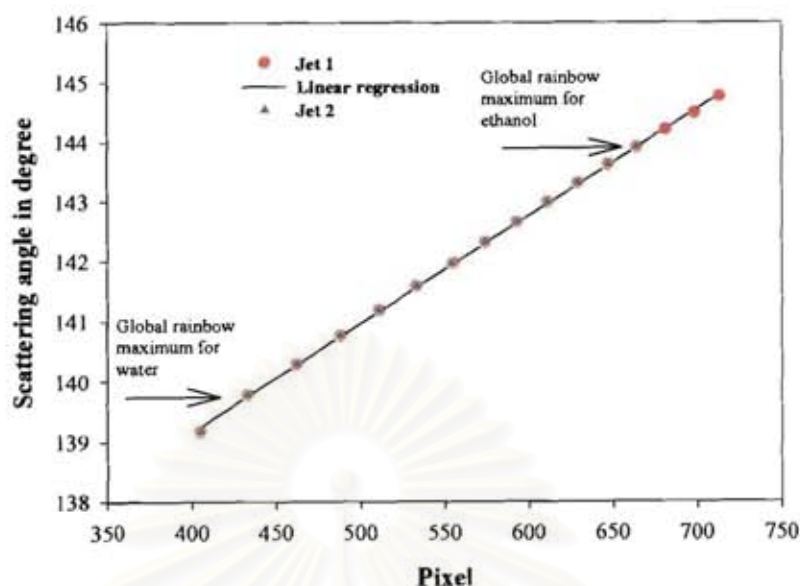


Figure 6.16: The calibration points and linear regression before and after the experiments.

Nevertheless, the linear regressions computed from these two cases differ a little bit. For the first case the relation is:

$$\text{Angle} = 131.97000 + \text{pixel} * 1.800 \cdot 10^{-2} \dots\dots\dots(\text{calibration 1})$$

While, for the second case, the following relation is obtained:

$$\text{Angle} = 131.96112 + \text{pixel} * 1.8028 \cdot 10^{-2} \dots\dots\dots(\text{calibration 2})$$

Then, this configuration gives the possibility to collect the scattered light between about 131.96° up to 150.40° for the first 1024 pixels, with a collecting angle equal to about 18.5° , or from 131.96° to 154.29° for the first 1240 points, or 131.96° to 157.17° for 1450 points, depending on the software used. The integration zone used to process the recorded global rainbow image is the position centered around liquid jet location with dimension of about 100 lines.

Water and ethanol spray have been created by an ultrasonic nozzle with the frequency equal to 70 kHz. The measurement is located at about 1 cm far from the orifice of the nozzle. Figure 6.17 exemplifies recorded global rainbow patterns by a section of water and ethanol spray and their scattered light distribution. The shift between water and ethanol is evident, corresponding to about $4\text{-}5^\circ$.

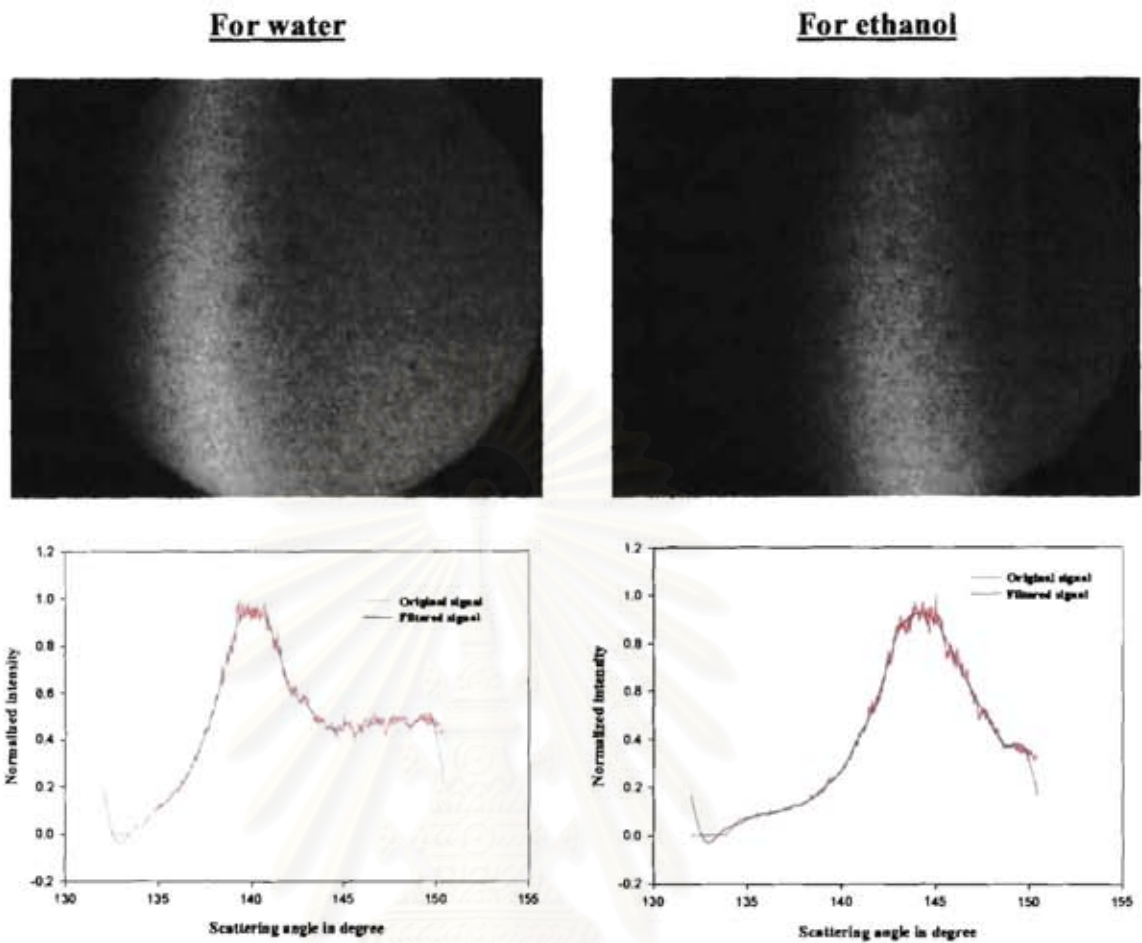


Figure 6.17: The recorded images of the scattered light by water and ethanol sprays and their scattered light distributions.

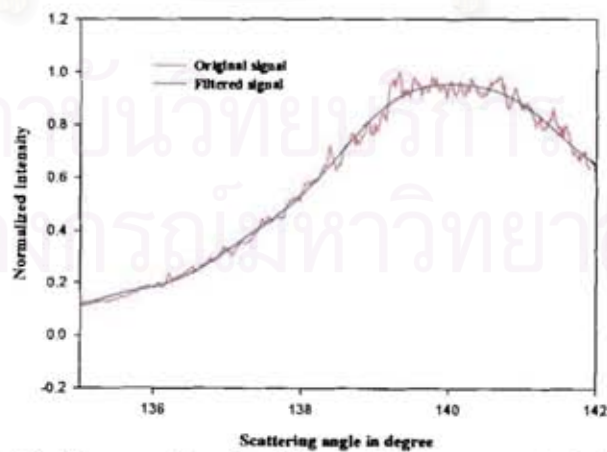


Figure 6.18: From enlarging figure 6.17 to exemplify the filtering.

By using the non-negative least square method based on Nussenzveig's theory, the size distribution and the refractive index are extracted.

Table 6.2 shows the extracted refractive index values of water and ethanol. A first remark is the stability of the extracted refractive index and associated temperature for the water and ethanol, with nearly no sensitivity to the calibration equation, realized before and after the series of experience. For each product a stable temperature is extracted. It will be noted that the confidence is better for the absolute refractive index and temperature values for water than for ethanol, as the water global rainbows are interpreted in the angular region where the calibration is carried out.

Table 6.2 *The measured refractive index values of water and ethanol sprays, for the two linear regressions, at short and large distance of the nozzle, at close and long distance of the nozzle*

Case at 1 cm	Refractive index, from Calibration 1	Associated Temperature (°C)	Refractive index, from Calibration 2	Associated temperature (°C)
Water, case1 (1 cm)	1.332231	27.15	1.332225	27.08
Water, case2 (1 cm)	1.332254	26.9	1.332295	26.5
Water, case3 (1 cm)	1.332751	22.4	1.332754	22.38
Ethanol, case1 (1 cm)	1.356798	38.78	1.356551	39.43
Ethanol, case2 (1 cm)	1.357301	37.45	1.357195	37.73
Ethanol, case3 (1 cm)	1.355455	37.73	1.357384	37.23
Case at 10 cm	Refractive index, from Calibration	Associated Temperature (°C)		
Water, case1 (10 cm)	1.3329	20.2°C		
Ethanol, case1 (10 cm)	1.3621	24.7°C		

In table 6.2, it is notable that the temperature measured close of the orifice are high and very different for water and ethanol. Several phenomena can explain this behavior:

1. The working temperature of ultrasonic nozzles is high : about 80-90°C. Then the liquid will be heat up in the nozzle but this heat up is a function of the physical properties of the liquid.
2. When created, the droplet temperature will evolve also differently according with the liquid properties.
3. Close of the orifice, gradient of temperature can exist in the droplets.

On the contrary, when far of the orifice (at about 10 cm) the temperature of the water and ethanol droplets are closer and nearly equal to the ambient air temperature.

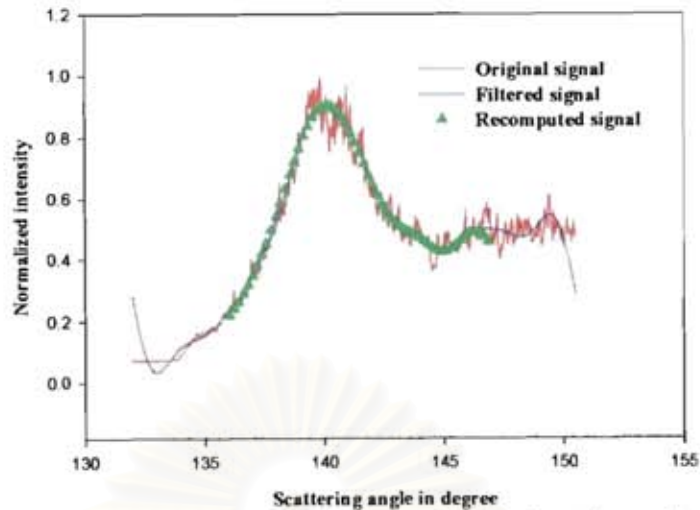


Figure 6.19: Comparison between the original global rainbow, the filtered one and the recomputed one with the extracted refractive index and size distribution. Case water 1 of table 6.2.

Figure 6.19 compares the original recorded global rainbow signal (in the red line), the filtered one (in blue line) and the recomputed one as green triangles. The agreement between the three global rainbows is very satisfactory in the angular domain of interest.

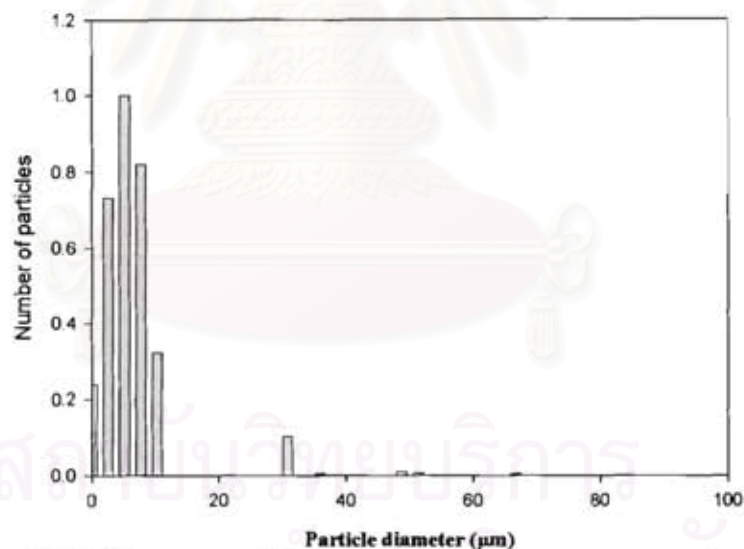


Figure 6.20: The extracted size distribution for water, case 1 of table 6.2.

The measured size distribution for water, case 1 of table 6.2, is displayed in figure 6.20. The extracted size distribution is representative of the size distributions extracted for all the studied cases. That is to say, for the experimental cases, an overestimation of the small particles is obtained, in opposition with the numerical study. This overestimation is not yet perfectly understood but it is assumed to be due to a light background. Nevertheless, as this overestimation of the importance of the small particles looks to have no effect on the refractive index determination, that is to say on the temperature measurement, we will continue the study focusing our attention only on refractive index measurements.

6.2.2 Biodiesel spray temperature measurement in combustion

Biodiesel (fatty acid alkyl esters) is a cleaner burning diesel replacement fuel made from natural, renewable sources such as new and used vegetable oils and animal fats. The production of biodiesel, or alkyl esters, is well known. As recall in the introduction, there are three basic routes to ester production from oils and fats. The majority of the alkyl esters produced today are done with the base catalyzed reaction because it is the most economic. Biodiesel can be used alone (B100) or blended with petroleum diesel in any proportion. Blends of up to 20% biodiesel (mixed with petroleum diesel fuels) can be used in nearly all diesel equipment and are compatible with most storage and distribution equipment. These low-level blends (20% and less) generally do not require any engine modifications.

Biodiesel used in this work is produced from palm oil by transesterification process whereby the glycerin is separated from the palm oil. The process leaves behind two products -- methyl esters (the chemical name for biodiesel) and glycerin (a valuable byproduct usually sold to be used in soaps and other products). The physical properties of different blending of biodiesel with diesel (by volume), measured in the laboratory, are displayed in table 6.3.

Table 6.3: *The liquid properties of different biodiesel concentrations*

Liquid	Density (g/ml)	Surface tension(mN/m)	Viscosity (mPa.s)
B5%	0.804	26.61 ± 0.33	4.19
B10%	0.806	26.82 ± 0.34	4.38
B15%	0.818	27.14 ± 0.2	4.53
B50%	0.824	27.75 ± 0.22	5.10
B100%	0.842	29.37 ± 0.44	7.09
Diesel	0.800	26.66 ± 0.37	4.13

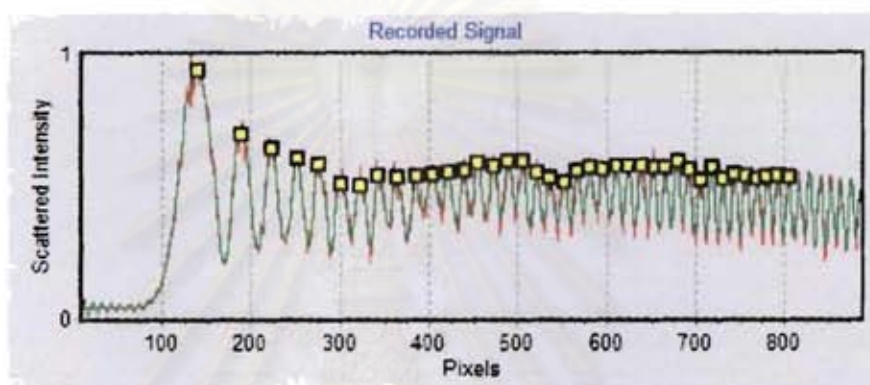
The measurement of the temperature and/or the composition of real fuels during combustion is a challenge. For a combustion in a flame with droplets of hexane/tetradecane or kerosine, according with Kneer et al [42] or Bachalo et al [43], the refractive index runs typically from about 1.45 to 1.3, due to the fact that the heat up induces change of density and composition in the droplets. For biodiesel the refractive index evolution must be of the same order. To these values of the refractive indices correspond geometrical optics rainbow positions equal to 152.31° and 132.86°: about 20° of displacement for the rainbow! The optics configuration has to be adapted to be able to collect the light on a so large angle.

Then this section is organized in two subsections. The first one is an experimental simulation to demonstrate the possibility of accurate global rainbow measurements on a large refractive index range. The second subsection presents measurements in a biodiesel spray flame without additive.

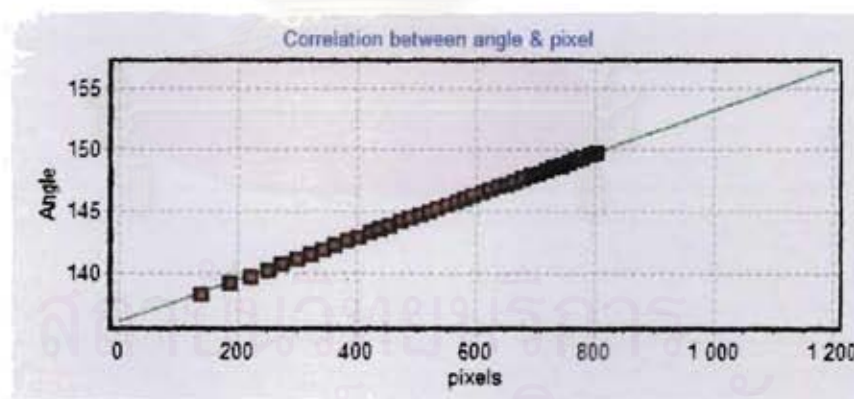
6.2.2.1 *Experimental simulation of combustion measurements.*

To establish the capability of such an optical configuration, the temperature dependence of the refractive index is simulated by using different liquids: water, ethanol and biodiesel. At ambient temperature the refractive indices of these products have been measured by using a refractometry as equal to 1.334, 1.36 and 1.45, respectively.

For this study, the calibration curve is plotted in figure 6.21. Note that up to 39 supernumerary peaks have been identified to compute the relationship between pixel and angle.



(a) the recorded liquid jet rainbow with the 39 supernumerary peaks



(b) The calibration curve determined from 39 supernumerary peaks.

Figure 6.21: Setup calibration for large refractive index range

This configuration gives the possibility to measure the scattered light between 136.104° and 157.306° .

The next step has been to record global rainbow images for the different products. Figure 6.22(a) displays such recorded global rainbow signal. The shift of the global rainbow position with the refractive index is clear. Furthermore, the capability of the developed setup to record the rainbow in a large angular range is proved.

The next step is to extract the associated relationship intensity/angle to be processed from such images. The intensity/angle relationships associated with image 6.22(a) are displayed in figure 6.22(b). The location of the maximum of the main global rainbow peak runs from about 140° for $m=1.334$ (water) up to 155° for $m=1.45$ (biodiesel 15%). Note that agreements between the measured rainbow pattern and the reconstructed rainbow pattern are very good.

The extracted size distributions are plotted in figure 6.22(c). It is notable that size distributions for water and ethanol are very similar, with a large peak corresponding to particles with a diameter below $10\ \mu\text{m}$ while for the biodiesel 15 only the peaks at $20\ \mu\text{m}$ and $40\ \mu\text{m}$ exist.

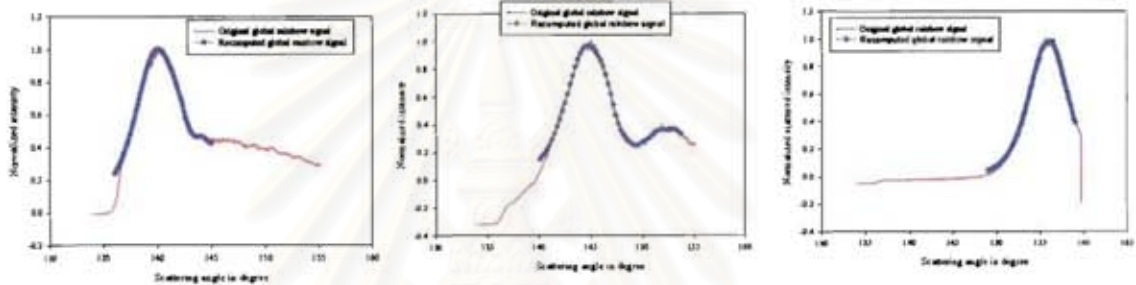
The extracted refractive index values are given in 6.22(d). The measured values are in agreement with the nominal values. The next step is to associate temperature at these refractive index values. If it is assumed that the product is kerosine, and that the relationship proposed by Sankar et al is applied, temperature given in 6.22(e) are obtained. The range of measurable temperature with the developed configuration is well adapted to the measurement of spray flame.



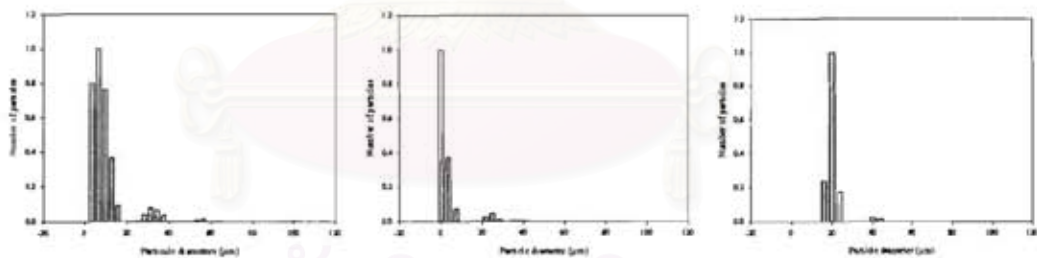
สถาบันวิทยบริการ
จุฬาลงกรณ์มหาวิทยาลัย



(a) The recorded images



(b) The global rainbow patterns



(c) The extracted size distribution

1.3315 1.3644 1.4588

(d) The extracted refractive index

580°K 500°K 280°K

(e) The associated temperature if the product is assumed to be kerosine

Figure 6.22: Example of global rainbow and their processing.

Then, for each product the spray has been measured at 1 cm and 5 cm of the orifice. Figure 6.23 plots the refractive index measured by the global rainbow technique versus the refractive index measured by a refractometer at ambient temperature. This curve proves that a quasi-linear relation is obtained on all the domain of study. Furthermore, an attentive observation show that all the measurements carried out at 5 cm of the orifice are associated with a refractive index larger than the one measured at 1 cm of the orifice, corresponding to a heat down of the droplets. If we assume that measurements have been carried out at different distance in a flame of kerosene droplets, the refractive index can be associated to temperature. The range of temperature where the measurements are possible by global rainbow with this configuration is equal to about 300°C. Remark also, that for biodiesel, the measurement have been carried out with four mixture of biodiesel: 5, 10, 15 and 50 % of palm ester in diesel.

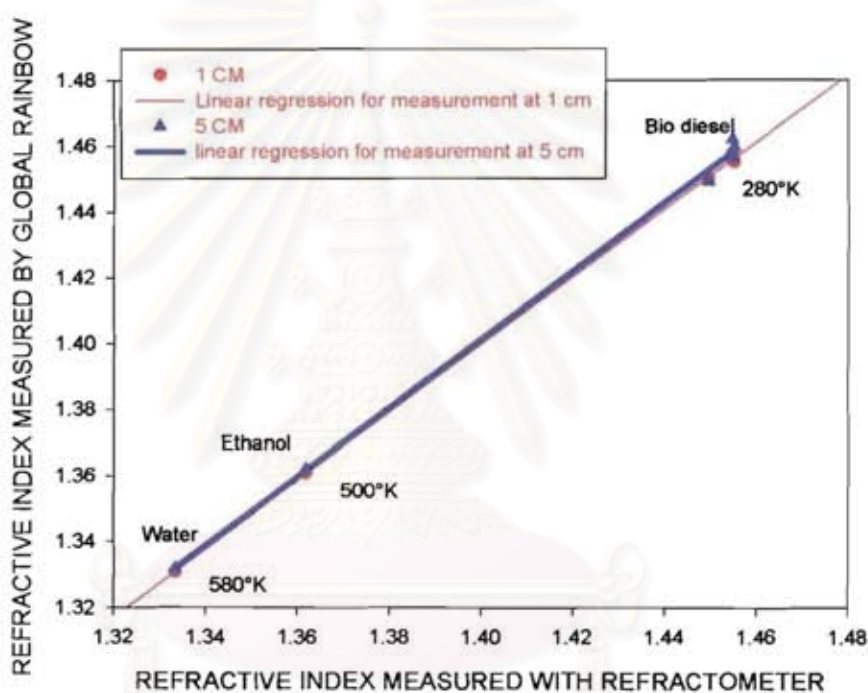


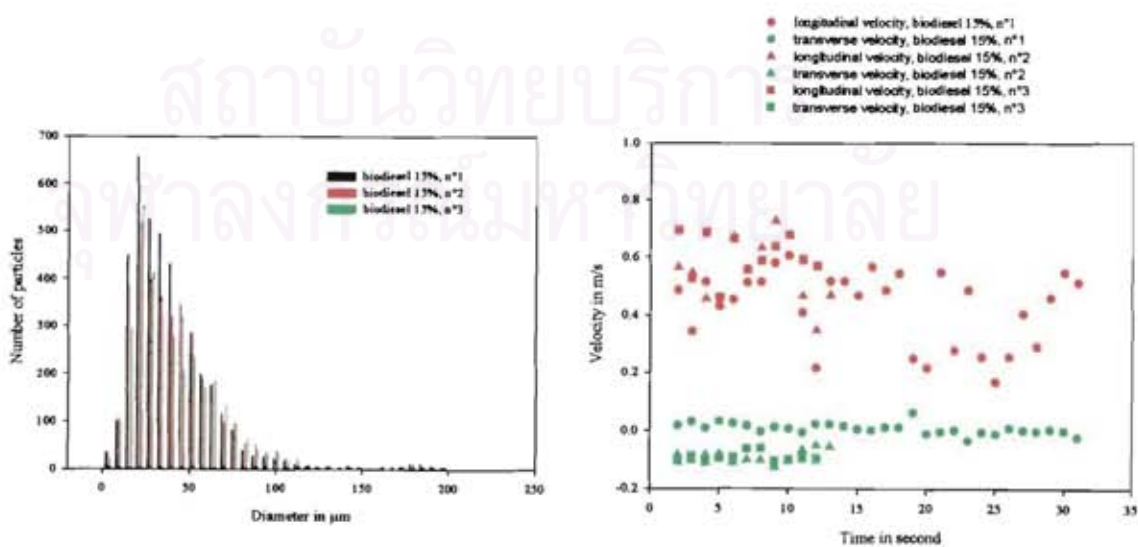
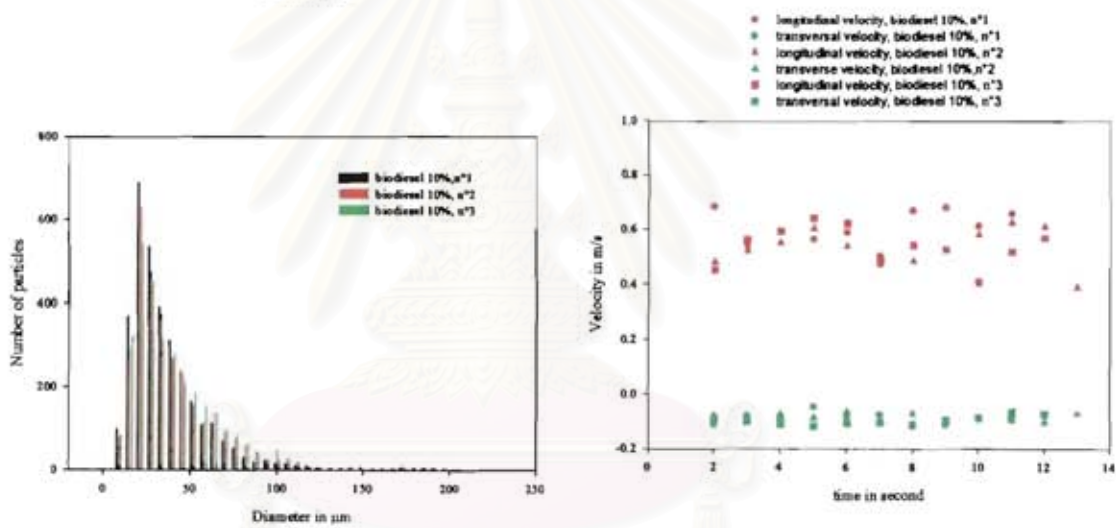
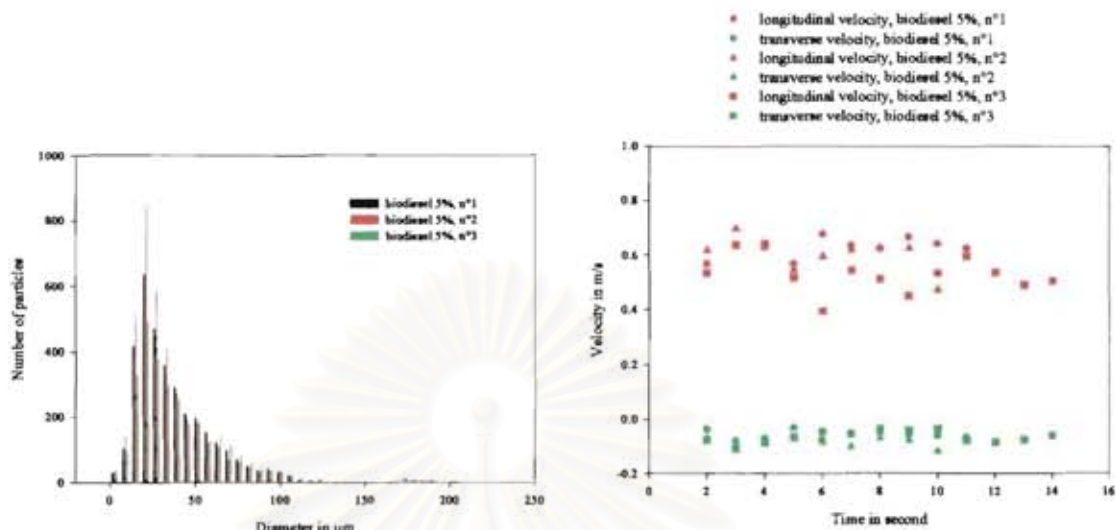
Figure 6.23: Measurement of the refractive index on a large range of refractive index by using a unique optical configuration.

The biodiesel spray has also been studied by PDA. Figure 6.24 displays size distributions and the velocities for the five biodiesel sprays. For each case, three series of measurements have been carried out. Size distributions are plotted in figure 6.24(a) while the longitudinal (red points) and transverse (green points) velocities are plotted versus time in figure 6.24(b). For the velocities (longitudinal and transverse) each plotted points corresponds to the mean velocity during one second. Each series of measurements corresponds to about 3,500 valid events.

Independently of the biodiesel composition, the size distributions are similar and show that the most probable size is equal to about 20 μm , with a comparable long tail up to about 120 μm , and a second peak at about 170 μm .

For all the studied cases, the mean longitudinal velocity is equal to about 0.5 m/s while the transversal velocity is equal to about 0.1 m/s. Nevertheless, especially

for the longitudinal velocity, temporal fluctuation of the mean velocity could be important.



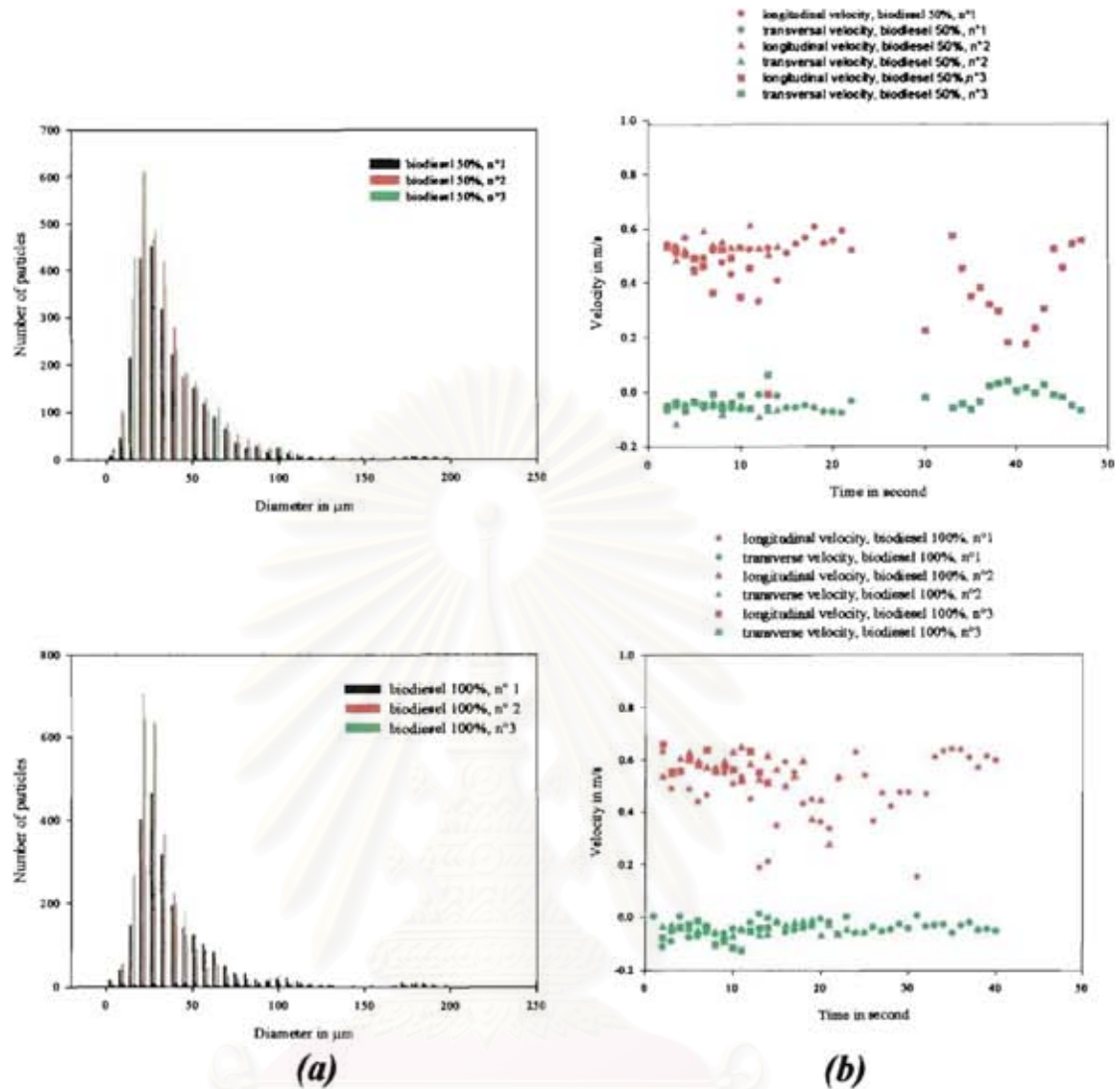


Figure 6.24: Properties of the biodiesel sprays generated by the ultrasonic nozzle used for biodiesel experiments (working frequency $60 \pm 1\text{kHz}$) (a): size distributions, (b): the longitudinal and transversal velocity versus the time, average on a temporal window equal to 1s.

สถาบันวิทยบริการ
จุฬาลงกรณ์มหาวิทยาลัย

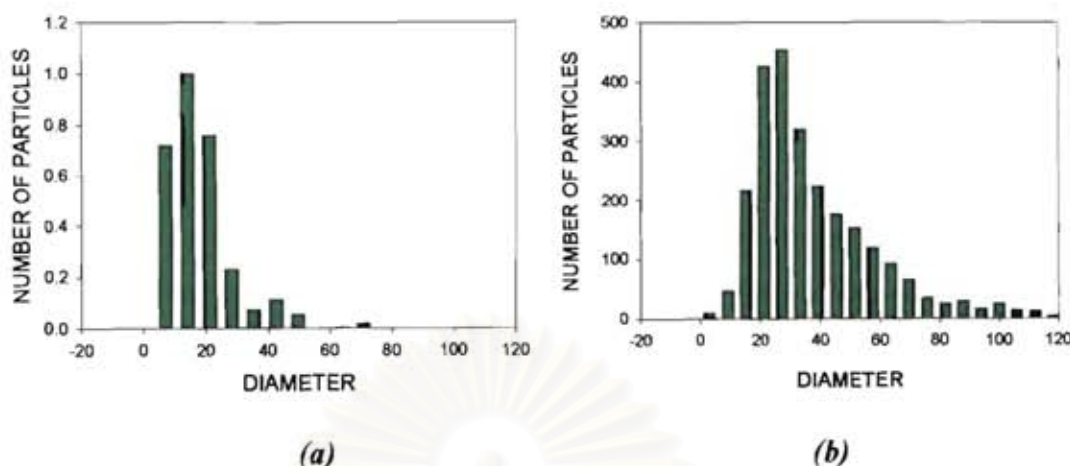


Figure 6.25: Comparison of the size distribution measured by global rainbow (a) and PDA (b) on a spray of biodiesel at 50%.

From global rainbow experiments, the size distributions could also be extracted. Figure 6.25 compares the size distributions measured by global rainbow technique and by PDA technique for the same spray (biodiesel 50%) created by the same nozzle. In both cases, the most probable size is at about 20 μm . Nevertheless, the shapes of the size distributions are different. This disagreement can be due to:

1. The range of measurement is not the same for the two techniques. The Global rainbow inversion code assume that the maximum size is equal to 100 μm while the PDA configuration measure up to 200 μm .

2. The measurement duration is equal to about 1-2 ms by PDA while the global rainbow images are recorded in about 10 ms : a ratio of 6000 to 12 000. Then the size distribution measured by global rainbow change more or less from one recording to the other. To be able to really compare an histogram measured by global rainbow with the one measured by PDA, tens or hundreds of instantaneous size distribution have to be combined together, a work to do in the future.

The robustness of the measurements can be illustrated by the study of a series of global rainbow. Figure 6.26 corresponds to twelve consecutive images recorded on a spray of biodiesel 15%. The acquisition frequency is of about three images by second. From figure 6.26 it is clear that the scattered intensity varies strongly from one recording to the other. These variations of intensity can be connected with change of diameter, refractive index and number of particles in the control volume.

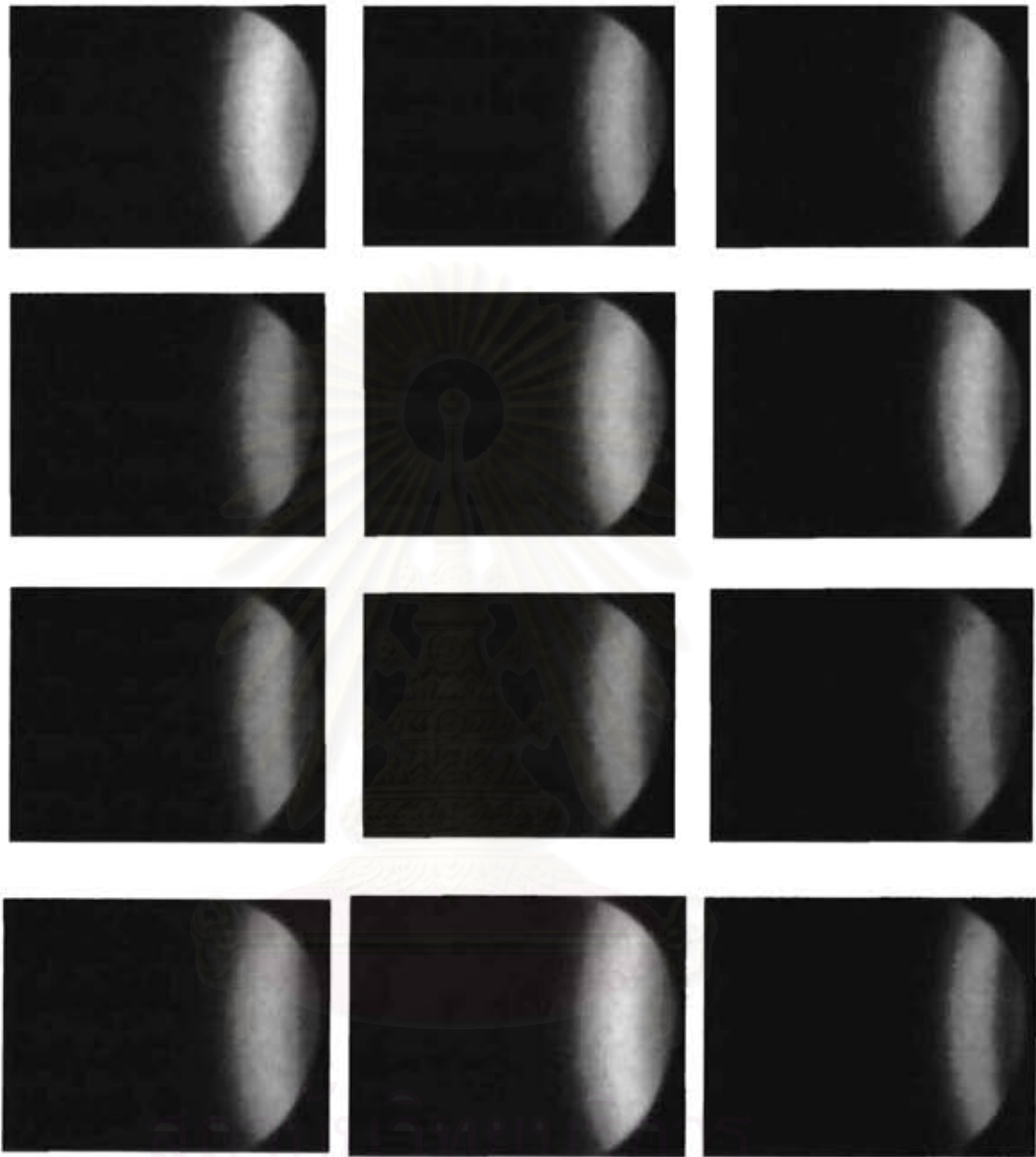


Figure 6.26: A series of consecutively recorded global rainbow from a biodiesel 15% spray.

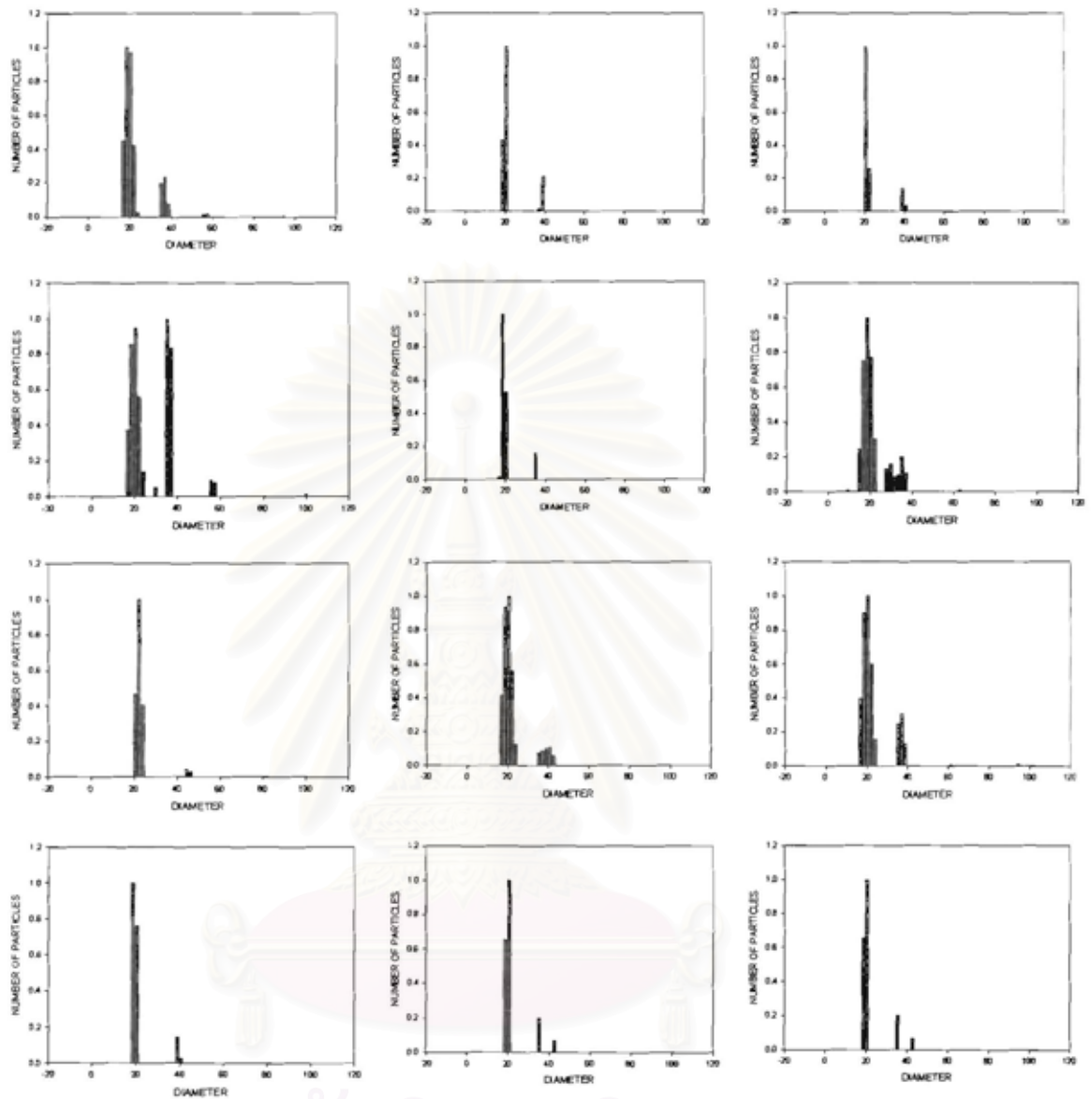


Figure 6.27: The size distribution extracted from the global rainbow images of figure 6.26.

จุฬาลงกรณ์มหาวิทยาลัย

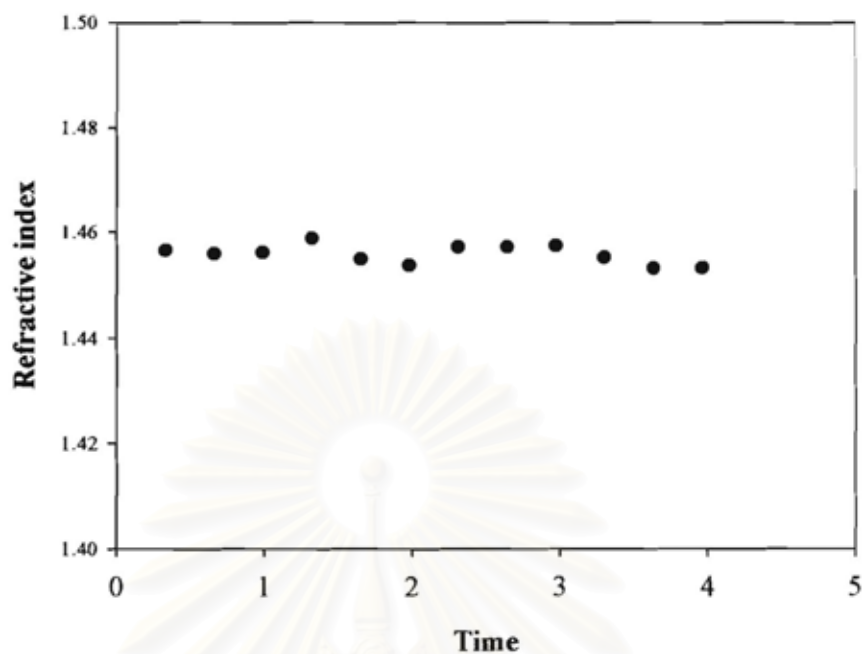


Figure 6.28: Measured refractive index versus time.

This preliminary study demonstrates that measurement of biodiesel spray under combustion is possible with the developed global rainbow set up.

สถาบันวิทยบริการ
จุฬาลงกรณ์มหาวิทยาลัย

6.2.2.2 *Experimental of combustion measurements.*

To be able to understand the burning properties of biodiesel spray, a burner has been designed and tested at Rouen university. Schematically, the burner is composed of three concentric rings (see figure 6.29): the central ring supports the developed ultrasonic nozzle, while the second and third rings are made by using porous bronze. Gas can be send independently to the second and third ring by three inlets to obtain a stable gas flow. The second ring (internal diameter equal to 11 mm and external diameter equal to 26 mm) furnishes fresh air for the burning of the droplets while the third ring (internal diameter equal to 28 mm and external diameter equal to 80 mm) gives the possibility to isolate the flame from ambient air by a flux of nitrogen or argon.

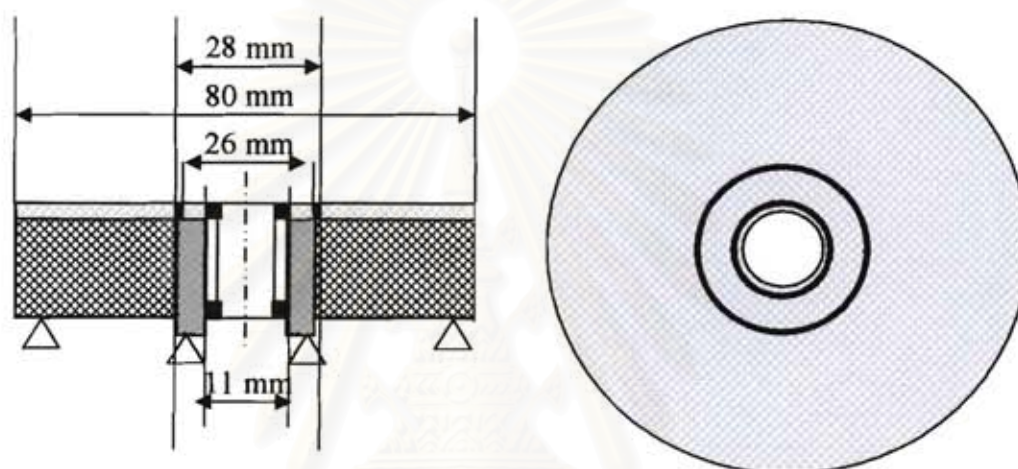


Figure 6.29: A side and a top schematic view of the burner.

A schematic view of the burner inside is given in figure 6.30. The ultrasonic generator is located at the middle of the blue part. The red part corresponds to the second ring. For this ring, the three inlets can be feed in air or any fuel gas to assure a stable combustion. The third ring is green can be feed with air or nitrogen (argon) to isolate the central flame from the ambient air.

Figure 6.31 and 6.32 are photos of the burner top and back respectively.

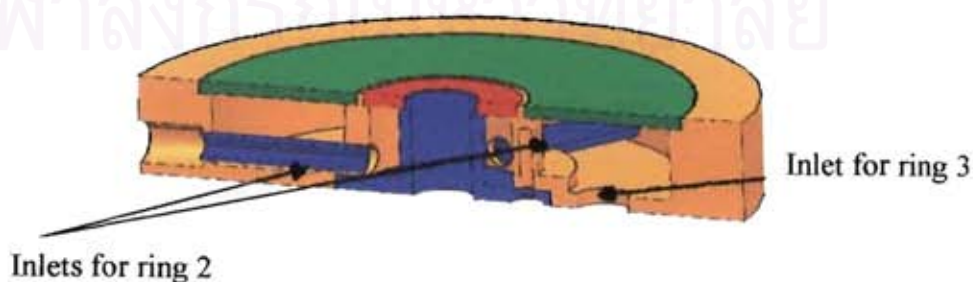


Figure 6.30: Scheme of the burner realized at Rouen University. Inside view.

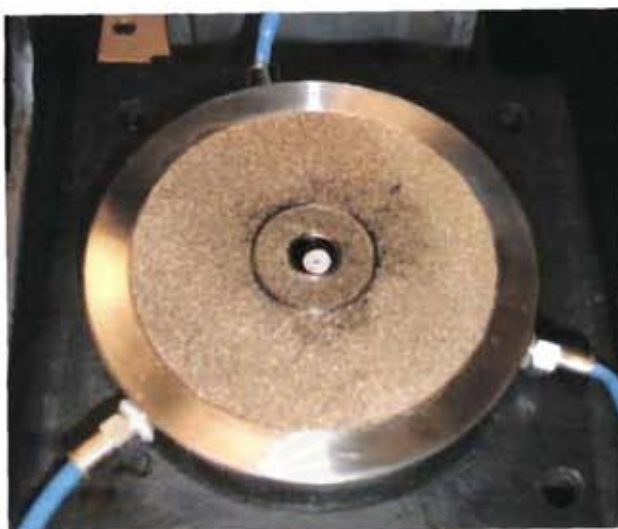


Figure 6.31: Photo of the burner: front view.

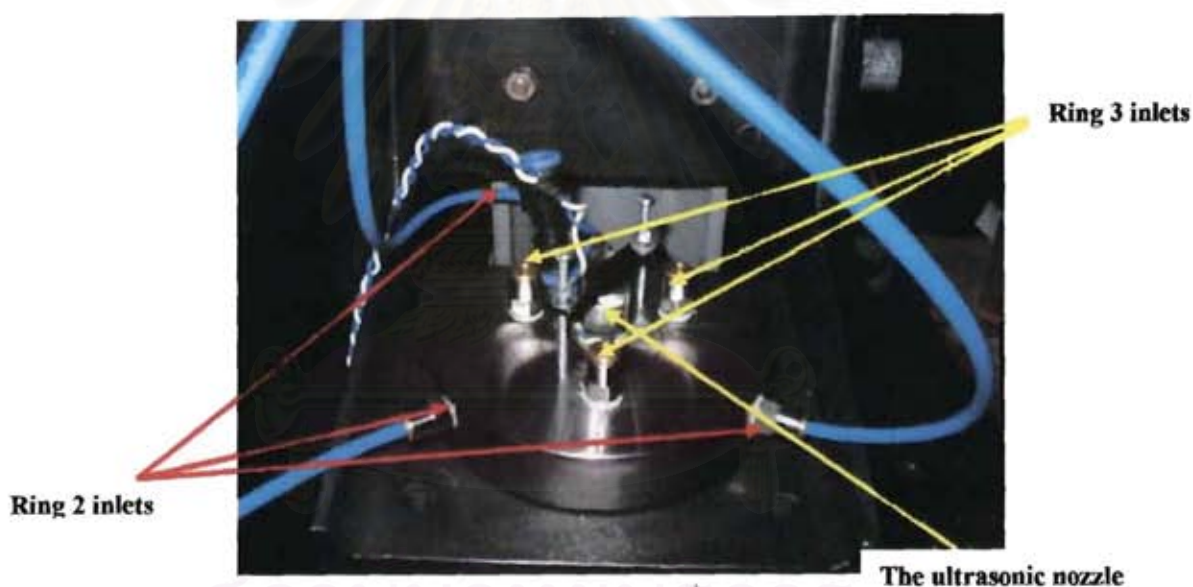


Figure 6.32: Photo of the burner: backward view.

In the experiments carried out with biodiesel, only one ultrasonic nozzle with a working frequency of about 60 kHz is used with the same excitation power. The liquid fuel flow rate is equal to 0.3 cc/min, and the air flow rate for the second ring is equal to 5 cc/min. For this flow rates, a stable flame has been obtained for mixture of ester of palm oil and diesel with the ratio of 5%, 10%, 15% and 50%, as displayed in figure 6.33.

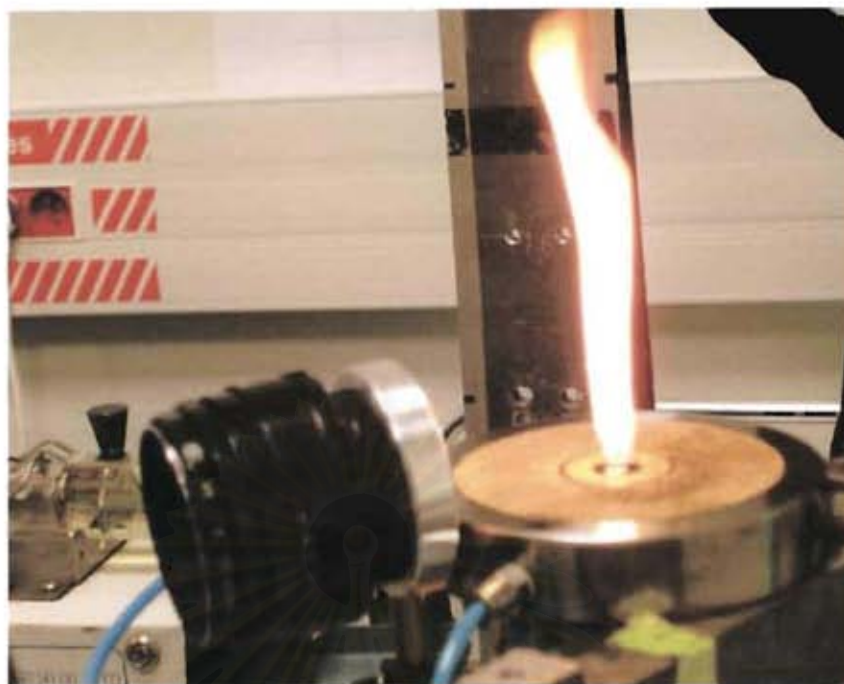


Figure 6.33: *View of a typical flame. The droplets of biodiesel 15% burn in air without adding other fuel.*

The following series of figure displays typical global rainbow pattern recorded in the biodiesel spray first without burning and then burning. The measurements have been carried out at 2 cm from the orifice.

A first remark is that when the flame is on, a large level of light is coming from it. This contribution is removed by using an interferential filter which transmits only the green line of the laser (5145 nm).

A second remark is the difficulty to use the ultrasonic nozzle when the droplets go upward. In this case, some of the droplets fall down and then create a liquid map which conducts the electricity perturbing and later stopping the creation of droplets.

As the relationship between the refractive index and the temperature is unavailable in the literature for biodiesel, and that any refractometer is suitable to measure refractive index at so high temperature, the relationship for the kerosine given by Sankar et al is used to transform the measured refractive index in temperature. The relation reads as :

$$T = \frac{\text{Measured refractive index} - 1.4506}{-0.0004}$$

(a) Without combustion: Below, only exemplifying results corresponding to biodiesel 15% are presented.

First, the global rainbow patterns corresponding to the biodiesel spray created by the ultrasonic nozzle without gas (no gas at ring 2 and 3) has been recorded and processed as displayed in figure 6.34. The global rainbow pattern is characterized by a bright bow, located at about 155° (see figure 6.34(a) and 6.34(b)). In this case the global rainbow pattern is changing in intensity very rapidly due to the high particle concentration and the small size of the spray. A tiny lateral air flow is able to dramatically change the number of particles in the control volume but the measured refractive index (about 1.4608) is very stable and corresponds to a temperature equal to about 25°C . The particle size distribution displays two peaks at about 20 and 40 μm .

Case 1: Biodiesel spray created by ultrasonic nozzle without gas

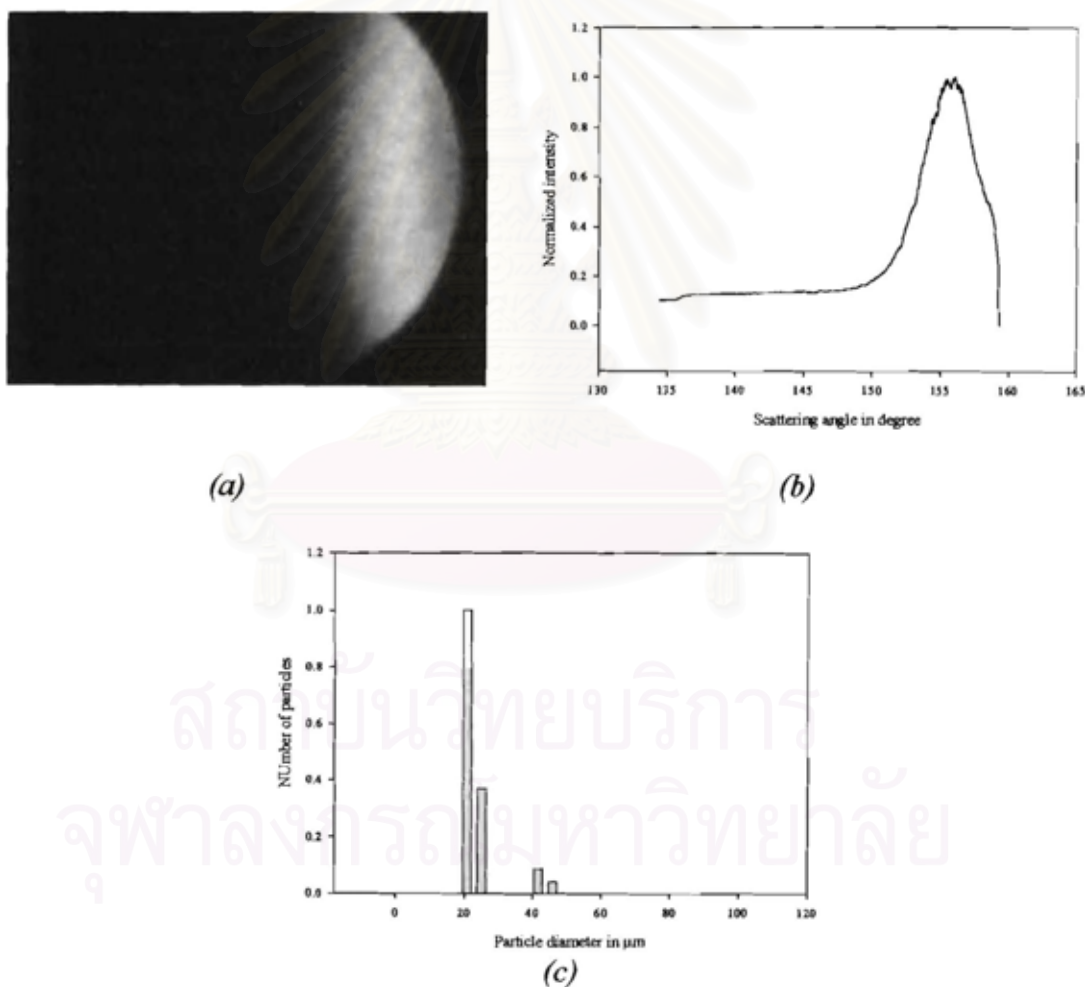


Figure 6.34: Snap-shot of biodiesel spray without air and combustion
 (a) Global rainbow image (b) Extracted global rainbow intensity
 (c) Measured droplet size distribution

The second case corresponds to the addition of a small flow of air at ring 2. In this case, the global rainbow pattern is very stable both in position (as for case 1) but also in intensity. This is due to the flow air which dilutes and stabilizes the spray of the droplets created by the ultrasonic nozzle. Nevertheless, the measured refractive index (1.4607) and size distribution are very close from the ones of case 1. The associate temperature is also equal to about 25°C.

Case 2: Biodiesel spray created by ultrasonic nozzle with gas at the second ring but without combustion.

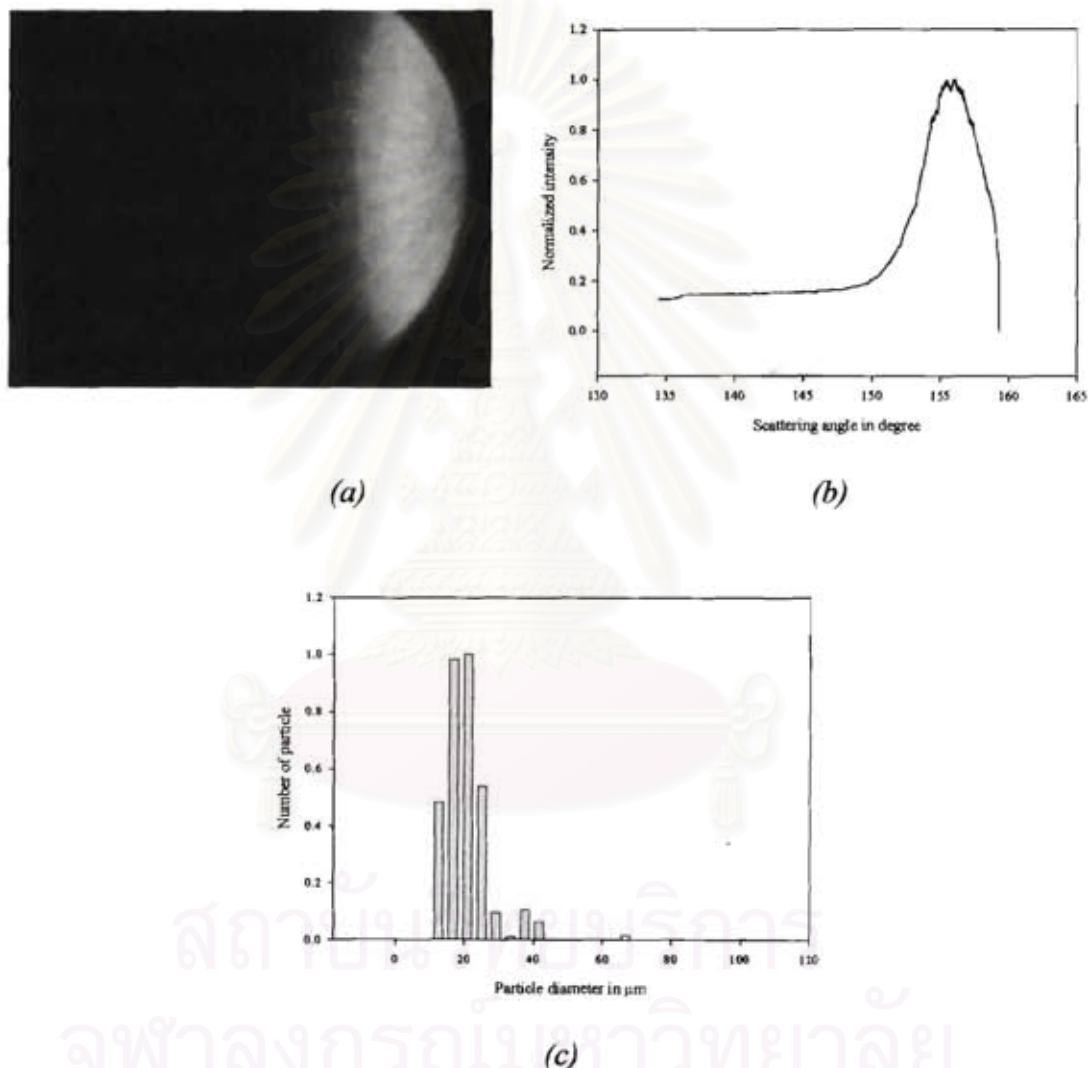


Figure 6.35: Snap-shot of biodiesel spray with air but without combustion
 (a) Global rainbow image (b) Extracted global rainbow intensity
 (c) Measured droplet size distribution

The results for biodiesel 5%, 10% and 50% are not presented here but are essentially identical to the ones for biodiesel 15%. Especially, the droplet temperature has been measured to be equal to 25° for all the mixture.

(b) Under combustion: Then, with the same air flow rate as in case 2, the flame was alight. Due to the flame radiation and turbulence, the global rainbow patterns are less stable than in cases without combustion (cases 1 and 2). The recorded global rainbow patterns are characterized by important change of the recorded intensity. Some images are very weak while some other are saturated, coming from the movement of the flame which is somewhat unpredictable. Some examples are given below.

Starting for the weakest signal, as displayed in case 3, the recorded global rainbow image is characterized by a series of very clear bows (see figure 6.36(a)). At this figure corresponds a global rainbow pattern with very clear oscillations, to which corresponds a size distribution dominated by 60 μm diameter particles with a refractive index equal to 1.3751: the droplets have been heat up to about 188°C. This signal can be interpreted as created by very few big droplets

Case 3: Biodiesel spray created by ultrasonic nozzle under the combustion, for weak signal.

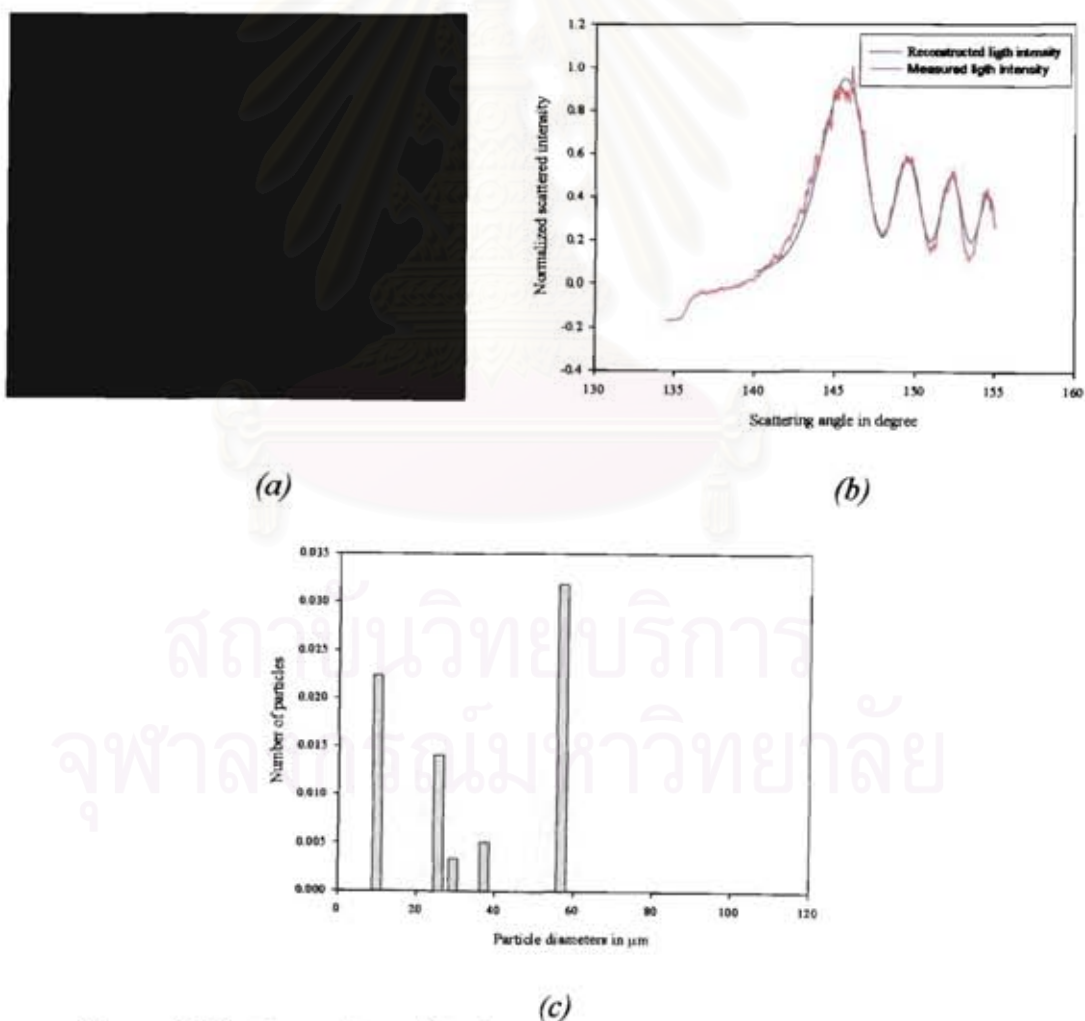


Figure 6.36: Snap-shot of biodiesel spray with air and under combustion.
 (a) Global rainbow image (b) Extracted global rainbow intensity
 (c) Measured droplet size distribution

A more intense signal is displayed in case 4. Here again some bows can be distinguished but their visibility is smaller than for case 3 (see figure 6.37(a)). The higher intensity, in this case, is due to a higher number of small droplets in the measurement volume (smaller than $20\ \mu\text{m}$ in diameter) but with some large of about $40\ \mu\text{m}$. The global rainbow pattern, as displayed in figure 6.37(b), shows that the extra bows now are located on the decreasing slope of the rainbow. The measured refractive index is equal to 1.3716, corresponding to 197°C

Case 4: Biodiesel spray created by ultrasonic nozzle under the combustion, for average intensity signal.

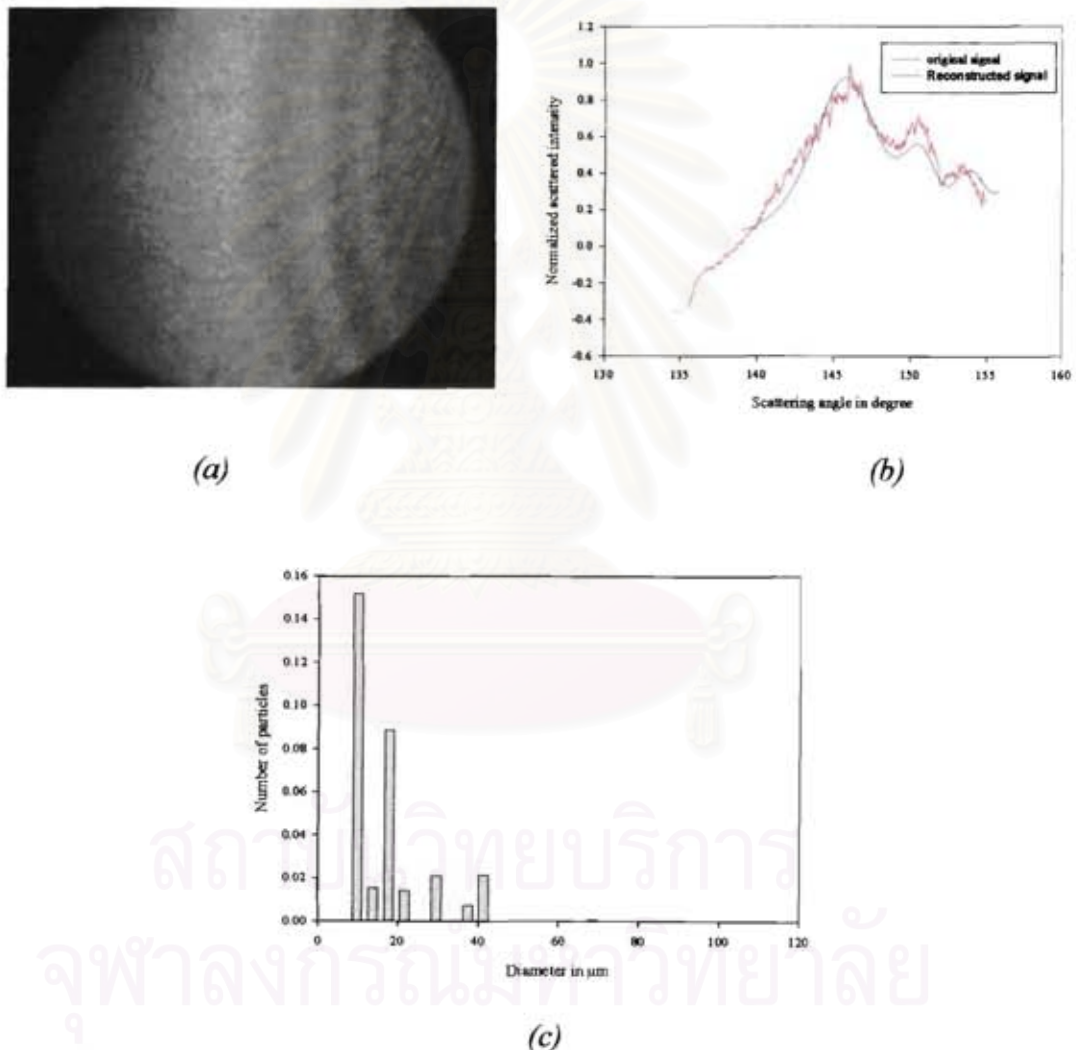


Figure 6.37: Snap-shot of biodiesel spray with air and under combustion.
 (a) Global rainbow image (b) Extracted global rainbow intensity
 (c) Measured droplet size distribution

The last case corresponds to a very intense scattered light, no more extra bows can be distinguished, only the main one is visible (see figure 6.38(a)). The rainbow pattern displayed in figure 6.38(b), is characterized by a long monotonic decreasing part, to which corresponds small particles (smallest than in case 4). The disappearing of the extra bows can be explained by the presence of a large number of small particles in the control volume. The extracted size distribution, as displayed in figure 6.38(c) is dominated by droplets smaller than about 15 μm . Now the refractive index is equal to 1.3739, corresponding to 191°C.

Case 5: Biodiesel spray created by ultrasonic nozzle under the combustion, for high intensity signal.

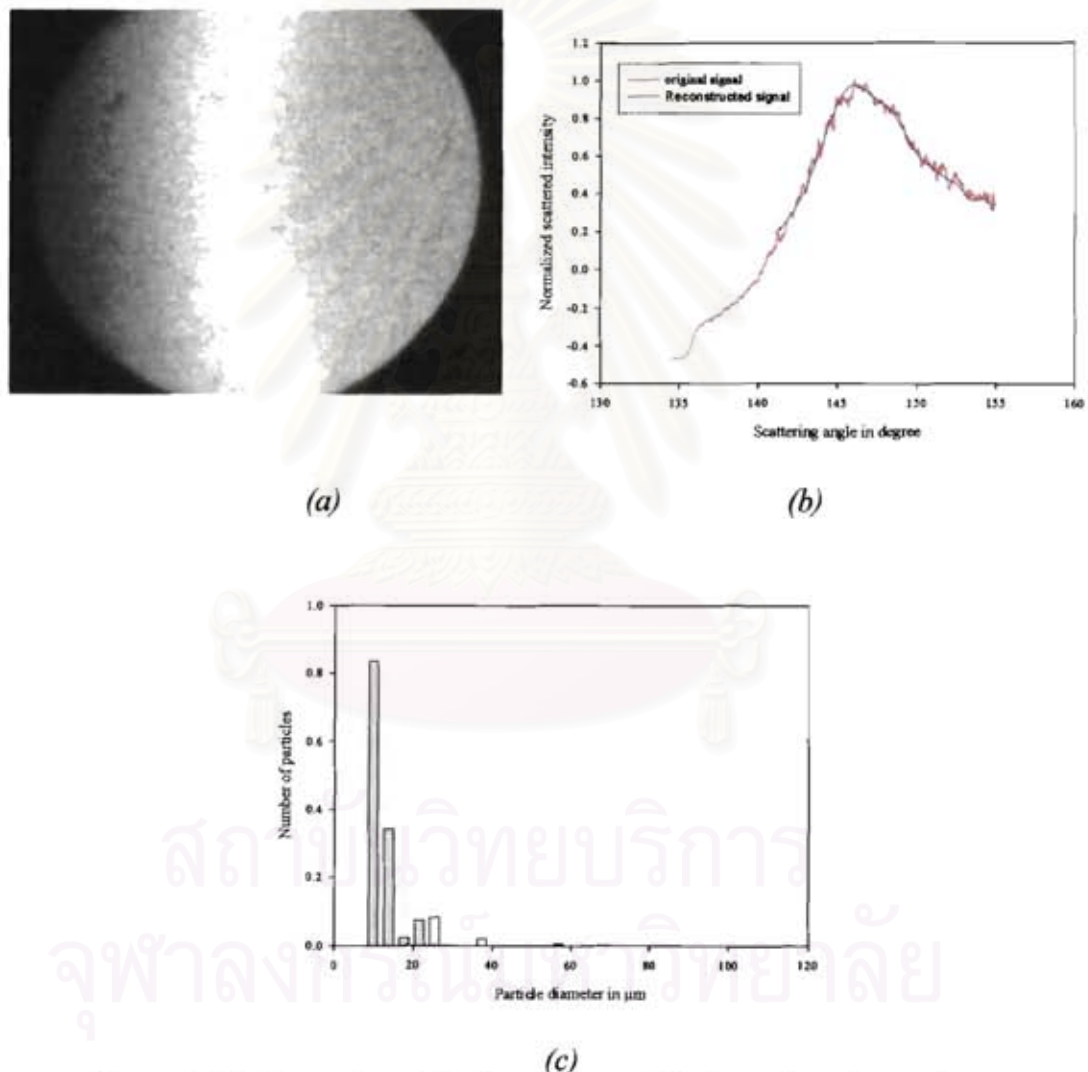


Figure 6.38: Snap-shot of biodiesel spray with air and under combustion.
 (a) Global rainbow image (b) Extracted global rainbow intensity
 (c) Measured droplet size distribution

These in situ measurements of biodiesel droplet temperature in a flame have been carried out, without any addition of other fuel, for biodiesel 15%. The results show a decreasing of the droplets size and a heat up of the droplet estimated to be equal to about 200 °C at about 2 cm. from the nozzle orifice.

Then the same measurements have been carried out, at the same location but for different percentage of blending ester of palm oil in diesel (5%, 10%, 15% and 50 %). The series of measurements permit to process: 20 images for biodiesel 5%, 10 for biodiesel 10%, 15 for biodiesel 15% and 14 for biodiesel 50%.

The recorded global rainbows are very similar to the ones presented previously, as well as the extracted size distributions. In this section, the size distributions will no be discussed because the quality of the extracted size distributions is not good enough to be able to distinguish a real behaviour between the different mixtures.

To the refractive indices measured at 2 cm of the nozzle, a temperature is associated by using the law given page 154. Figure 6.39 plots these temperatures versus the quantity of biodiesel in the mixture. The temperature seems to be higher when the percentage of biodiesel is higher.

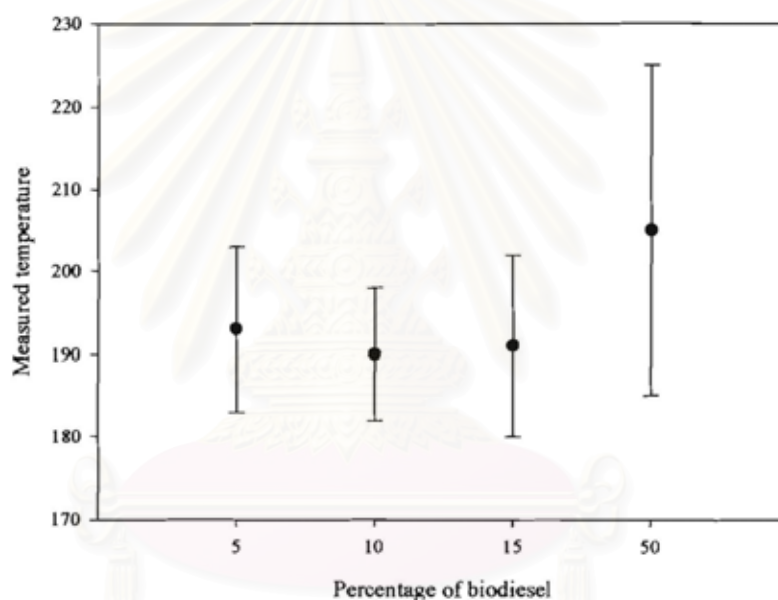


Figure 6.39: *The measured temperature versus the percentage of biodiesel.*

The fact that the temperature increases with the percentage of biodiesel in diesel could be explained as follow: when the droplet is essentially composed of diesel (which is lighter than biodiesel), a larger quantity of the warm flux is used to transform the liquid to vapor while when the droplet is mainly composed of biodiesel a larger fraction of the warm flux is use to increase the droplet temperature up to the biodiesel boiling point. In short, when the percentage of the biodiesel in diesel is higher the evaporation is less efficient.

However, to be fully validated, complementary experiments must be carried out as the measurement of the droplets velocity under combustion conditions (for biodiesel 15%, PDA measurements show that the main velocity is equal to 5.3 m/s), the measurement of the flame temperature, the exact

relationship between the refractive index and the temperature for the different biodiesel blends,

For all these experiments, the main difficulties (variation of intensity, lost of signal, ..) are due to the movement of the flame which is somewhat unpredictable. Environmental conditions and the position of the exhaust inlet can even cause the flame to bend one way or the other. Employing the chimney is possible. This can improve the stability of the flame, but small movements as large as the region of interest are unavoidable.

These first measurements are very promising, but still have to be developed. Especially, the effect of temperature gradient will be explored and experiments combining rainbow technique with other one less sensitive to the surface refractive index must be designated to quantify the gradient.

Conclusion

In this chapter an experimental global rainbow setup has been designed and realized. Then, this prototype has been used to measure the temperature and size distribution of water, ethanol and ester of palm oil biodiesel sprays created by an ultrasonic nozzle. Four different mixture of biodiesel in diesel have been measured (5%, 10%, 15% and 50% by volume of palm ester in diesel). The recorded global rainbows have been processed and the refractive indices have been extracted, without and with combustion. The results are stable and consistent.

Without combustion, it has been demonstrated that:

- ultrasonic nozzles create the spray with a size distribution independent of the biodiesel blend;
- the droplet temperature is equal to about 25°C independently of the biodiesel blend, with small fluctuations attributed to the effect of parasite air flow.

For biodiesel combustion, these preliminaries results demonstrate that, at 2cm from the injector:

- the mean diameter has strongly decrease when compared with no combustion cases
- the biodiesel droplet temperature is equal to about 200°C,
- small differences between the temperature measured for the different biodiesel blends look support the fact that evaporation is less efficient when the biodiesel proportion in the petroleum diesel increases.

Nevertheless, a better confidence is given to the absolute refractive index measurement, and associated temperature, for water and ethanol than for biodiesel. This better confidence is due to the fact that the exact relationship between the biodiesel refractive index and temperature is not yet known, and that the biodiesel measurements are far of the calibration region. This last limitation can be partially removed by doing a second calibration with a biodiesel liquid jet.

A second remark is that the extracted size distributions are always dominated by the small particles. The number of small particles is overestimated, in opposition with the case of numerical simulations. This fact is not yet completely understood but it is assumed to be related with the presence of a light background, multiple scattering and non-sphericity of the particles. Nevertheless, as this overestimation of the small particles looks to have no effect on the refractive index and temperature measurements, the study of it is postponed.



สถาบันวิทยบริการ
จุฬาลงกรณ์มหาวิทยาลัย

CHAPTER VII

CONCLUSIONS

In the framework of the international energy crisis, the improvement of liquid combustion processes, in terms of efficiency as well as emission pollutant reduction, is a major challenge for classical fuel as well as for bio diesel fuel.

To enable to design and develop efficient and stable combustors, it is necessary to develop a complete understanding of the fundamental phenomena that could affect and control the overall spray combustor. The combustion efficiency depends strongly on fuel droplet evaporation which is a function of droplet temperature. Then in order to obtain a better understanding of droplet vaporization rate, it would be advantageous to measure fuel droplet temperature. Especially for bio diesel spray as its physical properties are complicated. In gas flames it is possible to measure the gas temperature and the different species by using optical techniques. In contrast to the spray flames, only geometrical quantities as the particles velocity and size are today measurable.

Among other techniques, rainbow approaches, which are based on the high sensitivity of the rainbow location on refractive index therefore on the temperature, are very promising. Rainbow techniques do not necessitate additive (as fluorescence techniques) and then can be applied in situ in hostile media as flame or pressure chamber.

This thesis introduces new rainbow processing strategies based on an improvement of the Nussenzveig's theory which permits accurate and fast computations of the light scattered around the rainbow angle. By using this approach, fast automatic inversions of recorded rainbows has been realized, permitting to measure the droplet size with an accuracy of 0.01 μm (for individual droplets) while the refractive index is obtained with an accuracy typically equal to 0.0001, for droplet size running from 30 to 150 μm (both for individual droplets as well as for a section of a cloud).

This inversion strategy has been applied to experimental records from ONERA-Toulouse for individual particles, while a specific experimental set up has been developed during this thesis to measure the temperature of a bio diesel flame spray.

To realize the spray flame, a fundamental burner has been developed, exploiting the properties of the ultrasonic nozzles from Chulalongkorn University: small particles, narrow size distribution and low initial velocity. The bio diesel used is composed of 5% up to 50% of ester of palm oil in petroleum diesel. Measurements of the temperature of the droplets inside the pure bio diesel spray flame are reported, which are the firsts at the author knowledge. These preliminaries results show that the temperature of the droplet increases with the proportion of the biodiesel in diesel, supporting the assumption that evaporation is less efficient when quantity of biodiesel blend in the petroleum diesel could be increased.

When a radiant gradient of temperature (or composition) exists inside the droplets, the notion of equivalent particle has been introduced.

The main perspectives of this work are the systematic measurements of the temperature and size evolution inside a spray flame, given a direct access to the evaporation rate of realistic bio diesel under realistic combustion conditions.



สถาบันวิทยบริการ
จุฬาลงกรณ์มหาวิทยาลัย

REFERENCES

- 1 A.P.C. Faaij. Bio-energy in Europe: changing technology choices. Journal of Energy policy 30 (February 2006): 83-104.
- 2 M. Mikami, S. Miyamoto, N. Kojima, Journal of Proc. Combust. Inst 29 (2002): 593-599.
- 3 Berger H.L. Ultrasonic Liquid Atomization Theory and Application I (New York: Partridge Hill Publishers, 1998).
- 4 Daniel Sindayihebura, Jean Cousin and Christophe Dumouchel. Experimental and Theoretical Study of Sprays produced by Ultrasonic Atomizers. Journal of Part. Part. Syst. Charact 14 (1997): 93-101.
- 5 Francois Lacas, Philippe Versaevl, Philippe Scouflaire, Gerard Cœur-Joly. Design and performance of an Ultrasonic Atomization System for experimental Combustion Applications. Journal of Part. Part. Syst. Charact 11(1994): 166-171.
- 6 W.P. Mason. Physical Acoustics and properties of solid (New Jersey: Van Nostrand, Princeton, 1958).
- 7 R. Rajan and A.B. Pandit. Correlations to predict droplets size in ultrasonic atomisation. Journal of Ultrasonics 39(2001): 235-255.
- 8 Glover A.R, Skippon S.M. and Boyle R.D. Interferometric laser imaging for droplet sizing: a method for droplet-size measurement in sparse spray systems. Journal of Applied Optics 34, No. 36 (1995): 8409-8421.
- 9 Mounaïm-Rousselle C., Pajot O. Droplet Sizing by Mie Interferometry in a Spark Ignition Engine. Journal of Particle and Particle Systems Characterization 16 (1999): 160-168.
- 10 Girasole T., Ren K.F, Lebrun D., Gouesbet G. and Gréhan G. Particle Imaging Sizing: GLMT Simulations. Journal of Visualization 3, No.2 (2000): 195-202.
- 11 Kobayashi T., Kawaguchi T. and Maeda M. Measurement of spray flow by an improved interferometric laser imaging droplet sizing (ILIDS) system. 10th International Symposium on applications of laser techniques to fluid mechanics (2000).
- 12 Calabria R. and Massoli P. Experimental study of droplets in evaporating regime by 2D scattering analysis. 10th International Symposium on applications of laser techniques to fluid mechanics (2000).
- 13 Damaschke N., Nobach H., Nonn T., Semidetnov N. and Tropea C. Size and velocity measurements with the global phase Doppler technique. 11th International Symposium on applications of laser techniques to fluid mechanics (2002).
- 14 G. Chen, Md.M. Mazumder, R.K. Chang, J.C. Swindall and W.P. Acker. Laser diagnostics for droplet characterization: application of morphology dependent resonances. Journal of Prog. Energy Combust. Sc. 22 (1996): 163-188.
- 15 Q.Z. Lu and L.A. Melton. Measurement of transient temperature field within a falling droplet. AIAA Journal 38 (2000): 95-101.
- 16 G. Castanet, P. Lavielle, M. Lebouché and F. Lemoine. Measurement of the temperature distribution within monodisperse combusting droplets in linear stream using two colors laser-induced fluorescence. Journal of Exp. In Fluids 35 (2003): 563-571.

- 17 P. Massoli, F. Beretta, A. D'Alessio and M. Lazzaro. Temperature and size of single transparent droplets by light scattering in the forward and rainbow regions. Journal of Applied Optics 32, No18 (1993): pp 3295-3301.
- 18 K. Anders, N. Roth and A. Frohn. Light scattering at the rainbow angle: information on size and refractive index. Proc. 3rd Int. Congr. On Optical Particle Sizing (1997): 237-242.
- 19 J.P.A.J. van Beeck. Rainbow phenomena: development of a laser-based, non-intrusive technique for measuring droplet size, temperature and velocity. (Doctoral dissertation, Technische Universiteit Eindhoven, 1997).
- 20 S.V. Sankar, D.H. Buermann and W.D. Bachalo. Application of rainbow thermometry to the study of fuel droplet heat-up and evaporation characteristics. Journal of Engineering for gas turbines and power 119 (1997): 573-584.
- 21 H.C. van de Hulst. Light scattering by small particles. (New York: Dover, 1981). C.F. Bohren and D.R Huffman. Absorption and scattering of light by small particle. (New York: J. Wiley & sons, 1983).
- 22 H.M. Nussenzveig. High-frequency scattering by a transparent sphere. I Direct reflection and transmission. Journal of mathematical Physics 10, No.1 (1969): 82-124.
- 23 H.M. Nussenzveig. High-frequency scattering by a transparent sphere. II Theory of the rainbow and the glory. Journal of mathematical physics 10, No.1 (1969): 125-176.
- 24 V. Khare and H.M. Nussenzveig. Theory of the rainbow. Physical Review letters 33(1974): 976-980.
- 25 A. Frohn and N. Roth. Dynamics of droplets. Springer 2000.
- 26 P. Massoli, F. Beretta, A. D'Alessio and M. Lazzaro. Temperature and size of single transparent droplets by light scattering in the forward and rainbow regions. Journal of Applied Optics 32, No.18 (1993): 3295-3301.
- 27 S.L. Min and A. Gomez. High-resolution size measurement of single spherical particles with a fast Fourier transform of the angular scattering intensity. Applied Optics 35 (1996): 4919-4926.
- 28 K. Anders, N. Roth and A. Frohn. Light scattering at the rainbow angle: information on size and refractive index. Proc. 3rd Int. Congr. On Optical Particle Sizing (1993): 237-242.
- 29 Jackson J.D. From Alexander of Aphrodisias to Young and Airy. Physics Reports 320(1999): 27-36.
- 30 J.P.A.J van Beeck and M.L. Riethmuller. Nonintrusive measurements of temperature and size of single falling raindrops. Journal of Applied Optics 34 (1995): 1633-1639.
- 31 J.P.A.J. van Beeck and M.L. Riethmuller. Rainbow phenomena applied to the measurement of droplet size and velocity and to the detection of nonsphericity. Journal of Applied Optics (1996): 2259-2266.
- 32 N. Damaschke. Light Scattering Theories and their Use for Single Particle Characterization. (Doctoral dissertation, Technische Universitat Darmstadt, 3 December 2003).
- 33 Z.S. Wu, L.X. Guo, K.F. Ren, G. Gouesbet and G. Gréhan. Improved algorithms for electromagnetic scattering of plane wave and shaped beams by multilayered spheres. Journal of Applied Optics 36 (1997): 5188-5198.

- 34 N. Doué, "Modélisation de l'évaporation de gouttes multicomposants", DEA report at SUPAERO (2002).
- 35 S. Saengkaew, T. Charinpanitkul, H. Vanisri, W. Tanthapanichakoon, L. Méès and G. Gréhan. Rainbow refractometry :On the validity domain of Airy's and Nussenzveig's theories. Journal of Optics Communications 259, Issue1(March 2006): 7-13.
- 36 X. Han, K.F. Ren, Z.S. Wu, F. Corbin, G. Gouesbet and G. Gréhan. Characterization of initial disturbances in liquid jet by rainbow sizing. Journal of Applied Optics 37 (1998): 8498-8503.
- 37 Y.P. Han, L. Mees, K.F. Ren, G. Gouesbet, S.Z. Wu and G. Gréhan. Scattering of light by spheroids : the far field case. Journal of Optics Communications 210 (2002): 1-9.
- 38 Y.P. Han, G. Gréhan and G. Gouesbet. Generalized Lorenz-Mie theory for a spheroidal particle with off-axis Gaussian-beam illumination. Journal of Applied Optics 42 (2003): 6621-6629.
- 39 J.P.A.J. van Beeck, D. Giannoulis, I. Zimmer and M.L. Riethmuller. Global rainbow thermometry for droplet-temperature measurement. Optic Letters 24 (1999): 1696-1698.
- 40 M.R. Vetrano, J.P.A.J. van Beeck and M.L. Riethmuller. Global rainbow thermometry, improvements in the data inversion algorithm and validation technique in liquid-liquid suspension. Journal of Applied Optics 43, No.18 (2004): 3600-3607.
- 41 F. Corbin, A. Garo, G. Gouesbet and G. Gréhan. Réfractométrie d'arc-en-ciel : application au diagnostic des gouttes avec gradient d'indice. Recueil des actes du 5^e Congrès Francophone de Vélocimétrie Laser Rouen, France, 1996, E1.1-E1.8, Université et Institut des Sciences Appliquées de Rouen, URA CNRS 230/CORIA.
- 42 R. Kneer, M. Scheider, B. Noll and S. Wittig. Diffusion controlled evaporation of a multicomponent droplet: theoretical studies on the importance of variable liquid properties. Journal of Heat and Mass transfer 36 (1993): 2403-2415.
- 43 S.V. Sankar, D.H. Buermann and W.D. Bachalo. Application of rainbow thermometry to the study of fuel heat-up and evaporation characteristics. Journal of Engineering for gas turbines and power 119 (1997): 573-584.



APPENDICES

สถาบันวิทยบริการ
จุฬาลงกรณ์มหาวิทยาลัย



APPENDIX A

**THEORETICAL TOOLS FOR LIGHT
SCATTERING BY A SPHERICAL PARTICLE**

สถาบันวิทยบริการ
จุฬาลงกรณ์มหาวิทยาลัย

Appendix A: Theoretical tools for light scattering by a spherical particle

The Lorenz-Mie theory is a vectorial theory describing rigorously the scattering of a plane wave by a perfectly spherical particle. All the scattering modes are included in the Lorenz-Mie theory which provides a reference but does not distinguish the different paths of the light inside the particle. Furthermore, the computational time increases with size parameter and can be prohibitive especially for inverse problems for which iterations are necessary. In the far field approximation, the Lorenz-Mie theory provides electric field components written as:

$$E_{\theta} = \frac{iE_0}{kr} \exp(-ikr) \cos \varphi \sum_{n=1}^{\infty} \frac{2n+1}{n(n+1)} [a_n \tau_n(\cos \theta) + ib_n \pi_n(\cos \theta)] \quad (A1)$$

$$E_{\varphi} = \frac{-E_0}{kr} \exp(-ikr) \sin \varphi \sum_{n=1}^{\infty} \frac{2n+1}{n(n+1)} [a_n \pi_n(\cos \theta) + ib_n \tau_n(\cos \theta)] \quad (A2)$$

where the generalized Legendre functions are defined by:

$$\pi_n(\cos \theta) = \frac{P_n^1(\cos \theta)}{\sin \theta}, \quad \tau_n(\cos \theta) = \frac{dP_n^1(\cos \theta)}{d\theta} \quad (A3)$$

and the Mie scattering coefficients are given by:

$$\begin{aligned} a_n &= \frac{\psi_n(\alpha) \psi_n'(\beta) - N \psi_n'(\alpha) \psi_n(\beta)}{\xi_n(\alpha) \psi_n'(\beta) - N \xi_n'(\alpha) \psi_n(\beta)} \\ b_n &= \frac{N \psi_n(\alpha) \psi_n'(\beta) - \psi_n'(\alpha) \psi_n(\beta)}{N \xi_n(\alpha) \psi_n'(\beta) - \xi_n'(\alpha) \psi_n(\beta)} \end{aligned} \quad (A4)$$

with α the size parameter defined as $\alpha = \pi d / \lambda$ and $\beta = N\alpha$, d is the particle diameter, N is the complex refractive index, λ is the wavelength of the incident beam, k is the wave number $k = 2\pi / \lambda$, r is the distance between the particle and the observation point, and E_0 is the amplitude of the incident field.

Lorenz-Mie computations have been carried out by using a code developed under FORTRAN 95, and provided to me by L. Méès. The code interface is as follows:



Figure A1: The Lorenz-Mie code interface and the configuration window.

สถาบันวิทยบริการ
จุฬาลงกรณ์มหาวิทยาลัย

The Debye Theory can be considered as a post processing of the Lorenz-Mie theory in which the coefficients a_n and b_n are written under series forms. It also provides a vectorial and rigorous solution for the scattering of a plane wave by a perfectly spherical particle. However, Debye series gives the possibility to quantify the contribution of the different kinds of “rays”, i.e. the diffracted rays, the externally reflected rays, the rays which experiment k internal reflections before leaving the particle by truncating a_n and b_n computations. The computation time in Debye series approach is nearly identical to the one in Lorenz-Mie approach.

In Debye theory, the Lorenz-Mie coefficients a_n are given by:

$$a_n = \frac{1}{2} \left[1 + R_n^{22} - \sum_{p=1}^{\infty} T_n^{21} (R_n^{11})^{p-1} T_n^{12} \right] \quad (\text{A5})$$

with a similar relation for b_n . The coefficients R_n^{22} , R_n^{11} , T_n^{21} and T_n^{12} are, for the corresponding partial spherical wave, the reflection coefficient outside of the particle, the reflection coefficient inside of the particle, the coefficient of transmission from outside to inside the particle and the coefficient of transmission from inside to outside of the particle respectively. The above equation leads to the following interpretation:

- $a_n = \frac{1}{2}$: describes the diffraction of the incident wave around the spherical particle when inserted in the scattered coefficient expressions in the scattered field expressions in Lorenz-Mie (eqs 1 and 2), and summed over n,
- $a_n = \frac{1}{2} R_n^{22}$: similarly represents the outgoing scattered wave reflected from the surface of the spherical particle.
- $a_n = \frac{1}{2} \left[- \sum_{p=1}^{\infty} T_n^{21} (R_n^{11})^{p-1} T_n^{12} \right]$: this term takes the form of a geometrical series. Individual terms represent the light transmitted to the sphere and emerging from it after (p-1) internal reflections.

In both Lorenz-Mie and Debye frameworks, scattered intensities can be evaluated from :

$$I = E_{\theta} E_{\theta}^* + E_{\phi} E_{\phi}^* \quad (\text{A6})$$

Debye computations have been carried out by using a code developed under FORTRAN 95, and provided to me by L. Méès. The code interface is as follows:

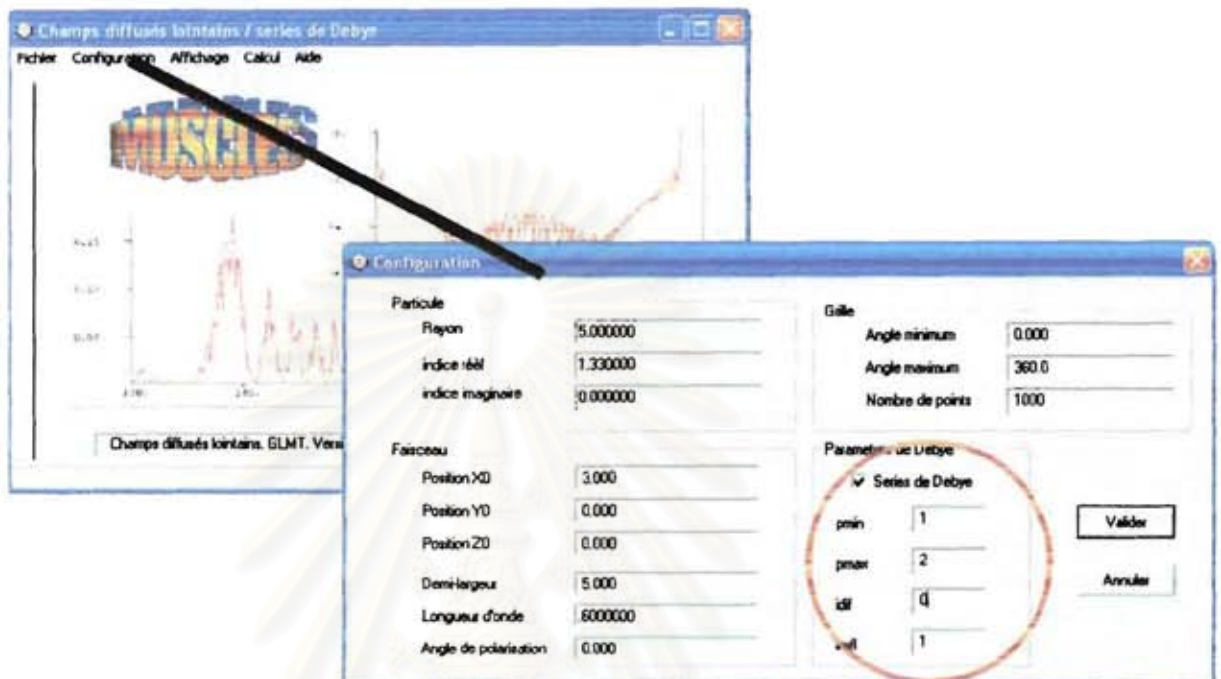


Figure A2: The Debye interface with the configuration window. The main difference with the Lorenz-Mie theory is the possibility to focus on the effect of some kinds of rays.

สถาบันวิทยบริการ
จุฬาลงกรณ์มหาวิทยาลัย

The Airy theory is a scalar theory which describes the scattering of rays experimenting k internal reflections before leaving the spherical particle, but in an angular region close to the geometrical rainbow of order $p-1$. The Airy theory is known to have a very limited range of application ($\alpha > 5000, \theta - \theta_R < 0.5^\circ$). The scattered intensity is given by¹:

$$I(\theta, \alpha) = (\varepsilon_1)^2 \left[\frac{81}{(16\pi^2 h^4)} \right]^{1/6} \cos \tau_p \alpha^{7/3} A_i^2(z) / \sin(\theta_R) \quad (\text{A7})$$

where A_i is the Airy function and the argument z is:

$$z = (-q) \left[\frac{12}{h\pi^2} \right]^{1/3} \alpha^{2/3} (\theta - \theta_R) \quad (\text{A8})$$

θ_R is the rainbow angle, q an integer equal to $+1$ or -1 in such a way that the rainbow angle is defined between 0 and π , and verify $2\pi l + q\theta_R = (\tau_p - p\tau'_p)$ with l an integer. τ_p and τ'_p are the complements of incident and refraction angles of the incident rainbow ray for $p-1$ internal reflections. N is the refractive index

$$\tan \tau_p = \left[\frac{N^2 - 1}{p^2 - N^2} \right]^{1/2} \quad (\text{A9})$$

$$\tan \tau'_p = \left[\frac{p^2(N^2 - 1)}{p^2 - N^2} \right]^{1/2} \quad (10)$$

h is given by:

$$h = [(p^2 - 1)^2 / p^2(N^2 - 1)] [(p^2 - N^2) / (N^2 - 1)]^{1/2} \quad (\text{A11})$$

and ε_1 is given by:

$$\varepsilon_1 = (1 - r_1^2)(r_1)^{(p-1)} \quad (\text{A12})$$

with:

$$r_1 = \frac{\sin(\tau_p - \tau'_p)}{\sin(\tau_p + \tau'_p)}, \quad r_2 = \frac{\tan(\tau_p - \tau'_p)}{\tan(\tau_p + \tau'_p)} \quad (\text{A13})$$

The computational time of equation (A7) is very small when compared to Lorenz-Mie theory (Eqs (A1 and A2)), and essentially independent of the particle diameter.

¹ Note that Wang and van de Hulst use the angles τ and τ' which are the complements of incident and refraction angles of an incident ray ($\tau = \pi/2 - \theta_1$).

The Geometrical Optics.

The Geometrical optics is used to describe the path of the light interacting with an individual spherical particle. Let us assume a perfectly spherical particle with a diameter larger than the wavelength of the incident beam. We could use the Snell-Descartes and the Fresnel laws to describe the interaction between a beam and the particle. The radius of the sphere is a and its relative refractive index is N .

The incident beam is represented by a series of individual rays. If x is the distance between an incident ray and the beam axis, we introduce the impact parameter $\rho = \frac{x}{a}$, ρ varies between -1 to $+1$. This notation is useful as $\sin i = \frac{x}{a} = \rho$ as shown in figure 2.1.

Direction of scattering

According to van de Hulst's notation, the rays experiencing one reflection on the surface of the sphere are noted $p=0$, the rays purely refracted twice are noted $p=1$, the rays experiencing one internal reflection and two refractions are noted $p=2$, and more generally the rays experiencing k internal reflections and two refractions are noted $p=k+1$, as shown in figure 2.1.

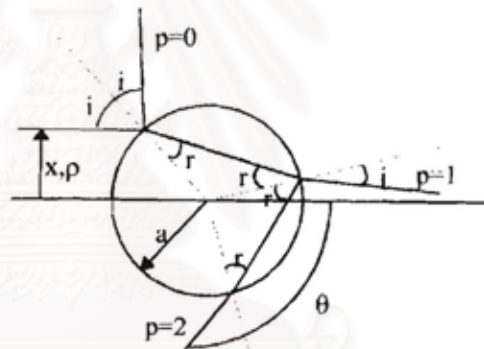


Figure A3 : Scheme to compute the deviation angle and definition of the different rays according to Van de Hulst.

The deviation of a ray by reflection is :

$$D = \pi - 2i = \pi - 2 \arcsin \rho \quad (\text{A.14})$$

To compute the deviation of a ray after k internal reflections, it should be remarked that the ray twice refracted is deviated of $(i-r)$ at each interface identified as $2(i-r)$ while at each internal reflection the deviation of the ray is $\pi - 2r$, we obtain a global deviation:

$$D_k(i) = k(\pi - 2r) + 2(i - r) \quad (\text{A.15})$$

Prediction of intensity.

To predict the intensity of a ray after each interaction with the particle, the Fresnel's coefficients must be used. Eight Fresnel coefficients are defined: 4 for one polarization, 4 for the other polarization. To write Fresnel coefficients, at a plane surface between two media i.e. 1 or 2, the following convention is used: x_{ij} where x stands for r (reflection) and t (transmission), i is the medium where the ray travels before impinging the surface and j is for the medium where the ray travels after impinging the surface.

- the external reflection : r_{11}^{pol}
- the refraction inside the droplet : t_{12}^{pol}
- the internal reflection inside the droplet : r_{22}^{pol}
- the refraction outside of the droplet: t_{21}^{pol} .

Then the intensity of the different kinds of rays, for a perfectly transparent particle, are given by:

- for externally reflected : $(r_{11}^{pol})^2$
- for a twice refracted ray : $(t_{12}^{pol} \cdot t_{21}^{pol})^2$
- for a ray refracted after k internal reflections:
 $(t_{12}^{pol} \cdot t_{21}^{pol} \cdot (r_{22}^{pol})^k)^2$

If the considered particle is not perfectly transparent, the attenuation of the light is predicted by the Beer's law. Then the length of the path of the light inside the particle must be computed. Remarking that all the chords are identical and equal to $2a \cos r$, the attenuation of the intensity for an absorbing particle is $e^{-\alpha(2a \cos r)^{k+1}}$.

phase

The absolute phase, or the phase difference between rays of different histories are of interest. To compute these phases, three effects must be taken into account:

- the change of phase at reflection (see Fresnel)
- the phase shifts due to focal lines
- the phase due to the length of optical path

Generally, the absolute phase is not relevant, but phase differences are. Then it is enough to compute the phase relatively to a reference ray. As a reference, a ray travelling in the medium surrounding the particle, going to the centre of the particle and from here in the direction of observation is selected.

- *Case of external reflection:*

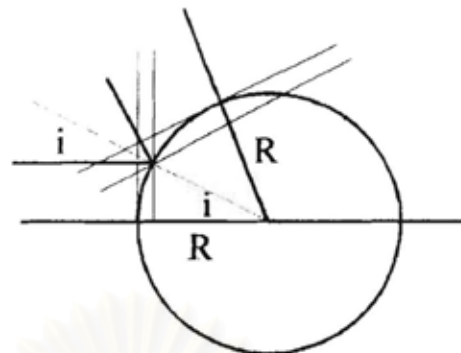


Figure A4: Scheme to compute optical path for reflected light.

As a reference path, the ray going to the center and then toward the ‘detector’ has been selected, while another ray is incident on the particle. When the two rays are parallel and in air, the two optical paths are identical. Afterward the path difference between the reference ray inside the particle and the reflected ray must be computed. For the reference ray inside the particle the optical path is equal to $2R$. For the ray reflected at the surface of the particle, the path is:

$$2(R - R \cos i) \quad (\text{A.16})$$

Then the difference is equal to:

$$\Delta\phi = 2(R - R \cos i) - 2R = -2R \cos i = -2R \sin \frac{\theta}{2} \quad (\text{A.17})$$

The sign (-) informs us that the path for the reflected light is shorter than for the path of reference.

- *Case of the ray experiencing two refractions:*

Figure 2.3 is a scheme presenting the reference path and a refracted light path.

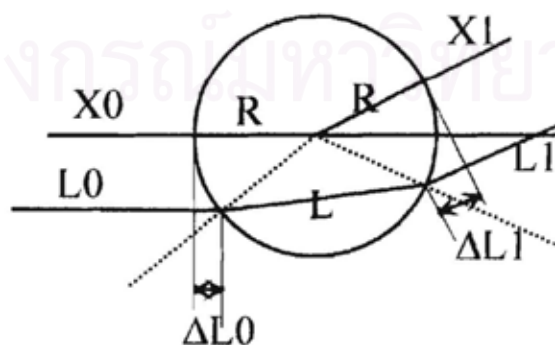


Figure A5: Scheme to compute optical path for refracted light

The reference path reads as:

$$D_{ref} = X0 + R + R + X1 \quad (A.18)$$

The refracted light path reads as:

$$D_{refract} = L0 + NL + L1 \quad (A.19)$$

or:

$$D_{refract} = X0 + \Delta L0 + NL + \Delta L1 + X1 \quad (A.20)$$

The difference of optical path is given by:

$$\Delta D = D_{ref} - D_{refract} = 2R - \Delta L0 - \Delta L1 - NL \quad (A.21)$$

as for the reflection case:

$$\Delta L0 = \Delta L1 = R - R \cos i \quad (A.22)$$

and L is given by :

$$L = 2R \cos r \quad (A.23)$$

The difference of path is :

$$\Delta D = 2R - 2R(1 - \cos i) - N2R \cos r = 2R(\cos i - N \cos r) \quad (A.24)$$

To have an expression which depends only on the deviation angle, the square of the difference of path is computed.

$$(\Delta D)^2 = (2R)^2 (\cos^2 i + N^2 \cos^2 r - 2N \cos i \cos r) \quad (A.25)$$

and using the classical relation between the square of sin and cos functions,

$$\begin{aligned} \cos^2 i &= 1 - \sin^2 i \\ N^2 \cos^2 r &= N^2 - N^2 \sin^2 r \end{aligned} \quad (A.26)$$

the following expression is obtained:

$$(\Delta D)^2 = (2R)^2 (1 - \sin^2 i + N^2 - N^2 \sin^2 r - 2N \cos i \cos r) \quad (A.27)$$

which can be rearranged as:

$$(\Delta D)^2 = (2R)^2 (1 + N^2 - (N^2 \sin^2 r + \sin^2 i) - 2N \cos i \cos r) \quad (A.28)$$

Remarking that:

$$(N \sin r - \sin i)^2 = N^2 \sin^2 r + \sin^2 i - 2N \sin r \sin i \quad (\text{A.29})$$

equation (A.25) reads now as:

$$(\Delta D)^2 = (2R)^2 \left(1 + N^2 - (N \sin r - \sin i)^2 - 2N \sin r \sin i - 2N \cos r \cos i \right) \quad (\text{A.30})$$

Noting that the term $(n \sin r - \sin i)$ is identically null, according with the second law of Descartes, using a bit of trigonometry, the final expression is:

$$(\Delta D)^2 = (2R)^2 \left(1 + N^2 - 2N \sin(i - r) \right) = (2R)^2 \left(1 + N^2 - 2N \sin\left(\frac{\theta}{2}\right) \right) \quad (\text{A.31})$$

Note: Geometrical optics predictions are not possible when two rays of the same kind are crossing, i.e. at all rainbows.

An example of predicted intensity of scattered light is shown in figure A.6.

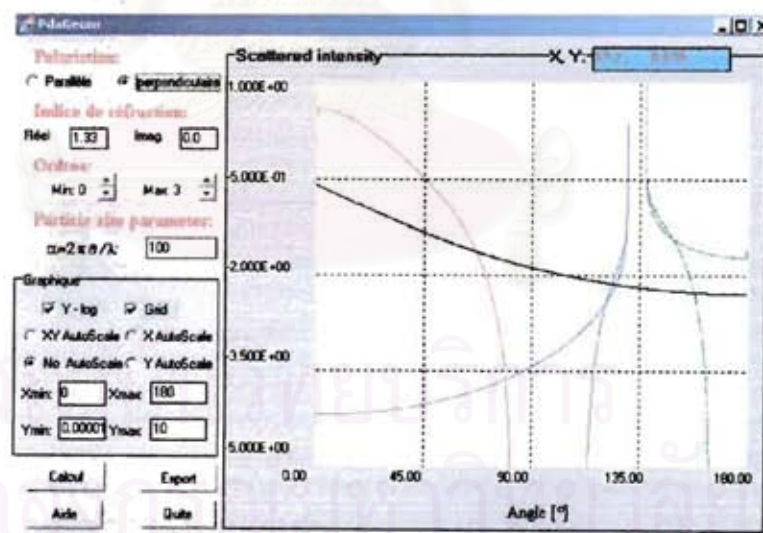


Figure A.6 : Example of scattered intensities predicted by geometrical optics. Software interface.



APPENDIX B
THE BRENT METHOD

สถาบันวิทยบริการ
จุฬาลงกรณ์มหาวิทยาลัย

Appendix B: The Brent method.

The Brent method is extensively described by Press et al in Numerical Recipes (section 9.3, page 352). The aim of the Brent method is to numerically solve equations as $f(x)=0$. The main fact is that this method asks only for the following conditions:

- Only the function $f(x)$ has to be known, its derivative $f'(x)$ is not used
- A domain $[x, y]$ on which the function will have only one zero
- The sign of the function must be different on $[x, z]$ and $[z, y]$, where z is the zero of $f(x)$,
- The accuracy at which z has to be determined.

The method is *guaranteed* (by Brent) to converge, so long as the function can be evaluated within the initial interval known to contain a root.

Brent's method combines root bracketing, bisection, and *inverse quadratic interpolation* to converge from the neighborhood of a zero crossing. While the false position and secant methods assume approximately linear behavior between two prior root estimates, inverse quadratic interpolation uses three prior points to fit an inverse quadratic function (x as a quadratic function of y) whose value at $y = 0$ is taken as the next estimate of the root x . Of course one must have contingency plans for what to do if the root falls outside of the brackets. Brent's method takes care of all that. If the three point pairs are $[a, f(a)]$, $[b, f(b)]$, $[c, f(c)]$ then the interpolation formula is:

$$x = \frac{[y - f(a)][y - f(b)]c}{[f(c) - f(a)][f(c) - f(b)]} + \frac{[y - f(b)][y - f(c)]a}{[f(a) - f(b)][f(a) - f(c)]} + \frac{[y - f(c)][y - f(a)]b}{[f(b) - f(c)][f(b) - f(a)]}$$

Setting y to zero gives a result for the next root estimate, which can be written as

$$x = b + P/Q$$

where, in terms of

$$R \equiv f(b)/f(c), \quad S \equiv f(b)/f(a), \quad T \equiv f(a)/f(c)$$

we have

$$P = S[T(R - T)(c - b) - (1 - R)(b - a)]$$

$$Q = (T - 1)(R - 1)(S - 1)$$

In practice b is the current best estimate of the root and P/Q ought to be a "small" correction. Quadratic methods work well only when the function behaves smoothly;



APPENDIX C
PUBLISHED AND CONFERENCE PAPERS

สถาบันวิทยบริการ
จุฬาลงกรณ์มหาวิทยาลัย



APPENDIX C1

**RAINBOW REFRACTOMETRY: ON THE
VALIDITY DOMAIN OF AIRY'S AND
NUSSENZVEIG'S THEORIES**

OPTICS COMMUNICATIONS 259 (2006) 7-13

สถาบันวิทยบริการ
จุฬาลงกรณ์มหาวิทยาลัย



Rainbow refractometry: On the validity domain of Airy's and Nussenzveig's theories

Sawitree Saengkaew^{a,b,*}, Tawatchai Charinpanitkul^{b,*}, Hathaichanok Vanisri^b,
Wiwut Tanthapanichakoon^b, Loïc Mees^a, Gérard Gouesbet^a, Gérard Grehan^a

^a UMR 6614/CORIA, CNRS/Université et INSA de Roue, n BP12, 76 800, Saint Etienne du Rouvray Cedex 8001, France

^b Center of Excellence in Particle Technology, Faculty of Engineering, Chulalongkorn University, Bangkok 10330, Thailand

Received 6 December 2004; received in revised form 13 June 2005; accepted 15 August 2005

Abstract

To measure the temperature of individual droplets or the average temperature in a section of a spray, the analysis of the light scattered around the rainbow angle provides an attractive approach. Up to now, the analysis of recorded rainbow signals has been carried out in the framework of the full Lorenz–Mie theory or of the Airy theory. In this paper, we consider four approaches (Lorenz–Mie, Debye, Airy and Nussenzveig approaches) to compute the light scattered around the rainbow angle, and we compare them in terms of accuracy and time-consumption. It is shown that the Complex Angular Momentum (CAM) theory proposed by Nussenzveig, modified by using empirical coefficients, allows one to accurately compute the light scattered around the rainbow angle in a large angular domain for particles with diameters as small as 10 μm .

© 2005 Elsevier B.V. All rights reserved.

1. Introduction

Nowadays, the measurement of thermophysical properties of sprays is of utmost interest. The aim is to measure the temperature and/or composition of moving droplets with diameters ranging typically from 1 to 200 μm . Different teams have developed various techniques to extract the temperature of spray droplets, including two-color Laser-Induced Fluorescence (LIF), Morphology Dependent Resonance spectroscopy (MDR), rainbow refractometry, extended Phase Doppler Anemometry (PDA) to name a few. It is worth mentioning that each of these techniques has advantages and limitations.

More particularly, rainbow refractometry relies on the sensitivity of the rainbow location with respect to the value of the refractive index. In a typical measurement, one re-

ords the light scattered around the rainbow angle, and one extracts the sizes (size distribution) and refractive indices of scattering particles from rainbow signal properties. The quality of the inversion depends on the quality of the theoretical model used to describe the scattered light. However, fast computations are also of interest because they offer the possibility of real time analysis. Therefore different approaches have to be compared in terms of accuracy and time-computation.

The paper is organized as follows. Section 2 recalls different theories which can be used to predict the light scattered around the rainbow angle by a single droplet. Section 3 is devoted to the comparison between predictions of rainbow signals from a single particle and global rainbow signals scattered by a cloud of water droplets by using Lorenz–Mie, Debye, Nussenzveig and Airy approaches. Nussenzveig approach is modified by using empirical correcting coefficients in order to obtain accurate and fast predictions in a large domain of scattering angles and refractive indices. This is supplemented by a discussion of the global rainbow technique. Section 4 is a conclusion.

* Corresponding authors. Tel./fax: +33 2 32 95 37 95 (S. Saengkaew); Tel./fax: +66 2 218 68 77 (T. Charinpanitkul).

E-mail addresses: sawitree@coria.fr (S. Saengkaew), ctawat@chula.ac.th (T. Charinpanitkul), grehan@coria.fr (G. Grehan).

2. Theoretical background

Rainbow is one of the most beautiful visual phenomena in nature. In the simplest case, it corresponds to the scattering of refracted rays impinging on to a spherical homogeneous sphere. To understand the physics of rainbow, an overview of theoretical approaches conducted by Adam [1] could be consulted. Other text books could also provide comprehensive information on the rainbow as by Grandy [2] or by Lee and Fraser [3]. More specifically, it is known that the Lorenz–Mie theory is a vectorial theory [4,5] describing rigorously the scattering of a plane wave by a perfectly spherical homogeneous particle. All scattering modes are included in the Lorenz–Mie theory but this theory does not distinguish between the different paths of the incident light inside the particle. Furthermore, the computational time increases dramatically with the size parameter and can become prohibitive, especially for inverse problems for which a huge number of iterations is necessary. In the far field approximation, the Lorenz–Mie theory provides expressions for electric field components which can be written as

$$E_\theta = \frac{iE_0}{kr} \exp(-ikr) \cos \varphi \sum_{n=1}^{\infty} \frac{2n+1}{n(n+1)} \times [a_n \tau_n(\cos \theta) + ib_n \pi_n(\cos \theta)], \quad (1)$$

$$E_\varphi = \frac{-E_0}{kr} \exp(-ikr) \sin \varphi \sum_{n=1}^{\infty} \frac{2n+1}{n(n+1)} \times [a_n \pi_n(\cos \theta) + ib_n \tau_n(\cos \theta)], \quad (2)$$

in which the generalized Legendre functions are defined by

$$\pi_n(\cos \theta) = \frac{P_n^1(\cos \theta)}{\sin \theta}, \quad \tau_n(\cos \theta) = \frac{dP_n^1(\cos \theta)}{d\theta} \quad (3)$$

and the Mie scattering coefficients are given by

$$a_n = \frac{\psi_n(\alpha)\psi'_n(\beta) - N\psi'_n(\alpha)\psi_n(\beta)}{\xi_n(\alpha)\psi'_n(\beta) - N\xi'_n(\alpha)\psi_n(\beta)}, \quad (4)$$

$$b_n = \frac{N\psi_n(\alpha)\psi'_n(\beta) - \psi'_n(\alpha)\psi_n(\beta)}{N\xi_n(\alpha)\psi'_n(\beta) - \xi'_n(\alpha)\psi_n(\beta)},$$

with the size parameter (α) defined as $\alpha = \pi d/\lambda$ and $\beta = N\alpha$, d the particle diameter, N the complex refractive index, λ the wavelength of the incident beam, k the wavenumber $k = 2\pi/\lambda$. Also r is the distance between the particle and the observation point, and E_0 is the amplitude of the incident field.

Next, the Debye theory [6–9] can be considered as a post processing of the Lorenz–Mie theory in which the coefficients a_n and b_n are written as series. Moreover, the Debye series provide the opportunity to distinguish the contribution of different kinds of “rays”, i.e. diffracted rays, externally reflected rays, rays which experiment $p-1$ internal reflections, ... before leaving the particle, by truncating a_n and b_n expressions according to

$$a_n = \frac{1}{2} \left[1 + R_n^{22} - \sum_{\rho=1}^{\infty} T_n^{21} (R_n^{11})^{\rho-1} T_n^{12} \right], \quad (5)$$

in which R_n^{22} , R_n^{11} , T_n^{21} and T_n^{12} are the reflection coefficient outside of the particle, the reflection coefficient inside of the particle, the coefficient of transmission from outside to inside the particle and the coefficient of transmission from inside to outside of the particle, respectively. In both Lorenz–Mie and Debye frameworks, scattered intensities are proportional to

$$I = E_\theta E_\theta^* + E_\varphi E_\varphi^*. \quad (6)$$

The two next theories considered below have been initially developed within a scalar framework and later generalized to a vectorial framework [10,11]. Nevertheless, because the polarization is fully mastered in rainbow experiments, we can focus our attention to the scalar version of these theories, for the appropriate polarization.

The Airy theory [12,13] in a scalar framework describes the scattering of rays leaving a spherical particle in an angular region close to the geometrical rainbow of order $p-1$. The Airy approach is known to have a very limited range of application [1,14]. The scattered intensity evaluated by Airy theory is given by

$$I(\theta, \alpha) = (\varepsilon_i)^2 \left[\frac{81}{(16\pi^2 h^4)} \right]^{1/6} \cos \tau_p \alpha^{7/3} Ai^2(z) / \sin(\theta_R), \quad (7)$$

in which Ai is the Airy function and the argument z is

$$z = (-q) \left[\frac{12}{h\pi^2} \right]^{1/3} \alpha^{2/3} (\theta - \theta_R) \quad (8)$$

with θ_R the rainbow angle, q an integer equal to $+1$ or -1 in such a way that the rainbow angle satisfies $2\pi l + q\theta_R = (\tau_p - p\tau'_p)$ with l an integer. τ_p and τ'_p are the complements of incident and refraction angles of the incident rainbow ray for $p-1$ internal reflections, given by

$$\tan \tau_p = \left[\frac{N^2 - 1}{p^2 - N^2} \right]^{1/2}, \quad (9)$$

$$\tan \tau'_p = \left[\frac{p^2(N^2 - 1)}{p^2 - N^2} \right]^{1/2}. \quad (10)$$

In Eq. (8), h is given by

$$h = \left[\frac{(p^2 - 1)^2 / p^2 (N^2 - 1)}{(p^2 - N^2) / (N^2 - 1)} \right]^{1/2} \quad (11)$$

and ε_i is given by

$$\varepsilon_i = (1 - r_i^2)(r_i)^{(p-1)} \quad (12)$$

with

$$r_1 = \frac{\sin(\tau_p - \tau'_p)}{\sin(\tau_p + \tau'_p)}, \quad r_2 = \frac{\tan(\tau_p - \tau'_p)}{\tan(\tau_p + \tau'_p)}. \quad (13)$$

The computational time of Eq. (7) is very small compared to that of Lorenz–Mie theory and essentially does not depend on the particle diameter.

Finally, a Complex Angular Momentum theory (CAM theory) developed by Nussenzveig [15–17] provides the possibility to transform series into integrals which are analytically solved by introducing various approximations, depending on the angular region and on the kind of ray of interest. It is found that, as a scalar theory CAM, is applicable within a range wider than for the Airy theory. In order to describe the first rainbow, Nussenzveig originally determines six angular regions requiring separate treatments and leading to six different formulae. Later he develops [18] a uniform asymptotic approximation which extends over an angular range including both limits (close to and far from the rainbow). Nevertheless the uniform asymptotic formula has been published with coefficients for water and its domain of application is limited to $|\theta - \theta_R| < \alpha^{-1/3}$, that is to say, for a 100 μm particle, the deviation from the geometrical rainbow must be smaller than 5°. In this paper we claim that the equation for the rainbow close to the geometrical rainbow (15) can be efficiently modified to evaluate the amplitude of scattered light in a large angular domain. For a totally reflected ray, the amplitude is evaluated by using

$$f_{\text{reflexion}}(\alpha, \theta) = -d \left(\frac{\sqrt{N^2 - \cos^2(\theta/2)} - \sin(\theta/2)}{\sqrt{N^2 - \cos^2(\theta/2)} + \sin(\theta/2)} \right) \times \exp(-2i\alpha \sin(\theta/2)) \left\{ 1 + \frac{i}{2\alpha} \left[\frac{1}{\sin^2(\theta/2)} - \frac{2N^2 - \cos^2(\theta/2)}{(N^2 - \cos^2(\theta/2))^{3/2}} + O(\alpha^{-2}) \right] \right\}. \quad (14)$$

Furthermore, for the first rainbow close to the rainbow angle, the rainbow amplitude can be evaluated by using

$$f_{\text{rainbow}}(\alpha, \theta) = \frac{d}{2} \cdot \frac{16e^{-i\pi/4}}{27\sqrt{3}} \left(\frac{\pi}{\sin \theta} \right)^{1/2} c(6s\alpha)^{1/2} \times \exp[6ic\alpha + is\alpha\epsilon + iA\alpha\epsilon^2 + O(\alpha\epsilon^3)] \times \left\{ [1 + O(\epsilon) + O(\alpha^{-1})] \times Ai \left[-\frac{c(2\alpha)^{3/2}\epsilon}{(3s)^{1/2}} (1 + B\epsilon + O(\epsilon^2)) \right] - \frac{iC}{(2\alpha)^{1/2}} [1 + O(\epsilon^2) + O(\alpha^{-1})] \times Ai' \left[-\frac{c(2\alpha)^{3/2}\epsilon}{(3s)^{1/2}} (1 + B\epsilon + O(\epsilon^2)) \right] \right\}, \quad (15)$$

in which

$$A = \frac{c(11c^2 - 15)}{36s^2}, \quad (16)$$

$$B = \frac{875c^6 - 1257c^4 + 657c^2 + 45}{8640(sc)^3}, \quad (17)$$

$$C = \frac{28 - 31s^2}{4c(3s)^{3/2}} \quad (18)$$

and

$$s = \sin \theta_{1R} = \left(\frac{4 - N^2}{3} \right)^{1/2}, \quad (19)$$

$$c = \cos \theta_{1R} = \left(\frac{N^2 - 1}{3} \right)^{1/2}. \quad (20)$$

Also θ_{1R} is the incident angle on the sphere generating the rainbow angle and ϵ is the difference between the observation angle and the rainbow angle ($\theta - \theta_R = \epsilon$). For rays emerging far from the rainbow angle, the amplitude of the scattered light is equal to the summation of two elementary amplitudes associated with geometrical optics rays, given by

$$f_2'(\alpha, \theta) = \frac{id}{2} \left\{ \left(\frac{\sin \theta_1}{\sin \theta} \right)^{1/2} \frac{(2N \cos \theta_1 \cos \theta_2)^{3/2}}{(N \cos \theta_2 - 2 \cos \theta_1)^{3/2}} \times \frac{(N \cos \theta_2 - \cos \theta_1)}{(N \cos \theta_2 + \cos \theta_1)^3} \exp[2i\alpha(2N \cos \theta_2 - \cos \theta_1)] \times \left[1 - \frac{iG(\theta, \theta_1)}{64\alpha \cos \theta_1} \right] \right\}_{\sin \theta_1 = \alpha}, \quad (21)$$

$$f_2''(\alpha, \theta) = -\frac{d}{2} \left\{ \left(\frac{\sin \theta_1}{\sin \theta} \right)^{1/2} \frac{(2N \cos \theta_1 \cos \theta_2)^{3/2}}{(2 \cos \theta_1 - N \cos \theta_2)^{3/2}} \times \frac{(N \cos \theta_2 - \cos \theta_1)}{(N \cos \theta_2 + \cos \theta_1)^3} \exp[2i\alpha(2N \cos \theta_2 - \cos \theta_1)] \times \left[1 - \frac{iG(\theta, \theta_1)}{64\alpha \cos \theta_1} \right] \right\}_{\sin \theta_1 = \alpha}, \quad (22)$$

in which

$$G(\theta_1, \theta) = 8 \cot \theta_1 \left[\cot \theta + \frac{\cot \theta_1}{2(2\chi - 1)} \right] + 6(9\chi - 11) - \frac{15}{2\chi - 1} - \frac{9}{(2\chi - 1)^2} + \tan^2 \theta_1 \left[56\chi^3 - 3\chi^2 + \frac{39}{2}\chi - \frac{79}{2} - \frac{33}{2(2\chi - 1)} - \frac{51}{4(2\chi - 1)^2} - \frac{15}{4(2\chi - 1)^3} \right] \quad (23)$$

with

$$\chi = \frac{\cos \theta_1}{\cos \theta_2}. \quad (24)$$

It is recalled that the angle of incident ray on a sphere and the angle of refracted ray are related by the following relation:

$$2\theta_2 - \theta_1 = (\pi - \theta)/2, \quad \sin \theta_1 = N \sin \theta_2. \quad (25)$$

Eq. (25) can be rewritten as

$$z^4 - 2mdz^3 - 4m(1 - m)z^2 + 4m^2dz + m^2d^2 = 0 \quad (26)$$

by setting

$$z = \sin \theta_1, \quad d = 2 \cos \left(\frac{\theta}{2} \right), \quad m = \frac{N^2}{4}. \quad (27)$$

The roots of Eq. (26) correspond to two incident angles for each scattering direction. The smaller root corresponds to a ray with an impact parameter smaller than the rainbow ray while the larger root corresponds to a ray with an impact parameter larger than the rainbow ray. The domain of application for Eqs. (21) and (22) is essentially defined by $\epsilon \gg \frac{2}{x(N^2-1)^2}$, that is to say for a water droplet with a size parameter equal to 500, ϵ must be larger than 0.25° .

For practical purposes, the computation time is essentially the same than for Airy theory but is about 300 times smaller than that for Lorenz–Mie theory.

3. Results and discussion

3.1. Investigation with a single droplet of water

To the best of our knowledge, Khare and Nussenzveig [18] are the only ones to provide a comparison between the CAM theory and other approaches for light scattering, close to the rainbow angle, in the range from 135° to 142° , for water. In global rainbow technique, the collecting angle can be larger while other previous works generally concentrate on the lower range of scattering diagrams. Therefore, in this work, we shall especially focus our attention, while still considering smaller angles, on the angular range from 142° to 150° . Figs. 1 and 2 display the normalized intensity vs. the scattering angle for a large angular range between 135° and 150° . The normalization has been defined in such a way that the maximum of the Debye predictions with $p=2$ is equal to unity. The same normalization factor has been afterward applied to the other approaches.

From Fig. 1, considering the main peak of primary rainbow, we observe a significant difference between Lorenz–

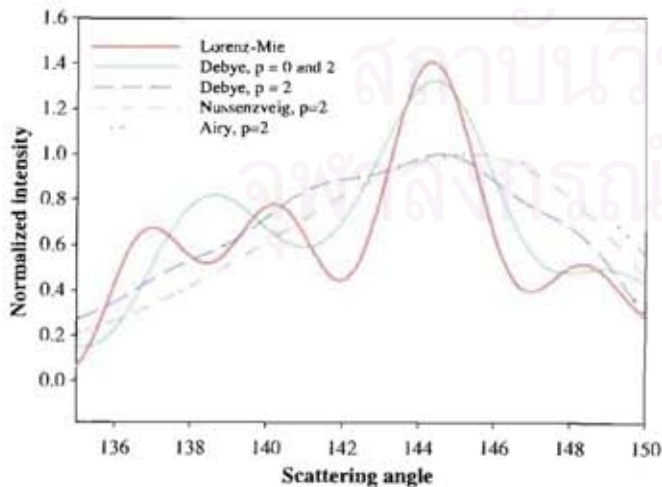


Fig. 1. Comparison of the rainbow ray intensity predicted by the Lorenz–Mie, Debye ($p=2$), Debye ($p=0$ and 2), Airy and Nussenzveig ($p=2$) theories. The size parameter is equal to 50 and the refractive index is equal to 1.33. The incident wavelength is $0.6 \mu\text{m}$.

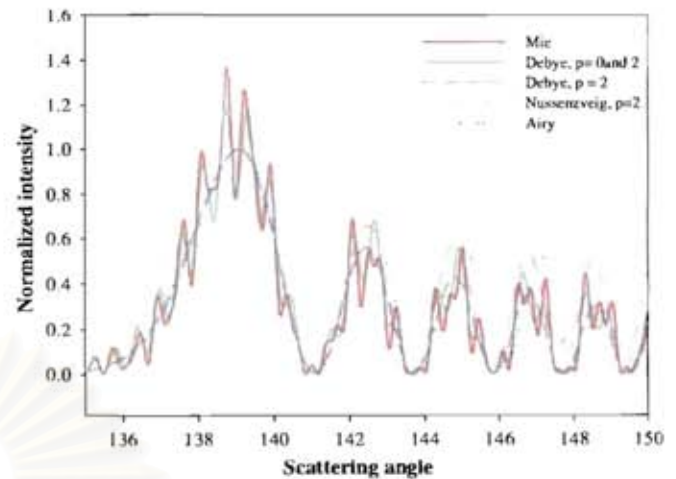


Fig. 2. Comparison of the rainbow ray intensity predicted by the Lorenz–Mie, Debye ($p=2$), Debye ($p=0$ and 2), Airy and Nussenzveig ($p=2$) theories. The size parameter is equal to 500 and the refractive index is equal to 1.33. The incident wavelength is $0.6 \mu\text{m}$.

Mie and Debye predictions (with $p=0$ and 2) to be attributed to interactions of higher order rays which are not negligible for the case of small enough particles (the size parameter is 50). Predictions from Debye (with $p=2$), Airy and Nussenzveig approaches perform more poorly. Although Nussenzveig and Airy predictions are in good agreement, they underestimate the scattered light intensity compared with Debye theory results within the angular range 136° – 142° and overestimate within the angular range 145° – 150° .

For the case of a larger particle with a size parameter equal to 500, Fig. 2 illustrates that the Airy and Nussenzveig predictions are identical and close to the Debye prediction for the main peak of the primary rainbow. Conversely, for the supernumerary bows both theories display intensities which are significantly larger than for Debye and Lorenz–Mie predictions (approximately twice for the fourth supernumerary bow). Concerning the peak locations, Nussenzveig predictions are nearly in phase with Debye predictions while Airy predictions progressively shift to higher angular values. This leads to the conclusion that Nussenzveig predictions are more accurate than Airy predictions especially when one considers supernumerary peak locations.

However, in order to obtain more accurate predictions for the light scattered far from the rainbow, a deeper discussion relying on Nussenzveig's equations (21) and (22) must be carried out, especially for the case when the scattering angle is larger than the geometrical optics rainbow angle. Fig. 3 compares the results obtained by using Eqs. (21) and (22) with results from Debye theory with $p=2$. It is observed that, for the increasing part of the main rainbow peak (scattering angle up to 139°), Nussenzveig predictions (with Eqs. (21) and (22)) exhibit significant differences with respect to Debye predictions. For higher scattering angles, an accurate enough prediction can be ob-

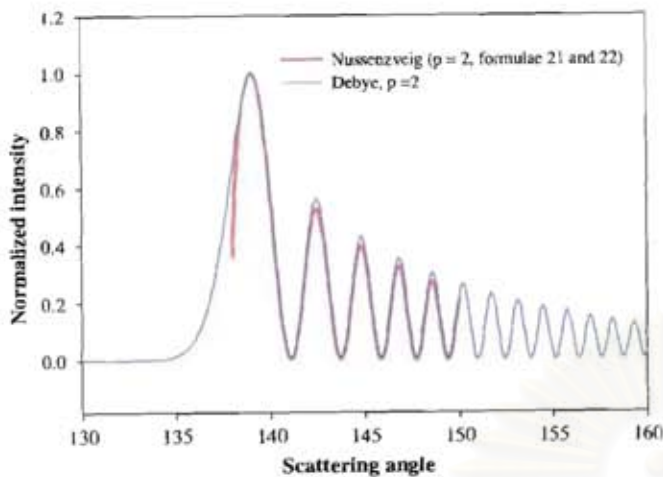


Fig. 3. Comparison between rainbow predictions by Nussenzweig ($p = 2$, formulae (21) and (22)) and Debye (with $p = 2$) theories. The size parameter is equal to 500 and the refractive indices is 1.33. The incident wavelength is $0.6 \mu\text{m}$.

tained but remain limited to a rather small computational domain. In the range from 139° to 151° , the predictions based on Eqs. (21) and (22) are more accurate than from Eq. (15). The locations of the supernumerary bows are very satisfactorily predicted but the intensity is underestimated by about 5%. Nevertheless, limitations towards high values of the scattering angle can be a penalty to accurately enough fit experiments in a large angular domain.

Relying on these observations, correction coefficients for intensity predictions with Nussenzweig theory are evaluated by using the following procedure:

- Compute normalized scattering diagrams for particle sizes ranging from 10 to $100 \mu\text{m}$ in the framework of Debye theory ($p = 2$) and with Eq. (15) of Nussenzweig theory.
- Then, compute the argument z of the Airy function as a function of the incident wavelength, particle diameter, particle refractive index and scattering angle.
- Plot the normalized scattered intensities obtained from Debye and Nussenzweig predictions versus z .
- Finally compute the ratio of the Debye normalized intensity over the Nussenzweig normalized intensity. The result is an empirical correction coefficient.

Fig. 4 displays the ratio of scattering intensity predicted by the Debye theory over Nussenzweig normalized intensity against z with particle size as a parameter. For these computations, the material is water with N equal to 1.33. Coefficients of linear regressions to be used for modified Nussenzweig prediction are displayed in Table 1.

After insertion of the empirical coefficients into Nussenzweig approach, it can be observed from Fig. 5 that the modified Nussenzweig predictions lead to scattering diagrams which are in excellent agreement with the ones from Debye theory with ($p = 2$) for all investigated particle sizes.

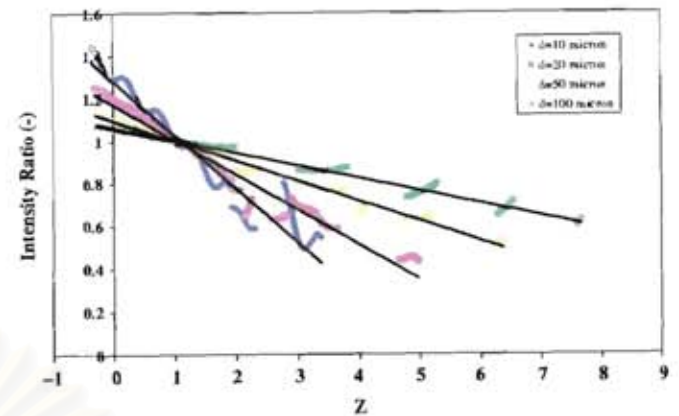


Fig. 4. Ratio of Debye normalized intensity over Nussenzweig normalized intensity for various particle sizes.

Table 1
Coefficients of linear regressions for modified Nussenzweig predictions

Particle size	Linear regression
$d < 15 \mu\text{m}$	$y = -0.2523z + 1.2807$
$15 \mu\text{m} < d < 30 \mu\text{m}$	$y = -0.1642z + 1.1722$
$30 \mu\text{m} < d < 75 \mu\text{m}$	$y = -0.0946z + 1.0982$
$75 \mu\text{m} < d < 125 \mu\text{m}$	$y = -0.0593z + 1.0639$

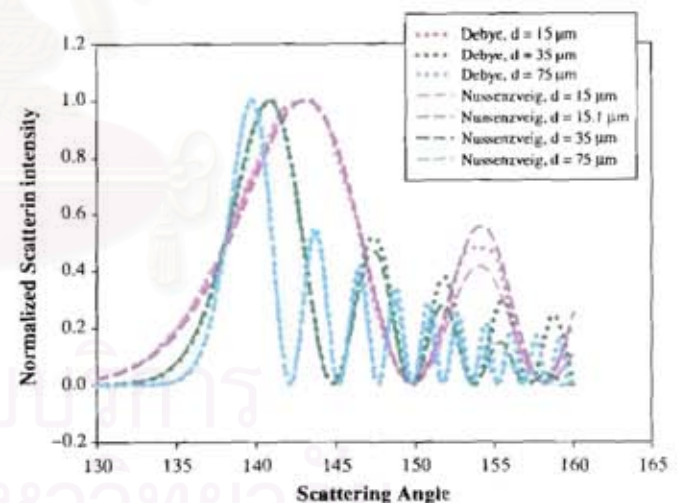


Fig. 5. Comparison of scattering diagrams obtained from the Debye and Nussenzweig (with modified formulae (15)) predictions for various particle sizes.

Although not shown here, computations carried out for different refractive indices between 1.3 and 1.4 confirm that the insertion of the correcting coefficients is efficient to quantitatively predict the rainbow structure within the angular domain from 130° to 160° . Also, sensitivity tests have been carried out at boundary between correcting coefficient domains. For instance, Nussenzweig predictions for $d = 14.9 \mu\text{m}$ and $15.1 \mu\text{m}$ depart of about 10% from Debye predictions for $15 \mu\text{m}$.

Moreover, to predict the reflected light intensity around the rainbow angle, Alexander's dark band has to be discussed in a specific way due to the fact that intensities predicted by Airy and Nussenzveig approaches decreases there very fast due to the absence of internal reflections. Fig. 6(a) displays the scattered intensity versus the scattering angle in the angular range from 130° to 160° . Debye (with $p=2$) and Nussenzveig approaches (with $p=2$) fail to predict the scattering intensity in Alexander's dark band. Interestingly enough, for scattering angles larger than 135° , can consistent predictions between Lorenz–Mie, Debye and Nussenzveig approaches can be obtained as shown in Fig. 6(b). Let us also note that different refracted rays can interfere, creating fringes of higher frequencies called “ripples”. These fringes carry some amount of information which can be useful for more accurate particle size measurements [19,20]. Also, Nussenzveig and Debye predictions with $p=0$ and 2 exhibit a consistent agreement within the scattering angle range smaller than 154° , which is a suitable range for water droplet measurements.

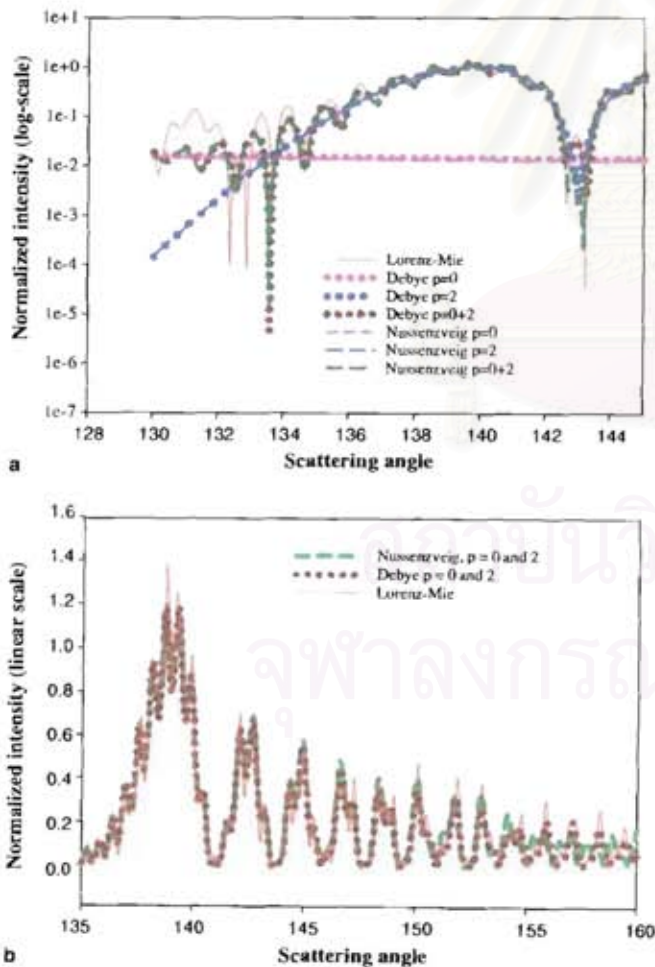


Fig. 6. Comparison of normalized intensities predicted by the Lorenz–Mie, Debye ($p=0$ and 2), Nussenzveig ($p=0$ and 2). The size parameter is equal to 500 and the refractive index is equal to 1.33. The incident wavelength is $0.6 \mu\text{m}$.

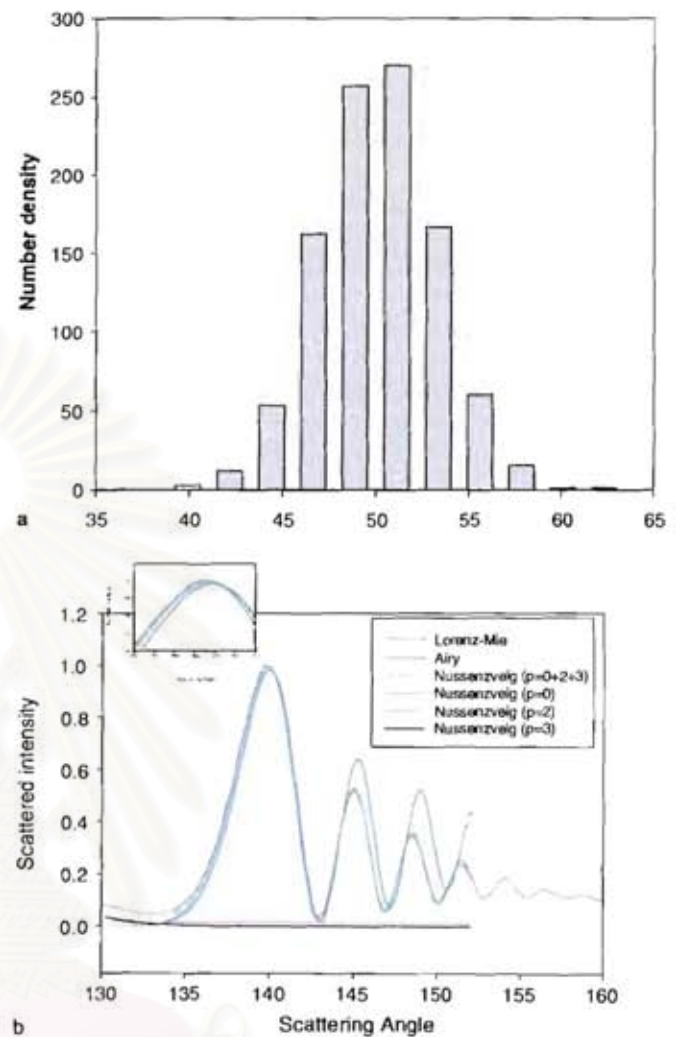


Fig. 7. (a) Assumed size distribution of water droplets used to assess the quality of different approaches. (b) Comparison between global rainbow intensities from Lorenz–Mie, Airy, and Nussenzveig theories.

3.2. Investigation for a cloud of water droplets

The light scattered around the rainbow angle by a cloud of water droplets is used for global rainbow refractometry. The reference signal, computed in the framework of the full Lorenz–Mie, is compared to predictions from Airy and Nussenzveig theories. The rainbow generated by refraction through droplets of water with N equal to 1.33 is used to check aforementioned approaches. The droplet size distribution with a Gaussian shape shown in Fig. 7(a) is used to assess the quality of the different approaches under study. Fig. 7(b) displays the global rainbow predicted by each approach under study. Red,¹ blue, green, pink, light blue and black curves represent scattered intensities from Lorenz–Mie, Airy, Nussenzveig with $p=0$, 2 and 3, Nussenzveig with $p=0$, Nussenzveig with $p=2$ and Nussenzveig with $p=3$, respectively. For small scattering angles

¹ For interpretation of color in all figures, the reader is referred to the web version of this article.

(between 130° and 135°), departures of predicted values from Lorenz–Mie results are significant due to the role of the secondary rainbow. This observation suggests that more refined empirical coefficients could be useful to generate better agreements in this range of angles.

Within the main rainbow peak domain, all predictions are essentially in good agreement. Nevertheless, a closer examination of displayed results reveals that Airy predictions globally shift toward larger scattering angles. Moreover, for Nussenzveig predictions, with the contribution of the secondary rainbow taken into account, the predicted results are in perfect agreement with Lorenz–Mie predictions. Nevertheless, for larger scattering angles, is observed that modified Nussenzveig predictions are better with respect to Airy predictions which produce overestimated intensities and supernumerary peaks shifts for larger scattering angles.

4. Conclusion

Rainbow refractometry analysis can provide accurate and fast measurements of particle size and refractive index requiring on the analysis of the light scattered around the rainbow angle. A theoretical description can be carried out by using the CAM theory as used by Nussenzveig. A modified Nussenzveig approach with empirical correction coefficients can successfully predict the light scattered in large range of angles, refractive indices and particle sizes. More specifically, the modified Nussenzveig theory provides predictions of rainbow refractive intensities close to Lorenz–Mie theory predictions but it requires dramatically smaller computation times, similar to the computation times in Airy approach.

Acknowledgments

This work is partially supported by the European Community by programs Interreg III, “the intelligent en-

gine II” and the MUSCLES.G4RD-CT-2002-00644 S.S. Another partial support has been obtained from the French Ministère délégué à la Recherche et aux Nouvelles Technologies in the framework of “cotutelle de thèse” and Royal Golden Jubilee Scholarship of Thailand Research Fund. T.C., H.V. and W.T. also acknowledge a partial support from TRF-RTA grant for Prof. W. Tanthapanichakoon. University-Industry Collaborative Research Fund for CEPT from Chulalongkorn University is also gratefully acknowledged for its financial support.

References

- [1] J.A. Adam, *Phys. Rep.* 356 (2002) 229.
- [2] W.T. Grandy, *Scattering of Waves from Large Spheres*, Cambridge University Press, 2000.
- [3] R.L. Lee, A.B. Fraser, *The Rainbow Bridge*, Pennsylvania State University Press, 2001.
- [4] L. Lorenz, *Vidensk. Selk. Skr.* 6 (1890) 1.
- [5] G. Mie, *Ann. der Phys.* 25 (1908) 377.
- [6] P. Debye, *Ann. der Phys.* 4 (30) (1909) 57.
- [7] J.A. Lock, C.L. Adler, *J. Opt. Soc. Am. A* 14 (6) (1997) 1316.
- [8] J.A. Lock, *J. Opt. Soc. Am. A* 10 (4) (1993) 693.
- [9] G. Gouesbet, *Part. Part. Syst. Char.* 20 (2003) 382.
- [10] R.L. Lee, *Appl. Opt.* 37 (1998) 1506.
- [11] G.P. Können, J.H. de Boer, *Appl. Opt.* 18 (12) (1979) 1961.
- [12] R.T. Wang, H.C. van de Hulst, *Appl. Opt.* 30 (1) (1991) 106.
- [13] J.D. Jackson, *Phys. Rep.* 320 (1999) 27.
- [14] H.C. van de Hulst, *Lighth Scattering by Small Particles*, Dover Publication, Inc., New York, 1957.
- [15] H.M. Nussenzveig, *J. Math. Phys.* 10 (1) (1969) 82.
- [16] H.M. Nussenzveig, *J. Math. Phys.* 10 (1) (1969) 125.
- [17] H.M. Nussenzveig, *Diffraction Effects in Semiclassical Scattering*, Cambridge University Press, 1992.
- [18] V. Khare, H.M. Nussenzveig, *Phys. Rev. Lett.* 33 (16) (1974) 976.
- [19] X. Han, K.F. Ren, L. Mees, G. Gouesbet, G. Gréhan, *Opt. Commun.* 195 (2001) 49.
- [20] X. Han, K.F. Ren, Z.S. Wu, F. Corbin, G. Gouesbet, G. Gréhan, *Appl. Opt.* 37 (36) (1998) 8498.



APPENDIX C2

**PROPERTIES OF SPRAYS CREATED BY AN
ULTRASONIC NOZZLE.**

**9TH INTERNATIONAL CONFERENCE ON
LIQUID ATOMISATION AND SPRAY SYSTEMS,
ICLASS 2003, SORRENTO, ITALY, JULY 13-18.**

สถาบันวิทยบริการ
จุฬาลงกรณ์มหาวิทยาลัย

Properties of sprays created by an ultrasonic nozzle.

Saengkaew S.^{1,3}, Mounaïm-Rousselle C.², Meunier-Guttin-Cluzel S.³,
Boulnois G.³, Méès L.³, Vanisri H.¹, Gréhan G.³

1. Particles and Technology Laboratory, Chulalongkorn University, Bangkok, Thailand

2. LME, IPO – ESEM, Université d'Orléans, France

3. LESP, UMR 6614/CORIA, CNRS/Université et INSA de Rouen, Saint Etienne du Rouvray, France

This paper is devoted to the study of spray characteristic created by ultrasonic nozzles. The major advantages of such nozzle are to create a spray with small size, narrow distribution and low velocity. Several optical techniques are applied to extract information close and far from the orifice.

1. Introduction

Ultrasonic nozzles use the ultrasonic vibrations to generate the liquid atomization. In contrast to conventional spraying mechanisms which rely on relatively high hydraulic pressure or high velocity gas streams for atomization of liquid media, ultrasonic nozzles could produce very fine droplets with a relatively uniform diameter, while no requiring high air compressor or high pressure pump to produce such small droplets. The atomization by the ultrasonic nozzle is possible even with a low liquid flow rate. Moreover, there is no problem of clogging because of the relative large aperture of the orifice. Therefore, ultrasonic nozzle spray technology is used in a wide range of industrial and research applications such as medical nebulizers, combustion and drying, paint spraying systems, encapsulation and surface coating [1,2,3]. Nevertheless, a better understanding of the characteristics of the spray produced by such ultrasonic nozzles is necessary to improve their use. The objective of this research is to study the behavior of a spray produced by such a nozzle.

The paper is organized as follow. Section 2 describes the nozzle used and its working conditions. Section 3 is devoted to the measurements. These measurements characterize the spray just at the orifice output (size, velocity, temperature) and far from the orifice (size and velocity). The section 4 consists of a conclusion where the behavior of the nozzle for other working conditions and liquids is considered.

2. Experimental set up

Figure 1 shows that an ultrasonic nozzle structure is an acoustically resonant device consisting of a pair of piezoelectric ceramic rings sandwiched between a backing piece (1) and a mechanical transformer (2). The atomization take place at the free end of the mechanical transformer forms called atomizing surface. The liquid is delivered to this surface through the hole (3).

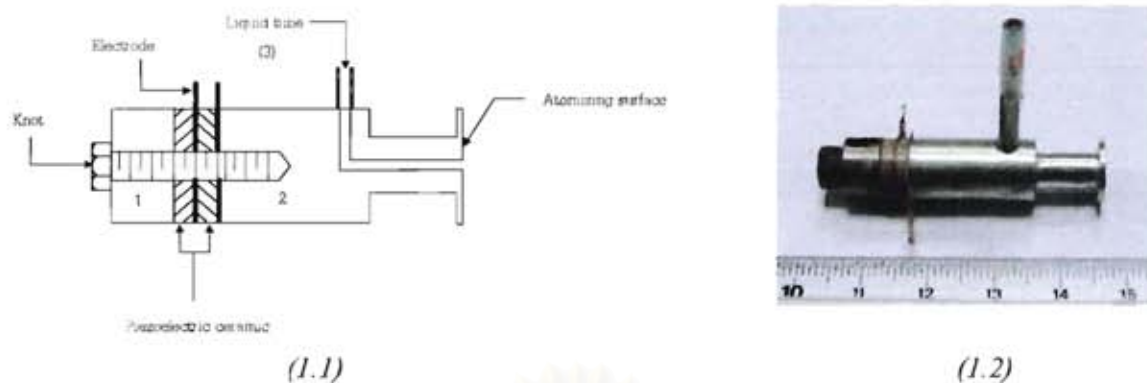


Fig. 1 : 1.1) Scheme of the ultrasonic nozzle. 1.2) Photography of the studied nozzle.

Ultrasonic nozzle used piezoelectric ceramic to generate ultrasonic energy by transforming electrical energy to mechanical energy in order to vibrate an atomizing surface. At the resonance frequency, which is a function of geometrical characteristics of the nozzle, the direction of vibration is perpendicular to the atomizing surface. When a liquid is introduced on to the atomizing surface, it spreads and forms a thin liquid film. The liquid film adsorbs a fraction of the vibration energy creating a unique wave pattern on the surface, known as capillary wave. When the amplitude of the underlying vibration is increased, the amplitude of the capillary waves increases correspondingly. Finally, when the critical amplitude is reached the height of the capillary wave exceeds that required to maintain its stability. The wave collapses and tiny drops of liquid are ejected from the top of the degenerating waves [3].

3. Measurements

3.1 PDA measurements

A first experiment has been carried out, measuring the size and the velocity of the droplets at 5 mm from the orifice on the axis of the canal orifice (see figure 1). The PDA configuration used was the standard PDA configuration and the processing of the events was carried out by using the Dantec PDA (58N80-58N81) and Dantec software. The duration of the measurement was about 5 minutes for 500,000 events. The experiment starts with the excitation of the nozzle.

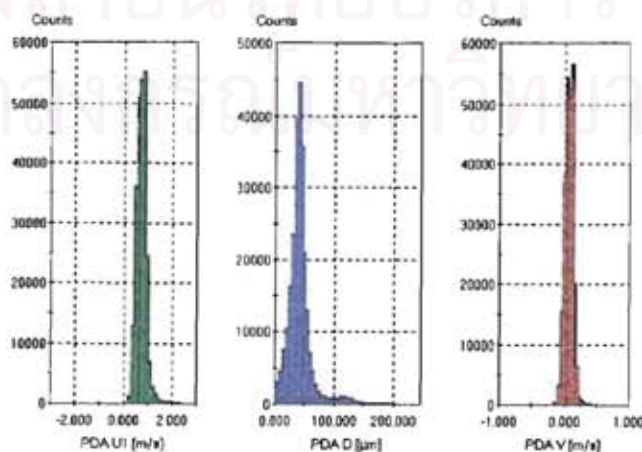


Fig. 2: Example of PDA measurement at 5 mm from the orifice.

Figure 2 displays histograms of longitudinal velocity, diameter and transverse velocity for a flow rate of $1.1 \text{ cm}^3/\text{min}$ and excitation frequency is 46 kHz , in the case of water. A nearly perfect Gaussian distribution of the particle size characterizes the spray. The spray parameter are $D_{10} = 46.68 \mu\text{m}$ and $D_{32} = 63.9 \mu\text{m}$.

Then the following post-processing has been applied to the measurement series:

1. The measurement series has been divided in windows of equal duration.
2. Each temporal window has a duration equal to 100 ms.
3. For each window, we compute and record: the number of particles, the average velocities (longitudinal and transverse), and the average diameter.

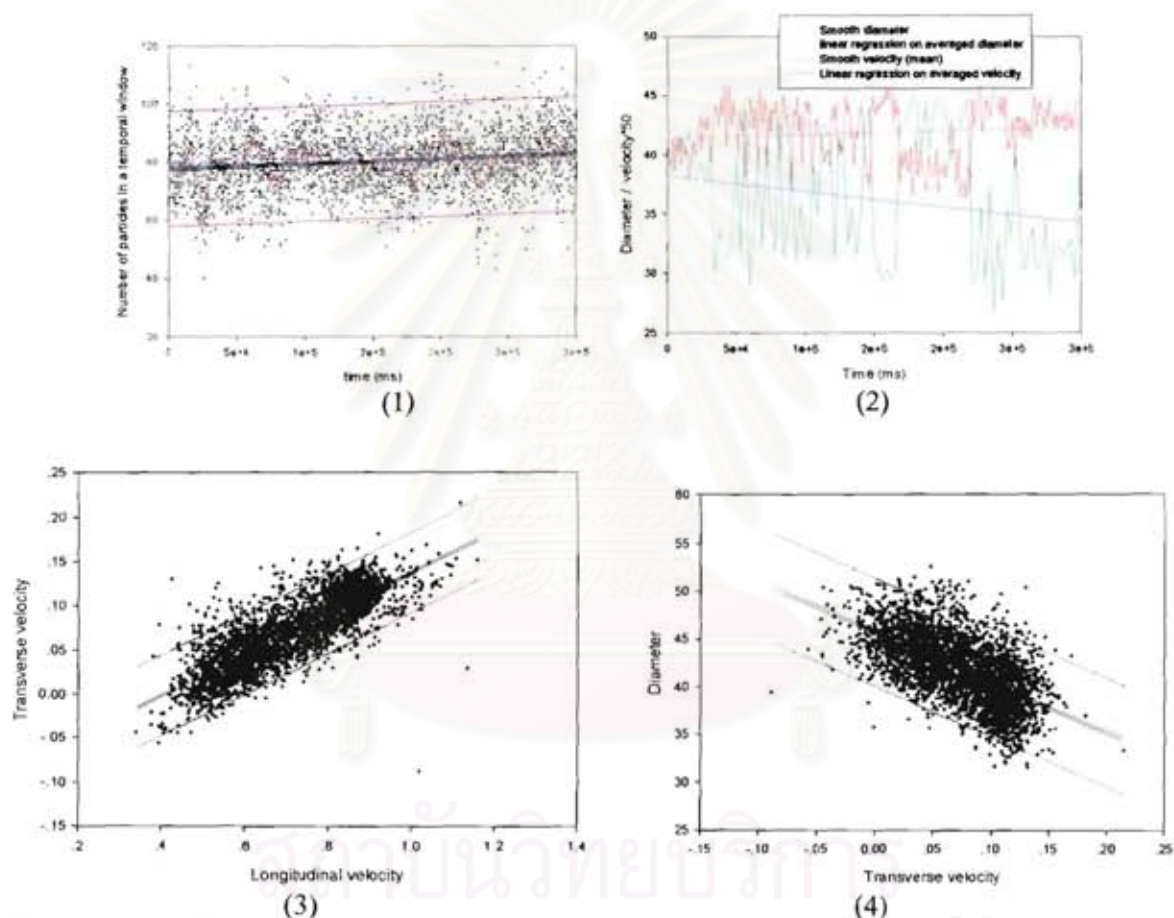


Fig. 3 : Processing of PDA temporal series. 3.1) number of particles versus time, 3.2) Longitudinal velocity and diameter versus time, 3.3) Transverse velocity versus longitudinal velocity, 3.4) diameter versus transverse velocity

The results are plotted in figure 3. Figure 3-1 displays the number of measured particles versus time. From this figure, it is shown that the flow of particles is essentially constant at this location (around 80 particles every 100 ms). Figure 3-2 displays the average mean velocity and the average diameter versus time. From these figures it can be concluded that:

1. The longitudinal velocity is small, about 60-80 cm per second.
2. A correlation between size and longitudinal velocity exists: the biggest the particles, the smallest the velocity.
3. The correlated size/velocity evolves on a short time scale.

4. A continuous evolution at long time scale of the size and velocity appears (see the linear regressions)

In order to confirm these remarks, the transverse velocity versus the longitudinal velocity and the diameter versus transverse velocity has been plot (see figures 3.3 and 3.4). A strong correlation still exists between the longitudinal and the transverse velocity as well as between the transverse velocity and the diameter.

From these results it can be explained that the changes of size at short time scale is due to the effect of a transversally fluctuating flow, while long time evolution must have another origin. We postulate that this effect could be related to the change of the nozzle temperature due to the excitation. The study of this effect is the aim of the next section.

3.2 Temperature measurements

3.2.1 Nozzle temperature

The temperature of the nozzle has been recorded by using an infra red camera (ThermalCAM PM595 LWB with objective of 24° from FLIR Systems). Figure 4.1 displays maps of the nozzle temperature at the beginning of the excitation and 15 minutes later while figure 4.2 displays the temperature at the nozzle orifice versus time.

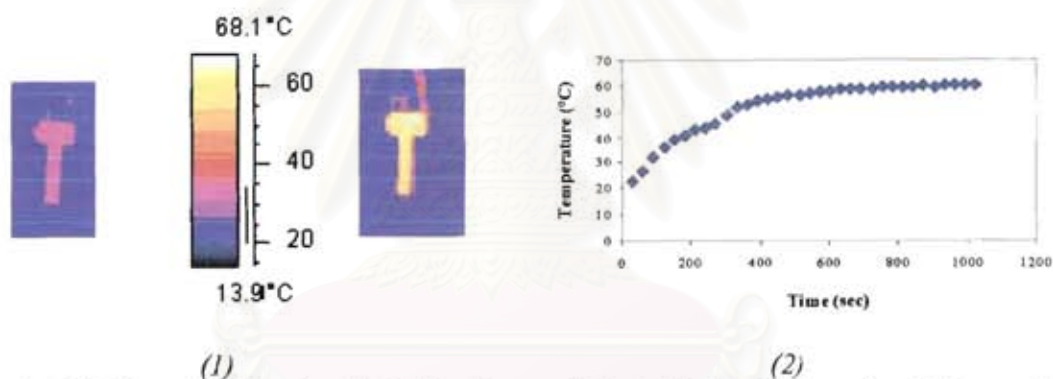


Fig. 4 : 4.1) Maps of infrared emission for the nozzle just at the beginning of excitation and 15 minutes later . 4.2) Temperature at the nozzle orifice versus time.

A strong increase of the nozzle temperature is observed. The increase of the nozzle temperature is estimated from the infrared images (after a calibration) to be of about 40°C. This temperature change of the nozzle will induce a temperature evolution of the liquid droplets. The next section is then devoted to temperature measurements of the droplets spray near the nozzle orifice.

3.2.2 Droplets temperature

To measure the temperature of the droplets just at the orifice of the nozzle a global rainbow refractometry experiment has been carried out. The concept of the global rainbow refractometry has been introduced by van Beeck and Riethmuller [4], from whom the complete details of the technique could be obtained. Here we just recall that contrary to the rainbow refractometry on individual droplet which is very sensitive to departure from perfect sphericity, the global rainbow created by a large number of droplets is insensitive to such an effect, under the assumption that the orientation of the droplets is fully random and that the

ellipticity of the particles is small enough to verify that the individual rainbow are only angularly shifted [5].

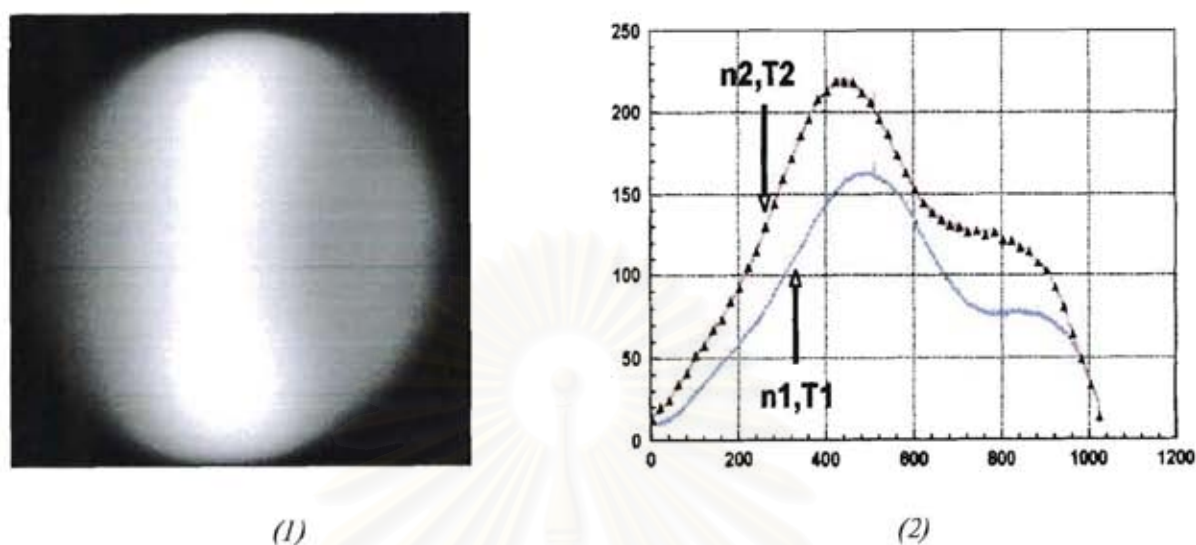


Fig. 5 : Example of global rainbow measurement at 5 mm of the nozzle orifice. 5.1) direct record of the light scattered around the first rainbow angle. 5.2) Comparison between global rainbow signatures just at the beginning of the excitation of the nozzle and 5 minutes later. The temperature T_1 and T_2 are estimated to 20°C and 50°C .

Figure 5.1 is an example of a recorded experimental rainbow while figure 5.2 displays the recorded intensity versus the pixel number (scattering angle), at the beginning of the excitation and 5 minutes later. From such curves the temperature evolution of the droplet can be extracted. In this case, the temperature is estimated to 50°C , essentially in agreement with the results of the previous section.

To this increase of the liquid temperature is connected an evolution of its physical properties, which could induce the observed diameter and longitudinal velocity evolutions at long time. This is a point still under study. Nevertheless the results reported below are sufficient to demonstrate that these ultrasonic nozzles are well adapted to create a stable, well-masterized cloud of small droplets with a low velocity, which could be easily transported by an accessory flow. When the cloud of droplets dilutes, its properties (mainly its size) may evolve and could not be longer measured by PDA as the waiting time between events increases prohibitively. The next section is devoted to the presentation of some Interferometric Laser Imaging Droplets Sizing (ILIDS) results obtained at 50 cm from the orifice in a free fall configuration.

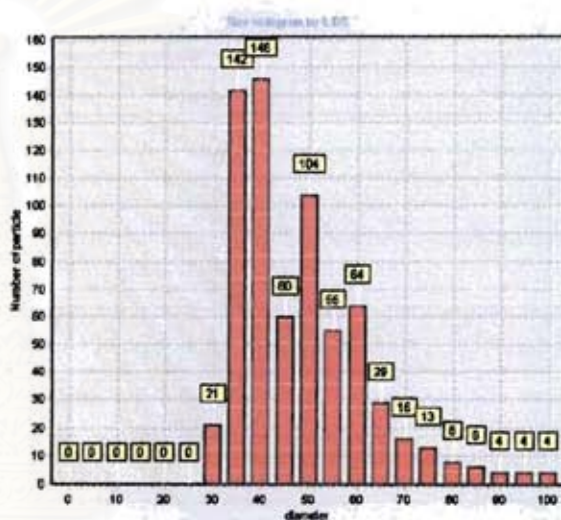
3.3 Measurement far from the orifice

To measure the characteristics of the spray far from the orifice, a suitable technique is ILIDS which has been introduced by Glover et al [6], and then studied and developed by several teams [7-11]. The measurement principle of ILIDS is based on the record of an off-axis, out-of-focus image. The size of the particle image is only a function of the lens aperture and the magnitude of the out-of-focus. The size information is coded in the fringes created by the interferences between the light reflected and refracted by the droplets. To study the spray at 50 cm from the orifice, a classical PIV set up (it is a classical TSI PIV set-up and the PIV processing is carried out by Matlab toolbox) is used. The only difference between a classical PIV measurement and an ILIDS measurement is that the recording camera has to be moved

towards the laser sheet (by 5 cm here) to obtain out-of focus configuration. The time between two pulses is equal to $600 \mu\text{s}$ and the repetitiveness is of 10 couples of images by second. Figure 6.1 displays such a recording (one image of a couple). By analyzing such images with devoted software, the size distribution displays in figure 6.2 has been obtained ($D_{10} = 50 \mu\text{m}$). This size distribution well compares with the size distribution obtained by PDA as previously shown in figure 2. Furthermore, by applying a classical PIV processing to the couple of out-of-focus couple of images it is possible to extract a map of velocities (the arrows in figure 7). The velocity is measured to run from about 0.1 m/s to 0.3 m/s which is in agreement with the free fall velocity for drops of this size, showing that the injection velocity is no longer dominating. Furthermore, from image as the one displayed in fig. 6.1, it is evident that the particles are not uniformly or randomly distributed but are organized in assembly of drops with close characteristics (velocity and size).



(1)



(2)

Fig. 6: ILIDS measurements. 6.1) Example of a recorded ILIDS image, 6.2) Size histogram obtained by analyzing 50 ILIDS images

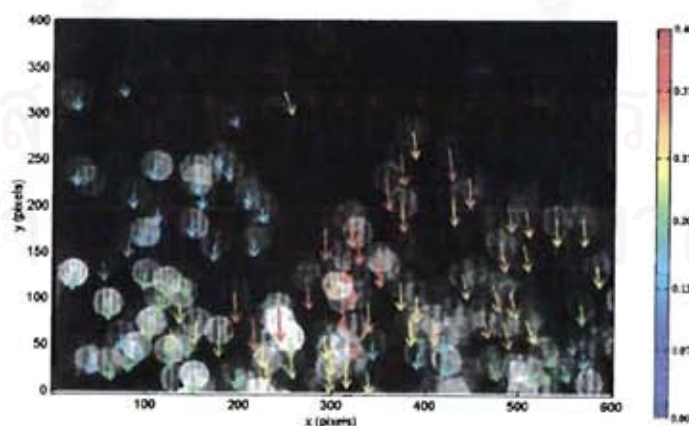


Fig. 7: Example of a PIV/ILIDS map. The arrows give the velocities (direction and amplitude). From the fringes the size of the droplets could be extracted while the velocity is obtained from standard PIV software

4. Conclusion

The behaviour of a water spray created by an ultrasonic nozzle has been studied. To reach this aim, an experimental procedure has been developed to measure the spray characteristics near the orifice (velocity, size, temperature) as well as far from it (velocity and size). The spray characteristics presented here for water droplets have also been obtained for other liquids and other flow rate.

5. Acknowledgements

This work is a part of a cotutelle PhD thesis between Bangkok and Rouen which is supported by INSA of Rouen and University of Rouen and S.S. and H.V. received partial financial support from Thailand Research Fund (TRF-RTA of Dr.Wiwut Tanthapanichakoon) and University-Industry Research Collaboration Project in Particle Technology FY2002 of Chulalongkorn University.

References

- [1] Toop M.N. and Eisenklam, 1972, *Ultrasonics*, 10 127-133
- [2] Lacas F., Versaevel and Scouflaire P., 1994, *Part. Part. Syst. Charact.*, 11 166-171
- [3] Berger H.L. 1998. *Ultrasonic Liquid Atomization Theory and Application*. New York: Partridge Hill Publishers.
- [4] van Beeck J.P.A.J. and Riethmuller M.L., 1996, *Applied Optics*, 35 2259-2266
- [5] Han Y.P., Mees L., Ren K.F., Gouesbet G., Wu S.Z. and Gréhan G., 2002, *Optics Communications*, 210 1-9,
- [6] Glover A.R, Skippon S.M. and Boyle R.D., 1995, *Applied Optics*, 34, 36 8409—8421
- [7] Mounaïm-Rousselle C., Pajot O., 1999 , *Particle and Particle Systems Characterization* 16 160-168
- [8] Girasole T., Ren K.F, Lebrun D., Gouesbet G. and Gréhan G., 2000, *Journal of Visualization*, 3, 2 195-202
- [9] Kobayashi T., Kawaguchi T. and Maeda M., 2000, Measurement of spray flow by an improved interferometric laser imaging droplet sizing (ILIDS) system, 10 th International Symposium on applications of laser techniques to fluid mechanics,
- [10] Calabria R. and Massoli P., 2000, Experimental study of droplets in evaporating regime by 2D scattering analysis, , 10 th International Symposium on applications of laser techniques to fluid mechanics,
- [11] Damaschke N., Nobach H., Nonn T., Semidetnov N. and Tropea C., 2002, Size and velocity measurements with the global phase Doppler technique, 11th International Symposium on applications of laser techniques to fluid mechanics,



APPENDIX C3

**MEASUREMENT OF DROPLET PROPERTIES BY
PDA AND RAINBOW REFRACTOMETRY**

**THE 4TH INTERNATIONAL SYMPOSIUM ON
MEASUREMENT TECHNIQUES FOR
MULTIPHASE FLOWS SEPT.10-12, 2003,**



สถาบันวิทยบริการ
จุฬาลงกรณ์มหาวิทยาลัย

MEASUREMENT OF DROPLET PROPERTIES BY PDA AND RAINBOW REFRACTOMETRY

Boulnois G.^{*}, Saengkaew S.^{*†}, Méès L.^{*}, Ren K.F.^{*}, Vanisri H.[†], Gréhan G.^{*}

^{*}LESP, UMR 6614/CORIA, CNRS/Université et INSA de Rouen, BP 12, 76801, Saint Etienne du Rouvray, France, grehan@coria.fr

[†] Center of Excellence in Particles Technology Laboratory, Faculty of Engineering, Chulalongkorn University, Bangkok, Thailand,

ABSTRACT

This paper is devoted to the *in situ* measurement of the refractive index of small droplets. The aim is to compare the advantages and limitations of two different techniques. One, the Dual Mode PDA, is based on a post-processing of the records of a commercial device working on individual droplets while the second, the Global Rainbow, works directly on an ensemble of droplets. A particular attention is devoted to define the validity of the Airy approach when the droplets are small.

Keywords: refractive index measurement, Debye theory, Lorenz-Mie theory, rainbow technique

1. INTRODUCTION

The measurement of the properties of liquid droplets in a flow is still a challenge. A large effort has been devoted to the measurement of the velocity and size of such particles during the last two decades. Now the challenge is to obtain information on the thermal properties of such moving particles inside a flow.

Our presentation to the Hangzhou conference is focused on the comparison between the measurement by Dual MODE phase Doppler and the Global rainbow refractometry of the refractive index of droplets with a diameter smaller than 50 μm . A particular attention is devoted to the discussion on the accuracy and measurement range of each technique for a given adjustment.

The paper is organized as the following : section 2 recalls the basis of the DUAL MODE PDA technique as well as for the global rainbow. section 3 describes the experimental spray, while section 4 compiles some preliminaries results obtained by the Dual Mode approach, section 5 is a conclusion.

2. THEORETICAL BACKGROUND

2.1 Dual Mode PDA

The Phase Doppler Anemometer allows the measuring of the velocity and the size of individual particles. The velocity is directly determined by the value of the frequency of the collected signal. The size is extracted from the phase difference which is defined as time delay between two detectors of which is normalized by the period and then is multiple by 360° . The Dual Mode PDA has been introduced few years ago [1]. The mean particularity of that approach is to combine behind a unique collecting lens two PDA systems: one is in the standard configuration while the other is in the planar configuration. Then the two systems don't have the same answer to the size and the refractive index of the particle. And, as exemplified in figure 1, the ratio of the two measured phases is a univoque function of the refractive index of the particle. Nevertheless, remark that with this technique the maximum of sensitivity (accuracy) is obtained for the lower refractive index.

Such an approach has been previously used to measure the refractive index of relatively large particles by using a prototype of a Dual Mode PDA. Here, we use a classical commercial PDA, and the refractive index information is obtained by realizing a post processing of the recorded data, available from the standard output of the commercial version.

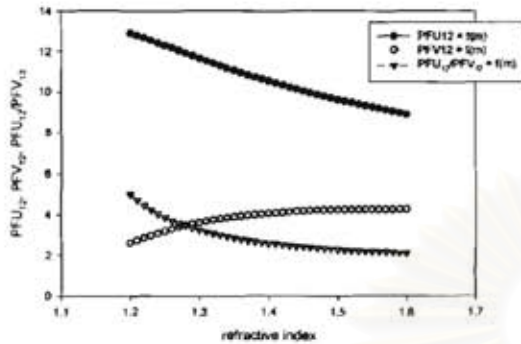


Figure 1: Slope of the relation phase/diameter versus refractive index, computed in the framework of geometrical optics. Black standard configuration. Red planar configuration. Green ratio of the phase.

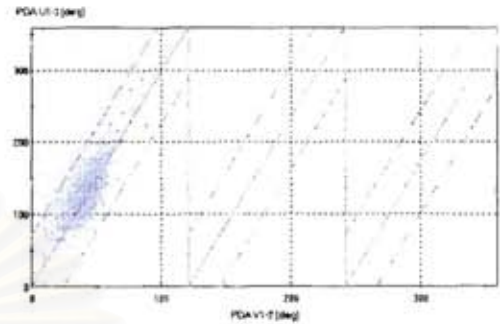


Figure 2: Example of a phase plot available from the commercial system. Standard phase versus planar phase

Figure 2 displays a phase plot as purposed by the software of the commercial version. In this phase plot, we remark a continue line, and on its sides two dashed lines. The continue line corresponds to the answer computed from a supposed refractive index and the dashed lines defined the limits of the acceptable measurements. In blue are the accepted points, in red the rejected ones.

The post processing algorithm that we have developed is as follow :

- We use the same phase plot, except that we don't suppose a refractive index and that all the events are accepted (see figure 3). The problem is now to find the slope of the linear regression describing these points at best.
- According with Press et al [2]. We select the following approach: first we compute the location of the maximum of the PDF (see figure 4), then, from these points, a linear regression is computed. Its slope is directly a measurement of the refractive index of the particle (see figure 4).

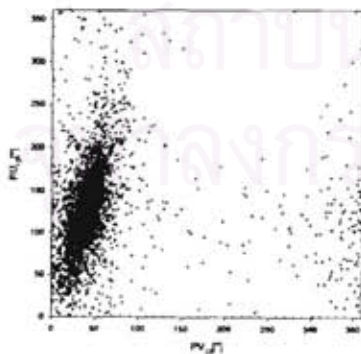


Figure 3 : A phase plot (for water droplet)

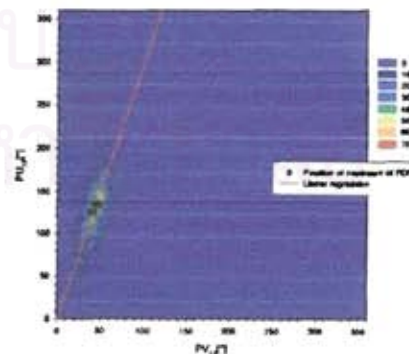


Figure 4 : The extracted points of maximum of pdf and the associated best linear regression

This post processing has been applied to various recording corresponding to sprays of various liquids created by an ultrasonic nozzle (see sections 3 and 4).

2.2 Global Rainbow Technique

It is well known that the main rainbow, which is created by the “rays” experimenting one internal reflection, is very sensitive to the value of the refractive index of the particles. Then the possibility to extract the refractive index and the particle size from the characteristics of the light scattered around the rainbow angles has attracted a lot of researchers. In the field of combustion of droplets, following the pioneer of Anders et al [3] whose worked on monodispersed, well spherical droplets, Van Beeck and Reithmuller [4, 5] try to measure refractive index and size of individual droplet in more complex sprays. Due to the high sensitivity of the rainbow to non sphericity and gradient, the difficulty was to select droplets which are nearly perfectly spherical. Then, Van Beeck and Reithmuller more recently introduce the global rainbow technique which is based on the analysis of the light scattered at the rainbow angle by a cloud of droplets. Under the assumption of a random orientation of the droplets and an independence of the refractive index with the particle size, they shown that the global rainbow is nearly no sensitive to the presence of non spherical particle. Nevertheless, the inversion (extraction of the refractive index and size distribution) is based on the use of the Airy theory. The validity of this approach has not yet be fully demonstrated for the small particles [6, 7]. Here, we will evaluate the validity of Airy theory to describe the light scattering around the rainbow angle in two cases: (i) for one particle (ii) for an ensemble of particles. When particles are small, the computation could be carry out in the rigorous, electromagnetic framework of the Lorenz-Mie theory (or GLMT) but in this case the interferences between the light externally reflected and the light who experiments one internal reflection create important fringes which complicate the exploitation of the results, especially for one individual particle (see figure 5). Alternatively Debye theory and Airy theory could be used. The Debye theory [8] is a post processing of Lorenz-Mie theory but give the possibility to sort the light which experiments diffraction, external reflection, refraction, and n internal reflections. Figure 5 compares the scattered intensity around the rainbow angle computed in the framework of the full Lorenz-Mie theory and in the framework of the Debye theory, when only the rays experimenting one internal reflection are taken into account. The particle is a water droplet ($m = 1.33 - 0.0i$) with a radius equal to 25 μm .

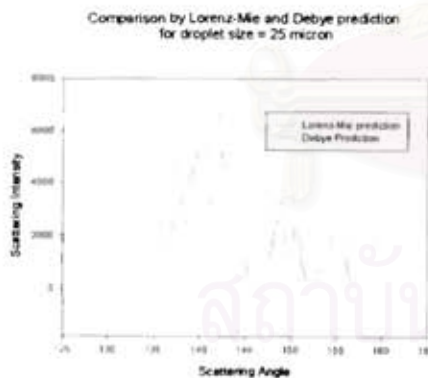


Figure 5: Comparison between Lorenz-Mie and Debye prediction for a water droplet with a diameter equal to 25 μm .

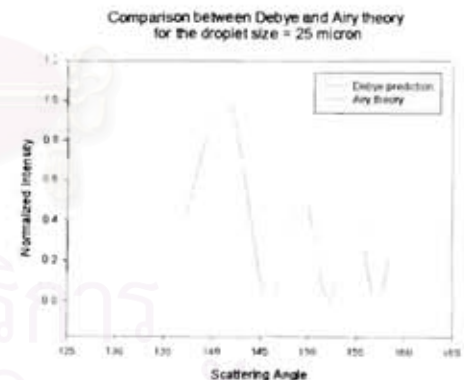


Figure 6: Comparison between Debye and Airy theory for a water droplet with a diameter equal to 25 μm .

The Airy theory also take into account only the rays experimenting one internal reflection, but the theoretical basis is “limited” to Huygens’ principle. Figure 2 compares, for the same particle, the Debye predictions and the Airy predictions. The conclusion is that the Airy predictions over evaluate the intensity of the supernumerary peaks and under evaluate the intensity in the Alexander’s dark band but the mean peak is relatively well described.

Then by analysing a real global rainbow scattering diagram by Airy theory we must be attentive to:

- A possible under estimation of the collected intensity in the Alexander’s dark band due to the light reflected by the particle
- A possible under estimation of the collected intensity as the scattering angle is upper of the rainbow

angle, resulting from the competition between the under estimation of the contribution of the reflected light and an over estimation for the supernumerary peaks.

This fact is exemplified in figure 7 which corresponds to a real global rainbow scattering diagram (computing in the framework of the full Lorenz-Mie theory) compared with Airy diagrams corresponding to the original distribution and two best fitting of the light distribution on recorded rainbow. Note the best fit is for a refractive index equal to 1.328. Figure 8 compares the original and the extracted size distribution. From such series of computation, we conclude that the global rainbow technique is potentially able to give the value of the refractive index with an accuracy on the 3 digit, and a relatively good information on the mean size and size distribution for droplet as small as 10 μm in diameter if precautions are taken when using the Airy theory.

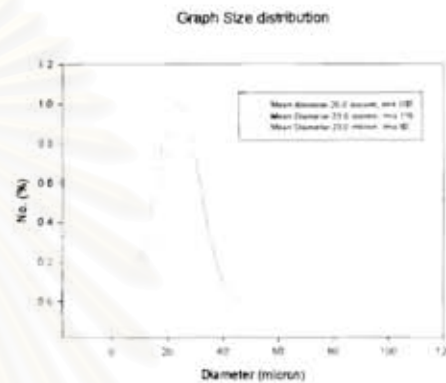
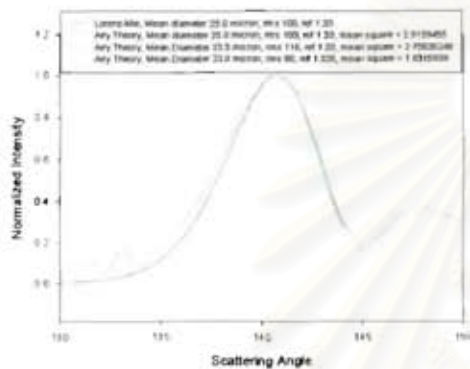


Figure 7 : Comparison between a global rainbow intensity distribution predicted by Lorenz-Mie theory and three Airy predictions corresponding to the original prediction and the best least square fitting.

Figure 8 : Comparison between the original size distribution and the size distribution extracted by fitting Airy prediction.

3. EXPERIMENTAL SETUP.

The droplets are produced by an ultrasonic nozzle designed by the Chulalongkorn University. Figure 9 shows that an ultrasonic nozzle structure is an acoustically resonant device consisting of a pair of piezoelectric ceramic rings sandwiched between a backing piece (1) and a mechanical transformer (2). The atomization takes place at the free end of the mechanical transformer form called atomizing surface. The liquid is delivered to this surface through the hole (3). These nozzles are characterized by a particle size distribution nearly Gaussian, as exemplified in figure 10. Furthermore, nearly all the droplets have a diameter smaller than 50 μm : the mean diameter D_{10} is equal 28.4 μm to and the Sauter diameter D_{32} is equal to 36.2 μm.

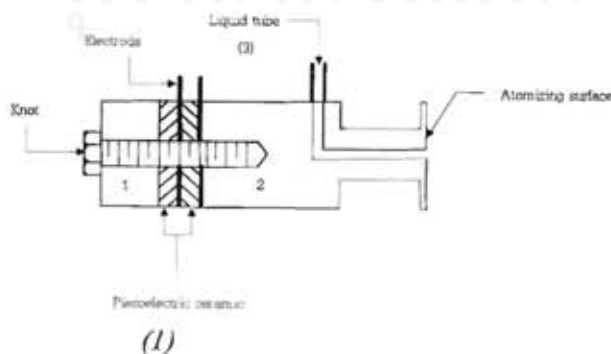


Figure 9: 9.1) Scheme of the ultrasonic nozzle. 9.2) Photography of the studied nozzle.

The PDA measurement has been carried out in forward scattering ($\theta = 30^\circ$), beams were 40 mm distant and were focused by a lens with a focal length equal to 310 mm. The scattered light was collected by a lens with a focal length equal to 160 mm, and the mask A, designed for small particles measurements, was used.

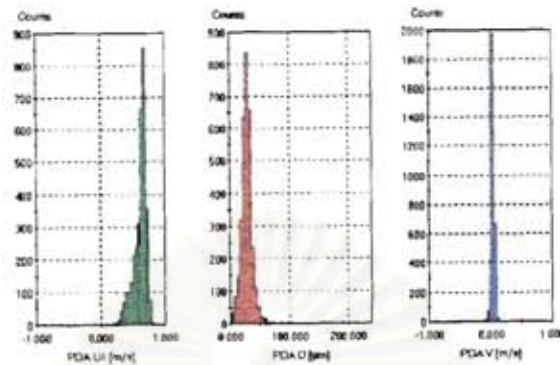


Figure 10: Example of mean velocity distribution, size distribution, and lateral velocity distribution measured with a standard commercial PDA

4. MEASUREMENTS

By using the same ultrasonic nozzle, excited at the same frequency and with the same power, Dual Mode PDA measurements have been carried out for various liquids. The aspect of the phase plot could change a lot from one product to the other (see figure 11 for diesel droplets), nevertheless the same procedure (code) has been applied in all cases. The results are compiled in table 1.

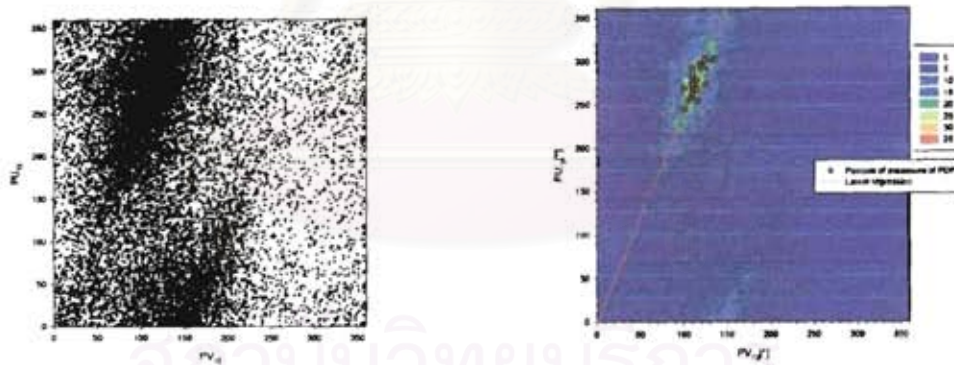


Figure 11 : Example of measurement for diesel droplets. The direct phase plot and the maximum of pdf with the associated linear regression.

For example, with water the calculated refractive index is 1.318 instead of 1.33

Liquid	Refractive index	PDA measured refractive index
water	1.33	1.318
Alcohol	1.362	1.357
CSL2	1.42	1.39
Gas-oil	1.464	1.432

We note that PDA measurements always under estimate the exact value of the refractive index and that the measurements are more accurate for low refractive index (a fact predicted in figure 1). PDA measurements are less accurate than the rainbow techniques but we must also recall that all these measurements have been carried out with exactly the same experimental configuration: this underlines the large dynamic of the PDA measurements of the

refractive index, on the contrary, measurement by global rainbow technique will run on a large scattering range (137 to 1530) to be able to extract information in the above range of refractive index. Furthermore, if the particles experiment a defect of sphericity: rainbow measurement will be more sensitive than PDA [9, 10].

5. CONCLUSION

The measurement of the properties of the droplets in a spray is still a challenge. If for the last decade, the main effort has been focused on the measurement of the velocity and the size of the droplets, a strong demand is in development for other characteristics of the droplets as temperature and composition.

Here we present the potential of application of two techniques to characterize the refractive index of small particles (diameter smaller than 50 μm). The next step is to realize a campaign of measurement by Global rainbow refractometry on the sprays created by our ultrasonic generator.

ACKNOWLEDGEMENTS :

This work is a part of a cotutelle PhD thesis between Bangkok and Rouen which is supported by INSA of Rouen and University of Rouen and S.S. and H.V. received partial financial support from Thailand Research Fund (TRF-RTA of Dr.Wiwut Tanthapanichakoon) and University-Industry Research Collaboration Project in Particle Technology FY2002 of Chulalongkorn University. We also thank the European commission which support partially the work presented in that paper in the framework of the contract DIME ENK6-2000-00101.

REFERENCES


1. Onofri F., Girasole T., Gréhan G., Gouesbet G., Brenn G., Domnick J., Xu T.H., and Tropea C. , Phase Doppler anemometry with the dual burst technique for measurement of refractive index and absorption coefficient simultaneously with size and velocity, Part. Part. Syst. Charact., 13, pp. 112-124, 1996
2. Press W.H., Flannery B.P., Teukolsky S.A. and Vetterling W.T., Numerical recipes, Cambridge University Press, 1986
3. Frohn A., Roth N., Dynamics of Droplets, Springer, ISBN 3 540 65887 4, 2000.
4. van Beeck J.P.A.P., Rainbow Phenomena: Development of a laser-Based, Non-Intrusive Technique for Measuring Droplet Size, Temperature and Velocity. PhD thesis, Technische Universiteit Eindhoven, 1997
5. van Beeck J.P.A.J. and Riethmuller M.L., Rainbow phenomena applied to the measurement of droplet size and velocity and to the detection of non sphericity, Applied Optics, 35, 13, 2259-2266, 1996
6. Wang R.T., van de Hulst H.C., Rainbows: Mie computations and the Airy approximation, Applied Optics, 30, 1, 106-117, 1991
7. Adam J.A., The mathematical physics of rainbows and glories. Physics Reports, 356, 229-365, 2002 (p 241 "Airy's approximation is a good one only for $\beta \geq 5000$).
8. Honevac E.A., Lock J.A., Assessing the contributions of surface waves and complex rays to far-field scattering by use of the Debye series, J. Opt. Soc. Am. A., 9, 5, 781-795, 1992.
9. Damaschke N., Gouesbet G., Gréhan G., Mignon H. and Tropea C. Response of PDA systems to non-spherical droplets, Applied Optics, 37, 10, 1752-1761, 1998
10. Han Y.P., Mees L., Ren K.F., Gouesbet G., Wu S.Z., and Gréhan, Scattering of light by spheroids : the far field case, Optics Communications, 210, 1-9, 2002



APPENDIX C4

**DESCRIPTION OF RAINBOW: COMPARISON
BETWEEN AIRY, NUSSENZVEIG AND DEBYE
APPROACHES**

**PROCEEDINGS OF THE 7TH INTERNATIONAL
CONGRESS ON OPTICAL PARTICLE
CHARACTERIZATION, KYOTO, 1-5 AUGUST
2004.**



สถาบันวิทยบริการ
จุฬาลงกรณ์มหาวิทยาลัย

**DESCRIPTION OF RAINBOWS: COMPARISON BETWEEN AIRY,
 NUSSENZVEIG AND DEBYE APPROACHES.**

Sawitree SAENKAEW^{1,2}, T.CHARINPANIKUL¹, H.Vanisri¹, Loïc MEES² and Gérard GREHAN²

¹Center of Excellence in Particle Technology, Faculty of Engineering,
 Chulalongkorn University, Bangkok, Thailand 10330

²LESP, UMR 6614/CORIA, CNRS/Université et INSA de Rouen,
 Saint Etienne du Rouvray, BP12, 76 801, FRANCE

Keywords: RAINBOW THEORY, LORENZ-MIE THEORY, REFRACTIVE INDEX
 MEASUREMENTS, THERMOMETRY.

INTRODUCTION

Rainbow is one of well known beautiful natural phenomena involving with light scattering due to suspension of fine droplet particles in the atmosphere. So far many efforts have been devoted to understand its behaviour in the field of mathematical physics¹⁾. To describe the scattering around the rainbow angle regarding to a perfectly spherical particle with a diameter equal to d and a refractive index equal to N , on which impinges a beam with a wavelength λ , one can choose some of following theory.

The Lorenz-Mie theory^{2,3)}, which is based on vectorial concept, can describe rigorously the scattering of a plane wave (arbitrary beam) impinging to a perfectly spherical particle. Almost every kind of the scattering could be explained by the Lorenz-Mie theory. However, it does not distinguish the different paths of the light scattering in the particle.

The Debye theory^{4, 5, 6)} could be considered as a postprocessing of the Lorenz-Mie theory. Debye theory could also provide a vectorial and rigorous solution of the scattering of a plane wave (arbitrary beam) scattered by a perfectly spherical particle. Moreover, it also gives the possibility to quantify the contribution of the different kinds of "rays". With the Debye theory, the a_n coefficients of the Lorenz-Mie theory could be given by:

$$a_n = \frac{1}{2} \left[1 + R_n^{22} - \sum_{p=1}^{\infty} T_n^{21} (R_n^{11})^{p-1} T_n^{12} \right] \quad (1)$$

where R_n^{22} , R_n^{11} , T_n^{12} and T_n^{21} are, for a partial spherical wave, the reflection coefficient outside the particle, the reflection coefficient inside the particle, the coefficient of transmission from inside to outside the particle and the coefficients of transmission from outside to inside the particle respectively. The above equation leads to the following interpretation:

- $\frac{1}{2}$: when one considers the scattered field by using the Lorenz-Mie equation, and summed over n describes the diffraction of the incident wave around the spherical particle.
- $\frac{1}{2} R_n^{22}$ represents the outgoing scattered wave reflected from the surface of the spherical particle.
- $\frac{1}{2} \left[- \sum_{p=1}^{\infty} T_n^{21} (R_n^{11})^{p-1} T_n^{12} \right]$ takes the form of a geometrical series. Individual term represents the light transmitted to the sphere and emerging from it after $(p-1)$ internal reflections.

The Complex Angular Momentum theory (CAM theory), which has been developed by Nussenzweig^{7, 8, 9}, is a scalar theory. Nussenzweig claims this theory could provide useful quantitative information down to a size parameter as small as 100 (diameter of about 15 μm in visible) and at least qualitative information down to a size parameter as small as 10 (diameter of about 1.5 μm in the visible)". CAM theory could be referred as the analytical integration of Debye theory. In Nussenzweig theory, the scattered amplitude are given by:

1) for reflection⁷⁾:

$$f_{\text{reflexion}}(\alpha, \theta) = -d \left(\frac{\sqrt{N^2 - \cos^2(\theta/2)} - \sin(\theta/2)}{\sqrt{N^2 - \cos^2(\theta/2)} + \sin(\theta/2)} \right) \exp(-2i\alpha \sin(\theta/2)) \left\{ 1 + \frac{i}{2\alpha} \left[\frac{1}{\sin^2(\theta/2)} - \frac{2N^2 - \cos^2(\theta/2)}{(N^2 - \cos^2(\theta/2))^{3/2}} + O(\alpha^{-2}) \right] \right\} \quad (2)$$

where α is the size parameter defined as $\alpha = \pi d / \lambda$ and θ is the observation angle.

2) for the first rainbow⁸⁾:

$$f_{\text{rainbow}}(\alpha, \theta) = \frac{d}{2} \cdot \frac{16e^{-i\pi/4}}{27\sqrt{3}} \left(\frac{\pi}{\sin \theta} \right)^{1/2} c(6s\alpha)^{1/6} \exp[6ic\alpha + is\alpha\epsilon + iA\alpha\epsilon^2 + O(\alpha\epsilon^3)] \left\{ \left[1 + O(\epsilon) + O(\alpha^{-1}) \right] A_i \left[-\frac{c(2\alpha)^{2/3}\epsilon}{(3s)^{1/3}} (1 + B\epsilon + O(\epsilon^2)) \right] - \frac{iC}{(2\alpha)^{1/3}} \left[1 + O(\epsilon^{1/2}) + O(\alpha^{-1}) \right] A_i' \left[-\frac{c(2\alpha)^{2/3}\epsilon}{(3s)^{1/3}} (1 + B\epsilon + O(\epsilon^2)) \right] \right\} \quad (3)$$

with :

$$A = \frac{c(11c^2 - 15)}{36s^2} \quad (4)$$

$$B = \frac{875c^6 - 1257c^4 + 657c^2 + 45}{8640(sc)^3} \quad (5)$$

$$C = \frac{28 - 31s^2}{4c(3s)^{3/4}} \quad (6)$$

and

$$s = \sin \theta_{1R} = \left(\frac{4 - N^2}{3} \right)^{1/2} \quad (7)$$

$$c = \cos \theta_{1R} = \left(\frac{N^2 - 1}{3} \right)^{1/2} \quad (8)$$

where θ_{1R} is the incident angle on the sphere for the rainbow angle θ_R , and ϵ verify $\theta = \theta_R + \epsilon$. $A_i(x)$ and $A_i'(x)$ are respectively the Airy function and its derivative.

The Airy theory^{10, 11)} which is also a scalar theory, describes the scattering of rays experiencing p internal reflection before leaving the sphere. However, the Airy theory has a very limited range of application ($\alpha > 5000$, $\theta - \theta_R \approx 0.5^\circ$)^{1, 12)}. It should be noted that, as mentioned by Nussenzveig, the Airy theory may be obtained from CAM theory by retaining only lowest term in all expressions ($A = B = C = 0$). Some other approaches are possible, as the one proposed by Mobbs¹³⁾, but they essentially give the same results, with a similar range of validity than the CAM theory.

Meanwhile, the light scattered around the rainbow angle is often recorded because its sensitivity to the value of the refractive index give a way to obtain information on the temperature/composition of droplets or liquid jets. Many efforts have been dedicated to the measurement of the temperature of droplets lines, the measurement of the temperature of individual droplets with arbitrary trajectory, the measurement temperature of a section of spray, the measurement of the temperature of droplets in levitation. These measurements are based on the location of Airy's peak¹⁴⁾, the frequency of the ripple structure¹⁵⁾ or the behaviour of the global intensity distribution¹⁶⁾. Furthermore, as the full structure of the rainbow is essentially created by interference of different kinds of rays, the rainbow is very sensitive to any change of size or shape of the scatterer¹⁷⁾.

To extract information from light scattered around the rainbow angle it is useful to compute quickly and accurately the properties of the scattered light. Then, in this paper we compare the prediction from Lorenz-Mie, Debye, Nussenzveig and Airy theory to predict the rainbow (single and global) behaviour. In this paper we focus essentially to the main rainbow. Then the main rainbow with p equal to 2 for one individual droplet will be discussed. Finally, the rainbow created by a cloud of droplets will be also explained and summarized.

COMPARISON AMONG LORENZ-MIE, DEBYE, AIRY AND NUSSENZVEIG THEORIES

Only few results have been reported comparing the CAM theory predictions for the rainbow with others approaches. Here the results of this work are compared and discussed regarding to that of Khare and Nussenzveig¹⁸⁾. Figures 1 and 2 display the normalized intensity versus the scattering angle. The normalization has been defined in such a way that the maximum of the Debye prediction for $p=2$ was equal to 1. The same normalization factor has been applied to the Lorenz-Mie theory results and to the Debye prediction for other values of p . With the Airy and Nussenzveig theories, the same normalization procedure has been applied.

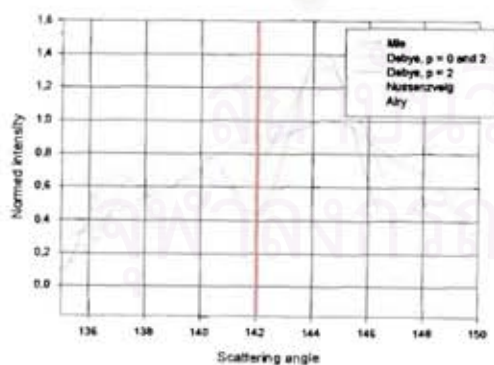


Figure 1: To compare with Ref 14. The particle diameter is equal to $9.55 \mu\text{m}$, the wavelength is $0.6 \mu\text{m}$ and the refractive index is 1.33.

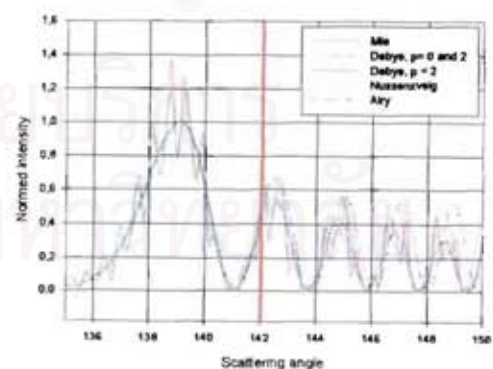


Figure 2: To compare with ref 14. The particle diameter is equal to $95.5 \mu\text{m}$, the wavelength is $0.6 \mu\text{m}$ and the refractive index is 1.33.

Figure 1 and 2 are divided into two sections by a vertical red line. The left side of figure 1 and 2, between 136° and 142°, corresponds to the results of V. Khare and H.M Nussenzveig^[18]. In figure 1 and 2 five curves are plotted. The first one, in red, corresponds to the Lorenz-Mie predictions. Two curves in green and bleu are predicted in the framework of the Debye theory for (p=2) and (p=0 and 2) respectively. It is important to remark that the disagreement between the Lorenz-Mie theory and Debye theory for (p=0 and 2), must be attributed to interaction of higher order. And then a pink continuous curve corresponds to Nussenzveig predictions (equation (3)) and a dashed dark green corresponds to Airy predictions.

From figure 1 it should be noted that the Nussenzveig and Airy predictions are identical for a scattering angle lower than 142° and slightly underestimate the Debye's predictions for p=2. For larger scattering angle, the Nussenzveig and Airy's predictions provide different results, which are both higher than the Debye's prediction for p=2. Nevertheless, in this angular range, the Nussenzveig's predictions are better than Airy's predictions.

In figure 2, for a diameter 10 times larger, it could be seen that Nussenzveig and Airy's predictions are in good agreement with Debye's prediction for p=2 and scattering angle between 136° and 142°. But for larger scattering angle their results become different. Nevertheless, the Nussenzveig's predictions are in agreement with the Debye's predictions for the location of maxima and minima, while the disagreement increases with the angle for Airy's predictions. Concerning the intensity of the supernumerary peaks, the Nussenzveig's predictions are essentially identical to the Airy's predictions. These observations have been confirmed by a large number of computations. Then it is decided to correct the intensities (amplitudes) predicted by equation (3) by an empirical factor. To define this empirical factor, the following procedure has been applied.

- Compute scattering diagram for particle diameter running from 10 to 100 μm, in the framework of the Debye (p=2) and Nussenzveig theories, for angle running from 130° to 160°.
- From the wavelength, particle diameter and scattering angle, compute the argument z of the classical Airy function for the first rainbow, as defined by Wang and van de Hulst :

$$z = (-q) \left[\frac{12}{h\pi^2} \right]^{1/3} \alpha^{2/3} (\theta - \theta_R) \quad (9)$$

- Plot the normalized scattered intensity computed by Debye (p=2) and Nussenzveig versus z
- When the normalized intensity (for Nussenzveig) is larger than 0.2, the ratio of the Debye intensity divided by the Nussenzveig intensity is computed.

Figure 3 displays the intensity ratio with respect to z, with the particle diameter as a parameter. All these computations have been carried out for water droplet (m = 1.33 - 0.0 i). Each curve is fitted by a linear regression.

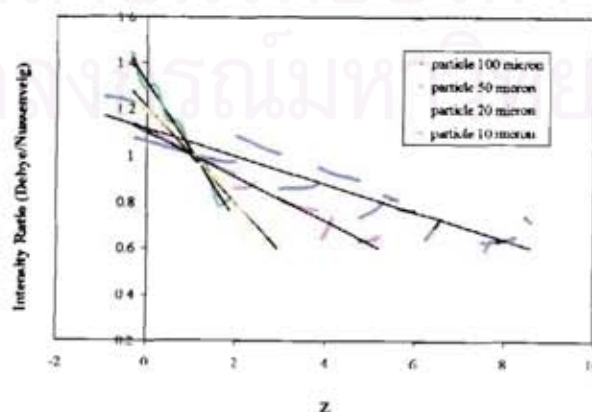


Figure 3: Intensity ratio of Debye on Nussenzveig versus z.

To compute the rainbow for particle with diameter ranging up to 100 μm and for refractive index running from 1.3 to 1.5, it is enough to introduce 4 correcting linear laws for the particle with diameter smaller than 15 μm , between 15 and 35 μm , 35 and 75 μm and 75 to 100 μm with an accuracy better than about 10%.

By using these correcting coefficients it is now possible to accurately compute the location and intensity of the Airy's peaks in a large angular domain. Furthermore, for small particle, the effect of the externally reflected light is strong, and is at the origin of the ripple structure. Then, the externally reflected light could be introduced from equation (2). By summing the amplitude of the externally reflected light with that of the internally reflected light, computing the intensity the rainbow structure for individual droplet could be conducted with a high accuracy as shown in figure 4. It should be noted that the agreement between Debye's and Nussenzveig's results, including on the location and intensity of the ripple, is nearly perfect. Then it leads to conclusion that the Nussenzveig theory could be employed efficiently to extract size and refractive index information form data recorded around the rainbow angle and due to an individual spherical particle (sphere or cylinder).

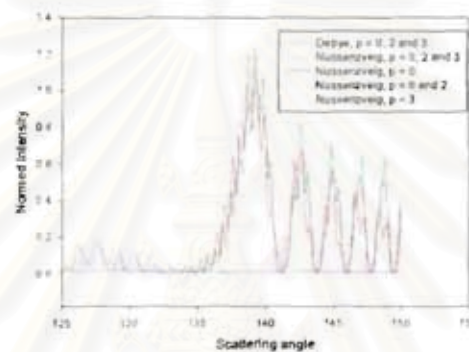


Figure 4 : Comparison for the first rainbow between Lorenz-Mie predictions and Nussenzveig predictions, for $p=0$ and 2

GLOBAL RAINBOW

The global rainbow technique is based on the analysis of the light scattered around the rainbow angle due to an assembly of particles. Figure 5 is a typical example of such light distribution based on computation of the size distribution shown in figure 6 for water droplet ($N=1.33-0.0i$). In figure 5, 3 regions could be defined:

1. scattering angle smaller than 136°
2. scattering angle between 136° and 143° ,
3. scattering angle larger than 143° .

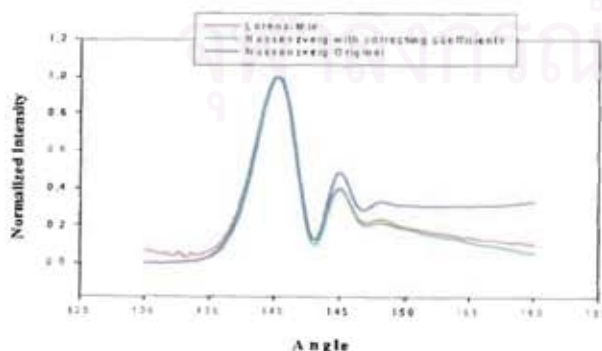


Figure 5 : Comparison between global rainbow computed in Lorenz-Mie, Airy and Nussenzveig (with correction) framework

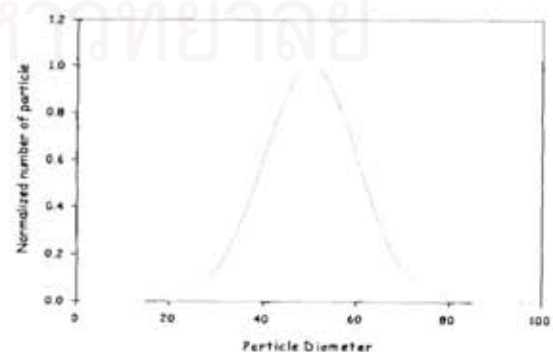


Figure 6 : the size distribution corresponding to the global rainbow of figure 5.

Within the central region, for scattering angle of 136° to 143° , the agreement between the different curves is essentially perfect. It reveals that the Lorenz-Mie's predictions, Airy's prediction's and Nussenzveig's predictions with or without correcting coefficients are in agreement. For larger scattering angle, the Airy's predictions and Nussenzveig's prediction without correcting coefficients exhibit consistent scattered intensity but higher than that of the Lorenz-Mie theory. On the contrary, the Nussenzveig's predictions with correcting coefficients agree perfectly with the Lorenz-Mie's predictions. In the third region representing the scattering angle smaller than 136° , the disagreement between the Lorenz-Mie's predictions and Airy-Nussenzveig's prediction is large because this region is essentially dominated by the second rainbow. The Nussenzveig theory can also predict the light scattered by high order rainbow. Then the same procedure as introduced here could be applied for the second rainbow to obtain an accurate and fast description of the light scattered at these angle

CONCLUSION

The possibility of application of the Nussenzveig theory to predict the rainbow behaviour in a large angular domain has been studied for particles in the range of 1 to 100 μm , which is of interest for liquid sprays. We have shown that by adding 4 correcting laws, an accurate quantitative description of the rainbow could be achieved, in a large range of refractive index ($N=1.3$ to 1.5). As computations are very fast in the Nussenzveig framework, this approach will be soon applied to extract information from experiment with single particle as well as from a section of a cloud.

ACKNOWLEDGEMENTS

We want grateful here the European community which support this work thank the program MUSCLE. We also want grateful the Royal Golden Jubilee Ph.D Program, Thailand Research Fund, and the French Ministry of Education which support the joint thesis of Miss S. Saengkaew.

REFERENCES

- 1) J.A. Adam, *Physics reports*, 356, 229-365 (2002).
- 2) L. Lorenz, *Vidensk. Selk. Skr.* 6, 1-62 (1890).
- 3) G. Mie, *Ann. der Phys.*, 25, 377-452 (1908).
- 4) P. Debye, *Ann. der Phys.*, 4 (30), 57-136 (1909).
- 5) J.A. Lock, *J. Opt. Am. A.*, 10 (4), 693-706 (1993).
- 6) J.A. Lock and C. L. Adler, *J. Opt. Am. A.*, 14 (6), 1316-1328 (1997)
- 7) H.M. Nussenzveig, *Journal of Mathematical Physics*, 10 (1), 82-124, (1969).
- 8) H.M. Nussenzveig, *Journal of Mathematical Physics*, 10 (1), 125-176, (1969).
- 9) H.M. Nussenzveig, *Diffraction effects in semi-classical scattering*, (Cambridge University Press, 1992).
- 10) R.T. Wang and H.C. van de Hulst, *Appl. Opt.* 30 (1), 106-117, (1991).
- 11) J.D. Jackson, *Physics Reports*, 320, 27-36 (1999).
- 12) H.C. van de Hulst, *Light scattering by small particles*, (Chapman and Hall, London 1957).
- 13) S.D. Mobbs, *J. Opt. Soc. Am.*, 69 (8), 1089-1092 (1979)
- 14) J.P.A.J. van Beeck and M.L. Riethmuller, *Appl. Opt.*, 35 (13), 2259-2266, (1996)
- 15) X. Han, K.F. Ren, Z. Wu, F. Corbin, G. Gouesbet and G. Gréhan, *Applied Optics*, 37 (36), 8498-8503 (1998)
- 16) J.P.A.J. van Beeck, D. Giannoulis, L. Zimmer and M.L. Riethmuller, *Opt. Lett.*, 24, 1696-1698 (1999)
- 17) Y.P. Han, L. Mees, K.F. Ren, G. Gouesbet, S.Z. Wu and G. Gréhan, *Optics Communications*, 210, 1-9, (2002).
- 18) V. Khare and H.M Nussenzveig, *Physical review Letters*, 33 (16), 976-980 (1974)



APPENDIX C5

THERMOETRIE PAR ARC-EN-CIEL

**20EME CONGRES FRANÇAIS SUR LES
AEROSOLS, ASSOCIATION FRANCAISE
D'ETUDES ET DE RECHERCHES SUR LES
AEROSOLS, ASFERA, 7-8 DECEMBRE 2004.**

สถาบันวิทยบริการ
จุฬาลงกรณ์มหาวิทยาลัย

THERMOMETRIE PAR ARC-EN-CIEL

S. Saengkaew (1 et 2), Loïc Méès (2) et G. Gréhan (2)

1) Excellence center in particle technology,
Chulalongkorn University, Bangkok (Thaïlande)
Sawitree_s@coria.fr

2) LESP, UMR 6614/CORIA,
CNRS/Université et INSA de Rouen, BP 12
76 800 Saint Etienne du Rouvray (France)

TITLE

Thermometry by rainbow

ABSTRACT

The mastery of an atomised liquid combustion for energetic efficiency as well as for pollution in plane engine or car engine for example, impose to understand the physic of atomisation and evaporation of the droplets. To table up this challenge, several techniques have been developed. Among these techniques, the rainbow refractometry is particularly attractive by its sensitivity and flexibility. This technique could be applied to individual particles or cloud of particle, without additive to add and is sensitive to refractive index gradient (then sensitive to temperature and composition gradient). Moreover, it does not require expensive device. But the quality of the measurement is strongly dependent on the quality of the theoretical description of the properties of the light scattered around the rainbow angle. This study is devoted to the description and exploitation of rainbow signals (single and global) in the framework of the Nussenzveig theory.

RESUME

La maîtrise de la combustion d'un liquide pulvérisé en terme de rendement énergétique et de pollution, telle que dans les moteurs automobiles et en avionique, impose de comprendre la physique de la pulvérisation, puis de l'évaporation des gouttes. Pour relever ce défi différentes techniques ont été utilisées. Parmi ces techniques, la réfractométrie d'arc-en-ciel est particulièrement attractive en raison de sa sensibilité et sa flexibilité. Cette technique peut s'appliquer à des particules individuelles ou des nuages, ne nécessite pas d'ajout de colorant. Elle est sensible au gradient d'indice (donc de température et de composition), et ne demande pas un matériel trop onéreux. Par contre la qualité de la mesure est dépendante de la qualité de la description théorique de la lumière diffusée aux alentours de l'angle d'arc-en-ciel. L'étude présentée est dédiée à la description et à l'exploitation de signaux arc-en-ciel (simple et global) dans le cadre de la théorie de Nussenzveig.

INTRODUCTION

La maîtrise de la combustion d'un liquide pulvérisé en terme de rendement énergétique et de pollution, dans les moteurs automobiles et en avionique par exemple, impose de comprendre la physique de la pulvérisation, puis de l'évaporation des gouttes. Depuis une ou deux décennies, les techniques optiques sont devenues un outil incontournable pour la mesure de la vitesse et de la taille des gouttelettes en écoulement. Ces travaux permettent de mieux comprendre, et de valider les modèles d'atomisation et de transport des gouttes. Cependant, la mesure de l'évaporation et de l'évolution thermochimique de ces gouttes est encore un défi, avec un fort potentiel d'application industriel.

Pour relever ce défi différentes techniques ont été utilisées : imagerie infrarouge⁽¹⁾, PDA dual burst⁽²⁾ et Dual mode⁽³⁾, imagerie des points chauds⁽⁴⁾, réfractométrie d'arc-en-ciel^(5,6), fluorescence induite par laser⁽⁷⁾, résonances morphologiquement dépendante⁽⁸⁾, ...

Parmi ces techniques, la réfractométrie d'arc-en-ciel est particulièrement attractive en raison de sa sensibilité et sa flexibilité. Cette technique peut s'appliquer à des particules individuelles ou des nuages, ne nécessite pas d'ajout de colorant, est sensible au gradient d'indice, et ne demande pas un matériel trop complexe. Par contre la qualité de la mesure est dépendante de la qualité de la description théorique de la lumière diffusée aux alentours de l'angle d'arc-en-ciel.

L'objectif principal de notre contribution est de quantifier la qualité de l'inversion de signaux mesurés en arc-en-ciel simple et global. L'inversion d'un arc-en-ciel simple, issu d'une goutte unique, exige une prédiction rigoureuse de la structure haute fréquence dite de « ripples », de même que l'inversion d'un arc-en-ciel global, issu d'une section d'un nuage de gouttes, exige la prise en compte de l'intensité diffusée par différents type de rayons. Les qualités des prédictions des théories approchées d'Airy et Nussenzveig sont discutées vis à vis des prédictions rigoureuses issues des théories vectorielles de Lorenz-Mie et Debye.

Cet article est organisé comme suit. La section 2 est un rappel des différents outils théoriques utilisés pour décrire la lumière diffusée par une particule sphérique, principalement aux alentours de l'angle d'arc-en-ciel. La section 3 est dédiée à l'arc-en-ciel d'une particule individuelle tandis que la section 4 est dédiée à l'arc-en-ciel créé par un ensemble de goutte. La section 5 est une conclusion.

CADRE THEORIQUE

Pour décrire la diffusion d'une onde plane ou d'un faisceau laser focalisé par une particule sphérique, l'outil théorique le plus puissant est la théorie de Lorenz-Mie⁽⁹⁾. Cette théorie est basée sur la résolution analytique des équations de Maxwell avec les conditions limites appropriées. L'extension aux cas de particules multicouches concentriques et de particules avec inclusions sphériques non centrées a été réalisé. Les résultats sont sous la forme de séries incluant les différents types d'interactions (réflexion externe, transmission directe, transmission après n réflexions interne.).

La théorie de Debye⁽¹⁰⁾ peut être vue comme un post-traitement de la théorie de Lorenz-Mie qui permet, dans le cas d'une particule homogène, de séparer les différents types d'interaction de la lumière avec la particule (réflexion externe, transmission directe, transmission après n réflexions interne).

La théorie de Moment Angulaire Complexe (CAM), introduite par Nussenzveig⁽¹¹⁾, consiste à intégrer analytiquement les séries de Debye pour un type d'interaction donné. Pour pouvoir effectuer cette intégration analytique, différentes approximations doivent être introduites en fonction du type d'interaction, de l'angle d'observation, de la taille de la particule. Ainsi pour décrire l'arc-en-ciel, cinq formules sont proposées, chacune correspondant à un domaine angulaire.

La théorie d'Airy est basée sur l'application de la loi de Huygens-Fresnel au front d'onde créé par réflexion interne. C'est l'approche la plus populaire pour l'interprétation des expériences mais aussi celle qui possède le domaine d'application le plus restreint.

Une étude comparative⁽¹²⁾ de ces quatre approches nous a permis de démontrer que :

- (1) l'approche de Nussenzveig est en parfait accord avec celles de Lorenz-Mie et Debye vis à vis de la position des pics surnuméraires et de leur intensité.
- (2) La théorie d'Airy décale rapidement les positions des pics surnuméraires et sur-estime fortement leur intensité.
- (3) L'approche de Nussenzveig, lorsque les interférences entre les rayons réfléchis à l'extérieur de la particule et les rayons ayant subi une réflexion interne sont pris en compte, décrit la

structure de ripples avec une précision proche de celle de la théorie de Lorenz-Mie pour un coût calcul équivalent à celui d'Airy.

Dans la suite de cet article, des signaux « expérimentaux simulés », calculés dans le cadre de la théorie de Lorenz-Mie, seront analysés à l'aide de la théorie de Nussenzveig. La qualité de l'inversion sera ainsi quantifiée.

ARC-EN-CIEL INDIVIDUEL

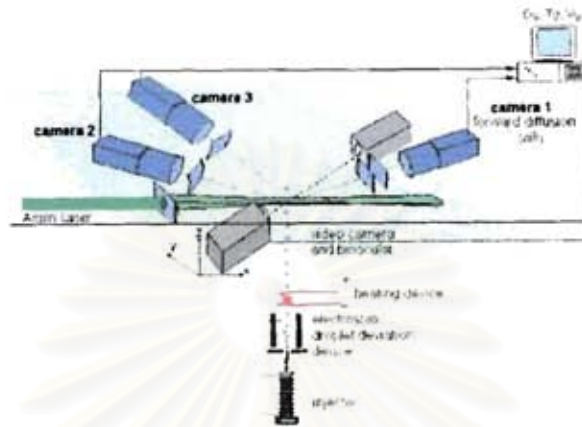


Figure 1 : Schéma d'une expérience d'arc-en-ciel pour une particule individuelle

Figure 1 présente le schéma d'une expérience d'arc-en-ciel sur une particule individuelle (une ligne de gouttes identiques). Cette expérience est celle développée à ONERA de Toulouse⁽¹³⁾. Dans cette expérience trois caméras sont utilisées. La première située en diffusion avant à 30° est dédiée à la mesure de la taille de la particule. A cet angle, la diffusion est supposée principalement indépendante de l'indice de réfraction et donc insensible à l'existence d'un gradient d'indice. La seconde caméra est dédiée à l'enregistrement de l'arc-en-ciel principal tandis que la troisième caméra est dédiée à l'enregistrement du second arc-en-ciel.

Dans les études précédentes, l'analyse consistait à mesurer la fréquence moyenne du signal, pour en déduire le diamètre de la particule par un calcul d'optique géométrique. La précision de cette mesure, pour une particule homogène, est de l'ordre de $2 \mu\text{m}$ pour des particules d'un diamètre de l'ordre de $100 \mu\text{m}$. Nous proposons ici d'effectuer l'analyse dans le cadre de la théorie de Nussenzveig. La figure d'interférence est supposée correspondre aux interférences des rayons réfléchis externe et transmis au travers de la particule. La figure 2a correspond au diagramme de diffusion entre 27° et 33° d'une goutte d'eau de $100 \mu\text{m}$. La figure 2b correspond à la transformée de Fourier de ce signal. Les courbes en vert correspondent aux prédictions de la théorie de Lorenz-Mie (signal expérimental, caméra 1, simulé par LMT) tandis que les courbes en rouge, bleu et rose correspondent aux prédictions de la théorie de Nussenzveig (la mesure). La mesure est réalisée suivant la procédure suivante : 1) le diamètre de la particule est ajusté pour avoir un accord des fréquences du spectre FFT, 2) l'indice est ajusté pour obtenir un accord en phase des diagrammes. Figure 2a, la courbe rouge correspond au diagramme Nussenzveig correspondant aux données de calcul de diagramme Lorenz-Mie. Les différences entre les courbes verte et rouge correspondent au rôle d'interaction d'ordre élevé (réflexion interne). Les courbes bleu et rose correspondent à d'autres couples mesurés diamètre/indice qui donne un bon accord en diffusion avant (d/m : $100/1.33$, $100.9/1.33$, $100.9/1.337$), en fréquence et en phase. bien que la qualité de cet accord se dégrade avec l'augmentation de l'angle de diffusion (voir figure 2c qui est un agrandissement de la figure 2a).

Le diamètre et l'indice obtenus en diffusion avant sont utilisés pour calculer la lumière diffusée aux alentours de l'arc-en-ciel principal. Puis l'indice de réfraction est ajusté pour obtenir le meilleur accord entre signal expérimental simulé (LMT, caméra 2) et mesure (signal recalculé à partir des résultats d'inversion par la théorie de Nussenzveig). Sur la figure 2d sont tracés les différents arcs-en-ciel correspondant aux trois couples possibles diamètre/indice extrait en diffusion avant. Seul une valeur de l'indice est susceptible de donner un accord simultanément en diffusion avant et arrière : 1.33 , quand au diamètre de $100.9 \mu\text{m}$, il produit un diagramme d'arc-en-ciel en opposition de phase : seul le couple $d = 100 \mu\text{m}$, $m = 1.33$ est en accord en diffusion avant et arrière, en fréquence et en phase.

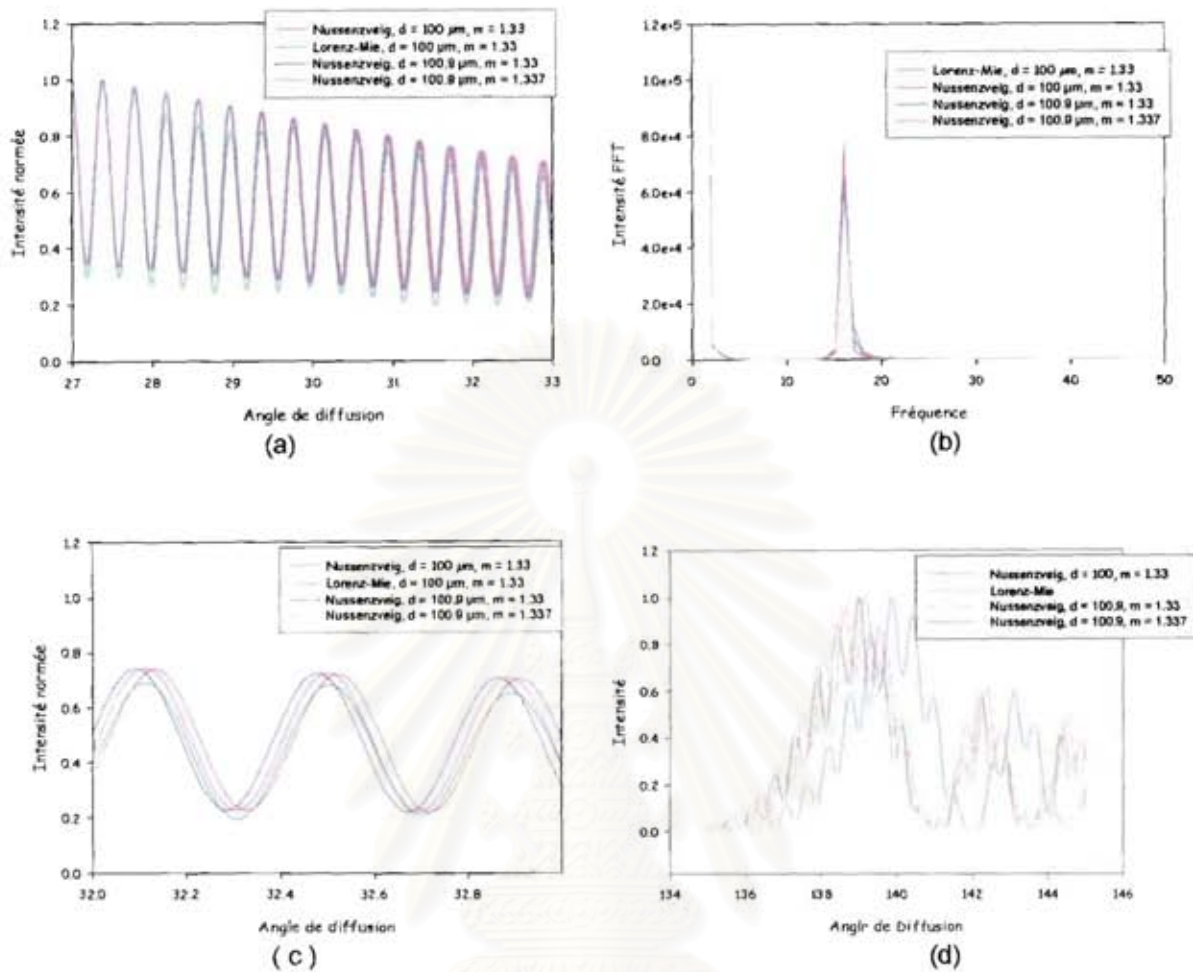


Figure 2 : 2a : diagrammes en diffusion avant .
 2b : Transformées de Fourier des diagrammes avants
 2c : agrandissement des diagrammes avants aux angles élevés
 2d : diagrammes arrières associés.

ARC-EN-CIEL GLOBAL

La réfractométrie globale d'arc-en-ciel a été introduite par l'équipe de VKI⁽⁶⁾ afin de résoudre certaines difficultés de la réfractométrie d'arc-en-ciel classique (principalement la sensibilité à la non sphéricité). Dans cette technique les arcs-en-ciel de plusieurs gouttes (plusieurs dizaines à plusieurs centaines) sont collectés simultanément comme pour l'arc-en-ciel naturel. Le signal résultant est la somme en intensité des contributions de chaque particule (hypothèse de position aléatoire des particules). Dans ce processus la structure de ripple disparaît, ainsi que les arcs surnuméraires qui sont remplacés par une structure continue. L'indice de réfraction ainsi que la distribution granulométrique sont extraites de ce signal. La figure 3 présente un tel signal correspondant à un nuage de goutte d'eau ($m=1.33$) d'un diamètre moyen de $50 \mu\text{m}$ avec une rms de 30.

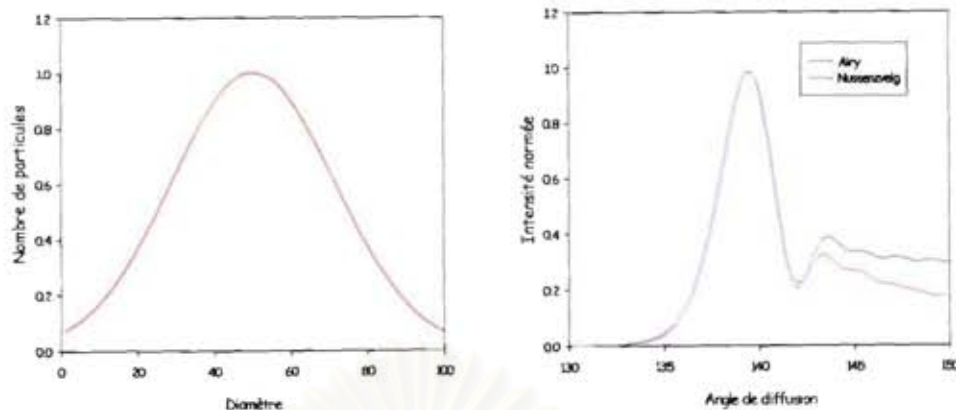


Figure 3 : Distribution granulométrique et arc-en-ciel global associé. L'arc-en-ciel associé est calculé dans le cadre de la théorie d'Airy (courbe en bleu) et de Nussenzweig (courbe rouge).

Les prédictions de la théorie de Nussenzweig sont confondues avec les prédictions issues de la théorie de Lorenz-Mie, et ceux sur un large domaine angulaire.

CONCLUSION

Dans le cadre de la théorie de Nussenzweig, les arcs-en-ciel individuels et globaux peuvent être analysés avec la précision de la théorie de Lorenz-Mie pour un coût de calcul équivalent à celui de la théorie d'Airy

REFERENCES

- (1) C. Amiel, Application de techniques optiques à l'étude du comportement dynamique et thermique de gouttes en interaction avec une paroi chauffée, thèse à SUPAERO, mars 2003
- (2) C. Tropea, T.H. Xu, G. Gréhan, F. Onofri and P. Haugen, Dual mode Phase Doppler Anemometry, Proceedings of the seventh International Symposium on applications of laser techniques to fluid mechanics, Lisbonne (Portugal), paper 18-3, July 11-14, 1994.
- (3) F. Onofri, T. Girasole, G. Gréhan, G. Gouesbet, G. Brenn, J. Domnick, T.H. Xu et C. Tropea, Phase Doppler anemometry with dual burst technique for measurement of refractive index and absorption coefficient simultaneously with size and velocity, Part. Part. Syst. Charact. 112-124, 1996.
- (4) Glare spot
- (5) J.P.A.J. van Beeck et M.L. Riethmuller, Nonintrusive measurements of temperature and size of single falling raindrops, Appl. Opt, 34, 1633-1639, 1995
- (6) J.P.A.J van Beeck, D. Giannoulis, L. Zimmer, et M.L. Riethmuller, Global rainbow thermometry for droplet-temperature measurement, Opt. Lett., 24, 1696-1698, 1999.
- (7) P. Lavieille, Etude expérimentale du comportement aérodynamique de gouttes en écoulement réactif ou non par l'utilisation de la fluorescence induite par laser à deux couleurs, thèse de l'Université Henri Poincaré, Nancy, 2001
- (8) G. Chen, Md.M. Mazunder, R.K. Chang, J.C. Swindal et W.P. Acker, Laser diagnostic for droplet characterisation : application of morphology dependent resonances, Prog. Energy Combust. Sci. 22, 163-188, 1996.
- (9) G. Gouesbet et G. Gréhan, Generalized Lorenz-Mie theories, from past to future, Atomization and sprays, 10, 277-333, 2000.
- (10) G. Gouesbet, Debye series formulation for generalized Lorenz-Mie theory with the Bromwich method, Part. Part. Syst. Charact., 20, 382-386, 2003.
- (11) H.M. Nussenzweig, High-frequency scattering by a transparent sphere. I Direct reflection and transmission, Journal of mathematical Physics, 10, 82-124, 1969, and II Theory of the rainbow and the glory, Journal of mathematical Physics, 10, 125-176, 1969.
- (12) S. Saengkaew, L. Méès et G. Gréhan, Article proposé à Optics Communications.
- (13) B. Frackowiak, G. Lavergne, G. Gréhan et L. Méès, Improvement of the rainbow technique in order to estimate the thermal gradient inside a droplet,



APPENDIX C6

**RAINBOW REFRACTOMETRY ON PARTICLES
WITH RADIAL REFRACTIVE INDEX
GRADIENTS.**

**SPRAY-05 INTERNATIONAL SYMPOSIUM HEAT
AND MASS TRANSFER IN SPRAY, ANTAYA,
TURKEY, JUNE 5-10 2005.**

สถาบันวิทยบริการ
จุฬาลงกรณ์มหาวิทยาลัย

Rainbow refractrometry on particles with radial refractive index gradients.

S. Saengkaew^(1,2), T. Charinpanitkul⁽¹⁾, H. Vanisri⁽¹⁾, L. Méès⁽³⁾, Yves Biscos⁽²⁾,
Nicolas Garcia⁽²⁾, Gérard Lavergne⁽²⁾, G. Gouesbet⁽³⁾
and G. Gréhan⁽³⁾

⁽¹⁾Center of Excellence in Particle technology,
Faculty of Engineering
Chulalongkorn University,
Bangkok, Thailand 10 330

⁽²⁾ONERA/DMAE, 02 Avenue Edouard Belin, 31 055, Toulouse

⁽³⁾UMR 6614/CORIA
CNRS/Université et INSA de Rouen, BP 12
76 800 Saint Etienne du Rouvray, CEDEX 8001, FRANCE

Abstract

The rainbow refractrometry, under its different configurations (classical and global), is an attractive technique to extract information from droplets in evaporation such as diameter and temperature. Nevertheless, for mono component as well as for multi component droplets, the presence of a temperature and/or of a concentration gradient induce the presence of a gradient of refractive index which affects the interpretation of the recorded signals. In this publication the effect of radial gradient on rainbow signals is exemplified (and quantified) for two rainbow configurations (classical rainbow for individual particles and global rainbow for section of clouds of droplets).

1) Introduction

In the combustion of liquid, classical as well as bio combustible, the liquid is often injected as a spray of tiny droplets which evaporate. The accurate measurement of the properties of the droplets under evaporation (size, mean temperature, gradient of temperature, mean composition, gradient of composition, ...) is still a challenge. Several experimental techniques have been or are under development to investigate such sprays. Among others, the techniques based on the collection of the light scattered around the rainbow angle (for individual droplets as well as for clouds of droplets) are attractive because they do not necessitate the addition of any product in contrast with methods based on fluorescence. Nevertheless the sensitivity of rainbow techniques to gradient of temperature and composition must be accurately understood. It is the objective of this paper to quantify and exemplify the effect of radial refractive index gradients on rainbow measurements.

This paper is organized as follows. Section 2, since a continuous gradient inside the particle can be modelled by a multilayer sphere, is devoted to the determination of an adequate number of layers to be used to compute reference scattering diagrams for non-homogeneous particles. Section 3 is devoted to the analysis of signals corresponding to classical rainbow measurements for mono-dispersed individual droplets, i.e. scattering distributions in the forward and backward regions are simultaneously used to extract the size and refractive index of individual particles. The analysis of the signal is carried out in the

framework of the Nussenzweig theory for homogeneous particles. Section 4 is devoted to the analysis of global rainbow signals which are collected only in the backward direction for an ensemble of droplets. Section 5 is a conclusion.

2) Computation of reference scattering diagrams

To evaluate the effect of a non-homogeneous and non uniform distribution of the refractive index inside a particle, a theoretical model must be used, which must give the possibility to compute the scattered light for range of sizes of interest (typically from 50 to 200 μm). In this paper, the reference computations will be carried out in the framework of the Lorenz-Mie theory for multilayered spheres. The computational algorithms have been previously described by Wu et al [1].

The refractive index inside the particle is defined by the refractive index at the particle centre, n_c , at the particle surface, n_s , and by a transitional law between these two points. In this paper, the following law is used:

$$n(x) = n_c + (n_s - n_c) \times \frac{e^{bx} - 1}{e^b - 1} \quad (1)$$

where x is the dimensionless distance from the particle centre. The parameter b governs the bent of the function. It depends mainly on the nature of the experiments (heating or cooling), and usually evolves during a process.

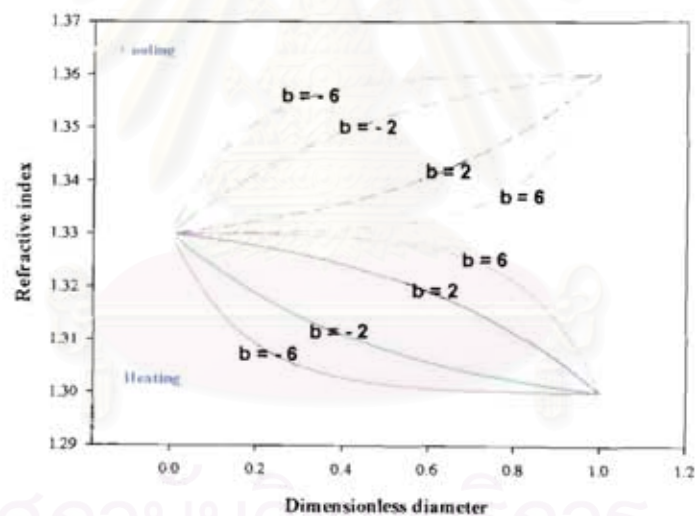


Figure 1: Examples of radial gradient. The parameter is the value of the coefficient b

Figure 1 displays the radial profiles of refractive index for different values of the parameter b . When b is positive the gradient is strong at the surface while when b is negative the gradient is strong at the center. The slope of the gradient is directly proportional to the modulus of b . Specifically, relying on several simulations from an evaporation model [2], b is set to 1.9, in the case of a droplet cooling (injection temperature 51°C, ambient temperature 20°C) which are realistic values when the measurements are carried out at a sufficient distance from the injector.

In order to determine the number of layers required to simulate a continuous gradient, computations have been carried out for a 100 μm diameter particle with n_c equal to 1.33, n_s

equal to 1.36 and b equal to 2. The number of layers has been varied from 10 to 1280. Figure 2 displays the scattering diagrams around the rainbow angle predicted from a Lorenz-Mie multilayer code while figure 3 displays the scattering diagram for the same case, but in the forward direction. From these two figures, it is concluded that 100 layers are sufficient to predict accurately enough the scattering diagrams both in forward and backward direction, including the rainbow ripple structure in frequency and phase. The low frequency evolution of the intensity is not investigated in this paper because it is more difficult to experimentally record.

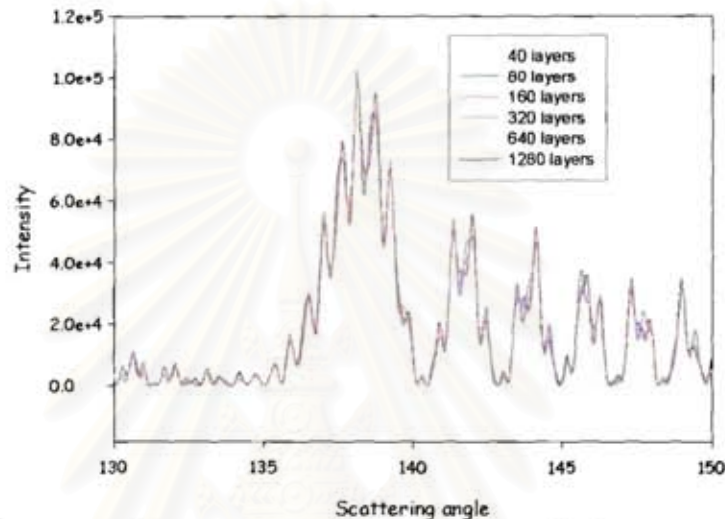


Figure 2: Scattering diagram around the rainbow angle for a particle with radial gradient. The parameter is the number of layers.

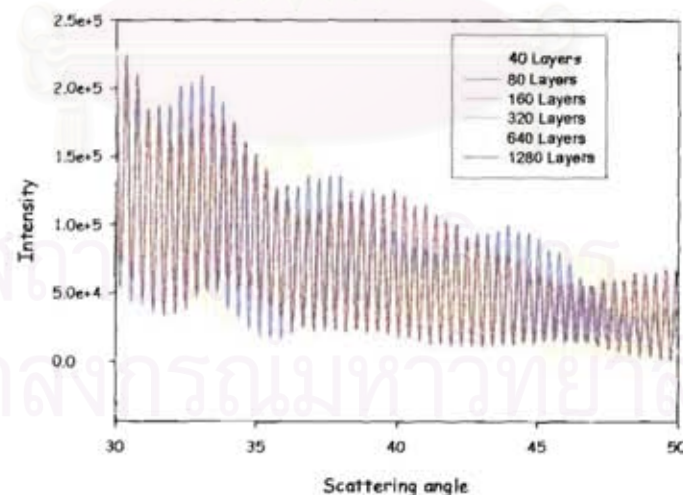


Figure 3: Scattering diagram in forward direction for a particle with radial gradient. The parameter is the number of layers.

3) Case of individual particles

3.1) The effect of the gradient

Figures 4 and 5 compare the scattering diagram for a homogeneous particle and for a non homogeneous particle, in forward and backward regions respectively. The computation

parameters are: a particle diameter equal to 100 microns illuminated by a plane wave with an incident wavelength of 0.5145 micron, a refractive index of 1.36 for homogeneous particle or n_c equal to 1.36 and n_s equal to 1.328 with b equal to 2 for non-homogeneous particle. Both cases have been computed in the framework of the Lorenz-Mie theory for multilayer spheres. In figure 4, the frequencies of the signal for the two cases are nearly identical, but the phase between them and the intensity are modified. Figure 5, in backward, around the rainbow angle, shows that the signal is shifted. The intensity and location of the ripple fringes are also modified. An important fact is that, when b is positive, the position of the rainbow corresponding to the particle with a gradient is not between the position of the rainbows for the minimum and maximum of refractive index values but larger than the position of the rainbow for the maximum refractive index. On the opposite, let us mention that, when b is negative, the position of the rainbow corresponding to the particle with a gradient is between the position of the rainbow for the minimum and the maximum of refractive index values. Naturally, the rainbow position is a function of the refractive index at the center, at the surface and of the gradient shape (coefficient b in this paper).

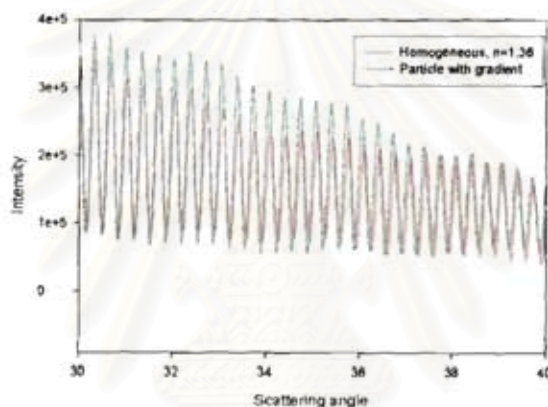


Figure 4: Effect of a gradient on forward scattering diagrams. Comparison between the forward scattering diagram for a homogeneous particle ($n=1.36$ and $d=100\mu\text{m}$) and for a non homogeneous particle ($d=100\mu\text{m}$, $n_c=1.36$, $n_s=1.328$ and $b=2$). The incident wavelength is equal to $0.5145\mu\text{m}$. The frequency signal is essentially unaffected.

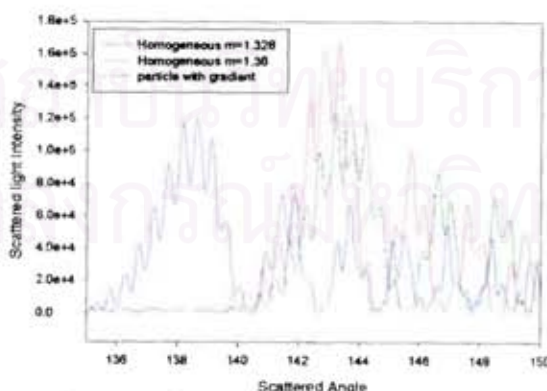


Figure 5: Effect of a gradient on backward scattering diagrams. Comparison between the backward scattering diagram for two homogeneous particles ($d=100\mu\text{m}$, $n=1.36$ or 1.328) and for a non homogeneous particle ($d=100\mu\text{m}$, $n_c=1.36$, $n_s=1.328$ and $b=2$). The incident wavelength is equal to $0.5145\mu\text{m}$. The rainbow is shifted, and for a positive value of b , the rainbow for the particle with gradient is not located between the rainbows for the two extreme refractive index values.

Figures 6 and 7 exemplify the sensitivity of the rainbow location with respect to the refractive index gradient. Figure 6 is devoted to the effect of coefficient b on the rainbow location while the effect of surface refractive index value, for a constant value of b equal to 2, is shown in figure 7. In figure 6, all the computations correspond to a particle with a diameter equal to 100 microns illuminated by a plane wave with an incident wavelength equal to 0.5145 micron. The refractive index at the center is the largest and is equal to 1.36 while, at the surface, the refractive index is equal to 1.315. The coefficient b runs from -4 to 6. As b increases from -4 to 4, the first rainbow location is shifted to larger angles (from 138° to 148°) while the second rainbow is shifted to smaller angles (from 132° down to 115°). Let us note that for $b=6$ the light distribution is essentially the same as for $b=4$.

Figure 7 displays computations for a particle with a diameter equal to 100 microns and the beam incident wavelength is equal to 0.5145 micron. The value of b is a constant equal to 2. The refractive index at the center is fixed to 1.36, while the refractive index at the surface is equal to 1.36 (homogeneous case), 1.356, 1.315 and 1.296 respectively. When the difference between refractive indices at the center and at the surface is increased, for b positive, the primary rainbow location is shifted to larger angles. The second rainbow is shifted to smaller scattering angles. The stronger the gradient, the larger the shift. In contrast, when b is negative, the primary rainbow location is shifted to lower angles.

In cases when the refractive index at the surface is larger than the refractive index at the center, the rainbow location for non-homogeneous particles will be smaller than the rainbow location corresponding to the refractive index at the center (minimum refractive index), for positive values of b , while for negative values of b , the rainbow location for non-homogeneous particles will be between the location of the rainbow for the minimum and for the maximum of refractive index values.

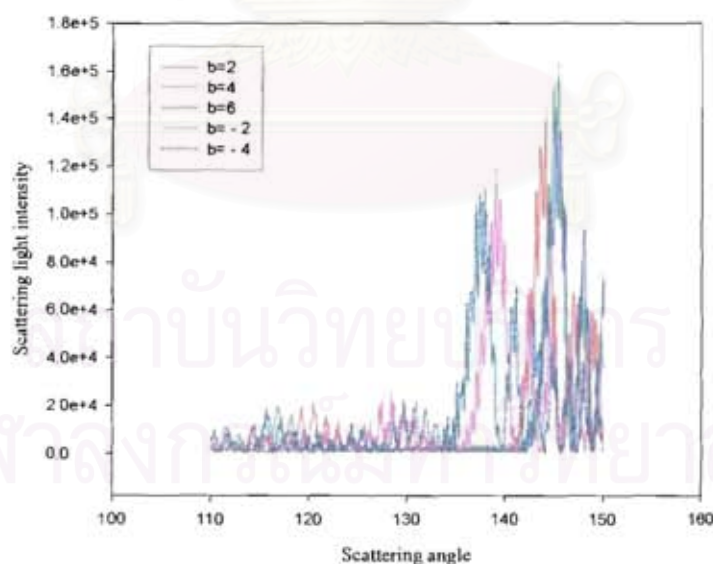


Figure 6: The scattering diagrams show the effect of coefficient b on rainbow location. (For wavelength=0.5145 micron, particle diameter=100 microns, $n_c=1.36$ and $n_s=1.315$ for 100 layers)

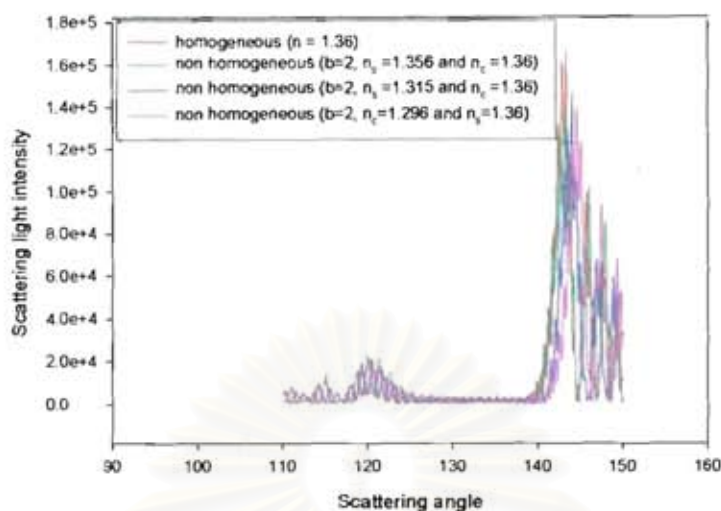


Figure 7: The scattered light distribution for different values of the refractive index at the surface with a constant value at the center equal to 1.36 (wave length = 0.5145 micron, particle diameter = 100 microns, $n_c = 1.36$, $b = 2$ and 100 layers)

3.2) Search for an equivalent particle

In the case of homogeneous particles it has been shown that the Nussenzveig theory can perfectly predict the scattered light in agreement with Lorenz-Mie theory by taking into account the external reflected light ($p=0$), the refracted light ($p=1$) and one time internal reflected light ($p=2$) [3]. In the case of non-homogeneous particles, a challenge is to exhibit an equivalent homogeneous particle with identical scattered light properties (if this equivalent particle does exist).

In order to find the refractive index and the particle size of the equivalent homogeneous particle which possesses a scattering diagram close to the one for a non-homogeneous particle, the intensity distribution from the particle with gradient is simulated by Lorenz-Mie theory for multilayered particles and then compared to the intensity distribution from a homogeneous particle, simulated by the Nussenzveig theory, in forward and backward regions.

The processing scheme is as follows;

Firstly: For an arbitrary refractive index, the Fast Fourier Transforms (FFT) of the forward scattering diagram (between $30-50^\circ$) for homogeneous and non-homogeneous particles are compared. The diameter of the homogeneous particle is adjusted to obtain the same frequency contribution as for the non-homogeneous particle under study. This process provides a relatively large range of admissible particle diameters.

Secondly: For the admissible diameter range, the refractive index is adjusted to obtain the same location of the main rainbow peak as for the non-homogeneous particle.

Thirdly: The particle diameter and refractive index are adjusted to obtain an agreement in frequency and phase [4,5] in forward and backward regions, including the ripple structure.

Figure 8 is an example of scattering diagrams computed by Lorenz-Mie theory for a multilayer sphere ($d=100 \mu\text{m}$, $n_c=1.36$, $n_s=1.352$, $b=2$) and by Nussenzveig theory at forward angles (in figure 8a) and around rainbow angle (in figure 8b). The scattered light for

the non-homogeneous case can be satisfactorily fitted by the scattered light from a homogeneous particle. The equivalent particle diameter is found to be equal to 100.07 microns and the equivalent refractive index is found to be equal to 1.361.

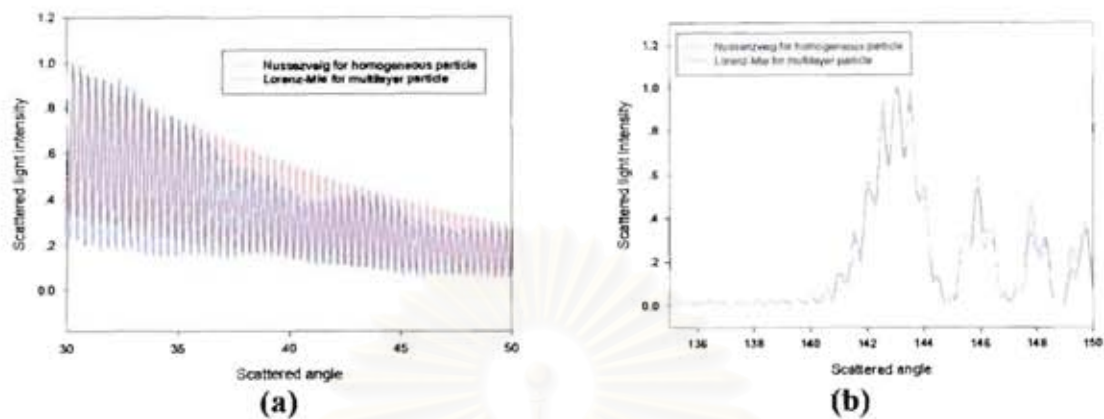


Figure 8: Comparison of the scattered light between Lorenz-Mie computations for a multilayer particle (diameter=100 microns, refractive index at the center=1.36 and at the surface=1.352, $b=2$) and Nussenzweig computation for a homogeneous particle (diameter=100.07, refractive index=1.361) (a) in forward region (b) in backward region

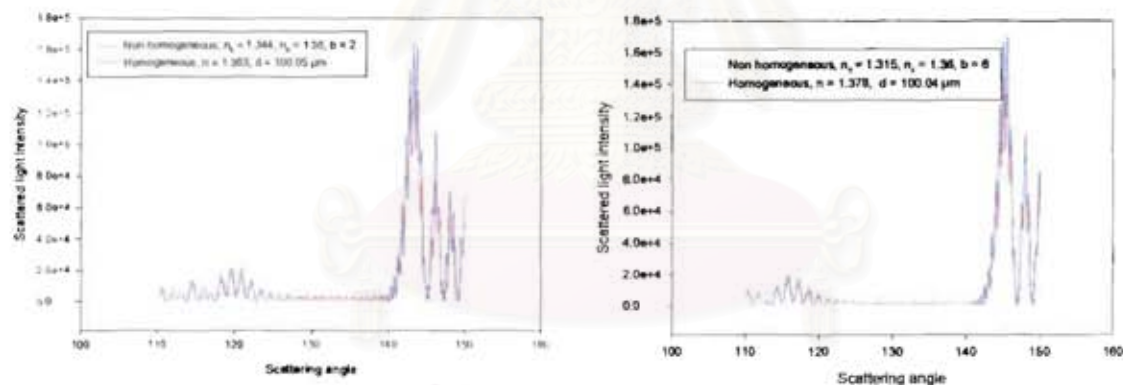


Figure 9: Comparison of the scattered light at primary and secondary rainbows for non-homogeneous particle and equivalent homogeneous particle.

Figure 9 compares the scattered light around rainbow angle computed by Lorenz-Mie theory for multilayered spheres for non-homogeneous particles and by Lorenz-Mie theory for homogeneous spheres with the parameters (size, refractive index) describing the equivalent particle in the Nussenzweig theory. Two cases of non-homogeneous particles having the same diameter (100 microns) and refractive index at the center (1.36) have been studied. For one case, the particle has the refractive index at the surface equal to 1.344 with b equal to 2. For the other case, the particle has the refractive index at the surface equal to 1.315 with b equal to 6. The results show that even when the gradient is stronger at the surface or the evolution faster (higher value of b) we can find a scattered light distribution of an equivalent homogeneous particle fitting well enough the scattered light distribution for non-homogeneous particles. Moreover, not only the primary rainbow of a non homogeneous particle can be fitted by the one of a homogeneous particle but the statement remains true for

the secondary rainbow. Moreover the second rainbow provides the same information as the first rainbow.

The aforementioned procedure has been applied to different multilayered particles. In this study, the refractive index at the center is set to a constant value equal to 1.36. Refractive indices at the surface are taken to be 1.359, 1.358, 1.356, 1.352, 1.344, 1.328, 1.315, 1.305 and 1.296. Also the coefficient b is assigned the values: $-4, -2, 1.5, 2, 2.5, 3, 4, 6$, i.e. 60 cases are studied. For each case, couples of equivalent refractive index and diameter for homogeneous particles are extracted.

Let us first note that the diameter of the equivalent particle is nearly constant (about equal to $100 \mu\text{m}$), nearly independently of the gradient amplitude and shape. Therefore only the equivalent refractive index is studied. The results are compiled in figure 10 where the equivalent refractive index is plotted versus the real surface refractive index n_s .

The results in figure 10 can be sorted in two families depending on the value of the parameter b . When b is positive, the equivalent refractive index is always larger than the largest real refractive index (1.36) while, when b is negative, the value of the equivalent refractive index is intermediary between the values at surface and at center. Furthermore, the relationship between the equivalent refractive index and the surface refractive index is essentially linear, with the slope coefficient depending on b .

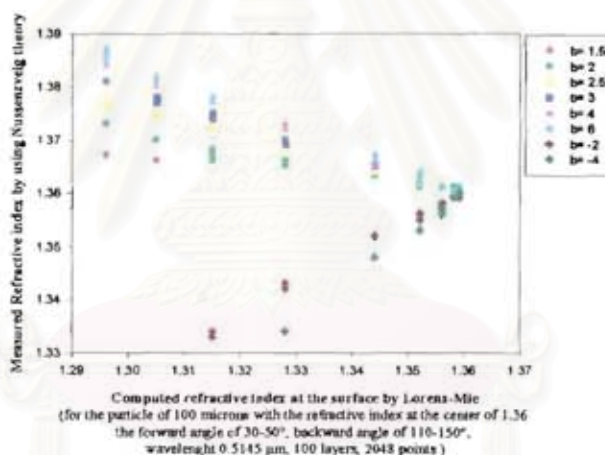


Figure 10 : The relationship between the equivalent particle refractive index and the real surface refractive index with different values of b

4) Case of clouds of particles (global rainbow)

Global rainbow results from the summation of a large number of individual rainbows. Then the global rainbow for a spray constituted of non homogeneous particles with a radial gradient is claimed to be identical to the global rainbow resulting from the summation of the **equivalent** homogeneous particles.

To illustrate the sensitivity of global rainbow measurements when particles are non homogeneous, the following realistic law between particle diameter and equivalent refractive index has been selected:

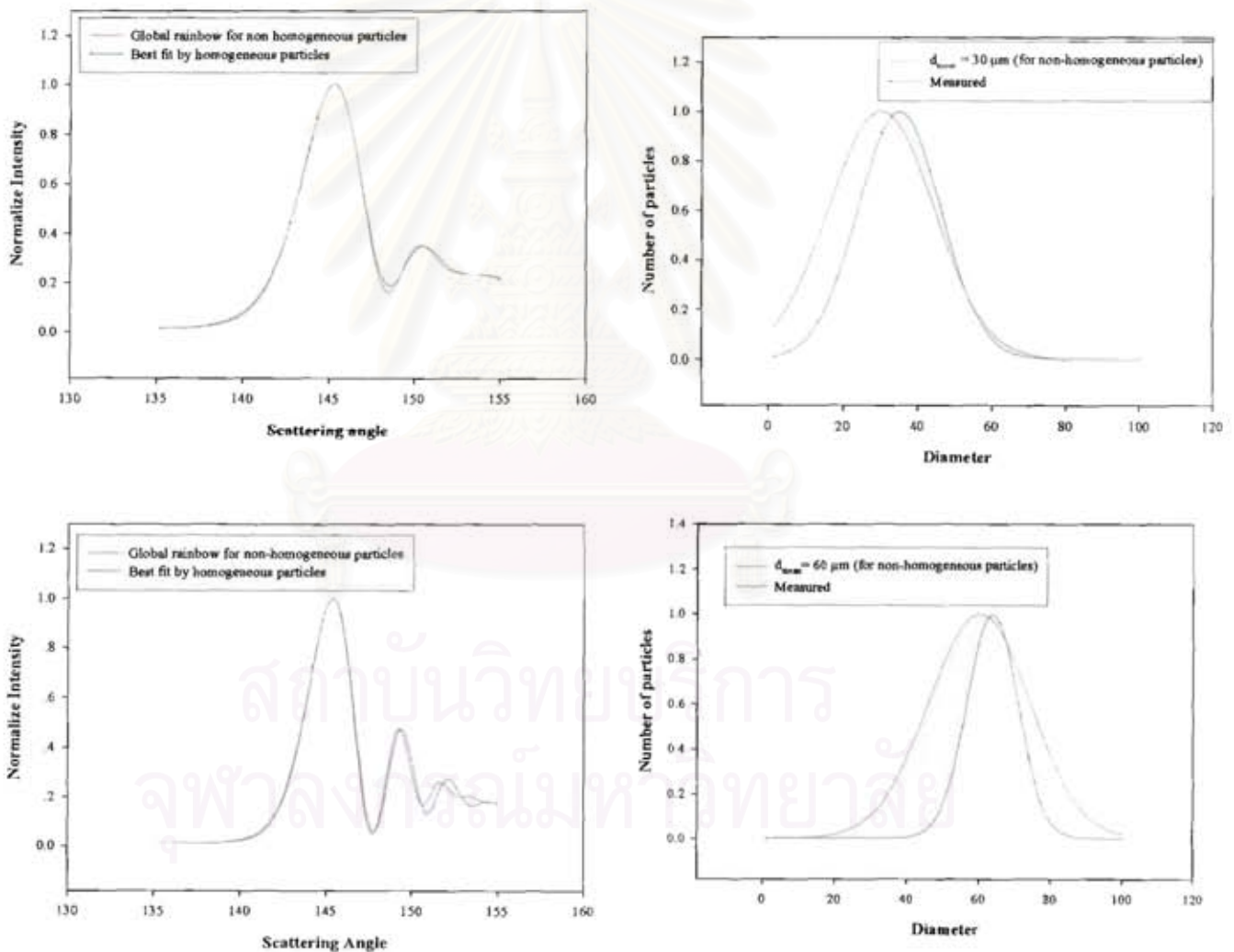
$$n_{\text{equi}} = 1.36 + d * (1.38 - 1.36) / 100 \quad (2)$$

Let us remember that an equivalent refractive index equal to 1.38 corresponds to a particle with b positive and a strong gradient at the surface.

Figure 11a displays, as red lines, three different global rainbow scattering diagrams corresponding to the law of equivalent refractive index given by equation (2) with different

size distributions shown in figure 11b, also in red lines. The size distributions are Gaussian with diameters running from 1 to 100 μm and the sigma is equal to 20. The mean diameters are respectively equal to 30, 60 and 90 μm .

These global rainbow scattering diagrams are then interpreted in the framework of the Nussenzveig theory (for homogeneous particles). The best fit of each global rainbow pattern and associated size distribution are also plotted in figures 11(a) and 11(b), as blue line. The fitting procedure assumes that size distributions are still Gaussian. Then only three quantities are to be found: mean diameter, refractive index and rms. Results are compiled in Table 1. When applied to global rainbow signals from a cloud of homogeneous particles, the extracted data exactly correspond to the initial data. The fit is assumed to be the best when the main global rainbow peak is well reconstructed. The presence of a gradient is observable at angles smaller than the main peak location as an overestimation of the recorded light intensity while at angles larger than the main peak location, the supernumerary peaks are shifted to smaller angles.



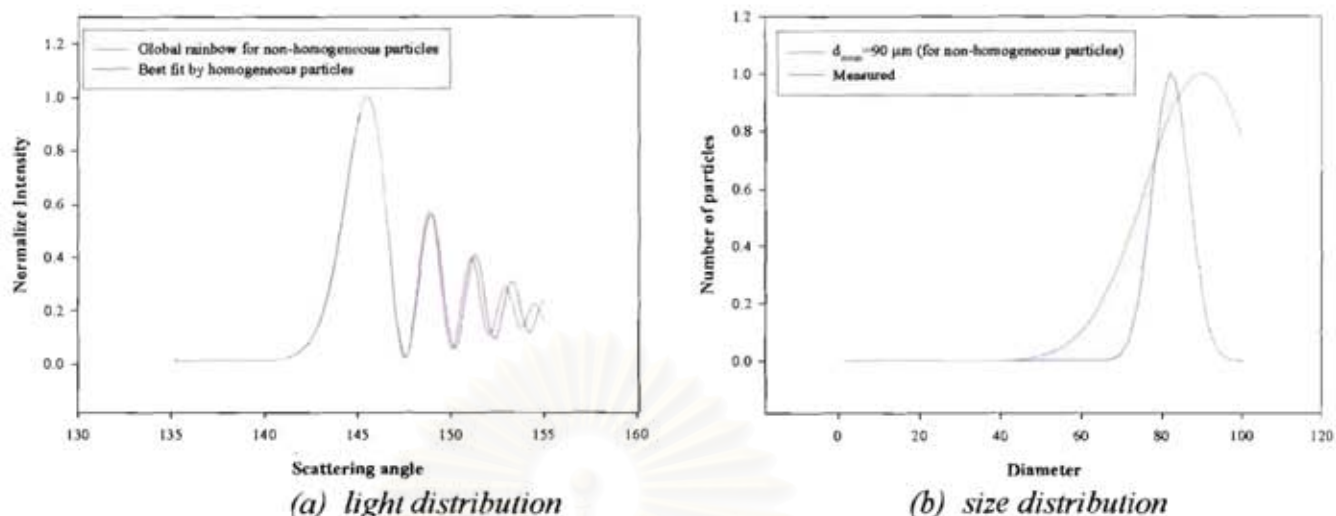


Figure 11(a) : the global rainbow from a cloud of non homogeneous droplets and its best fit by a cloud of homogeneous particles (Nussenzveig theory).
11(b): the size distribution of non-homogeneous and homogeneous droplets

Table 1: The extracted parameters corresponding to figure 11 data.

	Measured d_{mean}	Measured refractive index	Measured rms
$d_{\text{mean}} = 30 \mu\text{m}$	35 μm	1.369	$(236)^{(1/2)}$
$d_{\text{mean}} = 60 \mu\text{m}$	66 μm	1.374	$(124)^{(1/2)}$
$d_{\text{mean}} = 90 \mu\text{m}$	82 μm	1.377	$(42)^{(1/2)}$

The presence of a refractive index gradient (or equivalently of a correlation between the size and the refractive index (temperature)) will be essentially observable on the size distribution. The comparison of the size distribution measured by the global rainbow technique with the one obtained by an other technique as PDA is a possible way to assess the presence of such gradients.

5) Conclusion.

The sensitivity of the rainbow to radial refractive index gradients has been numerically studied.

For individual particles, an equivalent particle, defined as the homogeneous particle which scatters the light in forward and backward directions as does the particle with a radial gradient, can always be found. Then the gradient could be extracted only by adding extra knowledge coming from independent measurements (LIF, Infra-Red) or computations. Nevertheless, in the case of strong gradients at the particle surface, the value of the measured equivalent refractive index could depart enough from the physically possible values of the refractive index to unambiguously inform on the presence of a gradient.

For clouds of particles, when only the light in backward directions is collected, it is not possible to find a cloud of homogeneous particles which perfectly fits the global rainbow for particles with gradient, but the size distribution for the best fit can depart enough from the

actual size distribution to easily provide a gradient signature when comparing to size distribution measurements with an independent technique as PDA.

Acknowledgements: This work is partially supported by the European Community programs Interreg III “the intelligent engine II” and the “MUSCLES G4RD-CT-2002-00644” program. Miss Sawitree Saengkaew is partially supported by the French Ministère délégué à la Recherche et aux Nouvelles Technologies in the framework of “co-tutelle de these” and by the Thai Government by a Golden Jubilee Grant from the Thai Research Fund.

References.

- [1] Z.S. Wu, L.X. Guo, K.F. Ren, G. Gouesbet and G. Gréhan, *Improved algorithms for electromagnetic scattering of planes wave and shaped beams by multilayered spheres*, Applied Optics, 36, 5188-5198, 1997.
- [2] N. Doué, "Modélisation de l'évaporation de gouttes multicomposants", DEA report at SUPAERO, 2002.
- [3] S. Saengkaew, T. Charinpanitkul, L. Méès and G. Gréhan, *Rainbow refractometry :On the validity domain of Airy's and Nussenzveig's theories*, submitted to Optics Communications.
- [4] S.L. Min and A. Gomez, *High-resolution size measurement of single spherical particles with a fast Fourier transform of the angular scattering intensity*, Applied Optics, vol 35, 4919-4926, 1996
- [5] X. Han, K.F. Ren, Z.S. Wu, F. Corbin, G. Gouesbet and G. Gréhan, *Characterization of initial disturbances in liquid jet by rainbow sizing*, Applied Optics, vol 37, 8498-8503, 1998.



สถาบันวิทยบริการ
จุฬาลงกรณ์มหาวิทยาลัย



APPENDIX C7

**PROCESSING OF RAINBOW SIGNALS FROM
INDIVIDUAL DROPLETS.**

**PROCEEDINGS 20TH ANNUAL CONFERENCE ON
THE LIQUID ATOMIZATION AND SPRAY
SYSTEMS, ILASS EUROPE 2005, ORLEANS,
FRANCE 5-7 SEPTEMBER 2005.**

สถาบันวิทยบริการ
จุฬาลงกรณ์มหาวิทยาลัย

Processing of rainbow signals from individual droplets.

Sawitree Saengkaew^(1,3), Yves Biscos⁽²⁾, Nicolas Garcia⁽²⁾, Tawatchai Charinpanitkul⁽¹⁾, Hatachanok Vanisri⁽¹⁾, Gérard Lavergne⁽²⁾, Gérard Gouesbet⁽³⁾, Loïc Mées⁽³⁾ and Gérard Gréhan⁽³⁾

⁽¹⁾Center of Excellence in Particle Technology,

Faculty of Engineering,
Chulalongkorn University,
Bangkok, Thailand 10 330

⁽²⁾ONERA/DMAE, 02 Avenue Edouard Belin, 31 055, Toulouse

⁽³⁾UMR 6614/CORIA

CNRS/Université et INSA de Rouen, BP 12

76 800 Saint Etienne du Rouvray, CEDEX 8001, France

Abstract

The characterization of particles under evaporation is still a challenge. In rainbow refractometry, as for other techniques, recorded signals must be efficiently processed to extract relevant information as diameter and refractive index (i.e. the temperature and/or composition). This paper is devoted to the description of the latest developed processing strategy and its application to rainbow signals recorded at ONERA-Toulouse.

Introduction

In combustion of liquid, the liquid is most often introduced as a cloud of small droplets called spray. During the last decennials, a large effort has been devoted to enhance the understanding of the evolution of such sprays, essentially in connection with the improvement of the energy use and the reduction of the pollution. Nevertheless, these efforts have essentially been focused on the measurements of dimensional and geometrical quantities as particle velocities and size distributions. Nowadays, a challenge is to measure, not only these geometrical quantities, but also thermo-chemical quantities as temperatures and compositions of droplets in flows. To reach this aim, different techniques have been developed or are under development, each one with its advantages and limitations, each one with a particular way to probe the droplets, depending on the physical principles on which the technique is based.

Without being exhaustive, we can mention the following techniques: LIF, MDR, Infra-Red and rainbow as potentially able to extract thermo-chemical quantities from droplets.

LIF technique, or more specially, the two band LIF technique, is based on the ratio of the fluorescence emission from two spectral bands with a different sensitivity with respect to temperature. This technique has been developed by F. Lemoine et al at Nancy [1]. Numerical simulations show that LIF technique gives an information essentially depending on the central part of the droplet.

On the contrary, MDR's, as reviewed by R. K. Chang [2], are essentially sensitive to the periphery of the droplets while Infra-red measurements give access to the surface temperature of the droplets [3].

The rainbow refractometry has a strong sensitivity to refractive gradient close to the particle surface [4].

Nevertheless, before trying to measure the properties of complex particles, it is necessary to understand the limits of the different techniques when applied to homogeneous particles and, if possible, to extend the domain of applicability of the techniques and their accuracy.

This paper is devoted to the rainbow refractometry of individual particles with the experimental configuration developed at ONERA-Toulouse. The section 2 recalls and discusses a previous processing strategy. Section 3 presents a new processing strategy and discusses automatic processing algorithms. In this section, the processing algorithms are evaluated by "measuring" Lorenz-Mie computed "signals". Section 4 is devoted to the processing of real experimental signals recorded at ONERA-Toulouse. Section 5 is a conclusion.

Classical processing strategy

Rainbow refractometry is based on the fact that the location of the main rainbow (the rainbow created by the rays experimenting one internal reflection) depends on the refractive index which depends on the temperature and composition of the droplets. Figure 1 displays the real part of the refractive index of water versus the temperature. A variation of temperature of about 1°C corresponds to a variation of the refractive index of about 0.0002 by °C at 20°C, or 0.0006 by °C at 100°C. These variations of the refractive index correspond to an angular shift of the rainbow of about 0.01° to 0.04°.

With two parameters to be measured i.e. the diameter and the real part of the refractive index, the following strategy is used to process signals recorded from individual particles. The scattering diagram is recorded at two different locations: one in forward (from 27.18° to 32.82° at ONERA-Toulouse) is used to extract the diameter while a second one, recorded

around the rainbow angle (from 140.18° to 145.82° at ONERA-Toulouse), is devoted to extract the real part of the refractive index. The measurement is assumed to be satisfactory when, after a number of iterations, refractive index and diameter values are stable.

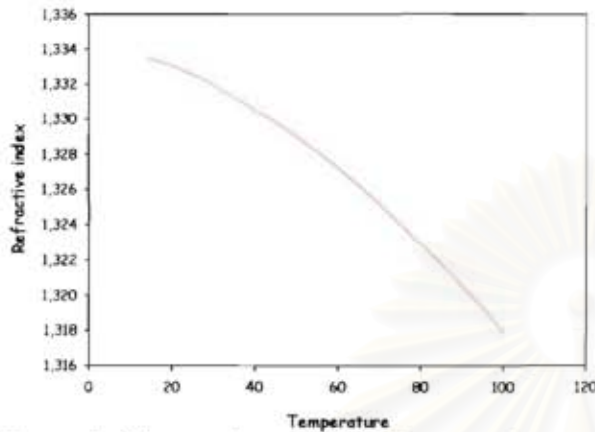


Figure 1 : Water real part of the refractive index versus temperature.

To obtain the diameter, it is assumed that the angular frequency of the forward signal is essentially a function of the particle diameter.

To obtain the refractive index, the recorded signal around the rainbow angle is filtered to remove high frequencies (ripples), then the maximum of the filtered signal is assumed to correspond to the Airy maximum. By applying Airy formula, using the diameter extracted from the forward range and the location of the maximum of the backward filtered signal, a refractive index value is obtained. This refractive index value is used to recompute the diameter from the forward signal and so on. The process ends after a number of iterations stable when diameter and refractive index values are stable, usually after 3-5 iterations.

The main limit of this approach is due to the filtering process, because it is more and more difficult to remove the ripple structure without perturbing the low frequency Airy structure when the particle diameter decreases. This fact is exemplified in figure 2, extracted from Damaschke PhD thesis [5]. Figure 2 displays the refractive index extracted from Lorenz-Mie theory computations versus the particle diameter. For diameters between 20 μm to 80 μm the effect is very important but for a particle of 100 μm the effect is still important enough to limit the refractive index measurement accuracy to the second digit, corresponding to an accuracy in degree of about 10 °C. This fact is exemplified by figure 3 which displays reconstructed rainbow signals by FFT with the number of points used for the FFT reconstruction as the parameter.

To solve this difficulty, Damaschke proposes to use femtosecond pulses in such a way that externally

reflected rays and internally reflected rays impinge on the detectors at different times, and then do not interfere, therefore suppressing the ripple structure.

Nevertheless, this approach is limited to large enough particles too, and is not easy to implement, beside being cost full.

Below we propose a new approach which includes the ripple structure in the processing scheme.

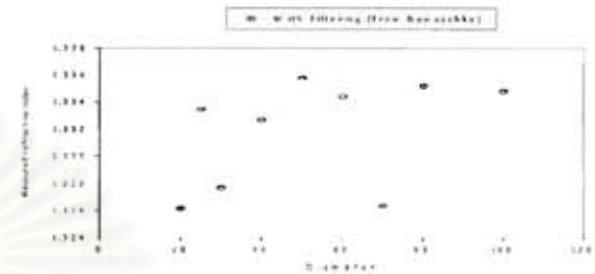


Figure 2: Measured refractive index versus particle diameter, from Damaschke PhD

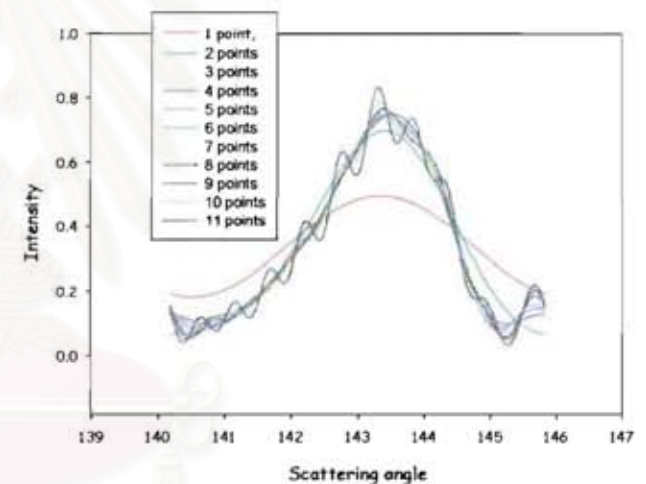


Figure 3: Reconstructed rainbow signal by FFT processing for a particle with a diameter equal to 100 μm . The parameter is the number of points for FFT reconstruction.

New processing strategy

In the proposed strategy, forward as well as backward signals are processed without any filtering. We are then searching for an agreement in frequency and angular absolute location (phase) for both forward and backward signals.

To be as accurate as Lorenz-Mie theory but as fast as Airy theory, the Nussenzweig theory is used [6]. First the strategy is evaluated by using numerical Lorenz-Mie signals.

Automatic processing

The aim is to find an algorithm to automatically process forward and backward sections

of scattering diagrams. To reach this objective, we first describe the automatic processing at forward assuming that the refractive index is known, secondly at backward assuming that the size is known, and finally at both ranges without any assumption.

Forward.

Forward, the main information is the signal frequency. Our processing strategy is then to find a diameter for which the Nussenzweig signal possesses the same maximum in the frequency FFT domain than the signal to study, then to refine the result by using the phase. To automatically find the diameter, the Brent method is used [7]. The Brent method has been selected because this method is guaranteed to converge, as far as the function can be evaluated within an initial interval known to contain a root.

The main difficulty when using the Brent method is to have one and only one root in the studied domain. For the main FFT peak location fitting, it is easy because the location of the main FFT peak is a monotonic increasing function of the diameter. For the phase, the function is periodic with respect to the diameter. For the ONERA-Toulouse configuration, the period for the phase function is equal to about 0.8 μm .

Our algorithm proceeds with the following steps:

- 1) Starting from a large diameter domain (typically 30-130 μm), for a given refractive index, a first diameter is obtained by fitting, with the Brent algorithm, the Lorenz-Mie FFT peak location and the Nussenzweig FFT peak location (the peak location is determined by using a spline approximation).
- 2) The phase difference between the Lorenz-Mie signal and the best Nussenzweig signal is computed.
- 3) Using this phase difference, a new domain of diameter for the Brent algorithm on phases is defined. This new subdomain of diameter is smaller than 0.8 μm .

Figure 4 displays the series of diameters tested by the Brent algorithm during the processing of a Lorenz-Mie signal. The Lorenz-Mie signal has been computed for a diameter equal to 100 μm and a refractive index equal to 1.364. In Figure 4 the seven first iterations (red circles) correspond to the main peak FFT fitting, while the four last iterations (green squares) correspond to the phase fitting. The convergence is fast (11 iterations), and the extracted diameter very accurate ($d_{\text{measured}} = 100.007 \mu\text{m}$).

Backward.

Backward, the main information is the main peak location. Then our processing strategy is to find a refractive index for which the Nussenzweig signal must possess the same location than for the Lorenz-Mie signal. Here again the Brent method is used, but the function to evaluate is depending of the correlation between the signal under study and the Nussenzweig prediction. More specifically, as exemplified in figure 5, the difference between the maximum of correlation between signal and measurement will code the

refractive index. When the refractive index value is too high the difference will be negative, while when the refractive index value is too small the difference will be positive (see figure 5). Nevertheless, this approach has been found to be too much sensitive to oscillations. Therefore we rather compare the values of the integral between 1 to 1024 and 1024 to 2048. Figure 6 displays the convergence of the algorithm when the size is assumed to be known. Here again the final result is efficiently obtained (only 9 iterations).

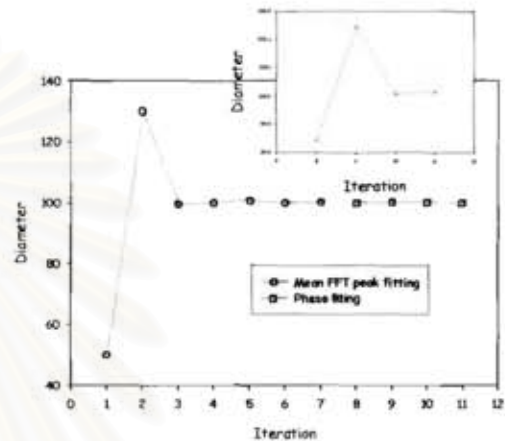


Figure 4: Convergence of the Brent method (forward). The refractive index is assumed to be known. The extracted diameter is equal to 100.007 μm .

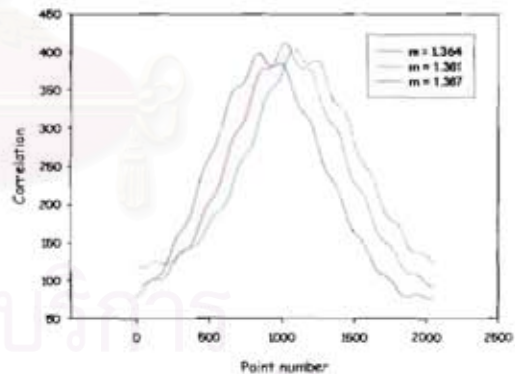


Figure 5: Behaviour for a particle with a diameter equal to 100 μm and a refractive index equal to 1.364. The parameter is the refractive index of the test particle: 1.361 in green, 1.364 in red and 1.367 in blue..

From the analysis of measurements, it is observed that the quality of the refractive index measurement decreases when the particle size decreases, especially for diameters smaller than 60 μm . A close examination of backward scattering diagrams shows that Nussenzweig predictions with $p=0$ and 2 do not fit well Lorenz-Mie predictions due to the perturbing influence of the second rainbow. For large refractive indices, the influence of the second rainbow is less significant and good refractive index measurements are possible for particles as small as 30 μm .

Measurements of smaller particles are may be possible but with an other experimental configuration.

The results previously displayed show that, when the refractive index is known, the size can be extracted with a high accuracy and that, when the size is known, the refractive index can be extracted with a high accuracy too. The next step is to simultaneously extract both size and refractive index.

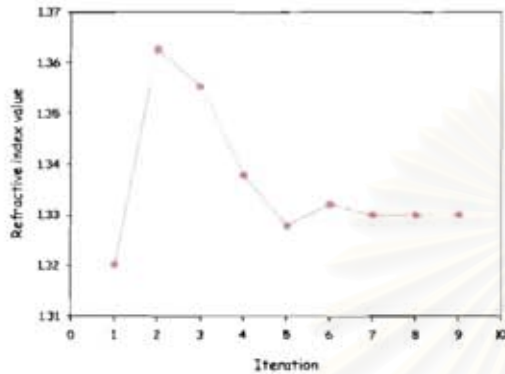


Figure 6: Convergence of the Brent method (backward). The extracted refractive index value versus iterations.

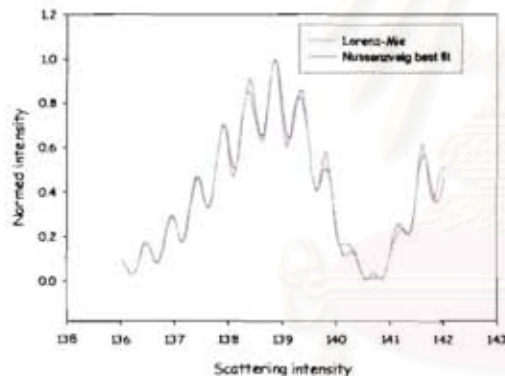


Figure 7: Comparison at between the Lorenz-Mie scattering diagram and the Nussenzweig scattering diagram for the extracted refractive index (backward).

Forward and backward.

To extract the couple diameter/refractive index from a couple of measurements, the following algorithm is used:

1. From the angular location of the backward signal, a first refractive index is computed in agreement with the geometrical optics law (the size is not taken into account).
2. With this value of the refractive index, the size is extracted from the angular frequency.
3. The size is refined by searching for a phase agreement.
4. With this size, the refractive index is researched by correlation
5. The steps 2 to 4 are repeated up to convergence when a stable determination of both diameter and the size is obtained.

The convergence iterative process is exemplified in Figure 8 where the different values of size and refractive index tested by the Brent procedure are plotted. We use circles for the diameter, in red by frequency fitting and in green by phase fitting, while the refractive index is marked with blue squares. For this case (diameter equal to 100 μm and refractive index equal to 1.364), the convergence has been obtained for 44 iterations.

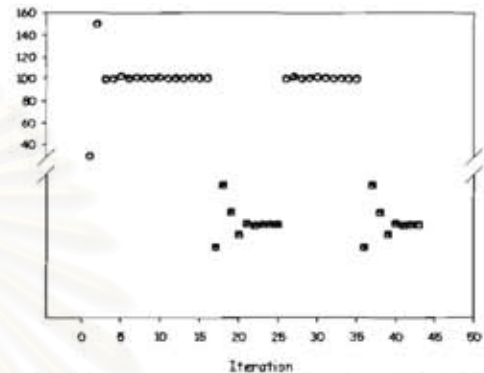


Figure 8: Convergence of the Brent method (forward and backward). The extracted diameter by frequency in red, the extracted diameter by phase in green and the extracted refractive index by correlation in blue.

The quality of the inversion is exemplified in Table 1 where extracted diameters and refractive indices are given for different particle sizes.

Diameter	Extracted diameter	Extracted refractive index
100 μm	99.98 μm	1.3642
98 μm	96.57 μm	1.3643
96 μm	95.97 μm	1.3644
94 μm	93.99 μm	1.3641
92 μm	90.60 μm	1.364
90 μm	90.00 μm	1.3642
80 μm	79.35 μm	1.3636
70 μm	69.36 μm	1.3633
60 μm	60.03 μm	1.3634
50 μm	50.82 μm	1.3620
40 μm	40.77 μm	1.3625
30 μm	30.09 μm	1.3623

Table 1: Dual processing of forward and rainbow signals. The extracted diameters and refractive indices.

From the results displayed in Table 1, we conclude that the proposed procedure is efficient to extract with a high accuracy the couple diameter/refractive index from computed signals. The next step is to evaluate its efficiency when apply to real signals.

Real signals.

In red, Figure 9 displays a real dual signal recorded at ONERA-Toulouse on a line of droplets created by a monodisperse generator. Figure 9a corresponds to the recorded forward signal and figure 9b corresponds to the recorded backward signal. Experimental signals are noisy, especially the backward one. Therefore, this signal is first filtered out from high frequencies. Because noise frequencies are very larger than the Airy and ripple frequencies, the choice of the cutting frequency before reconstruction is not critical. In figure 9b, (and 10b) the green line corresponds to the reconstructed experimental signal after filtering.

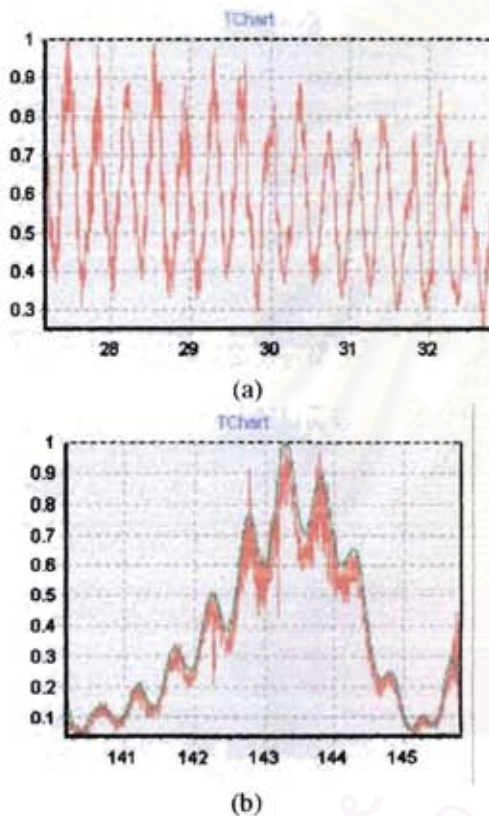


Figure 9: In red, recorded values in forward and backward domains (from ONERA-TOULOUSE). In green, the backward signal filtered out from high frequencies (noise).

The processing algorithm is close to the one previously described for computed signals but a new step has been added to ensure the unicity of the return:

1. From the angular location of the backward signal, a first refractive index is computed in agreement with the geometrical optics law (the size is not taken into account).
2. With this value of the refractive index, the size is extracted from the angular frequency.
3. The size is refined by searching for a phase agreement.
4. With this size, the refractive index is researched by correlation.

5. A new diameter estimation is obtained by searching phase agreements between the derivatives of backward signals (measured and computed).
6. The steps 2 to 5 are repeated up to convergence when a stable determination of both diameter and size is obtained.

Figures 10a and 10b display the experimental signal and its best fit computed in the Nussenzveig framework by applying this procedure. The agreement is satisfactory. Figure 11 displays the successive values of the diameter and refractive index tested by the Brent method. The convergence is obtained with about 60 iterations. The computation of one scattering diagram section by Lorenz-Mie theory for a diameter equal to 100 μm , with our code, takes about 6 s. Then, by using Lorenz-Mie theory, the inversion of an experimental couple of data will take about $6 \times 60 = 360$ seconds (6 minutes). By using the Nussenzveig approach, the full inversion is carried out in about 1.5 seconds.

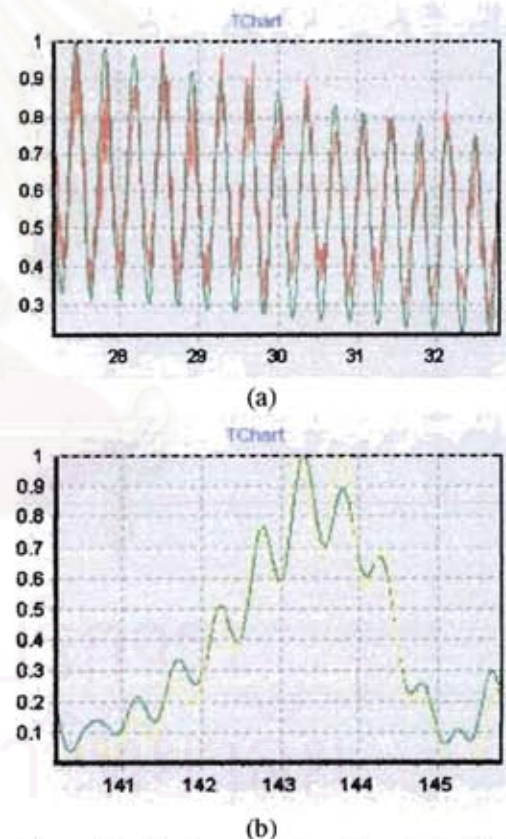


Figure 10: The forward signal in red, the filtered experimental backward signal (in green) and its best fit by Nussenzveig theory (in yellow).

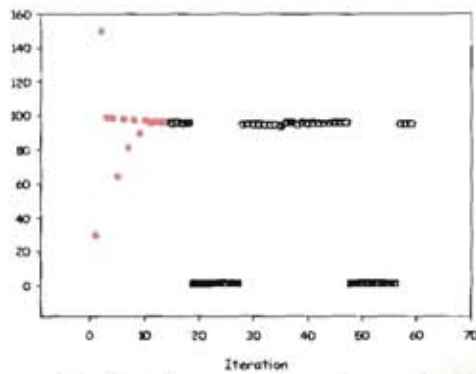


Figure 11: Iterations on diameters and refractive indices for a couple of experimental signals.

Figure 12 plots the measured refractive index versus the measured diameter, for an injection at 22°C in an air at 23°C and a distance to the nozzle from 30 mm to 50 mm by steps of 5 mm. For each measurement location, all the Onera signals have been fully processed. It is underlined that all points can be very well fitted by a linear regression. Furthermore, the measured refractive index at 30 mm corresponds to a temperature equal to 23°C while the refractive index at 50 mm corresponds to a temperature equal to 18°C.

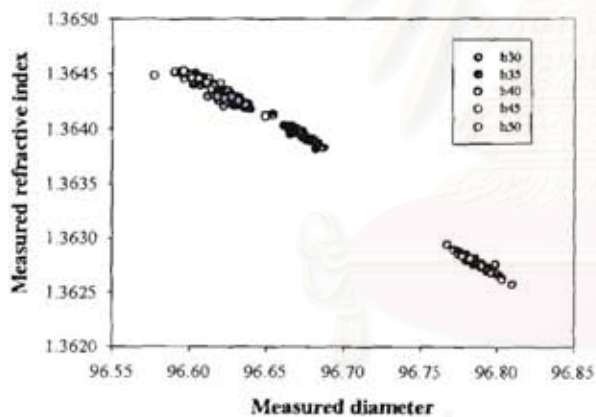


Figure 12: Measured refractive index versus measured diameter. The parameter is the distance from the nozzle.

Conclusion

In this paper we have demonstrated that the processing of experimental rainbow signals can be carried out taking into account the ripple structure, and that this processing can be carried out in real time by working with the Nussenzveig theory.

Extremely accurate measurements of droplet diameters and refractive indices have been carried out. The next step is to apply this approach to other experimental conditions (spray under combustion).

Acknowledgements

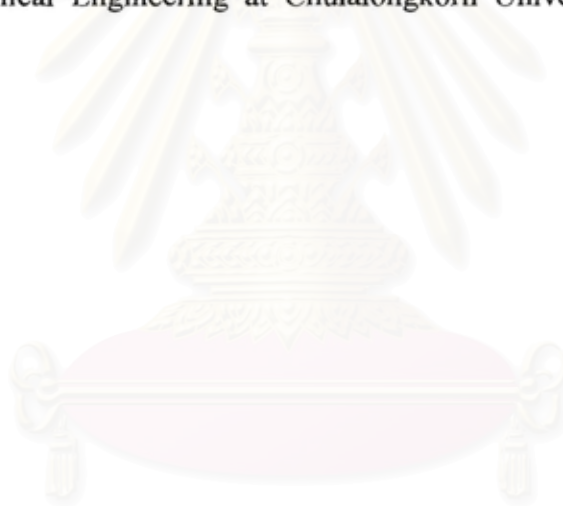
University-Industry Collaborative Research Fund of Chulalongkorn University for CEPT is gratefully acknowledged. Partial support from European Community programs Interreg III "The intelligent engine II" and the "MUSCLES G4RD-CT-2002-00644" programs are also acknowledged. S.S. is partially supported by the French Ministère à la Recherche et aux Nouvelles Technologies in the framework of « cotutelle de thèse » and the Royal Golden Jubilee Scholarship of Thailand Research Fund. T.C. and H.V. gratefully acknowledge partial support from TFR-RTA grant for Prof. W. Tanthapanichakoon.

References

- [1] Lavielle P. ; Lemoine, F. ; Lebouché M. (2002) Experimental investigation on interacting low evaporating droplets temperature in linear stream using two colors laser induced fluorescence, *Combustion Science and Technology* 174 (4) : 117-142
- [2] R.K. Chang and A.J. Campillo, in *Optical processes in microcavities*, World Scientific, 1996
- [3] C. Amiel, *Application de techniques optiques à l'étude du comportement dynamique et thermique de gouttes en interaction avec une paroi chauffée*, Thèse de PhD, Toulouse : Ecole Nationale Supérieure de l'Aéronautique et de l'Espace, 2003
- [4] S. Saengkaew, T.Charinpanitkul, H. Vanisri, L. Mées, Yves Biscos, Nicolas Garcia , Gérard Lavergne, G. Gouesbet and G. Gréhan, *Rainbow refractometry on particles with radial refractive index gradients*. Submitted to *Atomization and Sprays*.
- [5] N. Damaschke, *Light Scattering Theories and their Use for Single Particle Characterization*, PhD, Technische Universität Darmstadt, 3 December 2003.
- [6] H.M. Nussenzveig, High-frequency scattering by a transparent sphere. I Direct reflection and transmission, II Theory of the rainbow and the Glory, *Journal of Mathematical Physics*, vol 10, 82-124 and 125-176, 1969.
- [7] W.H. Press, S.A. Teukolsky, W.T. Vetterling and B.P. Flannery, *Numerical Recipes, The Art of the Scientific Computing*, Cambridge University Press, 1986.

Biography

Miss Sawitree Saengkaew was born on January 6 1976. She began her study in high school education at Satriwittaya School in Bangkok. In 1998, she received her Bachelor Degree of Engineering in Chemical Engineering specialty with 2nd class honor from faculty of Engineering, Rangsit University, Bangkok, Thailand. After that she continued her study in Chemical Engineering at Chulalongkorn University and graduated in 2001. In 2002, she enrolled her Doctoral Degree Program at Chulalongkorn University and also at Rouen University (France) under co-tutelle PhD program which is a collaboration between France and Thailand supported by French government. During first 3 years of her study she had been in France for 6 months each year. In December 2003, she was supported by Royal Golden Jubilee Scholarship of Thailand as a result she could spend time 6 months more in France to carry out her work for her last year of the study. She was awarded a Ph.D. degree in Physic Science from Rouen University with the mention “très honorable et félicitation du jury” (or 1st honor) in October 2005. In January 2006, she received her Ph.D degree of Chemical Engineering at Chulalongkorn University with mention very good.



สถาบันวิทยบริการ
จุฬาลงกรณ์มหาวิทยาลัย